UNIVERSITY OF LIVERPOOL

Department of Chemistry

Probing the Surface Chemistry of Peptide Hydrogels using NMR Spectroscopy

Thesis submitted in accordance with the requirements of the University of Liverpool for the degree of Doctor of Philosophy

By

Matthew Wallace

July 2017

Probing the Surface Chemistry of Peptide Hydrogels using NMR Spectroscopy

Matthew Wallace

Abstract

Self-assembled hydrogels are formed upon the assembly in aqueous solution of low molecular weight gelators (LMWGs) into fibrous networks. These networks immobilise the water, conveying solid-like properties to the material. Self-assembled hydrogels have a wide range of applications, from cell culturing to environmental sensing and remediation. In the majority of cases, the utility of the gels arises from their self-assembled nature and high water content. These two properties, however, mean that the gels are notoriously difficult to characterise. Over the past two decades, techniques to characterise the hydrogels on a molecular level in a non-invasive manner have become well established. For example, the existence of hydrogen-bonding interactions between the assembled molecules can be probed using infra-red spectroscopy while the interactions between aromatic groups can be probed using UV-Vis spectroscopy. A neglected aspect of self-assembled hydrogels has been the interfacial, or surface, chemistry of the self-assembled fibres. Properties such as the charge, hydrophobicity and ion binding dynamics of the fibres determine the fundamental structure and behaviour of the materials. For example, these properties determine the interactions between adjacent fibres forming the gel networks which, in turn, determine the macroscopic mechanical properties of the materials. Nevertheless, established analytical techniques cannot directly provide information on the surface chemistry of the gel fibres. In this Thesis, novel techniques based on nuclear magnetic resonance spectroscopy (NMR) were developed to study the surface chemistry. The techniques can be implemented on most modern NMR equipment and are thus available to the majority of researchers in the field.

Focussing on *N*-functionalised dipeptide LMWGs, it is demonstrated how the surface chemical properties of the gels can be measured by studying the interaction with the fibres of a range of probe molecules and ions. The probes include cations, cation-binders and hydrophobic organic solvents. A range of advanced NMR techniques has been developed to detect and quantify the interaction of these probe species with the NMR-invisible gel fibres. It is thus possible to study, for example, the loss of negative charge and increase in hydrophobicity of the gel fibres as the pH of a sample is decreased. The surface chemical properties of the gels can also be used to predict the interaction with the gel fibres of a number of model drug compounds as well as the stability of the gels when exposed to external solutions.

Methods for the direct measurement of the solution pH and Ca^{2+} concentration by NMR spectroscopy are also presented in this Thesis. These methods greatly aid the analysis of samples by NMR as they avoid the need for separate electrochemical measurements. It is also demonstrated how controlled pH and Ca^{2+} concentration gradients may be established in standard 5 mm NMR tubes and analysed using standard NMR equipment.

Acknowledgements

I am much indebted to Professor Dave Adams and Dr Jon Iggo for their guidance and encouragement during my PhD project as well as during my undergraduate studies. I am also very grateful to Unilever for generously providing 50% of the funding required for the research project through a CASE Award. The other 50% of the funding was supplied by the EPSRC under a DTA. Professor Dave Adams, Dr Mike Butler (Unilever) and Dr Bill Frith (Unilever) ensured that the required funding was in place.

All peptide materials used in this Thesis were synthesised by Professor Adams, with the exception of PBI-A (Chapter 4, Section 4.3.4.3) which was synthesised by Dr Emily Draper (Liverpool). Dr Iggo ensured that the NMR spectrometers were kept in operational condition and provided guidance on the NMR aspects of the project. Dr Frith provided guidance on the hydrogel aspects of the project and valuable advice concerning the rheological analysis of hydrogel materials. The NMR measurements at very high field (Chapter 2, Section 2.4.1) were performed at the NMR Centre for Structural Biology at the University of Liverpool with the assistance of Dr Marie Phelan. All confocal and scanning electron microscopy images were recorded by Andre Zamith Cardoso, a PhD student in the research group of Professor Adams. AZC also recorded all infra-red spectra and X-ray powder diffraction patterns.

This Thesis has benefitted from many helpful discussions with fellow researchers in the fields of NMR spectroscopy and self-assembled gels. Special mentions go to the following individuals: Andre Cardoso is thanked for helpful discussions regarding the fundamental aspects of peptide assembly and its characterisation using a range of analytical approaches. Emily Draper is thanked for helpful discussions regarding the magnetic alignment of photoconductive hydrogel materials. Dr Juan Miravet (Universitat Jaume 1, Castellón de la Plana, Spain) is thanked for helpful critique of my published papers and ideas for future work. Dr Miravet was also a generous host when I visited his lab to discuss my work and try out some NMR experiments.

Finally, I am very grateful to the anonymous referees of the published scientific papers appearing in this Thesis. This Thesis has greatly benefitted from their careful reading of the manuscripts and helpful suggestions.

Publications, Presentations and Awards Arising from this Thesis

Publications

"Kinetically Controlled Coassembly of Multichromophoric Peptide Hydrogelators and the Impacts on Energy Transport" H. A. M. Ardoña, E. R. Draper, F. Citossi, **M. Wallace**, L. C. Serpell, D. J. Adams, and J. D. Tovar, *J. Am. Chem. Soc.*, 2017, **139**, 8685–8692.

"Nonlinear Effects in Multicomponent Supramolecular Hydrogels" E. R. Draper, **M. Wallace**, R. Schweins, R. J. Poole and D. J. Adams, *Langmuir*, 2017, **33**, 2387-2395.

"Probing the surface chemistry of self-assembled peptide hydrogels using solution-state NMR spectroscopy" **M. Wallace**, J. A. Iggo and D. J. Adams, *Soft Matter,* 2017, **13**, 1716-1727.

"pH dependent photocatalytic hydrogen evolution by self-assembled perylene bisimides" M. C. Nolan, J. J. Walsh, L. L. E. Mears, E. R. Draper, **M. Wallace**, M. Barrow, B. Dietrich, S. M. King, A. J. Cowan and D. J. Adams, *J. Mat. Chem. A*, 2017, **5**, 7555-7563.

"Self-sorted photoconductive xerogels" E. R. Draper, J. R. Lee, **M. Wallace**, F. Jäckel, A. J. Cowan and D. J. Adams, *Chem. Sci*., 2016, **7**, 6499-6505.

"On the syneresis of an OPV functionalised dipeptide hydrogel" A. M. Castilla, **M. Wallace**, L. L. E. Mears, E. R. Draper, J. Doutch, S. Rogers and D. J. Adams, *Soft Matter*, 2016, **12**, 7848-7854.

"Using solution state NMR spectroscopy to probe NMR invisible gelators" **M. Wallace**, J. A. Iggo and D. J. Adams, *Soft Matter*, 2015, **11**, 7739-7747.

"Magnetically Aligned Supramolecular Hydrogels" **M. Wallace**, A. Z. Cardoso, W. J. Frith, J. A. Iggo and D. J. Adams, *Chem. Eur. J.*, 2014, **20**, 16484-16487.

Oral Presentations

"Probing the surface chemistry of peptide hydrogels using NMR spectroscopy" MC13: 13th International Conference on Materials Chemistry, 10-13th July 2017, Liverpool, UK.

"NMR investigations of self-assembled hydrogels" Invited departmental seminar at Universitat Jaume 1, Departament de Química Inorgànicai Orgànica, 30th June 2016, Castellón de la Plana, Spain.

"The surface chemistry of self-assembled hydrogels" GERMN 2016: 8th GERMN / 5th Iberian NMR Meeting, 27-29th June 2016, Valencia, Spain.

"Solution-state NMR spectroscopy of NMR invisible gels" MC12: 12th International Conference on Materials Chemistry, 20-23rd July 2015, York, UK.

Poster Presentations

"Titrations without the additions: The rapid measurement of pK_a values using NMR imaging techniques" RSC NMR Discussion Group Postgraduate Meeting 2017, 22nd June 2017, Glasgow, UK. (One of three runner-up poster prizes awarded).

"Solution-state NMR to Understand Peptide Fibre Surface Chemistry and Gelation" RSC Faraday Division Sponsored Meeting on Self-Assembling Materials for Biomedicine, 14th April 2016, Reading, UK.

"Solution-state NMR to understand peptide gel fibre surface chemistry and gelation" PepMat 2016: Peptide Materials for Biomedicine and Nanotechnology, 14-16th March 2016, Barcelona, Spain.

"Multinuclear NMR to Understand Peptide Surface Chemistry and Gelation" MASC 2015: RSC Macrocyclic and Supramolecular Chemistry Group Annual Meeting, 21-22nd December 2015, Durham, UK.

Awards

Royal Society of Chemistry Ronald Belcher Award 2017, "*Awarded for development of novel NMR methods for characterisation of gel fibres in NMR invisible soft materials*". Awarded by the Analytical Division of the Royal Society of Chemistry.

List of Abbreviations

Ac	Acetic acid
δ_{obs}	Observed chemical shift
CPMG	Carr-Purcell-Meiboom-Gill
CSI	Chemical shift imaging
DMSO	Dimethylsulfoxide
DSS	2,2-dimethyl-2-silapentane-5-sulfonate
EFG	Electric field gradient
ESI	Electronic supplementary information
Form	Formic acid
FTIR	Fourier transform infra-red
GdL	Glucono-δ-lactone
Gly	Glycine
H-bonding	Hydrogen bonding
HDO	Mono-deutero-water
IPA	Isopropanol
IUPAC	International Union of Pure and Applied Chemistry
K_{Ca}	Effective Ca^{2+} binding constant (Chapter 4, Section 4.3.7)
LMWG	Low molecular weight gelator
MeOH	Methanol
min	minutes
MPA	Methylphosphonate
NMR	Nuclear magnetic resonance
NOE	Nuclear Overhauser effect
PXRD	Powder X-ray diffraction
RDC	Residual dipolar coupling
RQC	Residual quadrupolar coupling
SEM	Scanning electron microscopy
STD	Saturation transfer difference
tBuOH	*tert*-Butanol
TEM	Transmission electron microscopy
TSP	3-(Trimethylsilyl)propionate

Contents

Chapter 1: Introduction

1.1 Introduction to self-assembled gels

Self-assembled supramolecular hydrogels are formed upon the self-assembly in solution of small molecules (low molecular weight gelators, LMWGs) into fibres. The fibres interact with one another to form a sample-spanning network which immobilises the water by capillary forces (Scheme 1-1).[1-4] LMWGs typically have a low molecular mass (< 1000 Da) and can thus be distinguished from supramolecular gels based on covalent polymers in which the chains are linked by non-covalent interactions.[5] Self-assembled hydrogels have been proposed for a wide range of applications in the fields of drug delivery systems,[6] cell culturing,[7] pollutant capture materials,[8] catalysis[9] and organic electronics.[10, 11]

In order to prepare hydrogels tailored for specific applications, it is important to have a good understanding of both the hydrogel materials and the processes by which they form. The utility of these gels most often arises from their self-assembled, stimuli-responsive nature and their high water content.[7, 8, 12] These two properties, however, mean that the gels are notoriously difficult to characterise. The non-covalent nature of the interactions between the LMWGs renders the materials very sensitive to changes in temperature or hydration, as may occur during preparation for many common analytical techniques such as scanning electron microscopy (SEM).[13, 14] It is thus desirable to study instead the materials in a non-invasive manner under their native conditions of temperature and hydration. NMR spectroscopy, in principle, allows for such an analysis; however, existing analytical approaches provide only limited insight into the materials. The aim of this Thesis is thus to develop new analytical techniques based on NMR spectroscopy for the non-invasive analysis of self-assembled hydrogels.

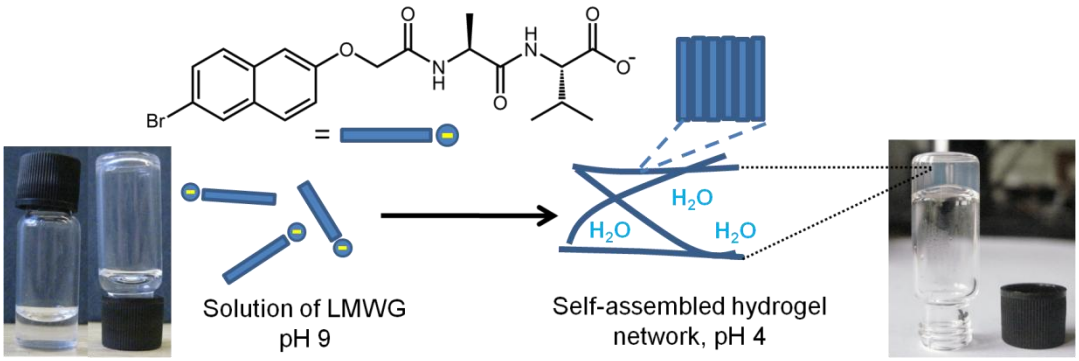

Scheme 1-1. Cartoon to illustrate the formation of hydrogels *via* the self-assembly of LMWGs into fibrous networks. In this example, the molecules are freely dissolved in solution at pH 9. If the pH is gradually reduced, the carboxylate group becomes protonated and self-assembly is initiated. Peptide-based LMWGs and methods by which gels may be prepared are reviewed in Section 1.4. The packing arrangement of the LMWGs in the self-assembled fibres is for figurative purposes only and does not necessarily represent the true packing motif of the LMWG.

As discussed more fully in Section 1.2, a notable deficiency of existing analytical approaches is their almost total inability to characterise the surface chemical properties of self-assembled hydrogels. Properties such as the charge, hydrophobicity and ion-binding dynamics of hydrogel fibres determine the interactions between adjacent fibres and thus the development of the gel network (Scheme 1-2).[15, 16] As discussed in Section 1.3, these properties also determine how the gels interact with other entities including drug molecules, living cells or pollutants. Such information is vital when designing hydrogel systems for specific applications.[17] A particular focus of this Thesis is thus the development of methods to study this surface chemistry.

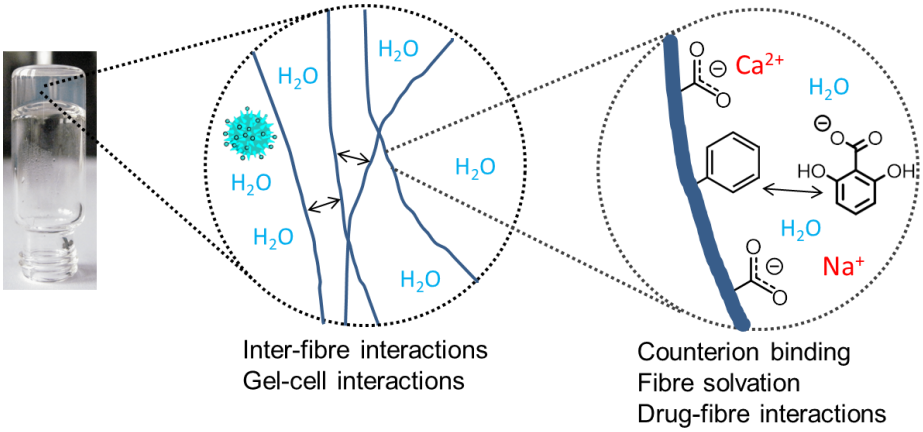

Scheme 1-2. Cartoon to illustrate the importance of the surface chemistry in determining the overall form and function of self-assembled hydrogel networks.

A very large number of LMWGs and assembly conditions have so far been reported and a complete review is beyond the scope of the project. The interested reader is directed to the extensive number of reviews dedicated to the topic.[12, 18-21] LMWGs based on short *N*-functionalised peptides (example in Scheme 1-1) are a particularly versatile and well-studied class. Many of the key challenges faced in the analysis of peptide-based systems are common to all other classes of LMWG.[22] As such, peptide-based LMWGs can be considered as excellent model systems for the development of new analytical techniques to study self-assembled hydrogels. It is in this capacity that *N*-functionalised peptide-based LMWGs are used throughout the project, with the understanding that the same approaches could be readily applied to other systems. Examples from the scientific literature are highlighted where this is the case.

In the following Sections, the literature relevant to the project is reviewed. Section 1.2 comprises a review of existing methods to characterise self-assembled hydrogels. The importance of the surface chemistry of hydrogels is discussed in Section 1.3. Peptide-based LMWGs are reviewed in Section 1.4. The aims of the Thesis are discussed in Section 1.5.

1.2 Existing techniques for the characterisation of self-assembled gels

A particular challenge when characterising self-assembled hydrogels is their hierarchical structure which spans multiple length scales (Scheme 1-3).[19, 23, 24] At the molecular level, individual LMWGs participate in a range of intermolecular interactions that facilitates their assembly into long fibres. At a larger length-scale, the fibres interact with one another to form an entangled network. The nature of the inter-fibre interactions determines the properties of the macroscopic gel material.[15, 25] The gel fibres should not be considered in isolation from the surrounding medium as factors such as the solvent composition and number and nature of ions can have a profound influence on the materials properties.[26-29] At the macroscopic level, the mechanical properties of the bulk gel determine the functionality of the materials. For biomedical applications, for example, the ability of a gel to be injected into a patient through a needle is controlled by the ability of the network to recover from shear.[30, 31] Complete characterisation of self-assembled hydrogels thus presents a formidable challenge requiring a multitude of analytical techniques to probe each length scale.[22] As NMR spectroscopy is the technique of principal importance to this Thesis, it is discussed in detail in Section 1.2.2 while non-NMR based techniques are briefly reviewed in Section 1.2.1.

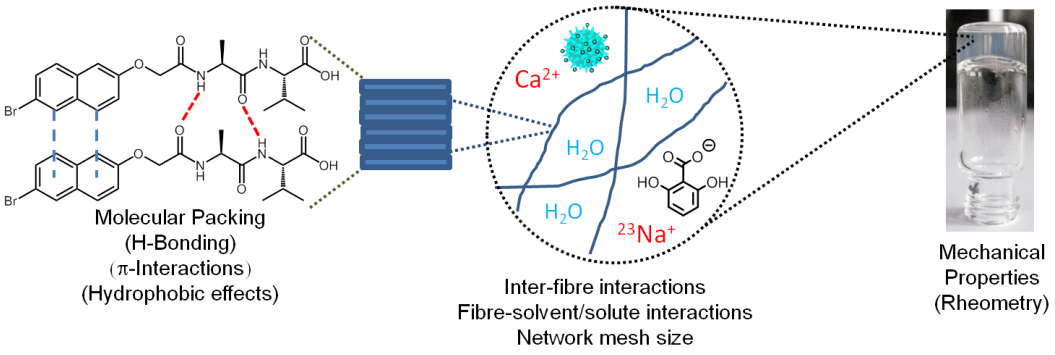

Scheme 1-3. Self-assembled hydrogels are hierarchical materials. A complete characterisation requires a range of analytical techniques to probe each length scale.

1.2.1 Non NMR-based techniques for the analysis of self-assembled hydrogels

Infra-red, UV-Vis and fluorescence spectroscopy have long been used to probe the molecular packing of the LMWGs in self-assembled gel fibres.[19] For LMWGs bearing amide groups, which includes almost all *N*-functionalised peptide LMWGs (Section 1.4), the position of the carbonyl stretch of amide groups depends upon the intermolecular hydrogen bonding motifs in the self-assembled fibres.[32-35] Changes to the vibration frequencies of other groups can also be studied;[34] however, the carbonyl stretch is the most commonly utilised. Many LMWGs contain large aromatic groups which promote the hydrophobic aggregation of the molecules and help provide directionality to their molecular packing in the assembled state (Section 1.3). These aromatic groups provide a sensitive probe of their environment through their UV-Vis and fluorescence spectra. Through analysis of these spectra, the aggregation of the LMWGs can be monitored and the relative stacking orientation of adjacent LMWGs in the gel fibres inferred in some cases.[10, 36, 37] In addition to LMWGs, the spectra of probe molecules can also be studied. The association of these molecules with the gel fibres causes changes to their fluorescence spectra which can be used to monitor the formation of the gel networks.[38, 39] Circular dichroism can be used to monitor the assembly of chiral LMWGS, including almost all peptide-based LMWGs, into chiral nanostructures. Information as to the arrangement of the LMWGs in the self-assembled fibres can also be deduced.[34, 40]

X-ray and electron diffraction techniques could potentially provide the molecular packing of the fibres at atomic detail.[41] However, relatively few systems possess the necessary order for diffraction patterns to be obtained in the hydrated gel state.[10, 42, 43] The self-assembly of molecules into fibres is often described as ‘crystallisation gone wrong’; while there is clearly some degree of directionality and order in the molecular packing of the LMWGs inside the fibres, the formation of a highly ordered crystal is somehow prevented.[44] While crystals of many LMWGs can be prepared and X-ray structures solved,[19, 45, 46] it is questionable as to what extent the packing in the crystal reflects that in the gel fibres.[42, 46-48]

For larger length scales, small angle X-ray (SAXS) and small angle neutron (SANS) scattering techniques can provide unique insights into the size, shape, arrangement

and flexibility of the self-assembled fibres.[15, 49-51] Both of these techniques usually require access to specialist facilities: synchrotron sources for SAXS and neutron sources for SANS. It should be noted, however, that lab-based SAXS measurements are becoming more common owing to improvements in instrumentation.[52-54] Microscopy techniques can be used to visualise the self-assembled gel networks with sub-micron resolution. Properties such as the persistence length and thickness of the fibres can be measured directly from images.[22, 35, 55] Great care is needed, however, as the sample preparation method employed can severely change the observed morphology from that of the native material.[13, 14, 56, 57] Conventional scanning electron microscopy (SEM) and transmission electron microscopy (TEM) are performed under high-vacuum conditions. This necessitates the removal of water from the samples. Given the non-covalent nature of the interactions between LMWGs in the gel fibres and the importance of solvent-LMWG interactions, it is questionable as to what extent the observed network morphologies represent those in the native hydrated state.[13, 14, 58] Drying of gels formed from *N*-functionalised peptide LMWGs has been shown to promote lateral association of the fibres.[14] Environmental scanning electron microscopy (ESEM), cryo-SEM and atomic-force microscopy (AFM) can be used to study gel materials without potentially disruptive drying procedures, although both techniques have their own limitations and sample preparation requirements.[22, 56, 58-60] At larger length-scales, techniques such as confocal microscopy[61] and polarising optical microscopy[62] can be used to study the materials under their native hydrated conditions.

At the macroscopic level, techniques to study the bulk mechanical (rheological) properties of the materials are well established.[30, 63, 64] The macroscopic properties of the gel can be related to smaller-scale properties such as the mesh size and persistence length of the fibres.[65, 66]

To conclude, a number of well-established techniques exist to study self-assembled hydrogels over a range of length-scales. A number of these techniques can be applied to study the hydrogels under their native conditions of temperature or hydration. However, none of the techniques mentioned in this Section can directly provide any information on the surface chemistry of the gel fibres. The use of NMR spectroscopy to study self-assembled hydrogels is discussed in detail in the following Section.

1.2.2 Previous studies of self-assembled hydrogels by NMR spectroscopy

NMR spectroscopy is a particularly attractive technique for the study of hydrogels owing to its non-invasive nature and potential to provide unique and detailed chemical information. Furthermore, as an indispensable technique in modern chemical research, most workers in the field of self-assembled gels have access to the required NMR equipment. A notable feature of self-assembled gels, however, is that in many systems the gel fibres are not directly observable by solution-state NMR spectroscopy owing to the low mobility of the assembled molecules (Scheme 1-4).[67-69] Nevertheless, in such cases, considerable amounts of information may still be obtained by solution-state NMR. In many systems, there is a degree of exchange between the LMWGs assembled into the fibres and those free in solution.[69, 70] The free LMWGs can thus report indirectly upon the self-assembled state.[70]

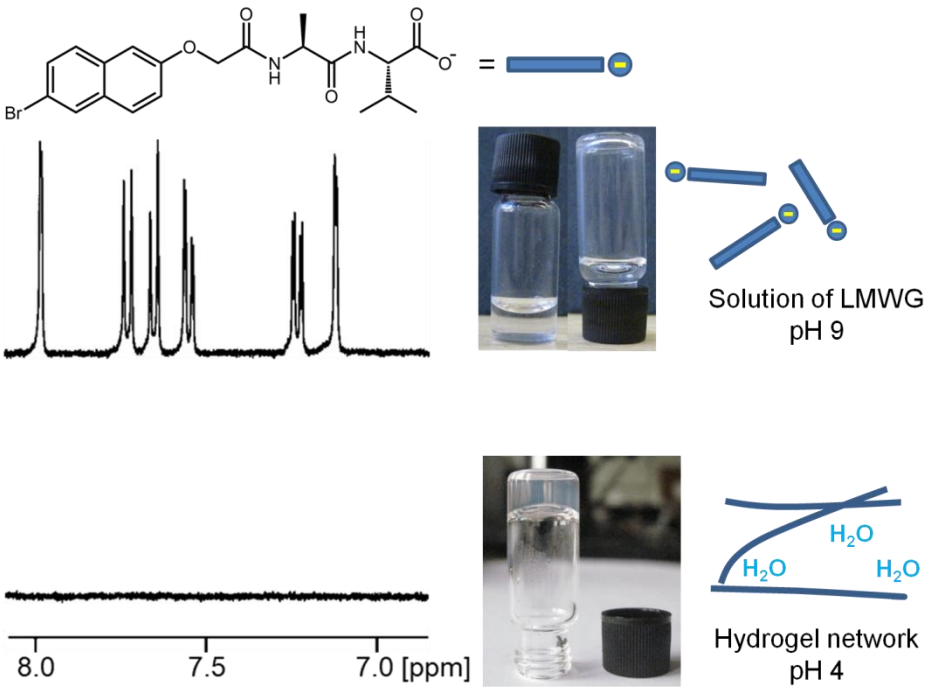

Scheme 1-4. Comparison of partial ^{1}H NMR spectra of a dipeptide sample at pH 9 (unassembled, NMR-visible) and at pH 4 (assembled, not NMR-visible).

Another approach to study self-assembled hydrogels is to include carefully selected probe molecules in the solution phase of the materials.[70, 71] Relative to the assembled fibres, these probes have a high degree of mobility and so give sharp resonances by solution-state NMR. From the perturbation of the NMR properties of these probes

due to their interaction with the fibres, it is possible to learn about the NMR-invisible gel network.

Studies concerning the direct observation of the LMWGs by NMR are reviewed in Section 1.2.2.1. Studies concerning the use of probe molecules to study the hydrogels are reviewed in Section 1.2.2.2. Studies of self-assembled gels formed in organic solvents (organogels) are discussed in addition to those in formed in water (hydrogels) as the same techniques can be applied to both classes of material.

1.2.2.1 Information available from direct observation of the LMWGs/gel fibres by NMR

The majority of works discussing the analysis of self-assembled gels by NMR concern the direct observation of the LMWGs by solution-state ^{1}H NMR.[22, 67, 68, 70] Other nuclei such as ^{13}C can also be studied;[72-74] however, ^{1}H is by far the most commonly observed nucleus.[22, 67] In the majority of systems, the LMWGs are not directly observable by NMR spectroscopy in the assembled state.[68-70, 75] In many systems, there is an exchange between the LMWGs free in solution and those assembled in the gel fibres.[69, 70] The fraction of NMR-visible LMWG can be measured by integration of its resonances against an internal standard. The solubility of the LMWG, thus measured, can be used to calculate a range of other properties.[68, 75-78] For example, measuring the solubility of the gelators as a function of temperature yields the thermodynamic parameters of assembly.[68, 75, 77-79] Angulo-Pachon *et al.*[75] compared the enthalpy and entropy of assembly of two groups of peptide gelators in $CHCl_3$, one appended with a hexyl chain and the other with a cyclohexyl moiety. Their analysis revealed that the increased gelation efficacy of the cyclohexyl-appended gelators was attributable to the lower loss of entropy upon assembly, relative to those appended with the more conformationally flexible hexyl chain. In systems where multiple components are present, analysis of the equilibrium solubilities clearly demonstrates which components are incorporated into the self-assembled fibres and which are not.[43, 79, 80] Edwards and Smith studied hydrogels formed upon the complexation between a lysine-derived gelator and different mono-amines.[80] In systems were multiple amines were present, they demonstrated that the relative amount of each amine incorporated into the NMR-invisible fibres depended

upon both the amine pK_a (complexation ability) and propensity of the amines to form self-assembled fibres when complexed.

The NMR-invisible nature of self-assembled hydrogel fibres also offers a handle by which the kinetics of gel formation can be studied, provided the kinetics of assembly are sufficiently slow for the fraction of NMR-visible (non-assembled) LMWG to be monitored with time. In some systems, the required slow kinetics can be deliberately introduced. Adams *et al.*[81] described a method for inducing gelation of *N*-functionalised peptides *via* a gradual pH switch. Starting from a solution of the peptides at alkaline pH, where the molecules are not assembled into fibres, the pH is gradually acidified *via* the slow hydrolysis in solution of glucono-δ-lactone (GdL). Slow acidification leads to the gradual assembly of the gelators into NMR-invisible fibres. The method was originally developed to provide much greater sample homogeneity than was attainable *via* the rapid acidification with HCl.[81] However, a further advantage of the method is that it allows the gelation of samples to be monitored over time. The GdL system has been used by a number of researchers for this purpose and was used extensively in this Thesis (Chapters 3 and 4).[40, 82, 83] For example, Tena-Solsona *et al.*[82] were able to extract detailed kinetic information about the pH-triggered assembly of a number of peptide LMWGs, revealing that the limiting step in the assembly process was the formation of dimeric species. In systems where multiple LMWGs are present, integration of the NMR resonances of the different components as the pH falls can be used to distinguish self-sorting of different LMWGs into separate fibres, or co-assembly into fibres of mixed composition.[83-87]

Another common approach to study self-assembled gels by NMR is to analyse the LMWGs under conditions of temperature, concentration or solvent composition where gelation is precluded. The LMWGs are not assembled into gel fibres and so remain visible by NMR. Nevertheless, the LMWGs can still associate with one another in solution to form small oligomeric species.[68, 75, 82] In such cases, valuable insights may be gained into the molecular interactions responsible for assembly. By changing the solution conditions, the resonances of groups participating in intermolecular interactions between molecules are commonly observed to shift as aggregation is favoured/disfavoured.[88-90] For example, Berdugo *et al.*[88] measured the ^{1}H amide (NH) shifts of alkyl-functionalised dipeptides as a function of the dipeptide

concentration. By analysis of this data, the authors were able to calculate the populations of dimeric and oligomeric species in solution. Techniques such as nuclear Overhauser effect (NOE) spectroscopy can also be used to deduce the conformations of the gelator molecules in the free and aggregated states.[88, 91-93]

Solid-state NMR spectroscopy can be employed for the direct study of the assembled fibres.[94] Solid-state NMR would seem the natural technique to study solid-like materials such as self-assembled gels. However, the very high water content of many self-assembled systems (≥ 99.5 wt%) can make the task of obtaining adequate signal very challenging.[73, 95] Solid-state NMR can reveal the presence of symmetrically inequivalent LMWGs in the self-assembled fibres and allow for a comparison of the packing of the LMWGs in the gel and crystal states.[91, 95] Insight is also available into the mobility of different parts of the LMWGs in the self-assembled fibres.[96] Although ^{13}C is the most commonly studied nucleus, other nuclei such as ^{31}P and ^{23}Na can also be studied.[72, 97] Using solid-state ^{23}Na NMR, Wu *et al.*[97] were able to distinguish between Na^+ ions bound to the surface and interior of a supramolecular fibre formed from guanosine-5'-monophosphate. The use of solution-state ^{23}Na NMR to study counterion association is discussed in the following Section.

To conclude, direct observation of the LMWGs by NMR spectroscopy provides valuable insights into the self-assembly processes of self-assembled gels. Particular insight is afforded into the kinetics and thermodynamics of gelation, as well as the molecular interactions between the LMWGs in the assembled state. Nevertheless, by virtue of their solid-like nature,[68, 98, 99] the gel fibres themselves cannot be directly observed by solution-state NMR. In some systems, solid-state NMR can provide insight into the molecular packing of the LMWGs in the fibres. However, no information is yielded on the surface chemical properties of the fibres.

1.2.2.2 Information available from the use of probe molecules

A complementary approach to the direct observation of the LMWGs is to use non-assembling probe species to study the gel network. The probe species can include hydrophilic polymers,[65, 100] small organic molecules[70, 71] and organic and inorganic ions.[101, 102] Using a range of NMR techniques including self-diffusion, relaxation and chemical shift measurements, it is possible to detect how and how strongly these probe species interact with the gel fibres. The known charge,

hydrophobicity/hydrophilicity, steric bulk or other properties of the probe species can then be used to infer the properties of the NMR-invisible gel network. A number of examples of this approach are now discussed.

In the field of self-assembled hydrogels, ionisable groups such as carboxylates or amines play a very important role in tuning the solubility of LMWGs. Adjustment of the pH to favour the non-ionised form is commonly used to induce self-assembly.[11, 19, 81, 82, 103-105] In other systems, assembly can be induced by the addition of salts which is attributed to a range of effects including the specific binding of ions to the LMWGs,[17, 25, 26, 106, 107] charge-screening[29, 108, 109] and Hofmeister effects.[110-112] Counterions to the charged groups on LMWGs thus form an intrinsic part of many samples and can, in principle, be used to probe the charge and assembly state of hydrogels. Furthermore, common counterions such as Na^+ and Cl^- are easily observable by NMR and are extensively used to study the ion-binding properties and phase behaviour of other systems including liquid crystalline materials,[113-115] polymers[116-118] and clay particles.[119, 120] However, despite its potential, little attention has been paid in the literature to the study by solution-state NMR of counterion association with self-assembled gel materials.[74, 102] Raue *et al.*[102] applied solution-state ^{23}Na NMR to follow the assembly of an LMWG. Upon the gelation of a succinamic acid-based gelator in saturated $NaHCO_3$ solution, the authors observed decreases in the T_1 and T_2 relaxation times of $^{23}Na^+$ as the ions interacted with the newly-formed fibres and their mobility was reduced. The relaxation times were observed to increase upon the melting of the gels to the non-assembled state. ^{23}Na relaxation measurements are used extensively in this project and are discussed in more detail in Chapter 3 and 4.

Small organic molecules can also be used probes. Escuder *et al.*[70] studied the selective interaction of two organic molecules with self-assembled gels formed in benzene. Using a combination of ^1H relaxation and NOE measurements, diphenylmethane was found not to interact significantly with the self-assembled fibres which was attributed to the good solvation of the molecule in benzene. In contrast, a strong interaction was detected for the similar compound, 2,2′-Biphenyldimethanol, which the authors attributed to H-bonding interactions between the hydroxyl groups of the compound and the gel fibres. Work by the same research group has further highlighted the potential to study by NMR the selective interaction

of molecules with the gel fibres.[71, 101, 121] As well as providing information on the gel fibres, this work may also aid the informed design of controlled drug-release systems.

Water soluble polymers can be used as probes to investigate the pore sizes of hydrogels. The molecular self-diffusion coefficient of the polymer can be related to the relative sizes of the pore and the hydrodynamic diameter of the polymer coil.[65, 122-125] Wallace *et al.*[100], during his undergraduate studies, presented such a method for measuring the pore sizes of self-assembled gels using hydrophilic dextran polymers as probes. Polymers with hydrodynamic diameters much smaller than the pore size of the network were freely diffusing. In contrast, the self-diffusion of polymers with hydrodynamic diameters comparable to or greater than the pore size was severely restricted.[100] This methodology has been adopted by a number of other workers in the field to study self-assembled hydrogels.[125, 126] In some systems, the self-diffusion of smaller molecular probes such as solvent molecules can also be used to investigate the physical structure of the porous networks.[62, 127] Tritt-Goc *et al.*[127] observed the diffusion-diffraction phenomenon[128] with the toluene solvent in a functionalised glucanopyranoside gel. By analysis of the data, the authors were able to obtain a value for the average separation of the fibres comprising the entangled network of the gel.

To conclude, probe molecules provide a simple and effective way to study gel fibres that are otherwise invisible by solution-state NMR. Great care is needed, however, in the selection of suitable probe species and in the analysis of data. For example, the diffusion of polymer chains through hydrogels is strongly influenced by any specific chemical interactions between the polymer chain and the gel network, as well as any steric effects.[65, 100, 129-131] Deconvolution of the two effects is a significant challenge in such cases.[65, 131] Care must also be taken to ensure that the selected probe molecules do not interfere with the gelation process. The selection of suitable probe molecules is discussed in more detail in Chapter 4, Section 4.3.1.

1.3 The importance of the fibre surface chemistry

As briefly discussed in Section 1.1, the chemical interactions between adjacent fibres determine the properties of the hydrogel network.[15, 16, 25, 132] These interactions can be expected to depend upon the surface chemical properties of the gel fibres, including their charge, hydrophobicity and ion-binding dynamics. Such properties will also determine the interactions of the gels with other entities of interest including living cells,[17, 133, 134] drug molecules[6, 101] or pollutants.[8, 135] For example, Jayawarna *et al.*[133] prepared a series of hydrogels from *N*-functionalised peptide gelators bearing different chemical functionalities on their amino acid side chains: hydroxyl, ammonium and carboxylate. The compatibility of the gels with different cell types differed markedly depending on the functionality of the gelators which the authors attributed to differences in the adhesion of the cells to the gel fibres. Elsewhere, Nagy-Smith *et al.*[6] compared the release rates of different model protein drugs from hydrogels prepared from peptide LMWGs whose net charge could be controlled by the variation of the amino acid side chains. The gels preferentially retained proteins of the opposite charge to the peptide. Knowledge of the surface chemical properties is thus vital in order to build a full picture of self-assembled gels and for their informed design for specific applications. Further examples highlighting the importance of the fibre surface chemistry and the difficulty encountered in its analysis are discussed in the remainder of this Section.

Gao *et al.*[15] demonstrated that the extent of association of fibres formed from octapeptides could be modulated by varying the fraction of arginine-containing peptide, with the arginine promoting strong interactions between adjacent chains. The extent of fibre association was probed using TEM and SANS. Although these techniques could provide extensive information on the morphology of the gel fibres, no direct information was afforded on the surface chemical properties of the fibres. The gelation ability of octapeptide LMWGs and the mechanical properties of the resultant gels can also be linked to the charge carried on the amino acid side-chains.[16, 136] In these works, the charge was calculated based on the pK_a values of the side chains in the unassembled state. However, in many self-assembling systems, the pK_a values of ionisable groups are known to shift dramatically upon assembly.[82, 105] The actual charge carried in the assembled state was thus not known with accuracy.

With a range of LMWGs, other authors have also linked the mechanical properties of their gels to the charge carried by the fibres.[82, 105, 137, 138] However, in the absence of techniques for the reliable measurement of the surface chemical properties, the details of any relationship remain obscured.

Very few works have attempted to directly study the surface chemical properties of hydrogels. A number of works have attempted to use infra-red spectroscopy to observe the stretches of carboxylate groups at 1550-1590 cm^{-1}.[17, 33] A limitation of this approach, however, is that infra-red spectra are often crowded and it can be very difficult to unambiguously assign the observed vibrations to those of the surface-born functional groups. For example, aromatic C=C stretches occur at very similar frequencies to the stretches of carboxylate groups.[50] Pioneering studies into the mobility of the solvent and LMWGs at the fibre-solution interface using fast-field-cycling relaxometry (FFC)[139-141] and electron spin paramagnetic resonance (EPR)[98, 99] have been reported. However, although the interplay between the solvent and the LMWGs is recognised to play an important role in determining the assembly and morphology of hydrogel fibres,[28] the precise relationship is not currently understood. The solvent mobility cannot be related in a simple manner to the surface chemical properties of the gels.

NMR spectroscopy (Section 1.2.2) is an especially appealing technique to study the surface chemistry of self-assembled hydrogels. As discussed in Section 1.2.2.2, the interaction of probe molecules and ions with the gel fibres depends upon the surface chemistry of those fibres. However, only a very small number of studies to date have attempted to measure any surface chemical properties this way.

1.4 Peptide-based LMWGs

Short peptides are a common and effective class of LMWGs that has received much attention.[11, 103, 142-144] The amide functionalities provide directional H-bonding interactions to promote self-assembly into long nanostructures.[4, 145] The assembly properties of the LMWG can be adjusted by variation of the constituent amino acids.[11, 15, 16] The twenty natural amino acids,[146] plus additional analogues,[147] provides an exceedingly large number of potential LMWGs. Furthermore, the biocompatible nature of amino-acid based materials makes the class particularly attractive for biomedical applications.[7, 17]

Self-assembly of 'pure' peptides comprising only natural amino acids is generally restricted to longer peptides bearing three or more amino acids.[15, 16, 142] Self-assembly of shorter peptides is rare.[43, 148] Nevertheless, the propensity of short peptides to assemble into fibrous networks can be greatly enhanced by appending different chemical groups.[103, 144] A particularly common strategy is to append a large aromatic moiety onto the *N*-termini of single amino acids or dipeptides. These LMWGs are collectively referred to as *N*-functionalised peptides (examples in Scheme 1-5). Common aromatic groups include naphthalene (**1**, **2**) and fluorene (**3**, **4**).[4, 11, 36, 104] Other groups such as perylene (**5**) or stilbene (**6**) can also be appended in order to provide special electronic properties to the assembled materials.[10, 85, 149, 150] The aromatic group provides extra hydrophobicity to promote aggregation of the LMWG and also provides directionality to the intermolecular interactions to promote the formation of long fibres.[4, 36] Relative to longer 'pure' peptides, short *N*-functionalised peptides are much cheaper to prepare in large quantities in pure form, making them particularly attractive as model systems to study self-assembly.[23]

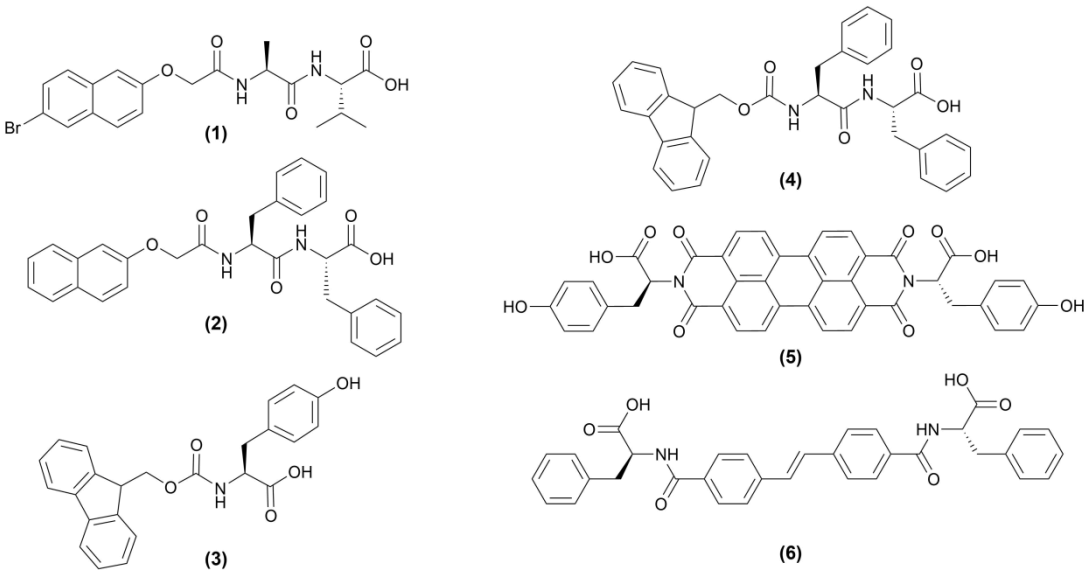

Scheme 1-5. Examples of *N*-functionalised dipeptide LMWGs. References are as follows: **1**,[40] **2,**[26] **3**,[151] **4**,[152] **5**[10] and **6**.[85]

A particularly attractive feature of *N*-functionalised peptide LMWGs is the diversity of methods by which hydrogels may be prepared. In many cases, different assembly methods lead to different final gel properties.[23, 153] The ability to produce materials with a range of tailored properties from the same LMWG is particularly attractive from a commercial perspective, especially given the difficulty of 'designing' LMWGs to form gels with specific properties.[23, 142, 154] Much of the diversity of gelation methods is attributable to the terminal carboxylic acid groups, in addition to any amino acid side chains, that most *N*-functionalised peptides bear.

The carboxylic acid groups render the LMWGs sensitive to pH. A common strategy to prepare gels is to solubilise the LMWGs by the addition of base to deprotonate the carboxylic acid groups. Upon a decrease in the solution pH, the carboxylates are, at least partially,[105, 138, 155] protonated and the solubility of the LMWGs reduced to the extent that they self-assemble into a fibrous network.[11, 40, 82, 104, 105] When deprotonated, the LMWGs are also sensitive to the nature and concentration of cations in the solution. Addition of salts to alkaline solutions of the gelators can be used to induce and control assembly.[10, 25, 26, 106, 110]

Another method to induce gelation, not specifically related to the terminal carboxylic acid, is to vary the composition of the solvent. As neutral compounds, *N*-functionalised dipeptides generally possess good solubilities in water-miscible

organic solvents such as DMSO or acetone, but low solubilities in pure water.[152, 156-158] To induce gelation, a concentrated solution of the dipeptide in the organic solvent is first prepared. Upon addition of water, the solubility of the gelators is reduced which causes the LMWGs to aggregate. The initial aggregates usually evolve over time to form a sample-spanning fibrous network.[27, 61, 152, 156-159] In some systems, upon heating the gels the solubility of the dipeptides is raised and they return to the unassembled state. Gels can then be formed upon subsequent cooling of the samples. The gels thus formed often have different properties to those of the initial gels.[27, 61] Other approaches to induce gelation include the use of an enzyme to convert a non-assembling precursor into an effective LMWG[151, 160-162] or the use of ultrasound to stimulate assembly.[163-165]

In this Thesis, *N*-functionalised dipeptide gelators will be used as model systems on which new NMR-based analytical techniques will be developed. The diversity in both the amino-acid sequences and gelation methods of *N*-functionalised dipeptides makes them excellent model gelators with which to develop new analytical techniques. For example, a gel prepared by the addition of salt to a solution of dipeptide at alkaline pH may be expected to have a different surface chemistry to a gel prepared upon acidification of the solution.[25, 26, 166] This hypothesis is tested in Chapter 4.

1.5 Aims of the Project

This Chapter has provided a general overview of self-assembled hydrogels and the challenges encountered in their analysis. A shortcoming of existing analytical approaches is their inability to characterise the surface chemical properties of the self-assembled gel fibres. Solution-state NMR spectroscopy is a particularly appealing technique to study self-assembled hydrogels owing to its widespread availability and ability to characterise the gels under their native conditions of temperature and hydration. A number of studies have highlighted the potential of solution-state NMR spectroscopy to study the interaction with the NMR-invisible fibres of probe molecules and ions (Section 1.2.2.2). These interactions are governed by both the surface chemical properties of the fibres and the chemical properties of the probes. The latter, in principle, are known and easily controlled through careful selection of the probes. By judicious choice of a set of probe species, it may thus be

possible to measure the surface chemical properties of the gel fibres. The possibility of measuring the surface properties this way has remained largely unexplored, despite the considerable prevalence of ^{1}H solution-state NMR in the study of self-assembled hydrogel materials (Section 1.2.2).

The central aim of the Thesis is therefore to develop solution-state NMR methods to measure the surface chemical properties of the fibres *via* their interaction with probe species. Three core objectives can thus be defined: firstly, sensitive NMR techniques must be developed in order to quantify the interaction of the probe species with the gel fibres. It is important that the interactions are as weak as possible, while still being detectable, in order to minimise any interference of the probe with the gelation process. Secondly, a series of suitable probe species must be selected that report on a range of properties including the charge, hydrophobicity/hydrophilicity and ion-binding dynamics of the gel fibres. Finally, once the surface chemical properties of the fibres can be measured, it is important to link these properties to other observable properties of the materials. For example, the mechanical properties and drug binding behaviour of the gels are both expected to depend upon the surface chemistry. The techniques developed in the project will help to shed light on these complex relationships.

1.6 References

1. N. Zweep and J. H. van Esch, in *Functional Molecular Gels*, eds. B. Escuder and J. F. Miravet, The Royal Society of Chemistry, 2014, pp. 1-29.
2. X. Du, J. Zhou, J. Shi and B. Xu, *Chem. Rev.*, 2015, **115**, 13165-13307.
3. R. G. Weiss, *J. Am. Chem. Soc.*, 2014, **136**, 7519-7530.
4. M. S. Ekiz, G. Cinar, M. A. Khalily and M. O. Guler, *Nanotechnology*, 2016, **27**.
5. W. Lu, X. Le, J. Zhang, Y. Huang and T. Chen, *Chem. Soc. Rev.*, 2017, **46**, 1284-1294.
6. K. Nagy-Smith, Y. Yamada and J. P. Schneider, *J. Mater. Chem. B*, 2016, **4**, 1999-2007.
7. X. Q. Dou and C. L. Feng, *Adv. Mater.*, 2017, **29**.
8. B. O. Okesola and D. K. Smith, *Chem. Soc. Rev.*, 2016, **45**, 4226-4251.

9. N. Singh, M. Tena-Solsona, J. F. Miravet and B. Escuder, *Isr. J. Chem.*, 2015, **55**, 711-723.
10. S. Roy, D. Kumar Maiti, S. Panigrahi, D. Basak and A. Banerjee, *RSC Adv.*, 2012, **2**, 11053-11060.
11. N. Singh, M. Kumar, J. F. Miravet, R. V. Ulijn and B. Escuder, *Chem. Eur. J.*, 2017, **23**, 981-993.
12. C. D. Jones and J. W. Steed, *Chem. Soc. Rev.*, 2016, **45**, 6546-6596.
13. M. Pyzalska, M. Smal and R. Luboradzki, *J. Non-Cryst. Solids*, 2011, **357**, 3184-3189.
14. L. L. E. Mears, E. R. Draper, A. M. Castilla, H. Su, Zhuola, B. Dietrich, M. C. Nolan, G. N. Smith, J. Doutch, S. Rogers, R. Akhtar, H. Cui and D. J. Adams, *Biomacromolecules*, 2017, DOI: 10.1021/acs.biomac.7b00823.
15. J. Gao, C. Tang, M. A. Elsawy, A. M. Smith, A. F. Miller and A. Saiani, *Biomacromolecules*, 2017, **18**, 826-834.
16. D. Roberts, C. Rochas, A. Saiani and A. F. Miller, *Langmuir*, 2012, **28**, 16196-16206.
17. E. V. Alakpa, V. Jayawarna, A. Lampel, K. V. Burgess, C. C. West, S. C. J. Bakker, S. Roy, N. Javid, S. Fleming, D. A. Lamprou, J. Yang, A. Miller, A. J. Urquhart, P. W. J. M. Frederix, N. T. Hunt, B. Péault, R. V. Ulijn and M. J. Dalby, *Chem*, 2016, **1**, 298-319.
18. G. M. Peters and J. T. Davis, *Chem. Soc. Rev.*, 2016, **45**, 3188-3206.
19. L. A. Estroff and A. D. Hamilton, *Chem. Rev.*, 2004, **104**, 1201-1217.
20. S. S. Babu, V. K. Praveen and A. Ajayaghosh, *Chem. Rev.*, 2014, **114**, 1973-2129.
21. N. M. Sangeetha and U. Maitra, *Chem. Soc. Rev.*, 2005, **34**, 821-836.
22. G. Yu, X. Yan, C. Han and F. Huang, *Chem. Soc. Rev.*, 2013, **42**, 6697-6722.
23. J. Raeburn, A. Zamith Cardoso and D. J. Adams, *Chem. Soc. Rev.*, 2013, **42**, 5143-5156.
24. A. Aggeli, I. A. Nyrkova, M. Bell, R. Harding, L. Carrick, T. C. B. McLeish, A. N. Semenov and N. Boden, *Proc. Natl. Acad. Sci. U. S. A.*, 2001, **98**, 11857-11862.
25. M. A. Greenfield, J. R. Hoffman, M. O. De La Cruz and S. I. Stupp, *Langmuir*, 2010, **26**, 3641-3647.

26. L. Chen, G. Pont, K. Morris, G. Lotze, A. Squires, L. C. Serpell and D. J. Adams, *Chem. Commun.*, 2011, **47**, 12071-12073.
27. N. A. Dudukovic and C. F. Zukoski, *Langmuir*, 2014, **30**, 4493-4500.
28. Y. Lan, M. G. Corradini, R. G. Weiss, S. R. Raghavan and M. A. Rogers, *Chem. Soc. Rev.*, 2015, **44**, 6035-6058.
29. Y. Feng, M. Taraban and Y. B. Yu, *Soft Matter*, 2012, **8**, 11723-11731.
30. S. Sathaye, A. Mbi, C. Sonmez, Y. Chen, D. L. Blair, J. P. Schneider and D. J. Pochan, *WIREs Nanomed. Nanobiol.*, 2015, **7**, 34-68.
31. D. Mandal, S. K. Mandal, M. Ghosh and P. K. Das, *Chem. Eur. J.*, 2015, **21**, 12042-12052.
32. S. Kiyonaka, K. Sugiyasu, S. Shinkai and I. Hamachi, *J. Am. Chem. Soc.*, 2002, **124**, 10954-10955.
33. S. L. Zhou, S. Matsumoto, H. D. Tian, H. Yamane, A. Ojida, S. Kiyonaka and I. Hamachi, *Chem. Eur. J.*, 2005, **11**, 1130-1136.
34. F. Rodríguez-Llansola, D. Hermida-Merino, B. Nieto-Ortega, F. J. Ramírez, J. T. L. Navarrete, J. Casado, I. W. Hamley, B. Escuder, W. Hayes and J. F. Miravet, *Chem. Eur. J.*, 2012, **18**, 14725-14731.
35. A. M. Smith, R. J. Williams, C. Tang, P. Coppo, R. F. Collins, M. L. Turner, A. Saiani and R. V. Ulijn, *Adv. Mater.*, 2008, **20**, 37-41.
36. S. Fleming, S. Debnath, P. W. J. M. Frederix, T. Tuttle and R. V. Ulijn, *Chem. Commun.*, 2013, **49**, 10587-10589.
37. S. Ghosh, X. Q. Li, V. Stepanenko and F. Würthner, *Chem. Eur. J.*, 2008, **14**, 11343-11357.
38. J. Raeburn, L. Chen, S. Awhida, R. C. Deller, M. Vatish, M. I. Gibson and D. J. Adams, *Soft Matter*, 2015, **11**, 3706-3713.
39. K. Kalyanasundaram and J. K. Thomas, *J. Am. Chem. Soc.*, 1977, **99**, 2039-2044.
40. L. Chen, K. Morris, A. Laybourn, D. Elias, M. R. Hicks, A. Rodger, L. Serpell and D. J. Adams, *Langmuir*, 2010, **26**, 5232-5242.
41. G. R. Desiraju, *Angew. Chem. Int. Ed.*, 2007, **46**, 8342-8356.
42. K. A. Houton, K. L. Morris, L. Chen, M. Schmidtmann, J. T. A. Jones, L. C. Serpell, G. O. Lloyd and D. J. Adams, *Langmuir*, 2012, **28**, 9797-9806.

43. S. M. Ramalhete, K. P. Nartwoski, N. Sarathchandra, J. S. Foster, A. N. Round, J. Angulo, G. O. Lloyd and Y. Z. Khimyak, *Chem. Eur. J.*, 2017, **23**, 8014-8024.
44. D. K. Kumar and J. W. Steed, *Chem. Soc. Rev.*, 2014, **43**, 2080-2088.
45. D. Gao, M. Xue, J. Peng, J. Liu, N. Yan, P. He and Y. Fang, *Tetrahedron*, 2010, **66**, 2961-2968.
46. E. R. Draper, K. L. Morris, M. A. Little, J. Raeburn, C. Colquhoun, E. R. Cross, T. O. McDonald, L. C. Serpell and D. J. Adams, *CrystEngComm*, 2015, **17**, 8047-8057.
47. I. Ramos Sasselli, P. J. Halling, R. V. Ulijn and T. Tuttle, *ACS Nano*, 2016, **10**, 2661-2668.
48. A. D. Martin, J. P. Wojciechowski, M. M. Bhadbhade and P. Thordarson, *Langmuir*, 2016, **32**, 2245-2250.
49. M. C. Nolan, J. J. Walsh, L. L. E. Mears, E. R. Draper, M. Wallace, M. Barrow, B. Dietrich, S. M. King, A. J. Cowan and D. J. Adams, *J. Mater. Chem. A*, 2017, **5**, 7555-7563.
50. A. Z. Cardoso, L. L. E. Mears, B. N. Cattoz, P. C. Griffiths, R. Schweins and D. J. Adams, *Soft Matter*, 2016, **12**, 3612-3621.
51. J. B. Guilbaud and A. Saiani, *Chem. Soc. Rev.*, 2011, **40**, 1200-1210.
52. D. Pirner, M. Dulle, M. E. J. Mauer and S. Förster, *RSC Adv.*, 2016, **6**, 42730-42738.
53. L. Travaglini, M. Gubitosi, M. C. Di Gregorio, N. V. Pavel, A. D'Annibale, M. Giustini, V. H. S. Tellini, J. V. Tato, M. Obiols-Rabasa, S. Bayati and L. Galantini, *Phys. Chem. Chem. Phys.*, 2014, **16**, 19492-19504.
54. D. J. Adams, E. Draper, H. Su, C. Brasnett, R. Poole, S. Rogers, H. Cui and A. Seddon, *Angew. Chem.*, DOI: 10.1002/ange.201705604.
55. S. Vauthey, S. Santoso, H. Gong, N. Watson and S. Zhang, *Proc. Natl. Acad. Sci. U. S. A.*, 2002, **99**, 5355-5360.
56. L. Muscariello, F. Rosso, G. Marino, A. Giordano, M. Barbarisi, G. Cafiero and A. Barbarisi, *J. Cell. Physiol.*, 2005, **205**, 328-334.
57. K. H. Tan, *Soil Sci. Soc. Am. J.*, 1985, **49**, 1185-1191.
58. R. Aston, K. Sewell, T. Klein, G. Lawrie and L. Grøndahl, *Eur. Polym. J.*, 2016, **82**, 1-15.

59. E. C. Barker, C. Y. Goh, F. Jones, M. Mocerino, B. W. Skelton, T. Becker and M. I. Ogden, *Chem. Sci.*, 2015, **6**, 6133-6138.
60. H. Kazazi, F. Khodaiyan, K. Rezaei, M. Pishvaei, M. A. Mohammadifar and S. Moieni, *J. Food Sci. Technol.*, 2017, **54**, 1168-1174.
61. L. Chen, J. Raeburn, S. Sutton, D. G. Spiller, J. Williams, J. S. Sharp, P. C. Griffiths, R. K. Heenan, S. M. King, A. Paul, S. Furzeland, D. Atkins and D. J. Adams, *Soft Matter*, 2011, **7**, 9721-9727.
62. M. Bielejewski, J. Kowalczuk, J. Kaszyńska, A. Łapiński, R. Luboradzki, O. Demchuk and J. Tritt-Goc, *Soft Matter*, 2013, **9**, 7501-7514.
63. C. Yan and D. J. Pochan, *Chem. Soc. Rev.*, 2010, **39**, 3528-3540.
64. A. Aufderhorst-Roberts, W. J. Frith, M. Kirkland and A. M. Donald, *Langmuir*, 2014, **30**, 4483-4492.
65. M. C. Branco, D. J. Pochan, N. J. Wagner and J. P. Schneider, *Biomaterials*, 2009, **30**, 1339-1347.
66. F. C. MacKintosh, J. Käs and P. A. Janmey, *Phys. Rev. Lett.*, 1995, **75**, 4425-4428.
67. Y. E. Shapiro, *Prog. Polym. Sci.*, 2011, **36**, 1184-1253.
68. A. R. Hirst, I. A. Coates, T. R. Boucheteau, J. F. Miravet, B. Escuder, V. Castelletto, I. W. Hamley and D. K. Smith, *J. Am. Chem. Soc.*, 2008, **130**, 9113-9121.
69. D. C. Duncan and D. G. Whitten, *Langmuir*, 2000, **16**, 6445-6452.
70. B. Escuder, M. Llusar and J. F. Miravet, *J. Org. Chem.*, 2006, **71**, 7747-7752.
71. B. Escuder, J. F. Miravet and J. A. Sáez, *Org. Biomol. Chem.*, 2008, **6**, 4378-4383.
72. A. J. Kleinsmann, N. M. Weckenmann and B. J. Nachtsheim, *Chem. Eur. J.*, 2014, **20**, 9753-9761.
73. F. S. Schoonbeek, J. H. VanEsch, R. Hulst, R. M. Kellogg and B. L. Feringa, *Chem. Eur. J.*, 2000, **6**, 2633-2643.
74. M. Borzo, C. Detellier, P. Laszlo and A. Paris, *J. Am. Chem. Soc.*, 1980, **102**, 1124-1134.
75. C. A. Angulo-Pachon, C. Gasco-Catalan, J. J. Ojeda-Flores and J. F. Miravet, *ChemPhysChem*, 2016, **17**, 2008-2012.
76. S. S. Rohner, J. Ruiz-Olles and D. K. Smith, *RSC Adv.*, 2015, **5**, 27190-27196.

77. I. W. Hamley, D. R. Nutt, G. D. Brown, J. F. Miravet, B. Escuder and F. Rodríguez-Llansola, *J. Phys. Chem. B*, 2010, **114**, 940-951.
78. V. J. Nebot, J. Armengol, J. Smets, S. F. Prieto, B. Escuder and J. F. Miravet, *Chem. Eur. J.*, 2012, **18**, 4063-4072.
79. W. Edwards and D. K. Smith, *J. Am. Chem. Soc.*, 2014, **136**, 1116-1124.
80. W. Edwards and D. K. Smith, *J. Am. Chem. Soc.*, 2013, **135**, 5911-5920.
81. D. J. Adams, M. F. Butler, W. J. Frith, M. Kirkland, L. Mullen and P. Sanderson, *Soft Matter*, 2009, **5**, 1856-1862.
82. M. Tena-Solsona, B. Escuder, J. F. Miravet, V. Casttelleto, I. W. Hamley and A. Dehsorkhi, *Chem. Mater.*, 2015, **27**, 3358-3365.
83. D. J. Cornwell, O. J. Daubney and D. K. Smith, *J. Am. Chem. Soc.*, 2015, **137**, 15486-15492.
84. K. L. Morris, L. Chen, J. Raeburn, O. R. Sellick, P. Cotanda, A. Paul, P. C. Griffiths, S. M. King, R. K. O'Reilly, L. C. Serpell and D. J. Adams, *Nat. Commun.*, 2013, **4**.
85. E. R. Draper, J. R. Lee, M. Wallace, F. Jäckel, A. J. Cowan and D. J. Adams, *Chem. Sci.*, 2016, **7**, 6499-6505.
86. H. A. M. Ardoña, E. R. Draper, F. Citossi, M. Wallace, L. C. Serpell, D. J. Adams and J. D. Tovar, *J. Am. Chem. Soc.*, 2017, **139**, 8685-8692.
87. E. R. Draper, M. Wallace, R. Schweins, R. J. Poole and D. J. Adams, *Langmuir*, 2017, **33**, 2387-2395.
88. C. Berdugo, B. Escuder and J. F. Miravet, *Org. Biomol. Chem.*, 2015, **13**, 592-600.
89. Nonappa, D. Šaman and E. Kolehmainen, *Magn. Res. Chem.*, 2015, **53**, 256-260.
90. M. Suzuki, M. Yumoto, M. Kimura, H. Shirai and K. Hanabusa, *Chem. Eur. J.*, 2003, **9**, 348-354.
91. F. Piana, D. H. Case, S. M. Ramalhete, G. Pileio, M. Facciotti, G. M. Day, Y. Z. Khimyak, J. Angulo, R. C. D. Brown and P. A. Gale, *Soft Matter*, 2016, **12**, 4034-4043.
92. Y. Zhang, N. Zhou, J. Shi, S. S. Pochapsky, T. C. Pochapsky, B. Zhang, X. Zhang and B. Xu, *Nat. Commun.*, 2015, **6**.
93. S. Bouguet-Bonnet, M. Yemloul and D. Canet, *J. Am. Chem. Soc.*, 2012, **134**, 10621-10627.

94. Nonappa and E. Kolehmainen, *Soft Matter*, 2016, **12**, 6015-6026.
95. Nonappa, M. Lahtinen, B. Behera, E. Kolehmainen and U. Maitra, *Soft Matter*, 2010, **6**, 1748-1757.
96. S. Iqbal, F. Rodríguez-Llansola, B. Escuder, J. F. Miravet, I. Verbruggen and R. Willem, *Soft Matter*, 2010, **6**, 1875-1878.
97. G. Wu and A. Wong, *Chem. Commun.*, 2001, 2658-2659.
98. A. Caragheorgheopol, W. Edwards, J. G. Hardy, D. K. Smith and V. Chechik, *Langmuir*, 2014, **30**, 9210-9218.
99. J. H. Ortony, C. J. Newcomb, J. B. Matson, L. C. Palmer, P. E. Doan, B. M. Hoffman and S. I. Stupp, *Nat. Mater.*, 2014, **13**, 812-816.
100. M. Wallace, D. J. Adams and J. A. Iggo, *Soft Matter*, 2013, **9**, 5483-5491.
101. M. D. Segarra-Maset, B. Escuder and J. F. Miravet, *Chem. Eur. J.*, 2015, **21**, 13925-13929.
102. M. Raue, A. Bernet, M. Kuppers, S. Stapf, H. W. Schmidt, B. Blumich and T. Mang, in *Intelligent Hydrogels*, eds. G. Sadowski and W. Richtering, Springer International Publishing, 2013, vol. 140, pp. 45-51.
103. D. J. Adams and P. D. Topham, *Soft Matter*, 2010, **6**, 3707-3721.
104. Z. Yang, G. Liang, M. Ma, Y. Gao and B. Xu, *J. Mater. Chem.*, 2007, **17**, 850-854.
105. C. Tang, A. M. Smith, R. F. Collins, R. V. Ulijn and A. Saiani, *Langmuir*, 2009, **25**, 9447-9453.
106. L. Wang, J. Mei, X. Zhang, M. Zhu, J. Wang and L. Wang, *RSC Adv.*, 2014, **4**, 1193-1196.
107. J. Shi, Y. Gao, Y. Zhang, Y. Pan and B. Xu, *Langmuir*, 2011, **27**, 14425-14431.
108. B. Ozbas, J. Kretsinger, K. Rajagopal, J. P. Schneider and D. J. Pochan, *Macromolecules*, 2004, **37**, 7331-7337.
109. T. Otsuka, T. Maeda and A. Hotta, *J. Phys. Chem. B*, 2014, **118**, 11537-11545.
110. V. J. Nebot, J. J. Ojeda-Flores, J. Smets, S. Fernández-Prieto, B. Escuder and J. F. Miravet, *Chem. Eur. J.*, 2014, **20**, 14465-14472.
111. M. Jaspers, A. E. Rowan and P. H. J. Kouwer, *Adv. Funct. Mater.*, 2015, **25**, 6503-6510.

112. S. Roy, N. Javid, P. W. J. M. Frederix, D. A. Lamprou, A. J. Urquhart, N. T. Hunt, P. J. Halling and R. V. Ulijn, *Chem. Eur. J.*, 2012, **18**, 11723-11731.
113. G. Lindblom, B. Lindman and G. J. T. Tiddy, *J. Am. Chem. Soc.*, 1978, **100**, 2299-2303.
114. A. Catte, F. Cesare-Marincola, J. R. C. van der Maarel, G. Saba and A. Lai, *Biomacromolecules*, 2004, **5**, 1552-1556.
115. A. Rapp, K. Ermolaev and B. M. Fung, *J. Phys. Chem. B*, 1999, **103**, 1705-1711.
116. H. Gustavsson, B. Lindman and T. Bull, *J. Am. Chem. Soc.*, 1978, **100**, 4655-4661.
117. L. Piculell, B. Lindman and R. Einarsson, *Biopolymers*, 1984, **23**, 1683-1699.
118. S. K. Kang and M. S. Jhon, *Macromolecules*, 1993, **26**, 171-176.
119. A. Delville, J. Grandjean and P. Laszlo, *J. Phys. Chem.*, 1991, **95**, 1383-1392.
120. P. Porion, M. Al-Mukhtar, A. M. Faugère and A. Delville, *J. Phys. Chem. B*, 2004, **108**, 10825-10831.
121. J. A. Sáez, B. Escuder and J. F. Miravet, *Chem. Commun.*, 2010, **46**, 7996-7998.
122. J. Sun, B. F. Lyles, K. H. Yu, J. Weddell, J. Pople, M. Hetzer, D. De Kee and P. S. Russo, *J. Phys. Chem. B*, 2008, **112**, 29-35.
123. S. J. Gibbs and C. S. Johnson Jr, *Macromolecules*, 1991, **24**, 6110-6113.
124. A. Pluen, P. A. Netti, R. K. Jain and D. A. Berk, *Biophys. J.*, 1999, **77**, 542-552.
125. L. Jowkarderis and T. G. M. Van De Ven, *Soft Matter*, 2015, **11**, 9201-9210.
126. J. V. C. Silva, S. Lortal and J. Floury, *Food. Res. Int.*, 2015, **71**, 1-8.
127. J. Tritt-Goc and J. Kowalczuk, *Langmuir*, 2012, **28**, 14039-14044.
128. P. T. Callaghan, A. Coy, D. MacGowan, K. J. Packer and F. O. Zelaya, *Nature*, 1991, **351**, 467-469.
129. M. A. Gagnon and M. Lafleur, *J. Colloid Interface Sci.*, 2011, **357**, 419-427.
130. X. Guo, Li, C. R. Pacheco, L. Fu and R. K. Prud'homme, 1st International Conference on Bioinformatics and Biomedical Engineering, ICBBE, Wuhan, 2007.
131. S. Matsukawa and I. Ando, *Macromolecules*, 1997, **30**, 8310-8313.

132. M. A. Elsawy, A. M. Smith, N. Hodson, A. Squires, A. F. Miller and A. Saiani, *Langmuir*, 2016, **32**, 4917-4923.
133. V. Jayawarna, S. M. Richardson, A. R. Hirst, N. W. Hodson, A. Saiani, J. E. Gough and R. V. Ulijn, *Acta Biomaterialia*, 2009, **5**, 934-943.
134. C. J. Newcomb, S. Sur, J. H. Ortony, O. S. Lee, J. B. Matson, J. Boekhoven, J. M. Yu, G. C. Schatz and S. I. Stupp, *Nat. Commun.*, 2014, **5**.
135. N. Nandi, A. Baral, K. Basu, S. Roy and A. Banerjee, *Biopolymers*, 2017, **108**.
136. S. Boothroyd, A. F. Miller and A. Saiani, *Faraday Discuss.*, 2013, **166**, 195-207.
137. A. Z. Cardoso, A. E. Alvarez Alvarez, B. N. Cattoz, P. C. Griffiths, S. M. King, W. J. Frith and D. J. Adams, *Faraday Discuss.*, 2013, **166**, 101-116.
138. C. Tang, R. V. Ulijn and A. Saiani, *Langmuir*, 2011, **27**, 14438-14449.
139. J. Kowalczuk, A. Rachocki, M. Bielejewski and J. Tritt-Goc, *J. Colloid Interface Sci.*, 2016, **472**, 60-68.
140. J. Tritt-Goc, A. Rachocki and M. Bielejewski, *Soft Matter*, 2014, **10**, 7810-7818.
141. J. Tritt-Goc, M. Bielejewski and R. Luboradzki, *Tetrahedron*, 2011, **67**, 8170-8176.
142. W. J. Frith, *Philos. Trans. R. Soc., A*, 2016, **374**, 20150135.
143. D. J. Adams, *Macromol. Biosci.*, 2011, **11**, 160-173.
144. G. Fichman and E. Gazit, *Acta Biomaterialia*, 2014, **10**, 1671-1682.
145. K. M. Eckes, X. Mu, M. A. Ruehle, P. Ren and L. J. Suggs, *Langmuir*, 2014, **30**, 5287-5296.
146. A. Ambrogelly, S. Palioura and D. Söll, *Nat. Chem. Biol.*, 2007, **3**, 29-35.
147. J. Nanda and A. Banerjee, *Soft Matter*, 2012, **8**, 3380-3386.
148. N. S. De Groot, T. Parella, F. X. Aviles, J. Vendrell and S. Ventura, *Biophys. J.*, 2007, **92**, 1732-1741.
149. E. R. Draper, B. J. Greeves, M. Barrow, R. Schweins, M. A. Zwijnenburg and D. J. Adams, *Chem*, 2017, **2**, 716-731.
150. S. Ghosh, V. K. Praveen and A. Ajayaghosh, *Annu. Rev. Mater. Res.*, 2016, **46**, 235-262.
151. M. Hughes, S. Debnath, C. W. Knapp and R. V. Ulijn, *Biomater. Sci.*, 2013, **1**, 1138-1142.

152. A. Mahler, M. Reches, M. Rechter, S. Cohen and E. Gazit, *Adv. Mater.*, 2006, **18**, 1365-1370.
153. C. Colquhoun, E. R. Draper, R. Schweins, M. Marcello, D. Vadukul, L. C. Serpell and D. J. Adams, *Soft Matter*, 2017, **13**, 1914-1919.
154. J. H. Van Esch, *Langmuir*, 2009, **25**, 8392-8394.
155. M. Wallace, J. A. Iggo and D. J. Adams, *Soft Matter*, 2015, **11**, 7739-7747.
156. J. Raeburn, C. Mendoza-Cuenca, B. N. Cattoz, M. A. Little, A. E. Terry, A. Zamith Cardoso, P. C. Griffiths and D. J. Adams, *Soft Matter*, 2015, **11**, 927-935.
157. J. Raeburn, G. Pont, L. Chen, Y. Cesbron, R. Lévy and D. J. Adams, *Soft Matter*, 2012, **8**, 1168-1174.
158. T. Liebmann, S. Rydholm, V. Akpe and H. Brismar, *BMC Biotechnol.*, 2007, **7**, 88.
159. R. Orbach, L. Adler-Abramovich, S. Zigerson, I. Mironi-Harpaz, D. Seliktar and E. Gazit, *Biomacromolecules*, 2009, **10**, 2646-2651.
160. Z. Yang, H. Gu, D. Fu, P. Gao, J. K. Lam and B. Xu, *Adv. Mater.*, 2004, **16**.
161. M. Zelzer, S. J. Todd, A. R. Hirst, T. O. McDonald and R. V. Ulijn, *Biomater. Sci.*, 2013, **1**, 11-39.
162. J. Zhou, X. Du, Y. Gao, J. Shi and B. Xu, *J. Am. Chem. Soc.*, 2014, **136**, 2970-2973.
163. C. G. Pappas, P. W. J. M. Frederix, T. Mutasa, S. Fleming, Y. M. Abul-Haija, S. M. Kelly, A. Gachagan, D. Kalafatovic, J. Trevino, R. V. Ulijn and S. Bai, *Chem. Commun.*, 2015, **51**, 8465-8468.
164. H. Geng, L. Ye, A. Y. Zhang, Z. Shao and Z. G. Feng, *J. Colloid Interface Sci.*, 2017, **490**, 665-676.
165. D. Bardelang, *Soft Matter*, 2009, **5**, 1969-1971.
166. L. Chen, S. Revel, K. Morris, L. C. Serpell and D. J. Adams, *Langmuir*, 2010, **26**, 13466-13471.

Chapter 2: Magnetically Aligned Supramolecular Hydrogels

2.1 Introduction

The analysis of materials by NMR spectroscopy inevitably entails their exposure to high strength magnetic fields. All of the NMR experiments reported in this Thesis were recorded on a 400 MHz (^{1}H) spectrometer which possesses a magnetic field of 9.4 T. As discussed in Section 2.2, magnetic fields of this strength are well-known to induce alignment of diamagnetic organic materials with respect to the applied field. For the present study, such alignment is of great importance for two reasons: Firstly, alignment of the gel fibres by the external magnetic field may significantly change either the self-assembly of the LMWGs and/or the subsequent formation of the gel network. It is thus necessary to quantify such affects in order to verify the validity of NMR spectroscopy as a non-invasive tool for the study of self-assembled hydrogels. Secondly, alignment of the gel fibres opens up the potential to observe residual anisotropic NMR properties of probe molecules as they interact with the gel fibres. As will be discussed in Chapters 3 and 4, these anisotropic parameters, including residual quadrupolar couplings (RQCs) and residual dipolar couplings (RDCs), offer a sensitive handle on the interaction of probe molecules with gel fibres. Magnetic alignment thus greatly facilitates the study of self-assembled hydrogel systems.

Section 2.2 comprises a paper, “Magnetically Aligned Supramolecular Hydrogels”, which was published in *Chemistry – A European Journal* as a communication article in 2014. In this contribution, it was demonstrated that the presence of the 9.4 T magnetic field of the spectrometer induces alignment of the wormlike micellar structures formed by a hydrophobic dipeptide LMWG at alkaline pH. In the absence of divalent cations, these samples exist as viscous solutions but are transformed into gels upon either a decrease in the pH or upon the addition of salts such as $CaCl_2$. If prepared in the magnetic field of the spectrometer, the fibres in these hydrogels possess a degree of alignment with respect to the spectrometer field. In Chapters 3 and 4 it is shown, using a range of techniques to be discussed, that the presence of the magnetic field does not significantly affect the self-assembly, surface chemistry or mechanical properties of the hydrogels studied. In this Chapter, it is shown using infra-red spectroscopy (Section 2.4.14) that the presence of the magnetic field does

not appreciably affect the primary molecular packing of the LMWGs in the self-assembled fibres. NMR spectroscopy is thus verified as an acceptable tool for the non-invasive analysis of self-assembled hydrogels.

The principal technique used to detect and quantify alignment is ^{2}H NMR, the theory of which is presented in Chapter 3, Section 3.2.5 and Chapter 4, Section 4.3.2.1. In essence, the interaction of deuterated probe molecules with anisotropically arranged fibres results in the splitting of their ^{2}H NMR resonances by an amount known as the residual quadrupolar coupling (RQC). D_2O and dioxane-d_8 were used as the probe molecules in this work. This Chapter focuses on particularly hydrophobic LMWGs that from wormlike structures at alkaline pH in the absence of divalent cations. In these systems, RQCs are seen in all samples for D_2O and/or dioxane-d_8. As discussed in Chapter 3 and 4, the magnitude of an RQC depends not only upon the alignment of the gel fibres but also upon the geometry of the interaction between the probe molecule and the fibre. Magnetic alignment of hydrogels formed from the gelator Br-AV (Figure 2-S17b, Section 2.4.17) was only detected when suitable probe molecules were found (Chapters 3 and 4).

2.1.1 Author Contributions

The author contributions are as follows: MW conceived the concept of the paper, designed the experiments, prepared all the samples and performed all of the NMR experiments. AZC performed all of the confocal microscopy, SEM, infra-red and powder XRD experiments, during which MW was present. WJF provided helpful guidance throughout the project. JAI provided guidance with the NMR experiments. DJA synthesised all of the gelators and provided guidance throughout the project. MW wrote the manuscript, aided by helpful suggestions from the other authors. AZC prepared Figures 2-1a, 2-S14, 2-S15a, 2-S15b, 2-S16 and 2-S19b and Sections 2.3.3.2 and 2.3.5. All other Figures were prepared by MW. The data of Figure 2-S1, Section 2.4.1 at field strengths higher than 11.7 T was collected at the NMR Centre for Structural Biology at the University of Liverpool with the assistance of Dr Marie Phelan.

2.2 Magnetically Aligned Supramolecular Hydrogels

Matthew Wallace,[a,*] Andre Z. Cardoso,[a] William J. Frith,[b] Jonathan A. Iggo[a] and Dave J. Adams[a,*]

[a] *Department of Chemistry, University of Liverpool, Crown Street, Liverpool, L69 7ZD, U.K. Email: d.j.adams@liverpool.ac.uk*

[b] *Unilever R&D Colworth, Colworth Science Park, Sharnbrook, Bedfordshire, MK44 1LQ, U.K.*

2.2.1 Abstract

The magnetic-field-induced alignment of the fibrillary structures present in an aqueous solution of a dipeptide gelator, and the subsequent retention of this alignment upon transformation to a hydrogel upon the addition of $CaCl_2$ or upon a reduction in solution pH is reported. Utilising the switchable nature of the magnetic field coupled with the slow diffusion of $CaCl_2$, it is possible to precisely control the extent of anisotropy across a hydrogel, something that is generally very difficult to do using alternative methods. The approach is readily extended to other compounds that form viscous solutions at high pH. It is expected that this work will greatly expand the utility of such low molecular-weight gelators (LMWG) in areas where alignment is key.

2.2.2 Main Article

Supramolecular hydrogels are formed by the self-assembly of low-molecular-weight gelators (LMWG) into fibrillar structures, which then entangle or cross-link to form the gel matrix.[1] These fascinating materials are currently being investigated for a vast number of applications including wound healing,[2] energy harvesting,[3] and pollutant capture.[4] Functionalised dipeptides, where the *N*-terminus is substituted with a large hydrophobic group such as naphthalene or fluorenylmethoxycarbonyl, are receiving an increasing amount of interest as LMWG.[5] These LMWG generally dissolve to form free-flowing solutions when the pH is adjusted above the pK_a of the terminal carboxylic acid.[6] Gelation of these solutions can be induced by the addition of salt[7] or by lowering the pH of the solution.[6, 8] Given the difficulty in 'designing' effective LMWG, there is much interest in how the properties of gels prepared from

these known compounds may be controlled and tailored for specific applications.[9] Relatively little has been reported on how the relative orientation of the supramolecular structures present in the gels can be controlled, with most studies focusing mainly on the bulk properties of the materials. Aligned materials are of significant interest for optoelectronics[3] and regenerative medicine,[10] for example. Zhou *et al.* recently reported that significant anisotropy in the orientation of fibres formed from naphthalene dipeptides and tripeptides could be obtained using a combination of aromatic–aromatic inter-fibre interactions and enzymatic hydrogelation.[11] With unrelated LMWG, anisotropy in the orientation of the self-assembled fibres has been induced with electric fields,[12] chemical gradients,[13] magnetic fields[14] and shear alignment.[15] High strength magnetic fields can induce anisotropy in supramolecular materials.[16] Here, we report that strong magnetic fields induce significant anisotropy in the relative orientations of the structures present in a solution of LWMG, which is retained upon gel formation (Figure 2-1a).

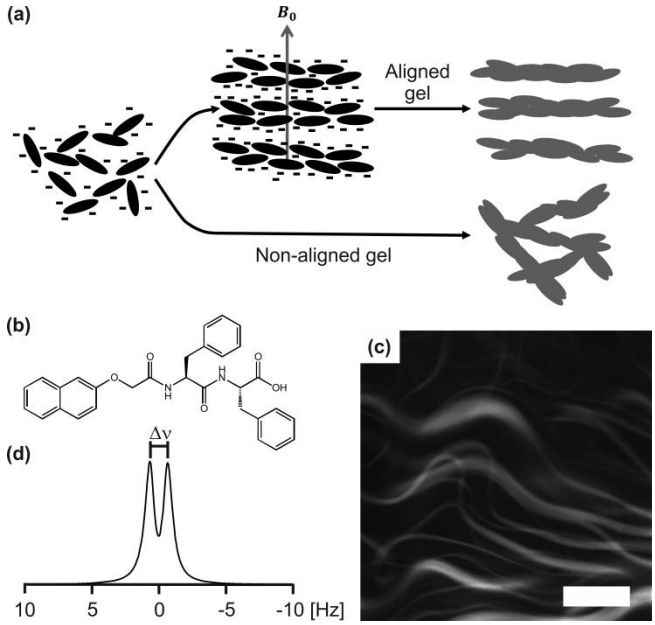

Figure 2-1. (a) NapFF exists in solution at high pH as worm-like micelles which align spontaneously in a strong magnetic field and can subsequently be transformed to gels with aligned fibres upon application of a suitable switch. (b) Structure of NapFF; (c) Confocal micrograph of a NapFF solution at pD 12.6 (0.5 wt%) showing worm-like micelles, stained with Nile blue. The scale bar represents 100 μm; (d) ^{2}H-NMR spectrum of a solution of NapFF at pD 12.6 (0.5 wt%), measured in a 9.4 T (400 MHz ^{1}H) NMR spectrometer, $|\Delta\nu|$ = 1.3 Hz.

We have previously demonstrated that solutions of NapFF (0.5 wt%; Figure 2-1b) contain highly anisotropic structures using viscosity measurements, electron microscopy and small-angle X-ray scattering.[7a, 17] Our model is that the carboxylates stabilise worm-like micelles with the core formed from the hydrophobic naphthalene and phenylalanine groups. This data is further confirmed here by confocal microscopy (Figure 2-1c), which also suggests that lateral association of the worms takes place.

We reasoned that the worm-like micelles formed at high pH by NapFF may spontaneously align in high-strength magnetic fields, due to their presumably high diamagnetic anisotropy resulting from their anisotropic shape and abundance of aromatic rings. To probe alignment, we used deuterium (^{2}H) NMR.[18] In a 400 MHz (^{1}H) spectrometer, the deuterium resonance of D_2O in a solution of NapFF at high pD exhibits a residual quadrupolar coupling (RQC) ($\Delta\nu$, Figure 2-1d), indicating that the worm-like micellar structures present in the solution share a common orientation with respect to the magnetic-field axis. Unlike previous examples, we can therefore gel pre-aligned solutions in a magnetic field, as opposed to having to first disassemble to the monomer state by heating to 90 ^{o}C.[14b] We note that the magnitude of the RQC is temperature- and concentration- dependent (Figure 2-S7, Section 2.4.7 and Figure 2-S8, Section 2.4.8). Solutions at 0.5 wt% sometimes contain birefringent domains. However, at 1.0 wt%, birefringent domains are formed that clearly show alignment after exposure to a magnetic field (Figure 2-S13, Section 2.4.13).

Addition of $CaCl_2$ to solutions of NapFF at high pH results in the formation of stable hydrogels.[7a, 17] This gelation arises as a result of the Ca^{2+} cross-linking the worm-like structures through formation of salt-bridges between adjacent carboxylate groups.[7a] When $CaCl_2$ is layered on top of a solution of NapFF in a 5 mm NMR tube and the sample left to stand in a 9.4 T field for the $CaCl_2$ to diffuse to the bottom of the tube, an RQC of D_2O is again observed and thus anisotropy in the orientation of the structures in the absence of Ca^{2+} is retained on gelation. The extent of magnetic-field-induced anisotropy— the magnitude of the RQC of D_2O—exhibits a distinct dependence on magnetic field strength, both in solutions of NapFF at high pD and in $CaCl_2$-triggered gels. ^{2}H NMR spectra of D_2O in $CaCl_2$-triggered gels prepared at 0, 4.7 and 9.4 T are shown in Figure 2a, in which the RQCs are 0.2, 0.9 and 1.4 Hz respectively. All spectra were recorded at 9.4 T, confirming that anisotropy is

'locked in' upon gel formation. Similar effects are seen with $MgCl_2$ (Figure 2-S11a, Section 2.4.11), although this gel had a larger splitting (2.7 versus 1.4 Hz in a similar $CaCl_2$ sample), with apparently a co-existing isotropic phase. Adding NaCl resulted in a slightly increased RQC (Figure 2-S11b, Section 2.4.11). This is as expected from our previous data,[7a] where we showed that $MgCl_2$ can induce gelation, but addition of NaCl resulted in only weak gels being formed.

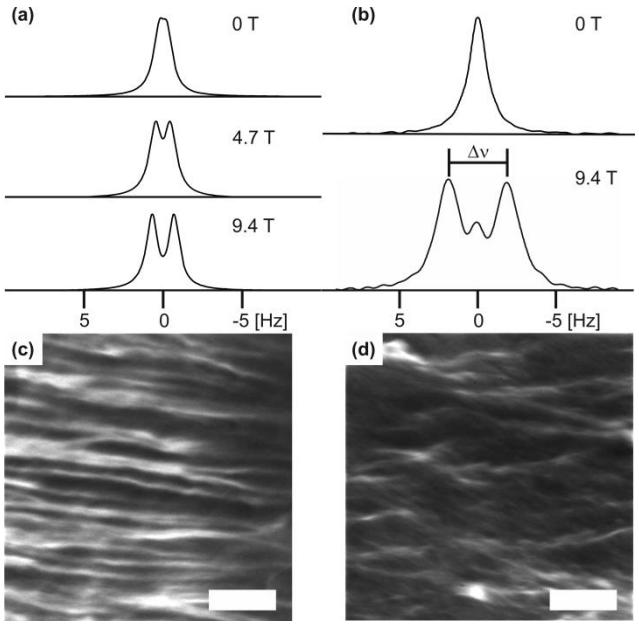

Figure 2-2. (a) ^{2}H-NMR spectra of D_2O in gels formed in the presence of magnetic fields of varying strengths by the addition of $CaCl_2$ to a solution of NapFF at pD 12.6. All spectra were recorded at 9.4 T; (b) ^{2}H-NMR spectra of dioxane-d_8 in gels formed by the addition of solid GdL to a solution of NapFF at pD 12.6 at magnetic field strength indicated. (c) Confocal micrograph of a $CaCl_2$-triggered gel prepared in a 9.4 T magnetic field; (d) Confocal micrograph of a $CaCl_2$-triggered gel prepared away from a magnetic field. The scale bars represent 100 μm.

The magnitudes of the RQC of D_2O in NapFF solutions at pD 12.6 (Figure 2-1d), measured after 40 min equilibration in the magnetic field, were 0.6 and 1.3 Hz at 4.7 and 9.4 T respectively. The RQC at 4.7 T also took longer to reach a steady value (Figure 2-S1, Section 2.4.1). The observed field dependence of the RQC, rather than merely the time to attain a steady RQC, suggests that the worm-like structures formed by the NapFF at high pD interact significantly with one another, such as by forming entanglements, and so the typical model for magnetic alignment of worm-like assemblies (a rigid rod rotating in a continuous medium under the influence of

an applied field)[19] is apparently not valid here. We note that this magnetic alignment seems to only affect the fibres; the supramolecular packing is unaffected by the magnetic field as shown by the similarity in the IR data for aligned and unaligned samples (Figure 2-S14, Section 2.4.14).

Chemical-shift imaging (CSI), which provides spatially resolved NMR spectra along the length of the sample adjacent to the RF coils,[20] reveals that the extent of anisotropy in a gel sample prepared at 4.7 or 9.4 T is uniform throughout this region of the sample (Figure 2-S2, Section 2.4.2). A gel prepared away from the magnetic field exhibits a very small RQC which increases towards the base of the NMR tube, perhaps indicative of a residual $CaCl_2$ concentration gradient leading to a 'softer' gel towards the bottom of the tube, which is more able to re-orient in the magnetic field. To determine the sense of the magnetic-field-induced alignment, we turned to confocal microscopy. A sample was prepared in a 9.4 T magnetic field so that the field axis lay perpendicular to the focal plane during imaging. Images of the sample (Figure 2-2c) show that the structures present lie distinctly in the focal plane, whereas in a gel prepared away from the field the structures have a discontinuous appearance (Figure 2-2d).

It can thus be inferred that the gel fibres align perpendicular to the magnetic field. We hypothesise that the in-plane alignment exhibited by the structures in the gel prepared in the field arises due to a combination of their mutual interactions and possibly a slight lateral component to the magnetic field. In isolation, the structures would be free to adopt any orientation in a plane perpendicular to a single magnetic field axis.[21]

Self-supporting hydrogels can also be prepared from solutions of NapFF by a decrease in the pH,[6] through the hydrolysis of glucono-δ-lactone (GdL),[6, 22] which serves to protonate the terminal carboxylate groups and drive the formation of a cross-linked network. The D_2O resonance in gels thus prepared in magnetic fields does not exhibit an RQC; however, splitting is seen on the resonance of 1,4-dioxane-d_8 (0.05 vol %), which was added as a hydrophobic probe molecule (see Figure 2-S4, Section 2.4.4 and Figure 2-S9, Section 2.4.9 for further details; the choice of probe is important, as shown in Section 2.4.10). We attribute these observations to differences in the way D_2O and dioxane order around the hydrophobic fibres,

resulting in the RQC of D_2O being averaged to zero, whereas that of dioxane is not. This points to the potential of ^2H NMR to study the solvation of gel fibres, something that is of relevance for many envisaged applications of hydrogels such as cell culturing.[23] Appreciable RQCs are also seen on the dioxane-d_8 resonance in solutions of NapFF at high pD and $CaCl_2$-triggered gels (Figures 2-S3a and 2-S3b, Section 2.4.3).

GdL was placed as a solid on top of a D_2O solution of NapFF/dioxane and the sample placed in the 9.4 T spectrometer field for 60 hours to allow the GdL to dissolve, hydrolyse to gluconic acid and diffuse to the base of the NMR tube. The dioxane resonance in this gel exhibits a distinct 'doublet' ($\Delta\nu$, Figure 2-2b), indicative of significant magnetic-field-induced anisotropy. Spectra taken as the gel formed show how the singlet (isotropic) peak between the doublet peaks grows in as the gluconic acid diffuses down the NMR tube (Figure 2-S4, Section 2.4.4). We attribute this singlet to 'strain-induced collapse' as the hydrophobic protonated fibrils pack together, destroying the alignment that they had at high pD to some degree. A gel formed away from the magnetic field shows no anisotropy (Figure 2-2b and Figure 2-S5, Section 2.4.5).

Diffusion of a gelation trigger, such as $CaCl_2$ or GdL, through a solution of NapFF is slow and can readily be followed by CSI.[24] Figure 2-3a shows the diffusion of $CaCl_2$ down through a solution of NapFF, monitored by changes in the RQC of D_2O. A $CaCl_2$ diffusion 'front' at which the RQC cannot be resolved (at 0 mm, Figure 2-3), being of appreciable magnitude both above and below this region of the sample, can be detected. ^1H spectra taken across the same region of the sample show how the signal from the NapFF present in the solution at high pD is not detectable above the 'front' (Figure 2-S6, Section 2.4.6). The 'front' can thus be taken to represent the boundary between a solution of NapFF and a Ca^{2+} crosslinked gel.

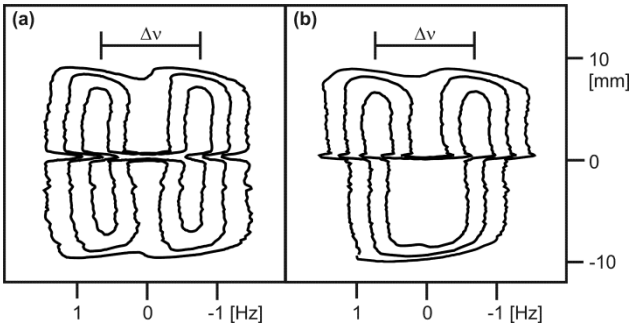

Figure 2-3. (a) ^{2}H image of sample just before removal from magnetic field, shown as a 2D contour plot. The 'front' is visible as a discontinuity in the ^{2}H splitting of D_2O. The vertical axis corresponds to the height above the centre of the NMR radiofrequency coil. (b) ^{2}H image of sample after ageing away from magnetic field for two weeks.

It is possible to remove a sample from the magnetic field before the trigger has reached the base of the NMR tube, allowing a gel to be prepared in which the top part of the sample is gelled in the magnetic field while the lower part of the sample is gelled away from the field. This allows us to control the extent of magnetic-field-induced anisotropy spatially across a sample. Figure 2-3b shows an image of the same sample from Figure 2-3a, removed immediately after NMR imaging and left to gel away from the magnetic field. There is a distinct decrease in the RQC of D_2O in the gel, just below the position of the 'front' when the sample was removed from the magnetic field. We have thus succeeded in controlling spatially the degree of anisotropy across our sample. The significant splitting observed in the lower portion of the gel (Figure 2-S6f, Section 2.4.6), compared to a sample prepared wholly away from the field (Figure 2-S2, Section 2.4.2), is attributable to the slow reorientation of the structures present in solution following removal of the sample from the magnetic field. The ability to control the extent of anisotropy across a gel sample, not just between gels, may prove invaluable to the production of new materials in which the mechanical, transport or electronic properties vary in a spatially controlled fashion.

Finally, we note that our approach to preparing aligned materials is not restricted to NapFF. A prerequisite, however, seems to be the formation of worm-like micelles at high pH[17] (Figure 2-S17a, Section 2.4.17). Related LMWG that do not form such anisotropic structures cannot be used to form aligned gels (Figure 2-17d, Section 2.4.17). However, where worm-like micelles are formed, the behaviour is analogous to that of NapFF. We expect that this work will greatly expand the utility of LMWGs

that form worm-like micelles at high pH, particularly in areas where alignment is key, such as conductive materials and cell culturing.[3, 10, 15]

2.2.3 Experimental Section

NapFF was prepared as described elsewhere.[6, 17] All other chemicals were purchased from Sigma–Aldrich and used as received. To prepare a solution of NapFF, solid NapFF was weighed into a 14 mL vial and an appropriate amount of D_2O added, followed by standardised NaOD (ca. 1 M, (1.2 ± 0.1) equivalents). The mixture was then stirred for 24 hours to yield a clear, slightly viscous solution with a pD of between 12.1 and 12.6 before being transferred in aliquots (560 mL) to NMR tubes (5 mm) by pipette. The samples were then aged for between 6 and 8 days at (295 ± 3) K before analysis or gel preparation. Analysis by ^{2}H NMR and polarised optical microscopy suggested that the solutions reached a steady state after 5 days (Figure 2-S18a, Section 2.4.18 and Figure 2-S2, Section 2.4.2). To prepare $CaCl_2$-triggered gels, $CaCl_2$ solution (0.75 M, 40 mL) was added to the top of the NapFF solution in the NMR tube using a long needle. The sample was then immediately transferred to the NMR spectrometer held at (298 ± 0.5) K, or, for gels prepared away from the magnetic field, a water bath held at (298 ± 0.3) K. After 60 hours, the samples prepared in the magnetic field were removed from the spectrometer and placed in the water bath. All samples were left to stand for at least 7 days following $CaCl_2$ addition prior to analysis. The height of the 560 mL solution in the NMR tube (41 mm) is sufficient so that, when first placed in the spectrometer, the sample adjacent to the radiofrequency coils of the spectrometer is completely free from the added $CaCl_2$, which slowly diffuses down the tube into the NMR-active region. Glucono-δ-lactone (GdL)-triggered gels were prepared as for $CaCl_2$-triggered gels, but with solid GdL (3–4 mg) added to the top of the NapFF solution using a Pasteur pipette. Where noted, the NapFF solutions were doped with dioxane-d_8 (0.05 vol%, 6 mM) to act as an additional probe for deuterium NMR.

2.2.4 Acknowledgements

We thank Unilever for a Case Award (MW) and the EPSRC for funding a DTA (MW). We thank the EPSRC for funding (EP/ C005643/1 and EP/K039687/1).

2.2.5 References

1. a) P. Terech and R. G. Weiss, *Chem. Rev*., 1997, **97**, 3133–3160; b) M. de Loos, B. L. Feringa and J. H. van Esch, *Eur. J. Org. Chem*., 2005, **2005**, 3615–3631.
2. J. Boekhoven and S. I. Stupp, *Adv. Mater*., 2014, **26**, 1642–1659.
3. S. S. Babu, V. K. Praveen and A. Ajayaghosh, *Chem. Rev.*, 2014, **114**, 1973–2129.
4. S. Kiyonaka, K. Sugiyasu, S. Shinkai and I. Hamachi, *J. Am. Chem. Soc*., 2002, **124**, 10954–10955.
5. a) G. Fichman and E. Gazit, *Acta Biomater*., 2014, **10**, 1671–1682; b) D. J. Adams, *Macromol. Biosci.*, 2011, **11**, 160–173.
6. L. Chen, S. Revel, K. Morris, L. C. Serpell and D. J. Adams, *Langmuir*, 2010, **26**, 13466–13471.
7. a) L. Chen, G. Pont, K. Morris, G. Lotze, A. Squires, L. C. Serpell and D. J. Adams, *Chem. Commun.*, 2011, **47**, 12071–12073; b) S. Roy, N. Javid, P. W. J. M. Frederix, D. A. Lamprou, A. J. Urquhart, N. T. Hunt, P. J. Halling and R. V. Ulijn, *Chem. Eur. J.*, 2012, **18**, 11723–11731.
8. V. Jayawarna, M. Ali, T. A. Jowitt, A. F. Miller, A. Saiani, J. E. Gough and R. V. Ulijn, *Adv. Mater.*, 2006, **18**, 611–614.
9. J. Raeburn, A. Zamith Cardoso and D. J. Adams, *Chem. Soc. Rev.*, 2013, **42**, 5143–5156.
10. J. B. Matson and S. I. Stupp, *Chem. Commun.*, 2012, **48**, 26–33.
11. J. Zhou, X. Du, Y. Gao, J. Shi and B. Xu, *J. Am. Chem. Soc.*, 2014, **136**, 2970–2973.
12. M. Yoshio, Y. Shoji, Y. Tochigi, Y. Nishikawa and T. Kato, *J. Am. Chem. Soc.*, 2009, **131**, 6763–6767.
13. I. Ziemecka, G. J. M. Koper, A. G. L. Olive and J. H. van Esch, *Soft Matter*, 2013, **9**, 1556–1561.
14. a) I. O. Shklyarevskiy, P. Jonkheijm, P. C. M. Christianen, A. P. H. J. Schenning, Del Guerzo, J.-P. Desvergne, E. W. Meijer and J. C. Maan, *Langmuir*, 2005, **21**, 2108–2112; b) D. W. P. M. Lçwik, I. O. Shklyarevskiy, L. Ruizendaal, P. C. M. Christianen, J. C. Maan and J. C. M. van Hest, *Adv. Mater.*, 2007, **19**, 1191–1195.

15. S. Zhang, M. A. Greenfield, A. Mata, L. C. Palmer, R. Bitton, J. R. Mantei, C. Aparicio, M. O. de La Cruz and S. I. Stupp, *Nat. Mater*., 2010, **9**, 594–601.

16. a) L. J. Michot, I. Bihannic, S. Maddi, S. S. Funari, C. Baravian, P. Levitz and P. Davidson, *Proc. Natl. Acad. Sci. USA*, 2006, **103**, 16101–16104; b) E. K. Tiburu, D. M. Moton and G. A. Lorigan, *Biochim. Biophys. Acta Biomembranes*, 2001, **1512**, 206–214; c) R. J. A. Hill, V. L. Sedman, S. Allen, P. Williams, M. Paoli, L. Adler-Abramovich, E. Gazit, L. Eaves and S. J. B. Tendler, *Adv. Mater.*, 2007, **19**, 4474–4479; d) S. O. Raja and A. K. Dasgupta, *Chem. Phys. Lett.*, 2012, **554**, 163–167; e) H. Enozawa, M. Hasegawa, E. Isomura, T. Nishinaga, T. Kato, M. Yamato, T. Kimura and M. Iyoda, *ChemPhysChem*, 2009, **10**, 2607–2611; f) R. S. M. Rikken, H. H. M. Kerkenaar, R. J. M. Nolte, J. C. Maan, J. C. M. van Hest, P. C. M. Christianen and D. A. Wilson, *Chem. Commun.*, 2014, **50**, 5394–5396; g) K. Takazawa, J.-i. Inoue and K. Mitsuishi, *Nanoscale*. 2014, **6**, 4174–4181; h) K. Matsumoto, F. Kimura, S. Tsukui and T. Kimura, *Cryst. Growth Des.*, 2011, 11, 945–948; i) I. O. Shklyarevskiy, P. Jonkheijm, N. Stutzmann, D. Wasserberg, H. J. Wondergem, P. C. M. Christianen, A. P. H. J. Schenning, D. M. de Leeuw, Z˘. Tomovic´, J. Wu, K. Millen and J. C. Maan, *J. Am. Chem. Soc.*, 2005, **127**, 16233–16237; j) I. O. Shklyarevskiy, P. Jonkheijm, P. C. M. Christianen, A. P. H. J. Schenning, E. W. Meijer, O. Henze, A. F. M. Kilbinger, W. J. Feast, A. Del Guerzo, J.-P. Desvergne and J. C. Maan, *J. Am. Chem. Soc.*, 2005, **127**, 1112–1113; k) J. C. Gielen, A. Ver Heyen, S. Klyatskaya, W. Vanderlinden, S. Hçger, J. C. Maan, S. De Feyter and P. C. M. Christianen, *J. Am. Chem. Soc.*, 2009, **131**, 14134–14135; l) T. M. Alam and S. K. McIntyre, *Langmuir*, 2008, **24**, 13890–13896; m) M. Liebi, P. G. van Rhee, P. C. M. Christianen, J. Kohlbrecher, P. Fischer, P. Walde and E. J. Windhab, *Langmuir*, 2013, **29**, 3467–3473.

17. L. Chen, T. O. McDonald and D. J. Adams, *RSC Adv.*, 2013, **3**, 8714–8720.

18. A. Delville, J. Grandjean and P. Laszlo, *J. Phys. Chem.*, 1991, **95**, 1383–1392.

19. A. Rapp, K. Ermolaev and B. M. Fung, *J. Phys. Chem. B*, 1999, **103**, 1705 – 1711.

20. P. Trigo-Mouriño, C. Merle, M. R. M. Koos, B. Luy and R. R. Gil, *Chem. Eur. J.*, 2013, **19**, 7013–7019.
21. T. Kimura and M. Yoshino, *Langmuir*, 2005, **21**, 4805–4808.
22. D. J. Adams, M. F. Butler, W. J. Frith, M. Kirkland, L. Mullen and P. Sanderson, *Soft Matter*, 2009, **5**, 1856–1862.
23. P. Lee, R. Lin, J. Moon and L. Lee, *Biomed. Microdevices*, 2006, **8**, 35–41.
24. Å. Östlund, D. Bernin, L. Nordstierna and M. Nydén, *J. Colloid Interface Sci.*, 2010, **344**, 238–240.

2.3 Supporting Information: Further experimental details

2.3.1 Confocal Microscopy

2.3.1.1 Sample preparation

All samples were prepared in D_2O in order to be fully comparable with the NMR experiments.

For the samples of Figures 2-1c, 2-2c,d, 0.5 wt% solutions of NapFF were prepared as for the NMR analysis but with the NapFF dissolved in a solution containing approximately 0.002 mg/mL Nile blue dye which was prepared by dilution of a 0.01 mg/mL stock solution. For the gel samples on Figures 2-2c,d, 900 μL of the NapFF solutions were transferred after mixing to 35 mm glass-bottom cell culture dishes (Greiner-Bioone) and left to stand for 6 days away from the magnetic field. To prepare gels, $CaCl_2$ solution (52 mg/mL, 40 μL) was added drop-wise to a small region on the side of the dish. Prior to addition of $CaCl_2$, the sample to be gelled in a 9.4 T NMR magnet (Fig. 2-2c) was first lowered down the bore of the spectrometer and left to stand in the field for one hour before it was raised, the $CaCl_2$ added, and the sample carefully lowered back into the field. Samples were left to stand overnight before imaging. Care was taken to ensure that the sample dishes were level until gelation was complete. For the high pD solution in Figure 2-1c, the solution of NapFF was instead transferred to a 5 mm NMR tube and aged for 6 days prior to imaging.

For the gel samples of Section 2.4.19, a 0.1 mg/mL suspension of Nile blue was prepared and stirred overnight before being passed through a 1 μm filter. The filtrate was diluted by a factor of 2.5 and used to prepare an 0.5 wt% solution of NapFF which was placed in 4 mL aliquots into 12 mL polypropylene syringes. The syringe barrels had been cut off near the top to give a tube while the plungers had been shortened in order to allow the syringes to fit in a home-built cradle which served to keep the samples vertical as they were lowered in/out of the magnetic field. After addition of the NapFF solution, the syringes were sealed with Parafilm and left to age away from the magnetic field for six days. To prepare gels, $CaCl_2$ solution (200 mg/mL, 114 μL) was added dropwise over the top of the NapFF solution and the syringes sealed with Parafilm. Samples were left to stand for ca. 60 hours before

analysis. As with the sample of Fig. 2-2c, the sample to be prepared in a 9.4 T magnetic field was exposed to the field for one hour prior to the addition of $CaCl_2$, whereupon the sample was promptly placed back in the field.

2.3.1.2 Confocal imaging

Confocal microscopy images were taken using a Zeiss LSM 510 Meta confocal microscope. Fluorescence from Nile blue was excited using a 633 nm Helium-Neon laser and emission detected above 650 nm.

The images in Figure 2-2c,d, were obtained with the lid of the dish removed, while Figure 2-1c was obtained by imaging directly through the NMR tube. It was not possible to image gels in 5 mm NMR tubes as the resolution imposed by the curved glass surface and the thickness of the sample was found to be insufficient for the observation of any structures. To obtain the images in Section 2.4.19, the gels were extruded from the syringes using the plunger and cut into ca. 2 mm thick slices, both perpendicular and parallel to the direction at which the 9.4 T magnetic field had been applied to the sample gelled in the field, using a fresh scalpel blade. Due to syeneresis of the gel, it was possible to extrude the gel without damage. The gel slices were transferred, immediately after cutting, to 35 mm glass-bottom cell culture dishes and imaged. The top 5 mm of the gels were discarded to ensure that only the part of the sample which had been gelled by the downward diffusion of $CaCl_2$ was studied.

2.3.2 NMR Spectroscopy

All NMR experiments were performed at (298 ± 0.5) K, the variation in the temperature being less than 0.1 K. All ^1H and ^2H NMR experiments, unless otherwise stated, were performed on a Bruker Avance II 400 MHz (^1H) wide bore spectrometer operating at 400.20 MHz for ^1H and 61.43 MHz for ^2H. Z-gradients were applied using a Bruker TBI-W1 probe controlled by a Bruker GREAT 10 A gradient driver delivering a maximum gradient intensity of 55 G/cm. Spectra recorded at 4.7 T (200 MHz ^1H) were recorded on a Bruker AMX II 200 or Bruker Avance I spectrometer operating at 30.72 MHz for ^2H. ^2H spectra of D_2O were recorded *via* the lock channel with 4096 data points, a 200 μs pulse ($\pi/2$), a sweep width of 10 ppm and a relaxation delay of 1.0 s. 8 scans were acquired giving a total

acquisition time of 35 seconds. ^{2}H spectra of dioxane-d_8 and other deuterated probe molecules at 0.05 vol% were recorded with presaturation applied to the D_2O resonance during the relaxation delay (1.0 s) followed by a spoil gradient (27 G/cm, 1 ms) to dephase any observable magnetisation before the $\pi/2$ pulse and data acquisition. 3072 data points were collected in 1024 scans giving a total acquisition time of 1 hour. After data acquisition, the FID was manually inspected and trimmed prior to Fourier transformation in order to maximise the signal to noise ratio of the solute resonance. More concentrated samples required fewer scans.

All chemical shift imaging experiments were performed using a gradient phase encoding sequence based on that presented by Trigo-Mouriño *et al.*[1] ($\pi/2$ - τ_1 - g - τ_2 - Acquire, where g is a gradient pulse in the form of a smoothed square and τ_1 and τ_2 are delays of length 10 μs and 200 μs respectively). For ^{2}H-NMR images, g was varied linearly in 128 steps from -52 to 52 G/cm with a pulse duration of 816 μs. 3072 data points were collected in one scan at every step with a sweep width of 10 ppm, giving a total experimental time of 6 minutes and a theoretical spatial resolution of 0.20 mm. For ^{1}H images, g was varied linearly in 128 steps from -27 to 27 G/cm with a pulse duration of 238 μs. 4096 data points were recorded in one scan at each step with a sweep width of 10 ppm and a relaxation delay of 2.2 s, giving a total acquisition time of 6 minutes and a spatial resolution of 0.20 mm. Pre-saturation of the residual solvent resonance (HOD) was applied during the relaxation delay to ease the task of phasing the 2D datasets and to allow the observation of NapFF resonances close to this peak. Images were obtained after 2D Fourier transformation of the raw datasets followed by 2D phase correction. No zero filling was applied in the gradient dimension. ^{1}H images were Fourier transformed with 8192 points in the direct dimension with an exponential window function applied, giving a line broadening of 3 Hz. ^{2}H images of D_2O were Fourier transformed with 16384 points in the direct dimension. No line broadening factor was applied to ^{2}H images or spectra. ^{2}H images of deuterated probe molecules were processed as for the images of D_2O but Fourier transformed in the gradient dimension with a sine function applied.

2.3.3 SEM, FTIR and Powder X-Ray Diffraction

2.3.3.1 Sample Preparation

The same hydrogel samples were used for SEM, FTIR and Powder X-Ray Diffraction (pXRD). To prepare these samples, a 0.5 wt% NapFF solution in D_2O was prepared and transferred in 3.5 mL aliquots to 12 mL polypropylene syringes, which had been prepared as described for the confocal imaging experiments (Section 2.3.1.1), and allowed to age away from the magnetic field for six days. To prepare $CaCl_2$-triggered hydrogels, $CaCl_2$ solution (200 mg/mL, 100 μL) was added dropwise over the surface of the NapFF solution. For GdL-triggered hydrogels, solid GdL (19 mg) was sprinkled over the surface of the NapFF solution. For samples to be gelled in the 9.4 T magnetic field, the NapFF solutions were placed in the field for one hour prior to the addition of the gelation trigger whereupon they were promptly sealed and returned to the magnetic field. Samples were exposed to the magnetic field for 50 hours and stood away from the magnetic field for a further 20 hours prior to analysis.

Syneresis of the gels made it possible to extrude the gels from the syringes without significant damage. For analysis, the gels were extruded from the syringes and the extruded section cut with a fresh scalpel blade before being transferred for analysis. The top 5 mm of each sample was discarded to avoid artefacts due to the initially very high concentration of gelation trigger in this region.

2.3.3.2 Scanning Electron Microscope (SEM)

SEM images were recorded using a Hitachi S-4800 FE-SEM at 1 KeV. Silicon wafers were used to dry and probe the hydrogels. The 2 mm (height) x 15 mm (diameter) circular $CaCl_2$ hydrogels were placed on the silicon wafers with the plane of the circle lying perpendicular to the axis of the magnetic field when the magnetically aligned gels were prepared. The gels were dried with both a minimal nitrogen flow for 2 hours or alternatively blotting for 20 minutes with a filter paper. A selection of representative images was taken from over 60 images across each sample. This was done to minimize the drying artifacts in the sample microstructure. To avoid charging effects, after drying the samples were Au coated for 1 min at 10 mA using a sputter-coater (EMITECH K550X) prior to imaging. With this coating, a

minimal 5 nm Au layer was deposited on top of the sample. Imaging was conducted with a low voltage mode (1 keV) at a 1.5 to 3 mm distance from the sample and a deceleration mode (i.e. deceleration voltage of 1.5 keV, from 2.5 to 1 keV).

2.3.4 Fourier transform infrared spectroscopy (FTIR)

A FTIR liquid transmission cell (OMNI Cell System, Specac) was used for all measurements. The samples were contained between two CaF_2 windows (thickness, 4 mm) separated by a 0.1 mm PTFE spacer. The hydrogels were cut to make a cylinder with approximately 15 (diameter) x 2 mm (height) from the syringe and subsequently deposited in the FTIR liquid cell. D_2O was used as the solvent for all the infrared spectral measurements. The NapFF solutions analysed by FTIR were freshly mixed in order to avoid any artefacts due to the shearing of aged solutions upon transferal to the IR cell. The CaF_2 windows and spacer were sealed together with Parafilm and the solution placed inside using a pipette. The sample was then placed inside the 9.4 T magnetic field of an NMR spectrometer for one hour before being mounted in the IR cell and the spectrum recorded. The procedure was then repeated but without the solution being exposed to the magnetic field. It was not possible to adequately seal the windows together so that NapFF solution could be aged inside.

FTIR spectra were acquired using a Bruker Vertex spectrometer. A spectrum was obtained from averaging 64 scans between 4000 and 700 cm^{-1} with a spectral resolution of 2 cm^{-1}. A D_2O background was obtained before each set of measurements.

2.3.5 X-Ray Powder Diffraction

A ‘background’ sample for $CaCl_2$-triggered hydrogels was prepared by drying a solution containing 0.012 M NaOH and 0.05 M $CaCl_2$ in air. Hydrogels (3 block of approximately 2 x 4 x 5 mm) and the calcium crystals were dried in the aluminium holder over 7 hours in air before the measurements.

Powder X-ray diffraction data were collected on a PANalytical X’pert pro multipurpose diffractometer (MPD) in transmission Debye−Scherrer geometry operating with a Cu anode at 40 kV and 40 mA. PXRD patterns were collected in 1 h

scans with a step size of 0.013° 2θ and a scan time of 115 s/step with 2θ range between 4 − 35°. The incident X-ray beam was conditioned with 0.04 rad Soller slits and an anti-scattering slit of 0.5°. The diffracted beam passed through 0.04 rad Soller slits before being processed by the PIXcel2 detector operating in scanning mode.

2.4 Supporting Information: Additional experimental data and discussion

2.4.1 Evolution of ^{2}H RQC of D_2O at different magnetic field strengths

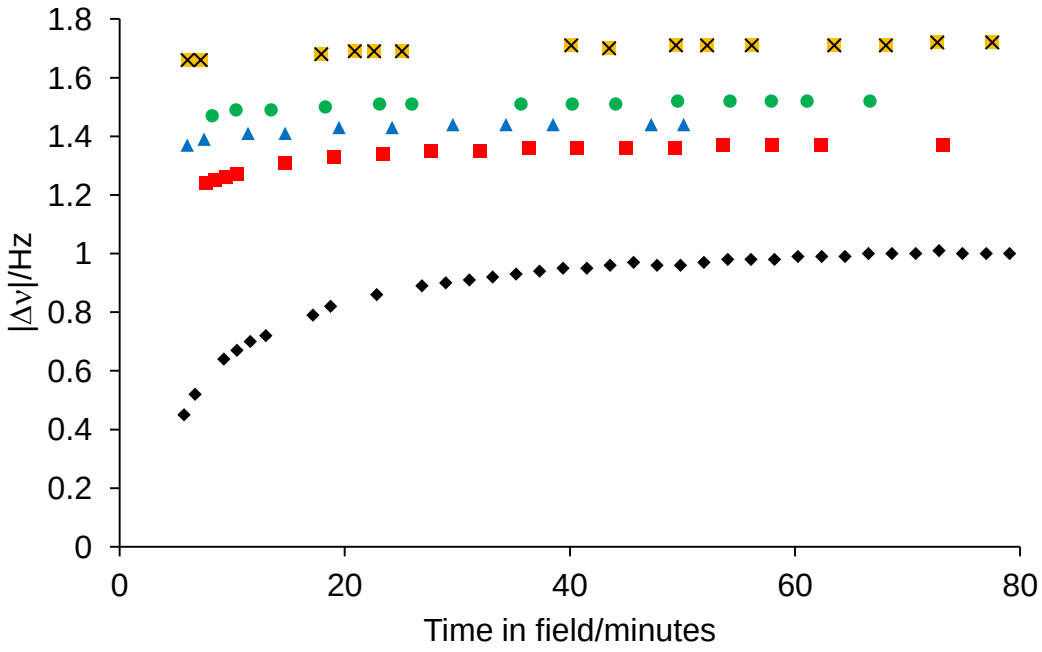

Figure 2-S1. Plot of the residual quadrupolar coupling (|Δν|) exhibited by the D_2O resonance in 0.5 wt% solutions of NapFF at pD 12.6 at different field strengths as a function of exposure time in the magnetic field: 4.7 T (black diamond), 9.4 T (red square), 11.7 T (blue triangle), 14.1 T (green circle) and 18.8 T (orange crossed square).

The dead time at the start of the experiment is the time taken to obtain a shim on the sample of sufficient quality for accurate determination of RQCs. The samples at all field strengths came from the same preparation of NapFF solution, aged for between 5 and 8 days. Measurements at field strengths above 11.7 T were recorded at the NMR Centre for Structural Biology at the University of Liverpool. The assistance of Dr Marie Phelan in acquiring these data series is gratefully acknowledged.

2.4.2 CSI analysis of $CaCl_2$ triggered gels prepared at different magnetic field strengths

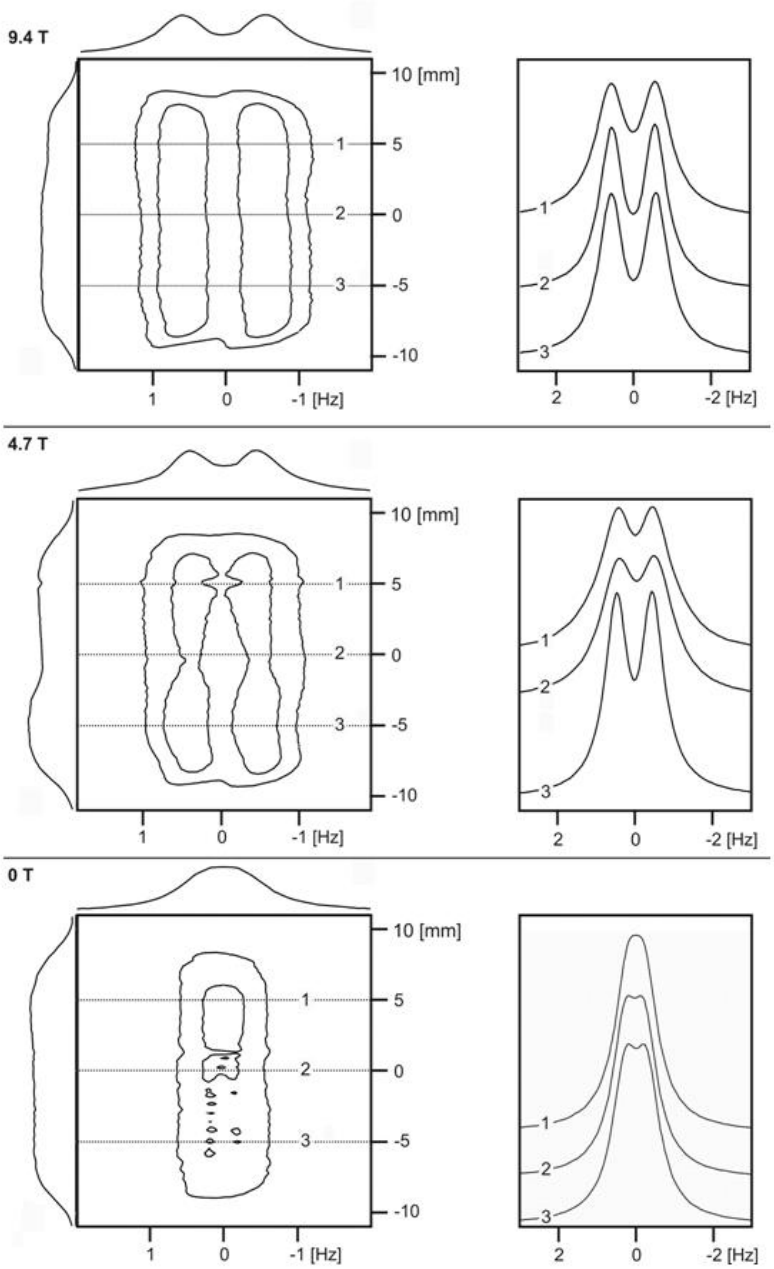

Figure 2-S2. Chemical shift images of $CaCl_2$ triggered gels prepared at 9.4 and 4.7 and 0 T. 0 T denotes a gel prepared away from a strong magnetic field. 0 T corresponds to preparation of the sample away from the magnetic field. The images are presented as 2D contour plots (left) with spectra (right) extracted from the positions indicated by dashed lines.

2.4.3 ^{2}H NMR spectra of dioxane-d_8 in $CaCl_2$ triggered gels and solutions of NapFF

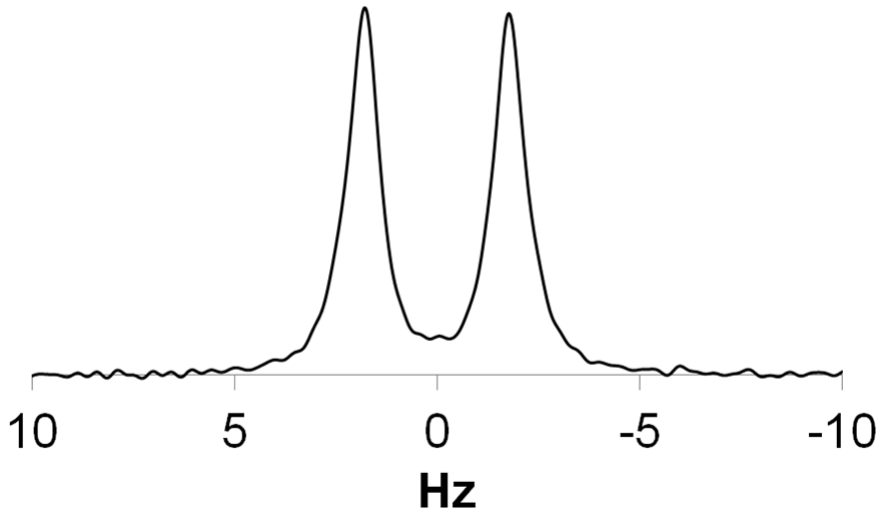

Figure 2-S3a. ^{2}H spectrum of dioxane-d_8 in an 0.5 wt% NapFF $CaCl_2$-triggered hydrogel.

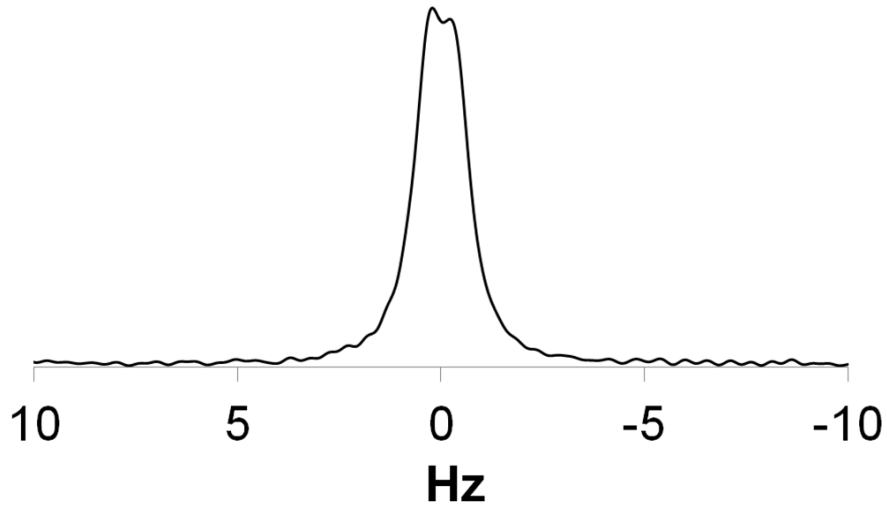

Figure 2-S3b. ^{2}H-NMR spectrum of dioxane-d_8 in a 0.5 wt% solution of NapFF at pD 12.6.

2.4.4 CSI analysis of the formation of GdL-triggered NapFF gel

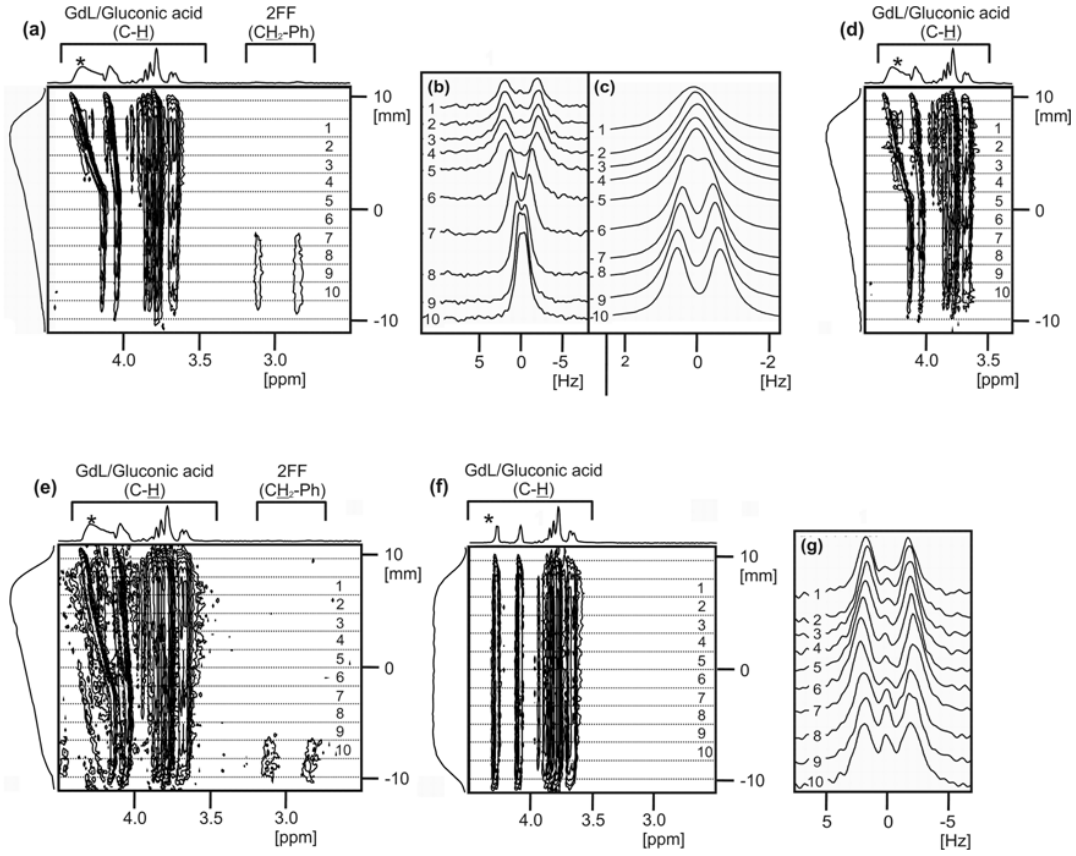

Figure 2-S4. Following the formation of a GdL-triggered NapFF gel by chemical shift imaging (CSI) (a) ^{1}H image of sample to show GdL/gluconic acid peaks and NapFF resonances. (b) ^{2}H-NMR spectra of dioxane-d_8 at regions indicated on (a). (c) ^{2}H-NMR spectra of D_2O at regions indicated on (a). (d) ^{1}H image of sample showing how little GdL had progressed down tube since (a) was recorded. Images (a)-(d) were recorded in alphabetical order. (e) ^{1}H image of sample before removal from magnetic field. (f) ^{1}H image of sample on (e) after ageing away from magnetic field for two weeks. (g) ^{2}H-NMR spectra of dioxane-d_8 at regions indicated on (e) and (f) in the sample after ageing for two weeks away from magnetic field.

The projection on the left of the CSI images (c, d, e) indicates the concentration gradient of the GdL. The signal falls away towards the top of the image due to the finite size of the radiofrequency coil of our instrument. The pD can be estimated from the peak marked*.[2] It can thus be inferred that the pD at and above region 5 is ≤ 7 and so, given an apparent pK_a of NapFF of 6,[3] the fibres will be protonated to a significant degree. The magnitude of the RQC exhibited by dioxane-d_8 (b) gradually

increases as the pD falls. Above region 5, a singlet peak becomes visible between the doublet indicative of an isotropic phase. The RQC of D_2O (c) gradually diminishes to zero as the pD falls. NMR-visible NapFF is apparent at the base of (a) indicating this region of the sample had not yet gelled fully. After ageing of the sample away for the magnetic field for two weeks (f), no residual concentration gradient of the GdL/gluconic acid is apparent and the pD appears uniform throughout the sample. The singlet (isotropic) peak of dioxane-d_8 (g) is noticeably larger in the lower portion of the sample (regions 9 and 10) where the sample had not completely gelled prior to removal from the magnetic field.

Images (b), (c) and (g) were recorded with 16 gradient steps giving a theoretical resolution of 1.6 mm. (b) and (g) were recorded with pre-saturation applied to the D_2O resonance along with a spoil gradient to de-phase any observable magnetisation generated. For (b), 256 scans were recorded at each gradient step with 2048 data points giving a total acquisition time of 3 hours while for (g) 1024 scans were recorded at each step giving a total acquisition time of 13 hours.

2.4.5 CSI analysis of a GdL-triggered NapFF hydrogel prepared away from the magnetic field

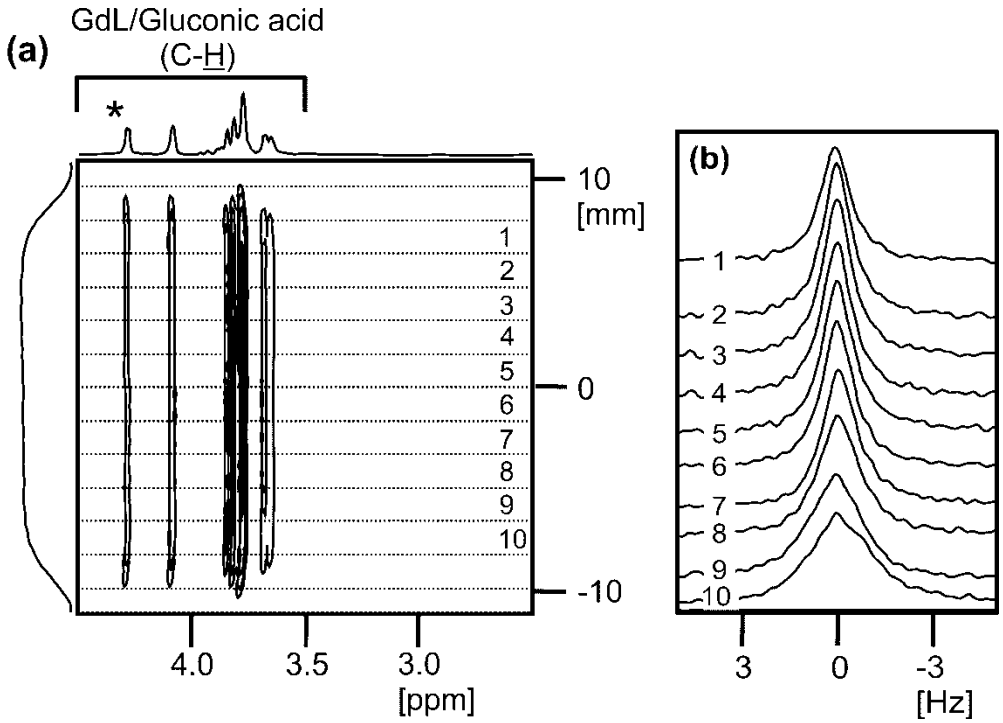

Figure 2-S5. CSI images of the GdL-triggered NapFF gel of Figure 2-2b prepared in a water bath away from the magnetic field. (a) ^{1}H image of sample recorded two weeks after addition of GdL to NapFF solution showing that the GdL/gluconic acid concentration and pD are uniform throughout the sample. (b) ^{2}H-NMR spectra of dioxane-d_8 at regions indicated on (a). No RQC is detectable indicating that the gel cannot re-orient in the magnetic field.

2.4.6 CSI analysis of the formation of a $CaCl_2$-triggered NapFF hydrogel by CSI

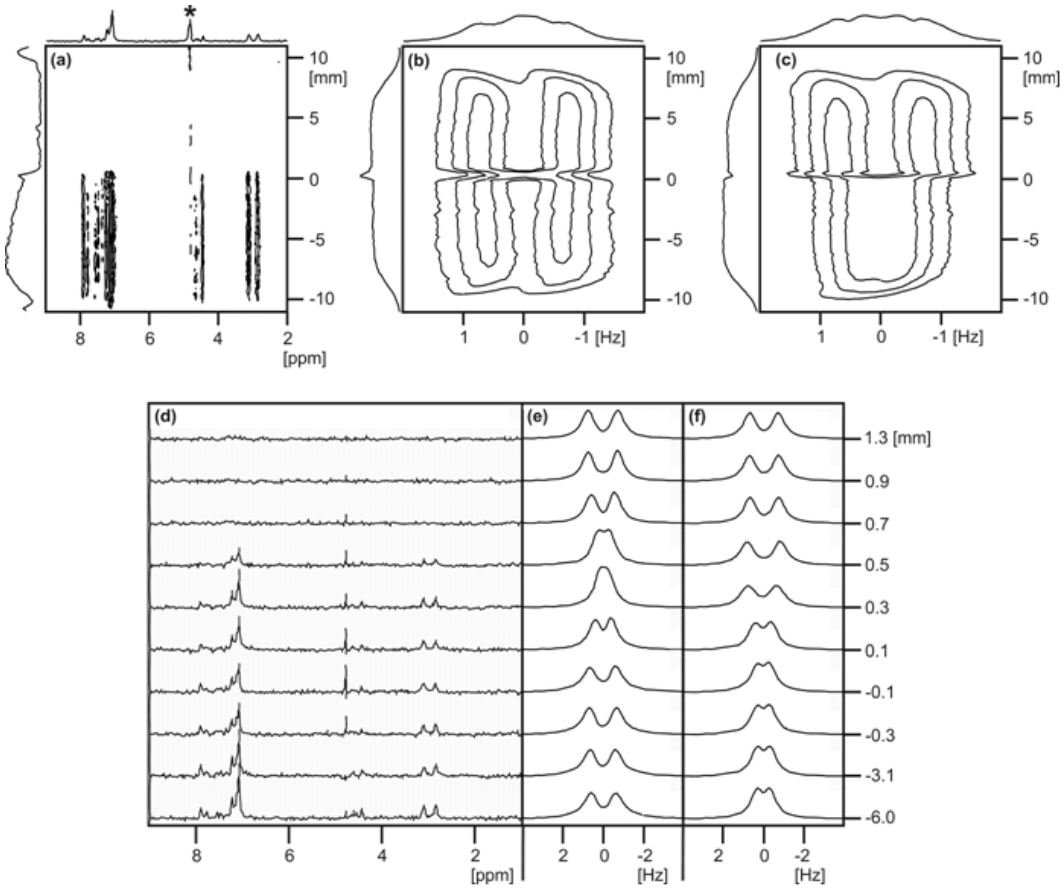

Figure 2-S6. Following the formation of a $CaCl_2$-triggered NapFF hydrogel by CSI. (a) ^1H image of the sample of Figure 2-3a, taken immediately before the ^2H image. The residual signal from HOD is marked *. All other resonances belong to NapFF. (b) Figure 3-3a, reproduced here for convenience: ^2H image of D_2O resonance in sample taken immediately before removal from magnetic field. (c) Figure 3-3b, reproduced here for convenience: ^2H image of D_2O resonance in sample after ageing away from magnetic field for two weeks. (d) Extracted ^1H spectra from (a) at vertical positions indicated on left of figure. (e) Extracted ^2H spectra from (b) at vertical positions indicated. (f) extracted spectra from (c).

The ^1H resonances of the NMR-visible NapFF in solution in the absence of Ca^{2+} (a), (d) – measured as 50±10 % of the total NapFF present with respect to an internal capillary in NapFF solutions with no Ca^{2+} present – all vanish at approximately the same point at which the RQC of D_2O temporarily diminishes to almost zero (b), (e). The loss of the ^1H signal from the NMR-visible NapFF is attributable to the formation of Ca^{2+}-coordinated species, which are presumably insoluble and therefore

not NMR-visible. The temporary decrease in the RQC of D_2O is attributable to the presence of a mixture of NapFF-Ca^{2+} and NapFF-Na^{+} coordination sites for D_2O which averages the RQC almost to zero.[4] The transformations taking place as a solution of NapFF at high pH is transformed to a $CaCl_2$-trigered gel are the subject of ongoing investigations.

2.4.7 Effect of temperature on the RQC of D_2O in an 0.5 wt% solution of NapFF

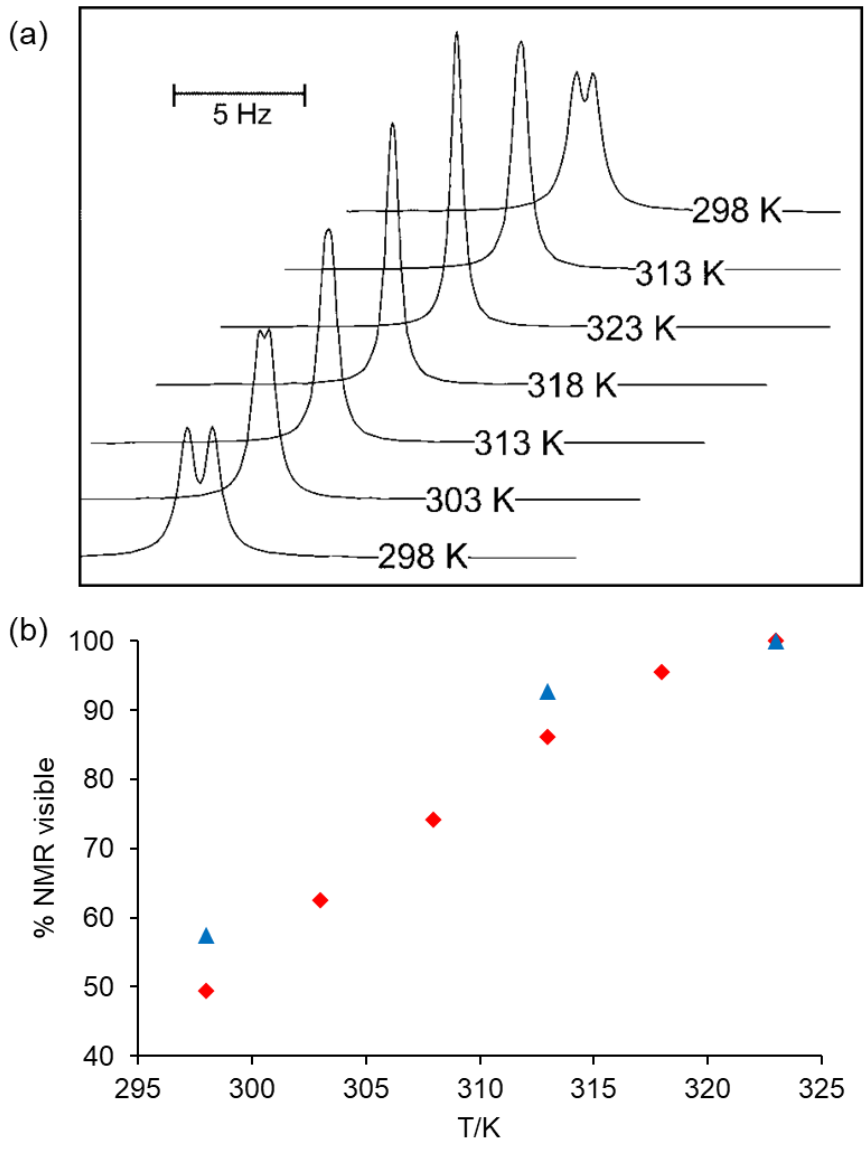

Figure 2-S7. (a) Effect of temperature on the RQC of D_2O in an 0.5 wt% solution of NapFF. ^2H spectra of D_2O at temperature shown are displayed on a staggered plot. (b) Plot of fraction of NMR-visible NapFF as a function of temperature as the sample was heated from 298 K (red diamond) to 323 K and cooled to 298 K (blue triangle).

The RQC of D_2O decreases as the temperature is increased up to 323 K at which the resonance is a single sharp Lorentzian peak (a). At this temperature, all of the NapFF is visible by ^1H NMR spectroscopy (b). Upon cooling down to 298 K there is an apparent hysteresis, the RQC being only 0.6 Hz compared to 1.0 Hz prior to heating while a higher fraction of the NapFF is visible by NMR. These results suggest that heating to 323 K 'melts' the aligned wormlike structures to give an isotropic solution, which upon cooling adopts a different state to the starting solution.

The sample was equilibrated at each temperature for 40 minutes before the ^2H spectra were recorded. The sample temperature was controlled using a Bruker BVT3200 temperature control unit which had been calibrated using a thermocouple immersed in water in an NMR tube.

2.4.8 Effect of NapFF concentration on the RQC of D_2O

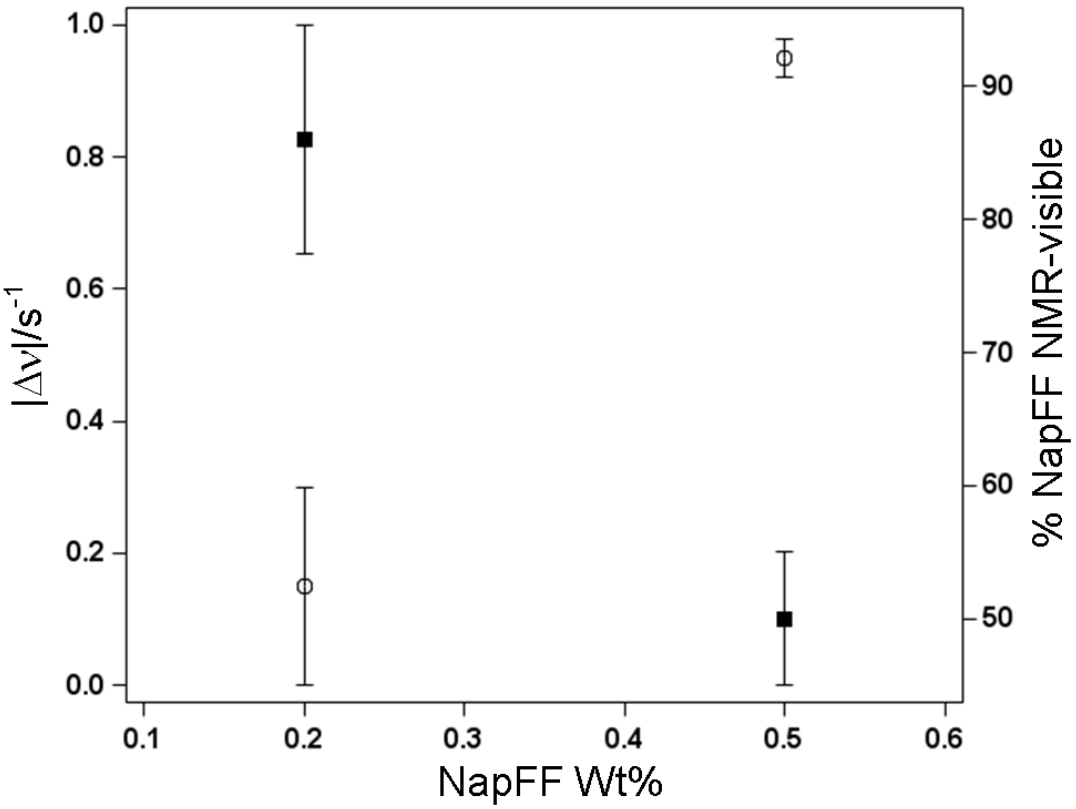

Figure 2-S8. Plot of the RQC ($|\Delta\nu|$) of D_2O (circle) and the percentage of NMR-visible NapFF (square) in solutions of NapFF, versus the wt% of NapFF.

At 0.2 wt% NapFF, the RQC of D_2O is indiscernible, being less than the natural linewidth of the D_2O resonance. An error on this point of ±0.15 Hz has been derived

based on a fitting of the resonance to Lorentzian doublets. An error of ±0.03 Hz has been assumed for the 0.5 wt% sample where the splitting is larger than the linewidth. The percentage of NapFF in the sample which is visible by ^{1}H-NMR was estimated by integrating the NapFF resonances (C$\underline{H_2}$-Ph) against the residual ^{1}H toluene resonance (methyl group) in an internal reference capillary filled with toluene-d_8. Prior to use, the capillaries had been calibrated using a 5 mg/mL sample of L-valine. A standard error of ±10% has been assumed in the determination of the percentage of ^{1}H-NMR visible NapFF. NapFF samples at 0.7 and 1.0 wt% were prepared but found unsuitable for analysis owing to the formation of dense liquid crystalline domains which seemingly sank to the bottom of the NMR tube as the sample was ageing (6-8 days) so that the RQC of D_2O was not homogeneous across the sample (Section 2.4.13)

The above results suggest that worm-like structures which are not NMR-visible are required in order to align in the magnetic field and give rise to an RQC of D_2O. Such structures – in which the assembled molecules have a very low degree of mobility and consequently very short transversal relaxation times – seem to exist at concentrations below the limit at which an RQC can be resolved. The phase behaviour of NapFF in solution is the subject of ongoing work.

2.4.9 Effect of dioxane concentration on the RQCs of D_2O and dioxane-d_8

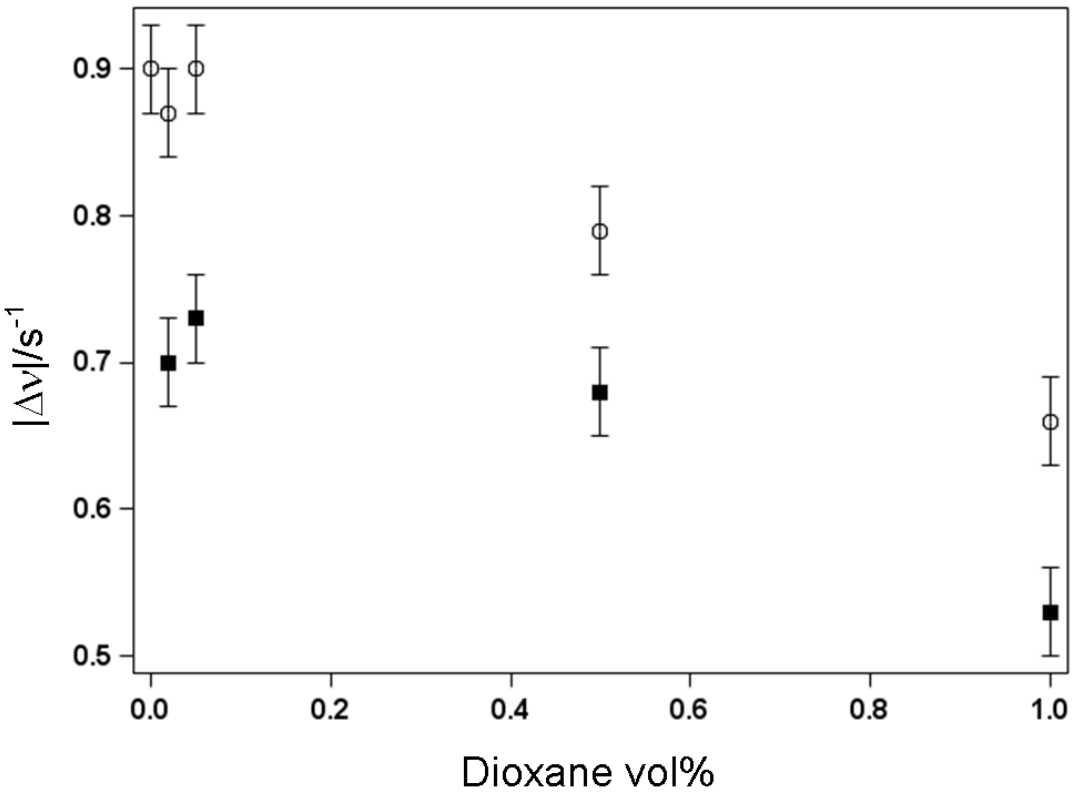

Figure 2-S9. Plot of the RQC ($|\Delta\nu|$) of D_2O (circle) and 1,4-dioxane-d_8 (square) in 0.5 wt% solutions of NapFF versus the percentage of dioxane in the solution. Each solution was allowed to equilibrate in the magnetic field for at least 40 minutes before measurement of the RQCs, after which no significant changes in the RQCs took place. All samples were prepared from the same stock solution of NapFF. A standard error in $|\Delta\nu|$ of ±0.03 Hz has been assumed.

The RQCs of D_2O at 0.05, 0.02 and 0 vol% dioxane-d_8 are the same within error. At higher concentrations, the RQCs of both D_2O and dioxane decrease due to a change in the supramolecular organisation of the Nap-FF and/or increased competition for binding sites between dioxane molecules themselves and D_2O. In $CaCl_2$-triggered gels formed in the magnetic field – which unavoidably had to be prepared from different stock solutions of NapFF due to spectrometer availability – the RQCs of D_2O and dioxane were 1.2 Hz and 3.6 Hz respectively at 0.05 vol% dioxane and 1.4 Hz and 5.5 Hz at 0.5 vol% dioxane.

2.4.10 Other probes

As well as dioxane-d_8, other water-soluble deuterated molecules can be used to study anisotropy in magnetically aligned NapFF hydrogels. CD_3CN and MeOD (CD_3OD) were chosen owing to their different properties. Formation of $CaCl_2$-triggered NapFF hydrogels incorporating these probes was then followed *in-situ* by CSI. Data for dioxane-d_8 is included for completeness. The concentration of all deuterated probe molecules was 0.05 vol%.

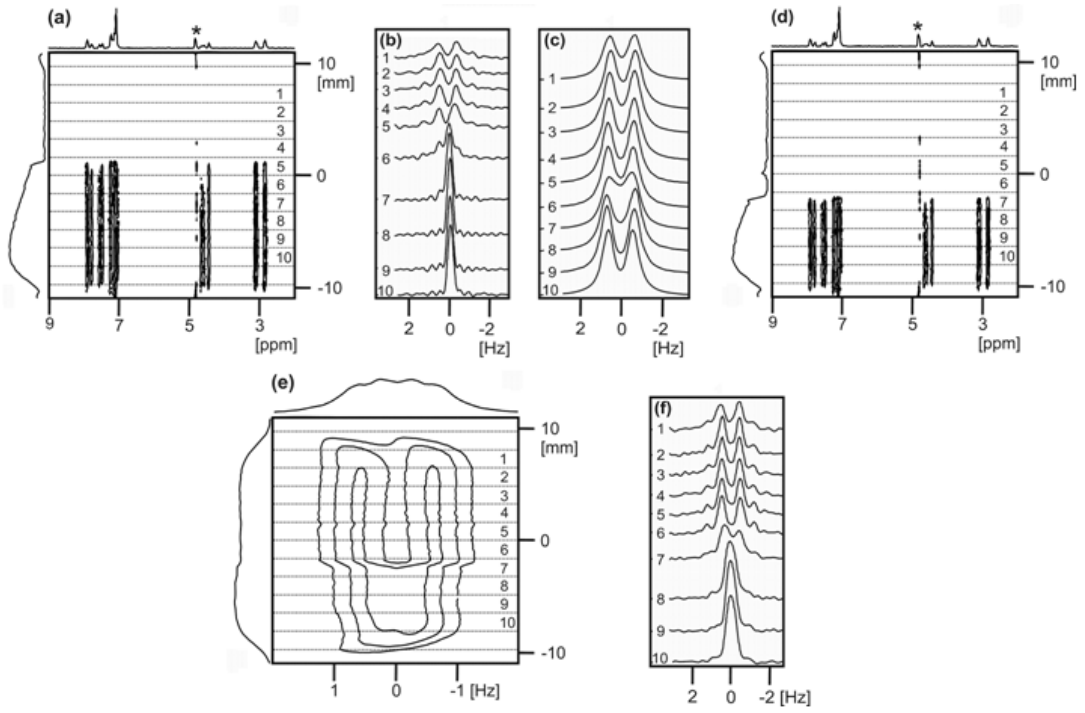

Figure 2-S10a. Use of CD_3CN as a probe molecule to follow formation of a $CaCl_2$-triggered 0.5 wt% NapFF hydrogel by CSI. (a) ^1H image of the sample taken before other images shown. The resonance marked * belongs to HOD, all other resonances belong to NapFF. (b) ^2H-NMR spectra of CD_3CN at regions indicated on (a) and (d). In the $CaCl_2$-triggered gel – above the 'front' where the signal from the NMR-visible NapFF disappears – the CD_3CN exhibits a clear splitting while in the 2FF solution below the 'front' the resonance is a singlet. The wiggles at the base of the spectra from regions 7-10 are due to truncation of the FIDs. (c) ^2H-NMR spectra of D_2O at regions indicated on (a) and (d). (d) ^1H image of sample to show how far $CaCl_2$ 'front' had progressed during the acquisition of (b). (e) ^2H image of D_2O in sample having aged in a water bath for eight days. (f) ^2H-NMR spectra of CD_3CN at regions indicated on (e). In the portion of the gel formed in the magnetic field, the CD_3CN exhibits a clear splitting whereas in the portion gelled away from the field the RQC is less than the linewidth and cannot be resolved.

The observation that CD_3CN (Figure 2-S10a) exhibits an RQC in a $CaCl_2$-triggered gel but not a solution of NapFF is attributable to the very different solvation environments around the NapFF structures present in both cases. Images (b), (c) and (f) were recorded with 16 gradient steps giving a theoretical resolution of 1.6 mm. (b) and (f) were recorded with pre-saturation applied to the D_2O resonance along with a spoil gradient to de-phase any observable magnetisation generated. For (b), 256 scans were recorded at each gradient step with 4800 data points and a sweep width of 15 ppm giving a total acquisition time of 4 hours while for (f) 512 scans and 8192 data points were recorded at each step giving a total acquisition time of 12 hours.

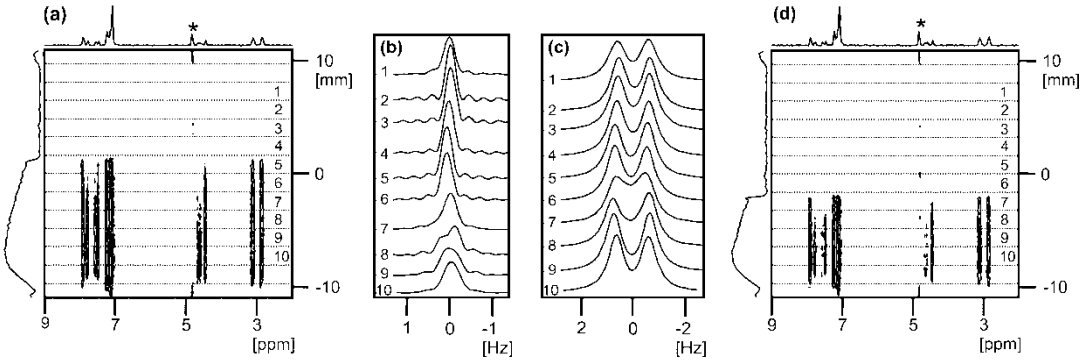

Figure 2-S10b. Use of MeOD as a probe molecule to follow formation of a $CaCl_2$-triggered 0.5 wt% NapFF hydrogel by CSI. (a) ^1H image of the sample taken before other images shown. The resonance marked * belongs to HOD, all other resonances belong to NapFF. (b) ^2H-NMR spectra of MeOD ($C\underline{D_3}$) at regions indicated on (a) and (d). The MeOD does not exhibit an RQC either in a solution of NapFF or in a $CaCl_2$-triggered gel. The wiggles at the base of the spectra from regions 1-8 are due to truncation of the FIDs. (c) ^2H-NMR spectra of D_2O at regions indicated on (a) and (d). (d) ^1H image of sample to show how far $CaCl_2$ 'front' had progressed during the acquisition of (b).

The lack of an observable splitting of the CD_3 group of MeOD is attributed to a relatively weak interaction between the hydrophilic molecule and the NapFF structures. Images (b) and (c) were recorded with 16 gradient steps giving a theoretical resolution of 1.6 mm. (b) was recorded with pre-saturation applied to the D_2O resonance along with a spoil gradient to de-phase any observable magnetisation generated. 256 scans were recorded at each gradient step with 5530 data points and a sweep width of 15 ppm giving a total acquisition time of 5 hours.

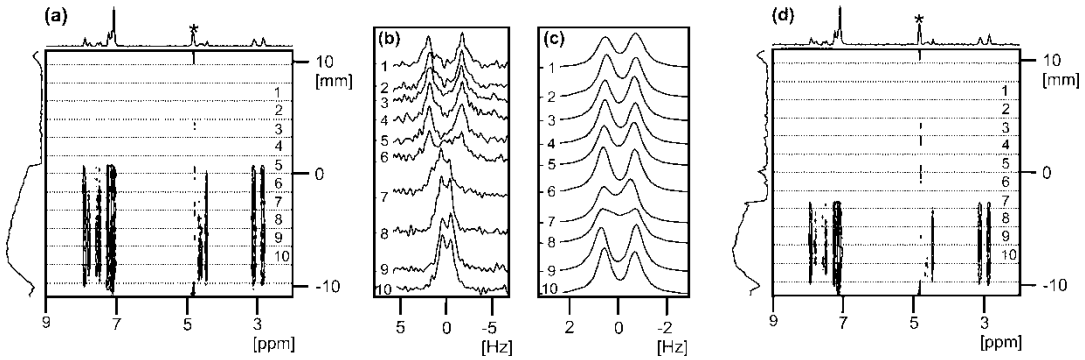

Figure 2-S10c. Use of dioxane-d_8 as a probe molecule to follow formation of a $CaCl_2$-triggered 0.5 wt% NapFF hydrogel by CSI. (a) ^1H image of the sample taken before other images shown. The resonance marked * belongs to HOD, all other resonances belong to NapFF. (b) ^2H-NMR spectra of dioxane-d_8 at regions indicated on (a) and (d). The dioxane exhibits an RQC both in solutions of NapFF and in $CaCl_2$-triggered gels (Section 2.4.3), the latter being considerably larger. (c) ^2H-NMR spectra of D_2O at regions indicated on (a) and (d). (d) ^1H image of sample to show how far $CaCl_2$ 'front' had progressed during the acquisition of (b).

Images (b) and (c) were recorded with 16 gradient steps giving a theoretical resolution of 1.6 mm. (b) was recorded with pre-saturation applied to the D_2O resonance along with a spoil gradient to de-phase any observable magnetisation generated. 256 scans were recorded at each gradient step with 5530 data points and a sweep width of 15 ppm giving a total acquisition time of 5 hours.

2.4.11 Other Salts

It has previously been demonstrated that hydrogels can be formed upon the addition of a range of salts to 0.5 wt% solutions of NapFF.[5] $MgCl_2$ and NaCl were chosen to study the effect of the counterion on the gel formation process which was followed by chemical shift imaging (CSI). For both $MgCl_2$ and NaCl, the concentrations of salt and the procedure used to prepare gels were the same as used for $CaCl_2$-triggered gels, the final concentration of salt being 0.05 M.

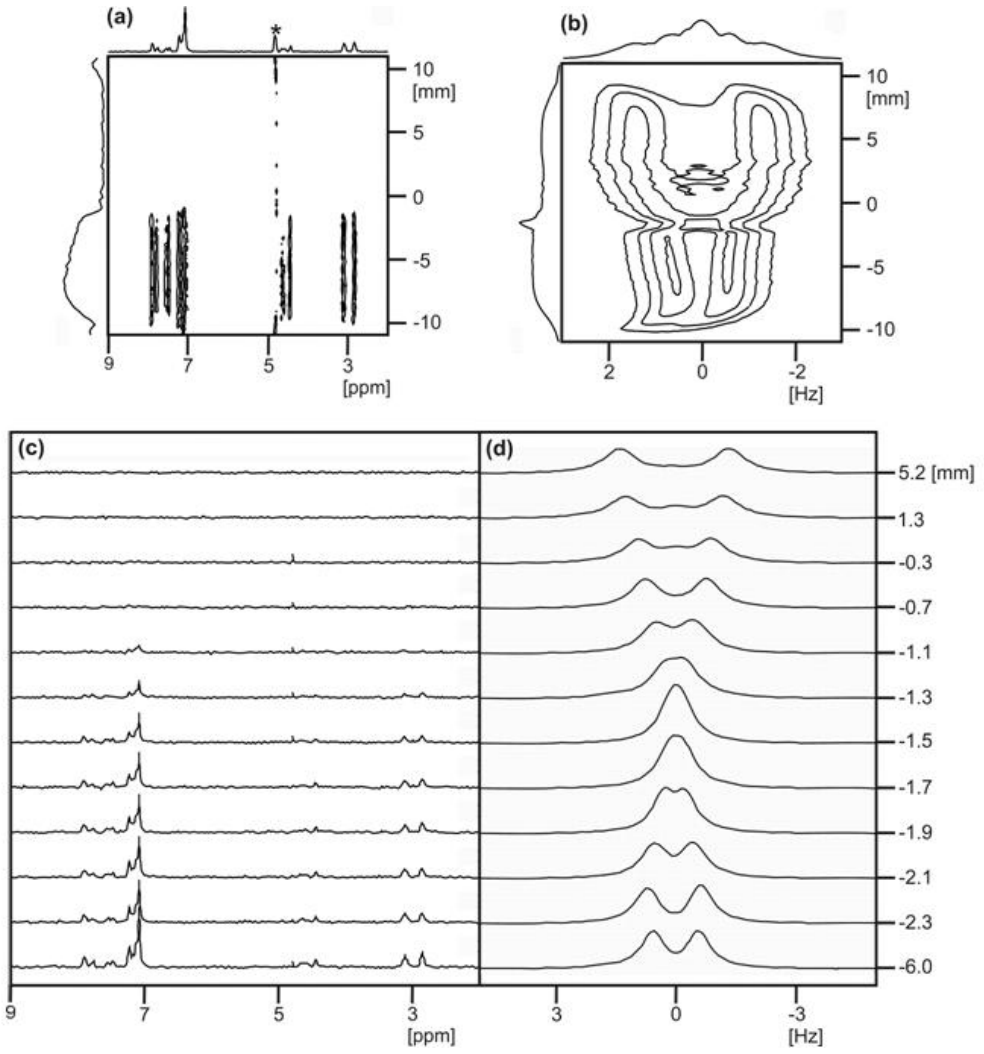

Figure 2-S11a. Following the formation of an $MgCl_2$-triggered 0.5 wt% NapFF hydrogel by CSI. (a) ^{1}H-image of sample. The resonance marked * belongs to HOD, all other resonances belong to NapFF. (b) ^{2}H-image of D_2O in sample, taken immediately after (a) was recorded. (c) ^{1}H spectra extracted from (a) at vertical position indicated. (d) ^{2}H spectra of D_2O extracted from (b) at vertical position indicated.

As with $CaCl_2$ (Section 2.4.6), the RQC of D_2O is indiscernible at around the position at which the ^{1}H signal from the NMR-visible NapFF disappears and is of appreciable magnitude both above and below this point – the salt diffusion 'front'. However, the RQC above the 'front' is considerably larger – 2.7 Hz compared to 1.4 Hz in the $CaCl_2$-triggered gel – and an additional singlet (isotropic) peak is apparent between the doublet peaks. These two observations are attributable to either a different structuring of D_2O around the NapFF fibres when Mg^{2+} is present, or a different gel microstructure compared to $CaCl_2$-triggered gels. It has previously been

shown that $CaCl_2$ and $MgCl_2$-triggered hydrogels have similar mechanical properties.[5]

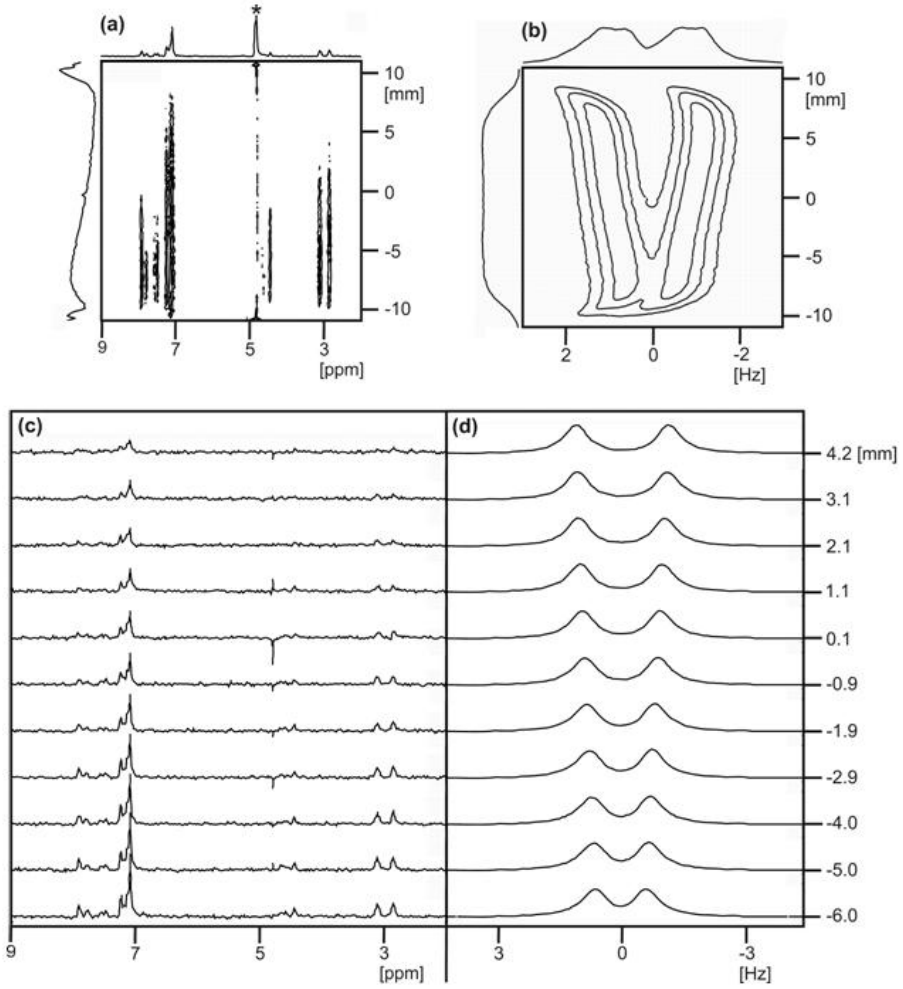

Figure 2-S11b. Following the formation of a NaCl-triggered 0.5 wt% NapFF hydrogel by CSI. (a) ^1H image of sample. (b) ^2H-image of D_2O in sample taken immediately after (a) was recorded. (c) ^1H spectra extracted from (a) at vertical position indicated. (d) ^2H spectra of D_2O extracted from (b) at vertical position indicated.

The ^1H signal from the NMR-visible NapFF gradually diminishes as the concentration of NaCl increases towards the top of the image while there is a concomitant increase in the RQC of D_2O. These observations – in particular the lack of a clear diffusion 'front' as observed with $MgCl_2$ and $CaCl_2$ – suggest that the addition of NaCl does not induce changes in the sample as significant as those that take place upon the addition of $MgCl_2$ or $CaCl_2$. It has previously been demonstrated that 'gels' formed upon the addition of NaCl to 0.5 wt% solutions of NapFF are very much weaker than those formed with $MgCl_2$ or $CaCl_2$.

2.4.12 Analysis of NapFF hydrogels and solutions by polarised optical microscopy

Optical micrographs of NapFF hydrogels and solutions were collected in transmission mode on a Nikon Eclipse LV100 microscope equipped with an Infinity 2 colour CCD camera (Lumenera Corporation, Ontario, Canada). The samples were contained in 5 mm NMR tubes which were mounted on a glass slide.

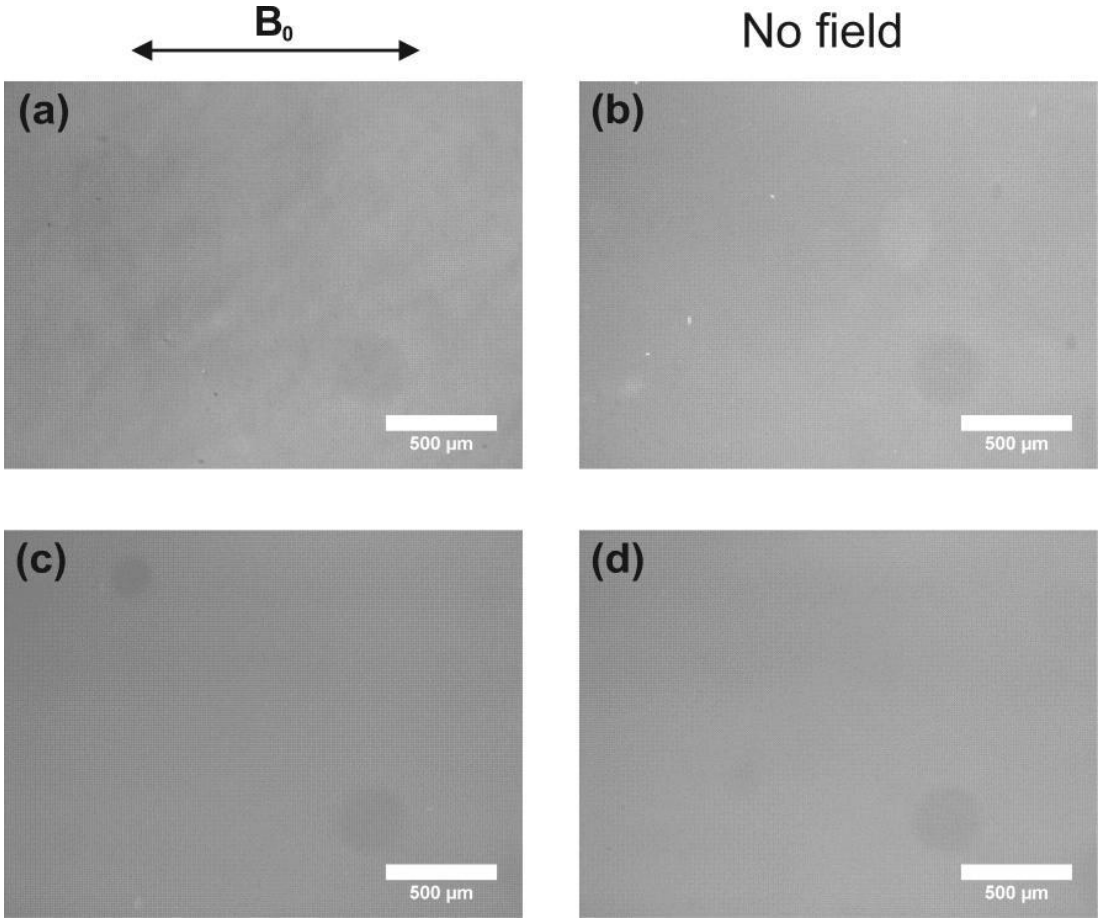

Figure 2-S12. Analysis of 0.5 wt% NapFF hydrogels by polarised optical microscopy. All images were taken with the sample in a 5 mm NMR tube between crossed polarisers. The gels on the left hand images were formed in a 9.4 T magnetic field with the axis of the field indicated. The images on the right are of gels formed away from the magnetic field; the gels had not been exposed to a magnetic field before these images were recorded. (a-b) GdL-triggered hydrogels. (c-d) $CaCl_2$-triggered hydrogels.

Here, none of the gels prepared at 0.5 wt% exhibit birefringence, with no apparent difference between gels formed in and away from the magnetic field. It can be inferred that although the gels prepared in the magnetic field are aligned, as

demonstrated by NMR spectroscopy, there is not enough material at 0.5 wt% to give appreciable birefringence. We note that solutions of NapFF at 0.5 wt% do sometimes contain birefringent domains; however, this effect seems very sensitive to the temperature at which the solutions are prepared, stored and imaged, and will be the subject of future investigations. However, all samples exhibited alignment by NMR.

2.4.13 Analysis of a 1 wt% solution of NapFF by polarised optical microscopy and CSI

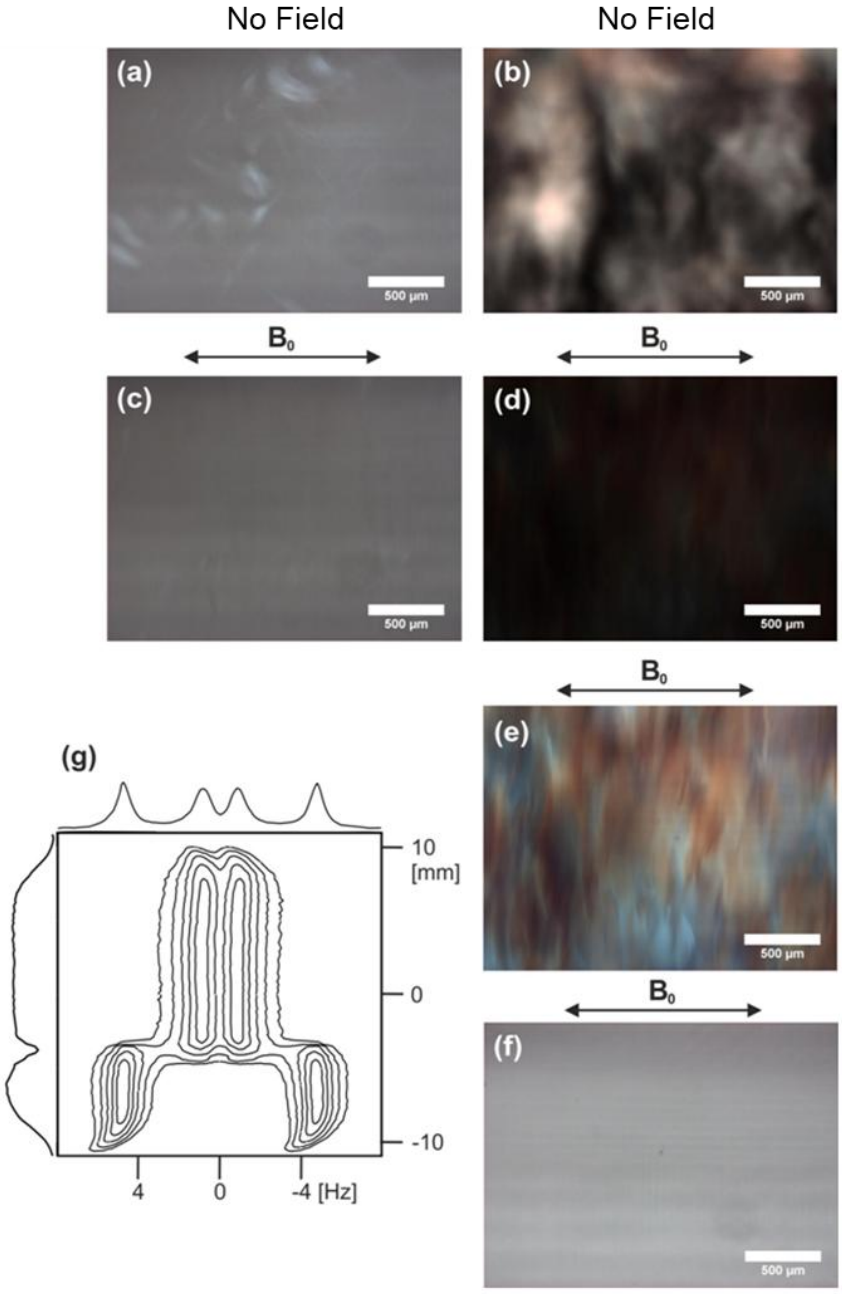

Figure 2-S13. Analysis of a 1 wt% solution of NapFF by polarised optical microscopy. Images (a) to (e) were taken with the sample in a 5 mm NMR tube between crossed polarisers. (f) was taken without crossed polarisers. (a) and (b) were recorded before a magnetic field had been applied to the sample while (c) to (f) were recorded after exposure to a 9.4 T magnetic field for one hour. (g) is a ^{2}H image of D_2O in the sample demonstrating the existence of two regions (*vide infra*). The lateral stripes apparent on images (a), (c) and (f) are an optical effect due to the presence of an internal reference capillary in the sample.

At 1 wt%, NapFF forms liquid crystalline phases. A 1 wt% NapFF solution was prepared and placed in a 5 mm NMR tube along with a standard capillary. The liquid crystalline phases over time (8 days) seemingly sink to the bottom of the sample giving a densely birefringent region in the lower part of the tube (b) and a less birefringent region (a) in the upper region of the sample. ^{2}H-imaging of the sample (g) reveals that the RQC of D_2O is very different in the two regions, being very much larger in the more birefringent region. Upon exposure to a magnetic field for one hour, the birefringent domains become a lot less apparent in both the upper (c) and lower (d) regions. Care was taken to ensure that (a) and (c), and (b) and (d) were recorded under the same brightness. Upon increasing the brightness in the lower region (e), domains are apparent which seem to have a net alignment perpendicular to the axis of the magnetic field. The birefringent domains in the lower region are not apparent without crossed polarisers (f). These images suggest a 1 wt% solution of NapFF contains randomly oriented domains prior to magnetic field exposure, whereupon the domains align perpendicular to the magnetic field.

2.4.14 Analysis of hydrogels by FTIR

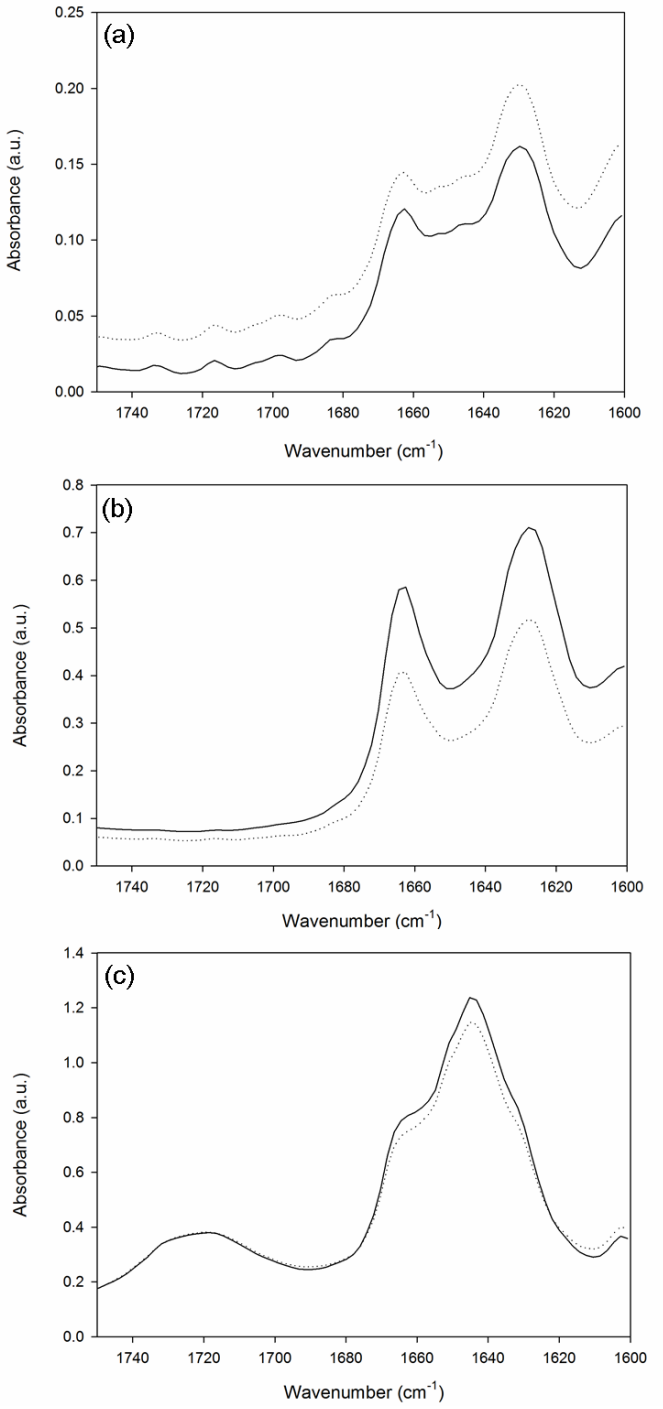

Figure 2-S14. Analysis of magnetically aligned and non-magnetically aligned NapFF solutions and gels by FTIR. Spectra of magnetically aligned samples are shown with solid lines and non-magnetically aligned samples are shown with dashed lines. (a) Freshly mixed 0.5 wt% NapFF solutions. (b) $CaCl_2$-triggered hydrogels. (c) GdL-triggered hydrogels.

No difference is apparent between the magnetically aligned and non-magnetically aligned samples, suggesting that magnetic alignment does not significantly alter the supramolecular organisation of the peptides in the self-assembled aggregates. Such a change would be expected to give rise to differences in the Amide I region (1600-1700 cm^{-1}).[6]

2.4.15 Analysis of magnetically aligned and non-magnetically aligned $CaCl_2$-triggered hydrogels by SEM.

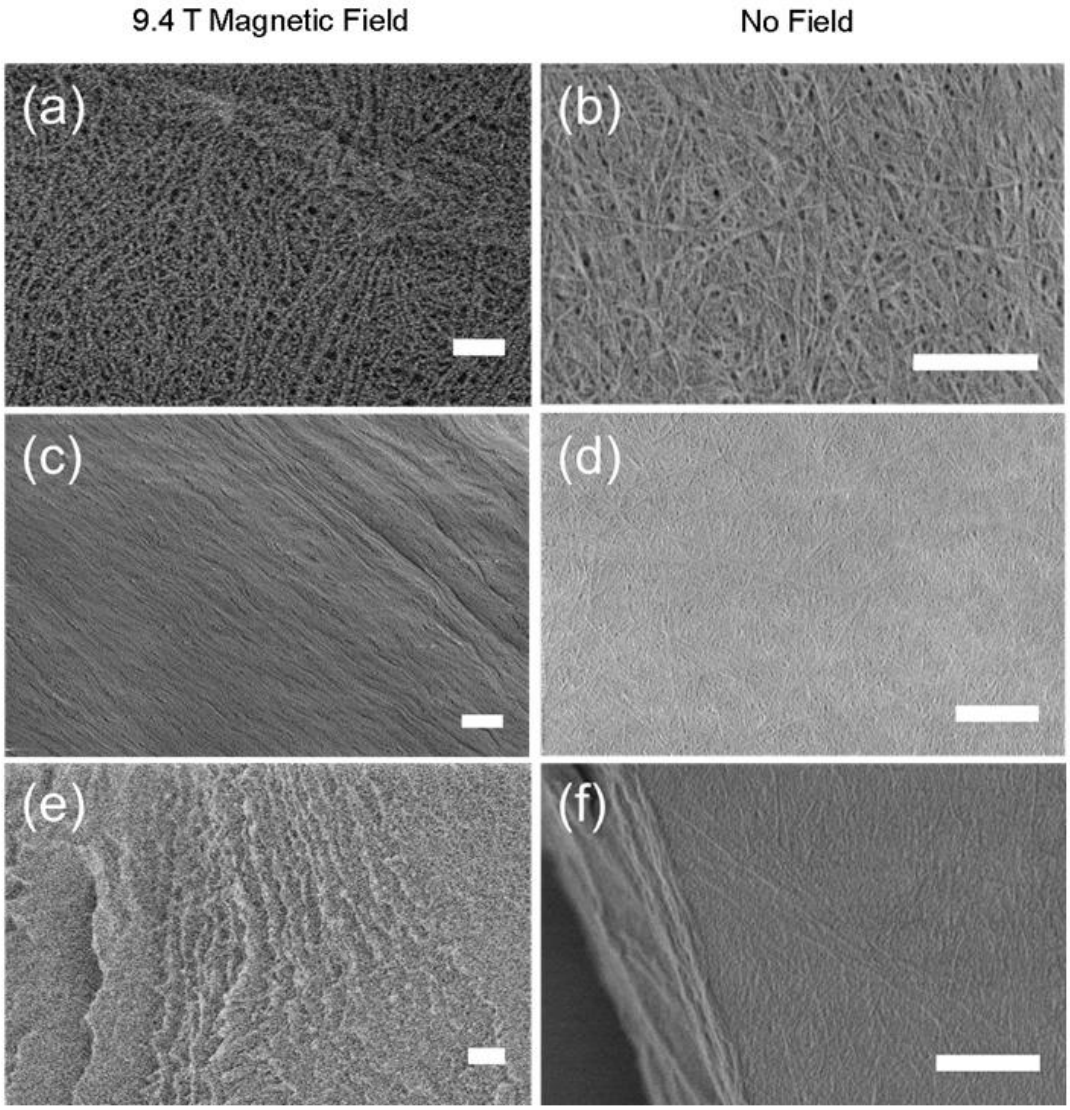

Figure 2-S15a. Side by side comparison of $CaCl_2$-triggered hydrogels gelled in a 9.4 T magnetic field (left) and with no magnetic field applied (right). (a, b, e, f) Scale bars = 500 nm. (c, d) Scale bars = 1 μm.

The fibres in the gel prepared in the 9.4 T magnetic field appear more aligned than the fibres in the gel prepared away from the magnetic field. The gels were dried so that the top surface of the gel lay perpendicular to the axis of the magnetic field during the formation of the gel prepared at 9.4 T. It was not possible to obtain good images of GdL-triggered hydrogels due to severe drying artefacts.

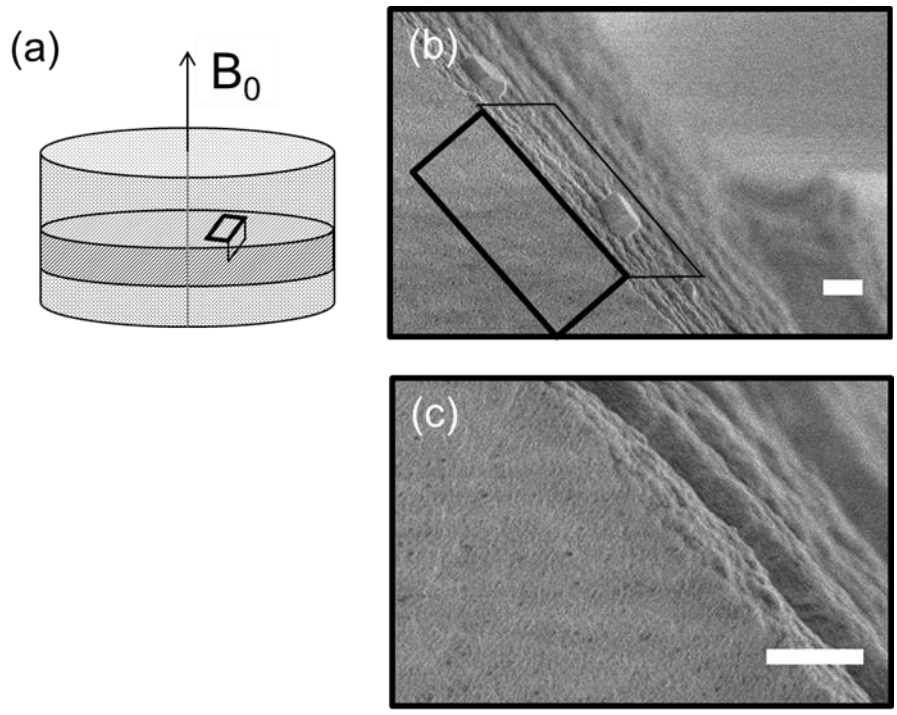

Figure 2-S15b. Cross-section at a fractured edge of a magnetically aligned $CaCl_2$-triggered hydrogel portion in the magnetic field. (a) Scheme to outline the coordinates of the magnetic field with respect to the SEM images (rectangle with thick line) and the fractured edge visible at a top view (rectangle with thin line). (b) SEM perspective of the edge from the plane perpendicular to the magnetic field (left) and the plane parallel to the magnetic field (right) with the presence of two crystals formed upon drying, possibly calcium chloride crystals; (c) Higher magnification at the fractured edge shows the dried fibrils aligned with the direction of view and layered films in the direction of the magnetic field, suggesting the hydrogels might have aligned bundles of fibers as it is packed in the dried state. Scale bars are 500 nm.

2.4.16 Powder X-ray Diffraction

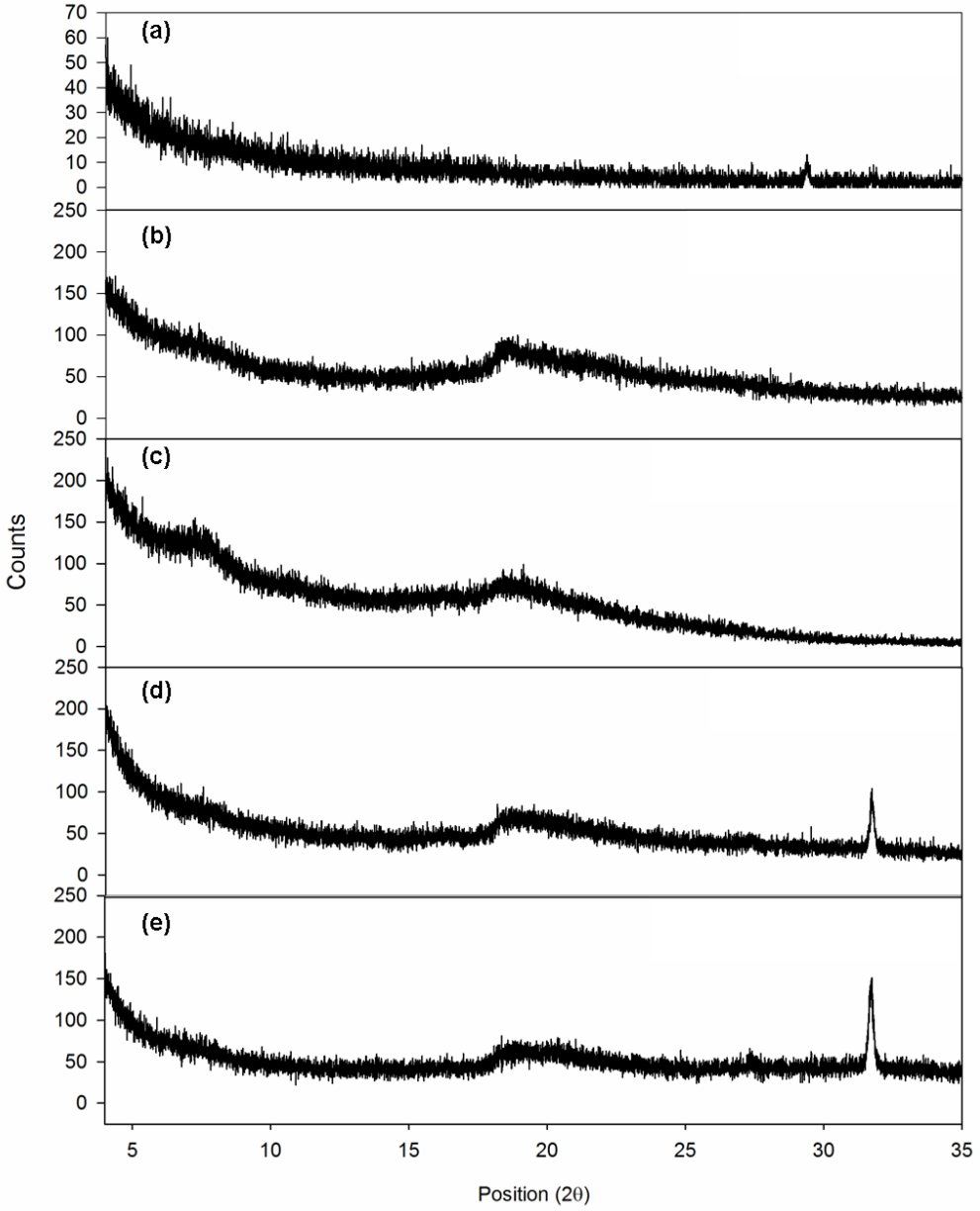

Figure 2-S16. Powder XRD analysis of magnetically aligned and non-aligned $CaCl_2$ and GdL-triggered hydrogels. (a) Dried solution of 0.05 M $CaCl_2$ and 0.012 M NaOD. (b) Magnetically aligned GdL-triggered hydrogel. (c) Non-magnetically aligned GdL-triggered hydrogel. (d) Magnetically aligned $CaCl_2$-triggered hydrogel. (e) Non-magnetically aligned $CaCl_2$-triggered hydrogel.

The sharp peak in the pattern of the $CaCl_2$-triggered hydrogels can be identified with calcium salts. The gels appear amorphous by powder X-ray diffraction.

2.4.17 Other Gelators

Analogous data was collected for a related gelator to NapFF, 3MeO-FF, which also forms worm-like micelles at high pH.[7]

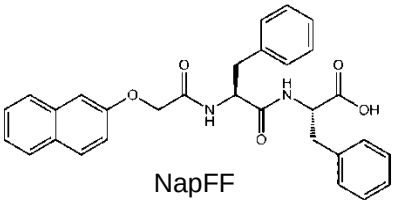

NapFF

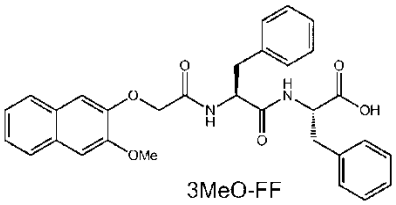

3MeO-FF

A solution of 3MeO-FF was prepared and $CaCl_2$ solution added following the same procedure used for NapFF (Section 2.2.3). Formation of a $CaCl_2$-triggered 3MeO-FF hydrogel was then followed by CSI.

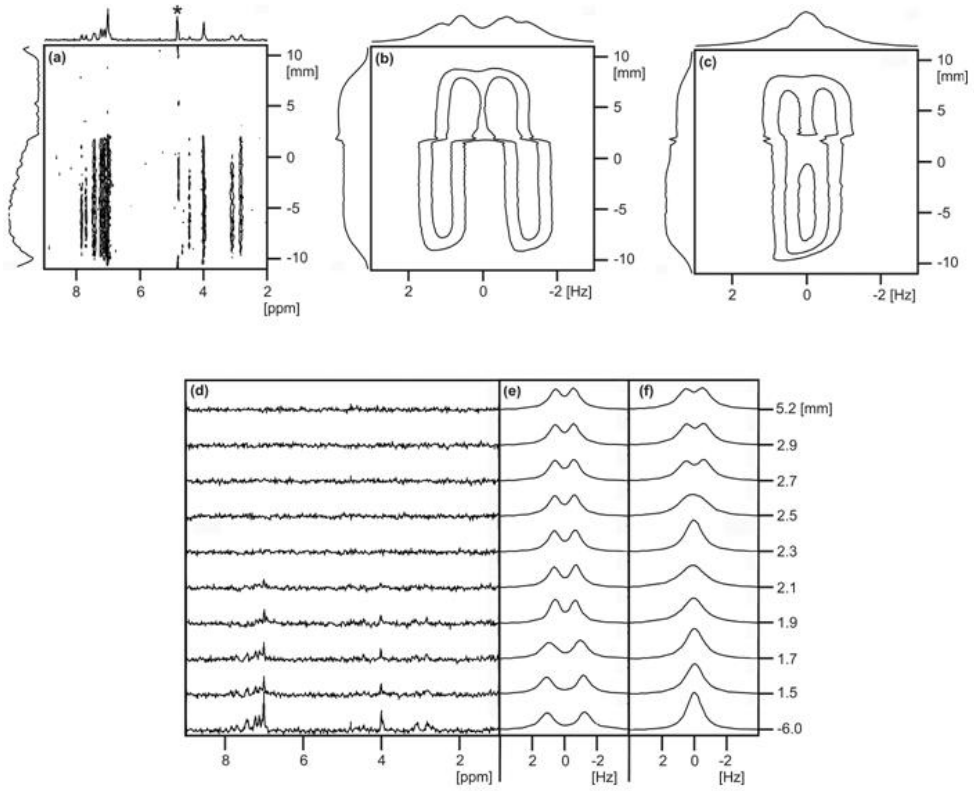

Figure 2-S17a. Following the formation of a $CaCl_2$-triggered 3MeO-FF hydrogel by CSI. (a) ^1H image of the sample. The residual signal from HOD is marked *. All other resonances belong to 3MeO-FF. (b) ^2H image showing D_2O resonance in sample taken immediately before removal from magnetic field. Acquisition of this image was started six minutes after (a) had completed. (c) ^2H image showing D_2O resonance in sample after ageing away from magnetic field for two weeks. (d) Extracted ^1H spectra from (a) at vertical positions indicated on left of figure. (e) Extracted ^2H spectra from (b) at vertical positions indicated. (f) Extracted ^2H spectra from (c) at vertical positions indicated.

In contrast to the case with NapFF (Section 2.4.6), the RQC of D_2O does not diminish to zero at approximately the same position that the signal from the NMR-visible gelator – measured as 20% of the total gelator present – vanishes (a), (d); however a noticeable discontinuity exists (e), the RQC decreasing abruptly between 1.7 and 1.9 mm. In the aged gel sample (c), (f), an RQC is detectable in the upper part of the gel which was gelled in the magnetic field; however, unlike with NapFF, no RQC is detectable in the region gelled away from the magnetic field. These observations indicate that 3Meo-FF and NapFF may form different structures at high pH which may respond differently to the addition of $CaCl_2$ despite the structural similarity of the two gelators.

In contrast, Br-AV cannot be used to form $CaCl_2$-triggered gels. Br-AV does not form worm-like micelles at high pH.[7]

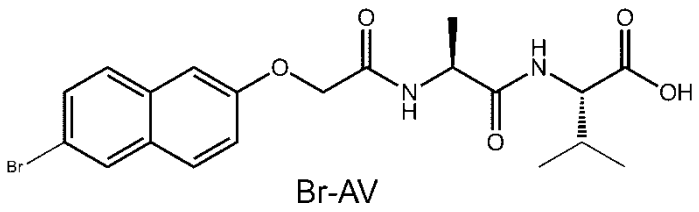

Br-AV

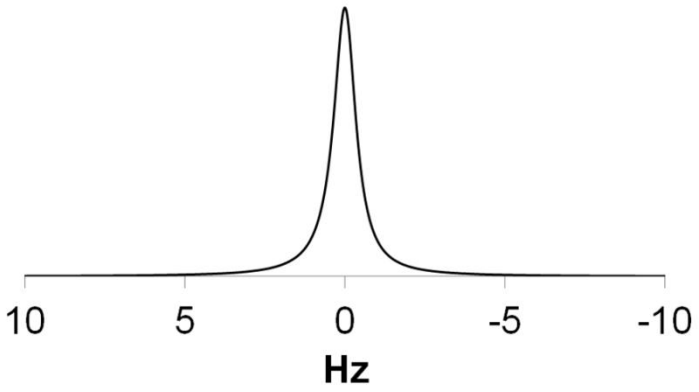

Figure 2-S17b. ^{2}H-NMR spectrum of D_2O in an 0.5 wt% solution of Br-AV at pD 12.1±0.1, aged for seven days.

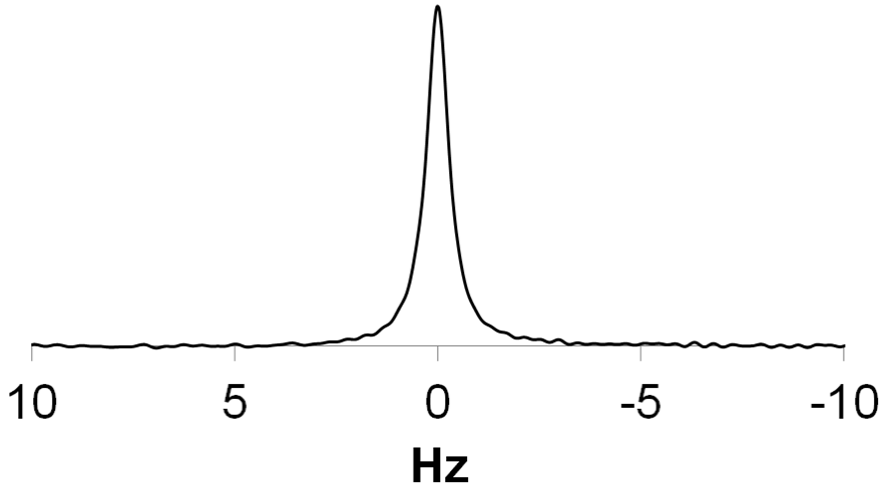

Figure 2-S17c. ^{2}H-NMR spectrum of dioxane-d_8 in an 0.5 wt% solution of Br-AV at pD 12.1±0.1, aged for seven days.

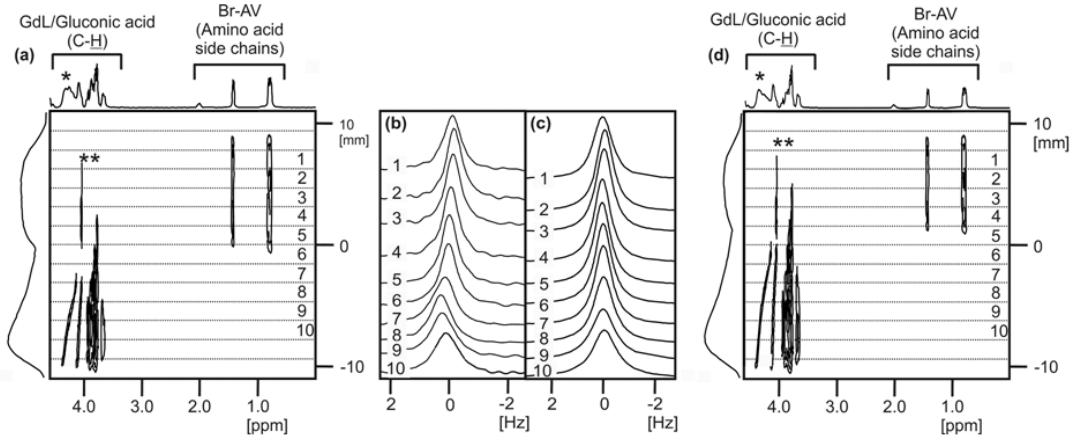

Figure 2-S17d. Following the formation of a GdL-triggered Br-AV gel by chemical shift imaging (CSI). Unlike the case with NapFF, when the GdL crystals were placed on top of the Br-AV solution, they promptly sank to the base of the NMR tube due to the much lower viscosity of the solution as compared to analogous NapFF solutions.[7] Diffusion of GdL/gluconic acid therefore took place upwards form the base of the NMR tube. (a) ^{1}H image of sample to show GdL/gluconic acid and Br-AV peaks. As discussed in Section 2.4.4, the peak marked * can be used to estimate the pD. The peak marked ** belongs to Br-AV. As the Gdl/gluconic acid diffuses up the tube, the peaks from the NMR-visible gelator – measured as 100% of the total gelator present in analogous 0.5 wt% solutions of Br-AV – disappear indicating hydrogel formation. Image was recorded before (b). (b) ^{2}H-NMR spectra of dioxane-d_8 at regions indicated on (a). (c) ^{2}H-NMR spectra of D_2O at regions indicated on (a) recorded before (b). (d) ^{1}H-image of sample taken after acquisition of (b) and (c) showing how far the diffusion of GdL had progressed since (a) was recorded.

Neither dioxane-d_8 nor D_2O exhibit an RQC at any stage of the transformation from a solution at high pD to a GdL-triggered gel suggesting that worm-like structures capable of aligning in the magnetic field are not present. (b) and (c) were recorded with 16 gradient steps giving a spatial resolution of 1.6 mm. (b) was recorded with 256 scans and 3072 data points giving a total acquisition time of 4 hours.

2.4.18 Effect of ageing on solutions of NapFF at pD 12.6

In order to investigate the effect of ageing on solutions of NapFF at high pD, a sample of NapFF was prepared and placed in 5 mm NMR tubes which were stored between 18 and 20 °C. Periodically, a tube was taken from storage and the splitting of the D_2O resonance measured. A plot of the splitting of the D_2O resonance versus the age of the sample reveals that the splitting reaches a plateau after six days. Optical micrographs of a sample between crossed-polarisers show how a nematic texture – indicative of the association of long fibrillar structures[8] – develops over the same time period and has stabilised after six days. The data presented here is in complete agreement with measurements of the viscosity of NapFF solutions presented elsewhere.[7] Images were collected as discussed in Section 2.4.12.

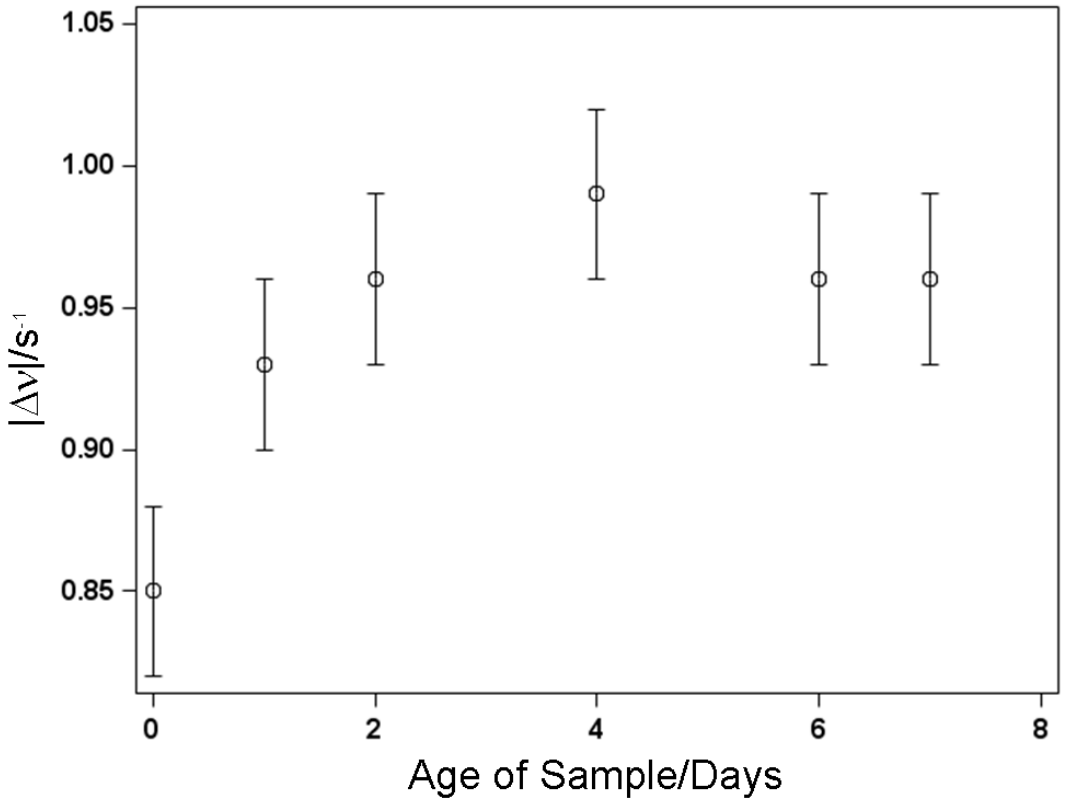

Figure 2-S18a. Plot of the RQC of D_2O ($|\Delta\nu|$) versus the age of the sample of NapFF. 0 days corresponds to a freshly mixed solution which has been stirred for 24 hours following the addition of D_2O and NaOD to solid NapFF. A standard error in $|\Delta\nu|$ of ±0.03 Hz has been assumed.

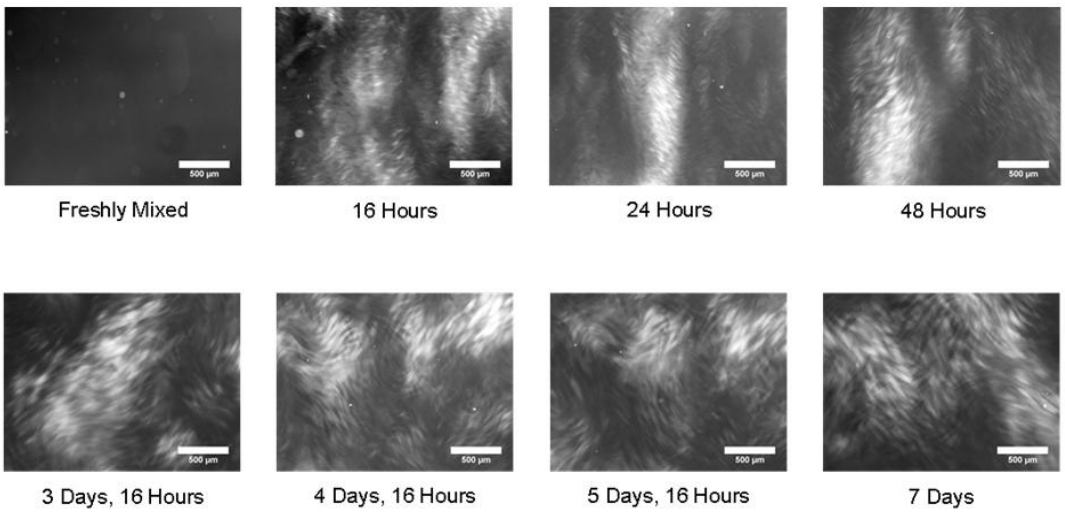

Figure 2-S18b. Optical micrographs of sample, taken between crossed-polarisers, of age indicated. Samples had not been exposed to a magnetic field before these images were taken.

2.4.19 Additional confocal microscopy images of $CaCl_2$-triggered gels prepared in the presence and absence of a magnetic field

Samples for confocal microscopy analysis were prepared according to the procedure described in Section 2.3.1 which allowed imaging of the sample in planes perpendicular and parallel to the direction at which the 9.4 T magnetic field had been applied to the sample gelled in the field.

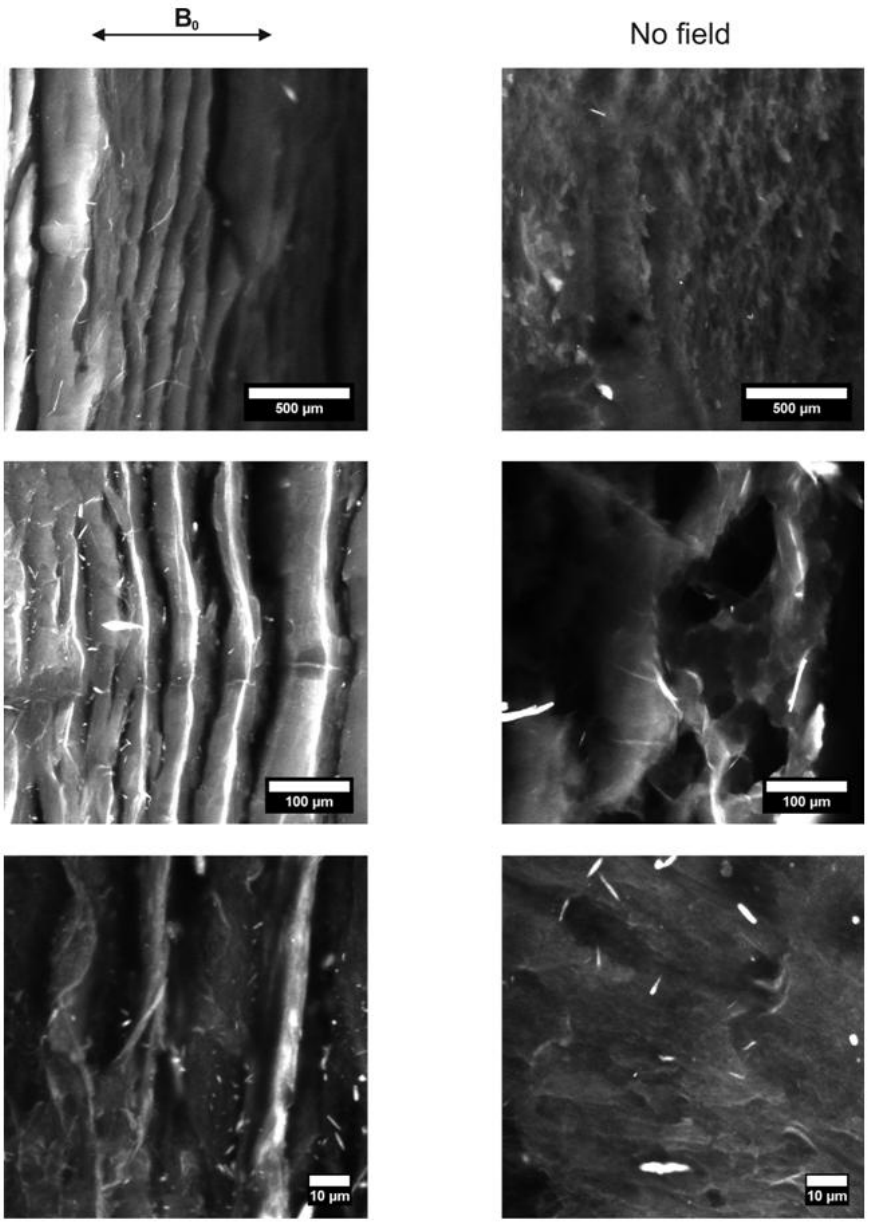

Figure 2-S19a. The images on the left are of the sample prepared in a 9.4 T field, with the axis of the field with respect to the focal plane indicated. Images on the right are of gels formed away from the magnetic field.

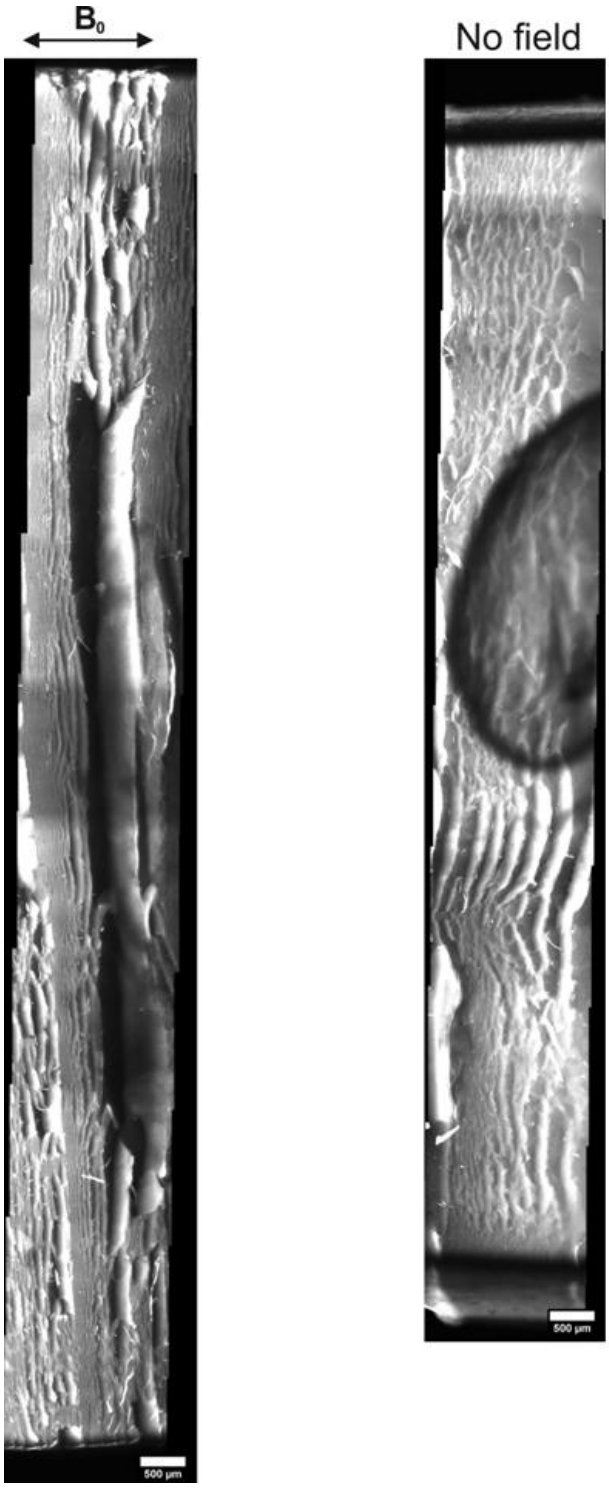

Figure 2-S19b. Composite images comprising individual images which have been fused together to form a complete image of the sample. The large round object on the image of the sample prepared away from the magnetic field is an air bubble which was trapped when mounting the sample for confocal microscopy.

2.4.20 Supporting Information: References

1. P. Trigo-Mouriño, C. Merle, M. R. M. Koos, B. Luy and R. R. Gil, *Chem. Eur. J.*, 2013, **19**, 7013-7019.
2. A. Pallagi, P. Sebők, P. Forgó, T. Jakusch, I. Pálinkó and P. Sipos, *Carbohydr. Res.*, 2010, **345**, 1856-1864.
3. L. Chen, S. Revel, K. Morris, L. C. Serpell and D. J. Adams, *Langmuir*, 2010, **26**, 13466-13471.
4. A. Delville, J. Grandjean and P. Laszlo, *J. Phys. Chem.*, 1991, **95**, 1383-1392.
5. L. Chen, G. Pont, K. Morris, G. Lotze, A. Squires, L. C. Serpell and D. J. Adams, *Chem. Commun.*, 2011, **47**, 12071-12073.
6. X. Mu, K. M. Eckes, M. M. Nguyen, L. J. Suggs and P. Ren, *Biomacromolecules*, 2012, **13**, 3562-3571.
7. L. Chen, T. O. McDonald and D. J. Adams, *RSC Adv.*, 2013, **3**, 8714-8720.
8. J. V. Selinger and R. F. Bruinsma, *Phys. Rev. A*, 1991, **43**, 2922-2931.

Chapter 3: Using Solution State NMR Spectroscopy to Probe NMR Invisible Gelators

3.1 Introduction

In Chapter 2, it was demonstrated that the presence of the spectrometer magnetic field during gelation can induce alignment of the hydrogel fibres. This alignment manifests as a splitting (RQC) of the ^{2}H NMR resonances of probe molecules. Comparing the RQCs of D_2O and dioxane-d_8 in $CaCl_2$ and H^+-triggered gels (Chapter 2, Section 2.2 and 2.4.4), it was clear that the size of an RQC depends not only upon the alignment of the fibres but also upon how the observed probe molecules interact with the fibres. In this Chapter, it is demonstrated how this property of RQCs provides an extremely useful handle by which to study the surface chemical properties of hydrogel fibres.

Section 3.2 comprises a paper, "Using Solution State NMR spectroscopy to probe NMR-invisible gelators", which was published in *Soft Matter* in 2015. The hydrogel system under study comprises a relatively hydrophilic LMWG which is not assembled into fibres at alkaline pH (Chapter 2, Section 2.4.17). Starting from an alkaline solution of the LMWG, the pH is gradually decreased *via* the hydrolysis of a lactone. The gradual decrease in the pH causes the gelators to self-assemble into a fibrous network. The first-formed network subsequently evolves over time as the pH continues to fall. Changes to the surface chemistry of the gel fibres can be inferred from changes to the RQCs of two contrasting probe species: $^{14}NH_4^+$ (positive, hydrophilic) and isopropanol-d_8 (neutral, hydrophobic). As both probes are incorporated in the same sample, changes in the anisotropy of the self-assembled network will affect the RQCs of both probes equally. However, if the surface chemistry of the fibres changes then the RQCs of the probes will be affected in different ways. Following initial assembly of the gel network, it is thus possible to follow changes to the charge and hydrophobicity of the gel fibres *via* changes to the RQCs of $^{14}NH_4^+$ and isopropanol-d_8. Changes to the charge of the hydrogel fibres can also be inferred from changes to the T_1 and T_2 relaxation times of $^{23}Na^+$. The theory of RQC and $^{23}Na^+$ relaxation measurements is briefly discussed in Section 3.2.5 and is revisited in more detail in Chapter 4, Section 4.3.2.

In this Chapter, the macroscopic mechanical properties of the sample are measured in parallel with the NMR experiments discussed above. This approach allows, for the first time, the evolution of the mechanical properties of the material to be linked to changes in the surface chemistry of the gel fibres. The methods allow the observed mechanical stiffening and contraction (syneresis) of the gel network as the pH is decreased to be linked to a loss of negative charge and an increased hydrophobicity of the gel fibres. Previous investigations on the same system were unable to prove the existence of such a link, despite the wide range of analytical techniques employed, as the surface chemistry of the gel fibres could not be studied directly.

In Section 3.3.4, it is demonstrated that the added probe species do not significantly interfere with the gelation process or alter the surface chemical properties of the fibres. In Section 3.3.8 and 3.3.15, it is demonstrated that the presence of the magnetic field during gelation does not significantly affect either the mechanical or surface chemical properties of the gels. These topics are revisited in Chapter 4, Section 4.3.1. The analytical approaches presented in this Chapter are thus non-invasive. Section 3.3.16 was not included in the original publication for reasons of space but is nevertheless included in this Thesis.

3.1.1 Author Contributions

The author contributions are as follows: MW conceived the concept of the paper, designed the experiments, prepared all of the samples and performed all of the NMR experiments. MW also wrote the manuscript and ESI, aided by helpful suggestions from the other authors. JAI provided guidance with the NMR experiments. DJA synthesised all of the LMWG and provided guidance throughout the project. Andre Zamith Cardoso, of the Department of Chemistry at the University of Liverpool, collected confocal microscopy images of the gels. Due to the low resolution of this microscopy technique, no fibrous structures could be observed and no useful information was afforded. Nevertheless, AZC is thanked for collecting the images.

3.2 Using Solution State NMR Spectroscopy to Probe NMR Invisible Gelators

Matthew Wallace,[a,]* Jonathan A. Iggo[a] and Dave J. Adams[a,]*

[a] *Department of Chemistry, University of Liverpool, Crown Street, Liverpool, L69 7ZD, U.K. Email: d.j.adams@liverpool.ac.uk*

3.2.1 Abstract

Supramolecular hydrogels are formed *via* the self-assembly of gelator molecules upon application of a suitable trigger. The exact nature of this self-assembly process has been widely investigated as a practical understanding is vital for the informed design of these materials. Solution-state NMR spectroscopy is an excellent non-invasive tool to follow the self-assembly of supramolecular hydrogels. However, in most cases the self-assembled aggregates are silent by conventional ^{1}H NMR spectroscopy due to the low mobility of the constituent molecules, limiting NMR spectroscopy to following only the initial assembly step(s). Here, we present a new solution-state NMR spectroscopic method which allows the entire self-assembly process of a dipeptide gelator to be followed. This gelator forms transparent hydrogels by a multi-stage assembly process when the pH of an initially alkaline solution is lowered via the hydrolysis of glucono-δ-lactone (GdL). Changes in the charge, hydrophobicity and relative arrangement of the supramolecular aggregates can be followed throughout the assembly process by measuring the residual quadrupolar couplings (RQCs) of various molecular probes (here, $^{14}NH_4^+$ and isopropanol-d_8), along with the NMR relaxation rates of $^{23}Na^+$. The initally-formed aggregates comprise negatively charged fibrils which gradually lose their charge and become increasingly hydrophobic as the pH falls, eventually resulting in a macroscopic contraction of the hydrogel. We also demonstrate that the *in situ* measurement of pH by NMR spectroscopy is both convenient and accurate, representing a useful tool for the characterisation of self-assembly processes by NMR.

3.2.2 Introduction

Solution state NMR spectroscopy has been widely used to follow non-invasively the self-assembly of low molecular weight gelators (LMWGs) into supramolecular gel networks.[1-3] However, most studies consider only the resonances of the gelators in solution as the self-assembled aggregates are usually not visible by solution-state NMR spectroscopy due to the very low mobility of the assembled molecules. By studying the resonances of the free gelator molecules, which generally decrease in intensity, broaden and shift in frequency as the molecules assemble,[4, 5] it is possible to obtain valuable information on the hydrogels, including the ratio of assembled to unassembled gelator,[6, 7] the kinetics of network formation,[8] component selection,[9] and the thermal stability of the gel networks.[6, 10, 11] Nevertheless, by conventional solution-state ^{1}H NMR spectroscopy it is not possible to probe the nature of the initially formed supramolecular aggregates or follow any subsequent rearrangement these may undergo *en route* to the final gel. Solid state NMR has been used in some cases,[12, 13] but the low concentration of the LMWG often precludes a detailed understanding, especially in the solvated state.

We recently demonstrated that NMR-strength magnetic fields can induce significant anisotropy in the arrangement of the fibrillar aggregates formed by certain dipeptide gelators. This anisotropy manifests as splittings of the NMR resonances of deuterated probe molecules present in solution (D_2O and/or water miscible deuterated organic solvents) that transiently interact with the gelator aggregates (Chapter 2).[14] We showed that the magnitude of the line splitting observed, the residual quadrupolar coupling (RQC), depends not only on the relative alignment of the gelator aggregates but also on the nature of the surface interaction between the aggregates and the deuterated solutes.

The nature of the fibre-solution interface is increasingly recognised as important for an understanding of both the final hydrogel and the process by which it forms; however, it is extremely difficult to study.[15, 16] Here, we show that a range of NMR probes including deuterated solvents and quadrupolar ions ($^{23}Na^{+}$, $^{14}NH_4^{+}$) can be used to follow the entire gelation process of a dipeptide gelator from a solution of mobile molecules at high pH to a

hydrophobic gel network at low pH. This approach allows us to gain significant insight into the self-assembly process as well as providing a means of understanding key parameters such as the charge and hydrophobicity of the self-assembled fibres. Approaches similar to ours have been used to glean valuable information on surface-solute interactions in a variety of systems including clays and liquid crystals.[17-20]

3.2.3 Results and discussion

Functionalised dipeptides can be extremely effective gelators.[21-23] We have previously shown that gels with highly reproducible rheological properties are formed on lowering the pH of solutions of a number of functionalised-dipeptide low molecular weight gelators.[24, 25] To form the gels, a solution of the dipeptide at high pH is first prepared. Hydrolysis of glucono-δ-lactone (GdL) to gluconic acid[26] is then used to cause a slow and uniform lowering of the pH which triggers gelation.[24] Since the hydrolysis occurs over hours, we are able to probe the assembly over time. We used NMR to monitor the disappearance of the gelator from solution;[24, 25] however, as the self-assembly proceeds, solid-like self-assembled fibres are formed which are NMR invisible. This is a common observation for many low molecular weight gelators triggered by different methods.

Here, we focus on a single gelator (**1**, Scheme 3-1), the self-assembly process of which we have previously studied using a range of techniques including circular dichroism, fibre X-ray diffraction, fluorescence and electron microscopy.[27, 28] This has allowed us to compare and verify the new techniques outlined here against our previous data. This gelator begins to form gels at the apparent pK_a of the terminal carboxylic acid (5.8) and the gel is formed by an entangled network of fibres.[27]

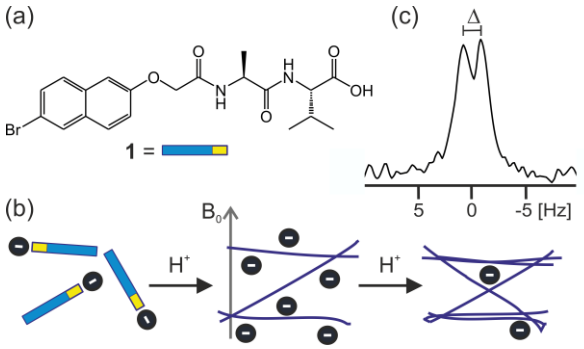

Scheme 3-1. a) Structure of gelator **1**. b) Cartoon to illustrate that upon a decrease in pH, molecules of **1** assemble to form fibres which bear a significant negative charge (*vide infra*). Upon further decreases in pH, these lose charge and bundle together. The presence of the magnetic field, B_0, induces significant anisotropy in the orientations of the fibres leading to the observation of residual quadrupolar couplings (RQCs), Δ, on the ^{2}H and ^{14}N NMR resonances of probe molecules (c).

Solution pH is obviously an important parameter in studies of GdL triggered gelation. Previous studies have correlated NMR data with *ex situ* parallel pH measurements. For the present study, we have developed an *in situ* method to follow the pH of the system using NMR spectroscopy. The method is based on the pH dependence of the chemical shifts of groups of nuclei within molecules possessing acid/base behaviour in water and has previously been reviewed in detail.[29-31] A full description of the specific methods used in the present work is provided in the Methods section below (Section 3.2.5).

To probe the self-assembly process, NH_4Cl and isopropanol-d_8 (IPA) were added to the solution for ^{14}N and ^{2}H NMR studies respectively. Briefly, as stated above, when these probe molecules interact with anisotropic structures in solution, a residual quadrupolar coupling (RQC) is observed (Scheme 3-1c) which depends on both the anisotropy of the structures and the affinity of the probe for their surfaces. $^{14}NH_4^+$ can be expected to have a significant affinity for negatively charged carboxylate sites on the gel fibres while IPA, a molecule with surfactant-like behaviour,[32] will have a higher affinity for more hydrophobic sites. Thus, by studying how the relative RQCs of $^{14}NH_4^+$ and IPA change during the assembly process we can infer how the charge and hydrophobicity of the self-assembled fibres are evolving. To further probe assembly, the T_1 and T_2 relaxation times of $^{23}Na^+$ were also recorded. A

decrease in the mobility of Na^+ ions due to interaction with, for example, carboxylate sites on the gel fibres results in a decrease in both T_1 and T_2. The $^{23}Na^+$ T_1 and T_2 may thus reflect the $^{14}NH_4^+$ RQCs to some extent. A more complete discussion of the theory of RQCs and ^{23}Na relaxation pertinent to the present study is provided in Section 3.2.5.

Profiles of the pH, ^1H integrals of **1**, RQCs of $^{14}NH_4^+$ and IPA, and rheological data (storage modulus (*G'*) and loss modulus (*G''*)) versus time as the sample gelled are shown in Figure 3-1. The data points at t=0 were recorded on the sample prior to the addition of GdL. Due to time limitations during the experiment, the ^{23}Na relaxation measurements and gelator integrals were recorded on a different sample to that on which the $^{14}NH_4^+$ and IPA RQCs were recorded. Nevertheless, the pH profiles in all experiments were very similar and so the data are directly comparable. Importantly, the rheological properties, pH, RQCs of IPA and NH_4^+, integrals from **1** and the $^{23}Na^+$ T_1 and T_2 values follow similar profiles in the presence/absence of NH_4Cl and IPA and so we can be confident that the inclusion of these probe molecules does not significantly affect the gelation process (Section 3.3.4). Gels prepared in the presence and absence of the strong magnetic field of the NMR instrument were found to have similar final mechanical properties (Section 3.3.15).

In agreement with our previous rheological investigation of a similar system,[33] four distinct phases can be identified. These phases can be summarised as follows: In Phase I, the gelators are not assembled into large structures and behave as free molecules. During Phase II, the molecules assemble into large fibrillar structures which possess a significant negative charge while the rheological properties of the sample develop into those of a cross-linked network. In Phase III, the network loses some of its negative charge leading to stronger fibre-fibre interactions and a large increase in mechanical strength. During Phase IV, the stronger fibre-fibre interactions lead to a significant macroscopic contraction of the entire gel network. These four phases, which are sketched in Figure 3-1e, are now discussed in detail.

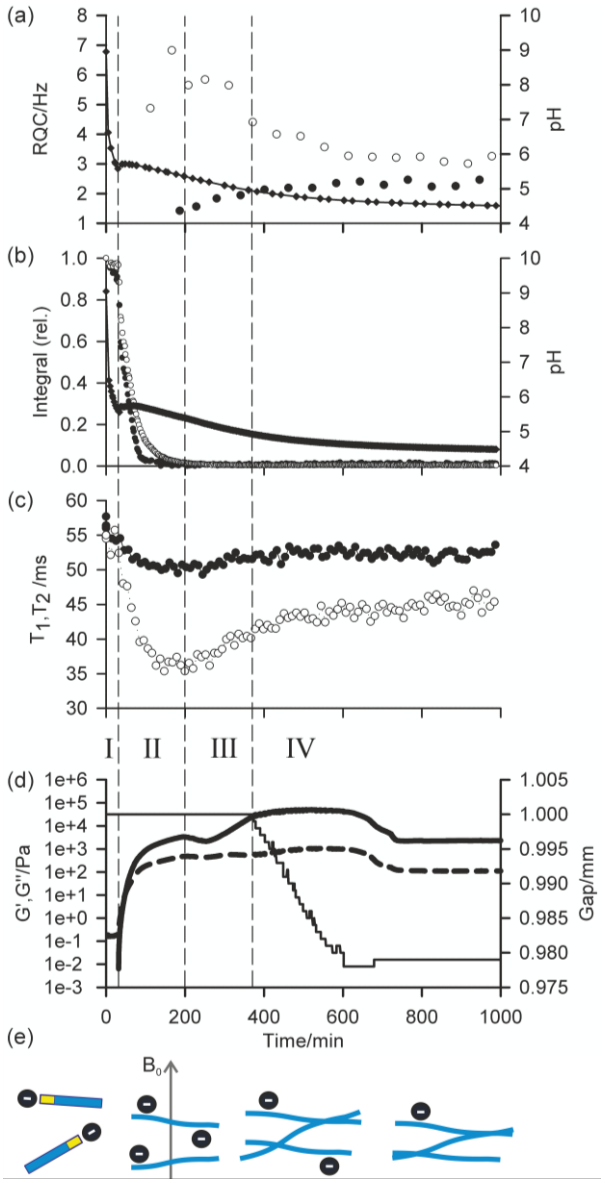

Figure 3-1. Time dependent profiles of experimental observables during gelation of **1**. The Roman numerals and dashed lines indicate the different phases of the gelation process, discussed in the text. a) Profile of $^{14}NH_4^+$ (white circle) and IPA (black circle) RQCs. pH is indicated with black diamonds, the solid line is there to guide the eye. b) Plot of integrals of valine methyl (white circle) and aromatic resonances (black circle) of **1**. Integrals are normalised to the largest integral obtained during the experiment. pH is indicated with black diamonds. c) Profile of T_1 (black circle) and T_2 (white circle) relaxation times of $^{23}Na^+$. These observables were recorded on the same sample as (b). d) Profile of G' (thick solid line), G" (dashed line) and the gap between the plates of the rheometer (thin line). e) Cartoon to illustrate the proposed assembly and charge state of the gelators at different stages of the process. Free gelator molecules are illustrated as blue rectangles which assemble into fibres that gradually lose negative charge and associate together. The relative amount of negative charge on the fibres is indicated by the number of black circles.

During Phase I, the pH falls rapidly while the gelator remains mobile in solution with essentially all of the gelator detectable by NMR, as measured in the absence of GdL against an internal standard capillary. The aromatic resonances shift upfield while the valine methyl resonances remain at a relatively constant frequency (Section 3.3.5), suggesting the gelators may be assembling into micellar structures with the naphthalene rings forming the hydrophobic core.[4] The resonance of the α-proton of the valine residue does not shift significantly, indicating that the NMR-visible gelator remains deprotonated during this phase. The resonances of $^{14}NH_4^+$ and IPA remain as sharp single lines (Figure 3-2a; Section 3.3.6) and the $^{23}Na^+$ T_1 and T_2 are similar to those in a comparable solution in the absence of gelator which were measured as (56±1) ms and (55±2) ms respectively (Section 3.3.7). In Phase I, the rheological properties of a parallel sample are that of a liquid, with G' and G" both being essentially zero. Solutions of **1** at high pH have comparatively low viscosity[34] and the self-diffusion coefficient of **1** at pH 9 was measured as 4.1×10^{-10} $m^2 s^{-1}$ using pulsed field gradient NMR (PFG-NMR) which, from the Stokes-Einstein equation, corresponds to a hydrodynamic diameter of approximately 1.2 nm.

We were unable to detect any structures using confocal microscopy. These observations indicate that, at this stage, the gelator behaves predominantly as free molecules and has not yet assembled into fibrillar structures such as the wormlike micelles formed by related gelators,[34] although the transient existence of micellar aggregates cannot be ruled out.

At the end of Phase I, the pH rises followed by a gently falling plateau (Phase II). This rise in pH is also observed using a conventional pH meter (Figure 3-4, Section 3.2.5.1) and is attributed to a sudden increase in the pK_a of the gelators upon self-assembly.[35-37] Self-assembly of the gelators is evidenced by a number of observations: There is a sudden increase in the mechanical properties of the parallel sample, G' being initially approximately equal to G" but gradually increasing to dominate as gelation begins. There is a dramatic decrease in the amount of NMR-visible gelator while the aromatic resonances of the gelator display an abrupt downfield shift consistent with a phase separation between the mobile NMR-visible gelator in solution and the NMR-

silent structures (Section 3.3.5). The integral of the valine methyl groups decreases at a noticeably slower rate than that of the aromatic protons, pointing to a lower degree of mobility of the naphthalene ring as the gelator interacts/exchanges with the NMR silent aggregates. The $^{23}Na^{+}$ T_1 and T_2 both decrease sharply while a splitting of the $^{14}NH_4^{+}$ resonance becomes apparent, observations which strongly suggest these aggregates are anisotropically oriented fibrillar structures that possess a significant negative charge. We attribute these observations to the formation of worm-like micelles in which the naphthalene rings form the core of the micelles, stabilised by the charged carboxylates.[34] The existence of such charge on the surface of fibres formed by related gelators has previously been suggested;[36] however, this had been extremely difficult to prove experimentally. For example, previous investigations of the **1**/GdL system by infra-red spectroscopy were inconclusive as to the protonation state of the carboxylates.[27] We note here that the slight anisotropy that gives rise to the RQCs is due to the presence of the magnetic field during self-assembly since no RQCs are observed in samples prepared away from the field (Section 3.3.8).

Towards the end of Phase II, the pH again begins to fall. The $^{14}NH_4^{+}$ RQC passes through a maximum before beginning to decrease while the $^{23}Na^{+}$ T_1 and T_2 pass through a minimum and a RQC for the IPA becomes apparent. At the end of Phase II, all of the gelator has assembled into NMR invisible structures and G' exceeds G" by approximately one order of magnitude, indicating a cross-linked network has been formed. The existence of thin fibrils at this stage has previously been demonstrated by TEM.[27]

During Phase III, the pH continues to decrease as does the $^{14}NH_4^{+}$ RQC, while the $^{23}Na^{+}$ T_1 and T_2, and the IPA RQC all increase. These observations are consistent with the self-assembled structures becoming less charged and more hydrophobic. G' and G" decrease before increasing again towards a second plateau, while the normal force experienced by the upper measurement plate of the rheometer decreases (Section 3.3.14). These observations suggest that the sample may be undergoing syneresis and contracting slightly as the fibrils pack together, resulting in a weaker contact between the measurement plate and the sample. The monotonic decrease and singularity of the $^{14}NH_4^{+}$ RQC

and increase in the IPA RQC suggest that charge is gradually and uniformly lost from the fibres rather than in 'patches', as previously proposed for a related system.[33] This would instead lead to broad lineshapes with unresolvable splittings comprising superpositions of different RQCs. If any patches do form, they are smaller than the length scales, l, probed by the observed molecules given approximately by the expression:[38]

$$l \approx \sqrt{\frac{D}{\pi\Delta}} \qquad (3.1)$$

where Δ is the observed RQC and D the diffusion coefficient of the molecules; $1.9\text{x}10^{-9}$ m^2 s^{-1} for NH_4^+,[39] and $1.0\text{x}10^{-9}$ m^2 s^{-1} for IPA at 0.05 vol% in H_2O, as measured using PFG-NMR. The sample thus appears uniform on length scales of ca. 10 μm.

In the final phase, Phase IV, the rate of pH decrease slows as does the rate at which the NMR observables are changing. The gel continues to contract and the rheometer decreases the gap between the plates in order to maintain a constant normal force of 0 N. The apparent G' has reached a plateau; however, the contraction of the gel eventually leads to a decrease in the apparent G' and G'' at long times. During this phase, the $^{14}NH_4^+$ and IPA RQCs and the $^{23}Na^+$ T_1 and T_2 approach a plateau and a singlet (isotropic) peak becomes visible in the ^2H and ^{14}N NMR spectra between the doublet peaks of IPA and $^{14}NH_4^+$ (Section 3.3.6) suggesting that, from Equation 3.1, the contraction has produced regions of bulk fluid of almost macroscopic dimensions. Such regions are apparent in the final gel (Figure 3-2b). The isotropic component of the IPA resonance in this gel is ca. 20% the area of the doublet which, assuming the isotropic resonance arises solely from bulk fluid exuded during the contraction of the gel and thus comprises ca. 20% of the sample volume, would require a concentric contraction of the gel by only 10% (0.2 mm). From Figure 3-2b, the longitudinal contraction of the gel is of a similar extent. That such a concentric contraction takes place is supported by chemical shift imaging (CSI) analysis of the sample which demonstrated that the sample was homogeneous throughout the NMR-active region (Section 3.3.9), and by the observation that the gels could fall down to the base of the tube if knocked.

Time-lapse photography of a parallel sample during gelation revealed that the macroscopic contraction of the gel approximately coincides with the appearance of the resonance of the isotropic phase in the NMR spectra (Section 3.3.10). The isotropic peak first becomes apparent on the $^{14}NH_4^+$ resonance after approximately 700 minutes and on the IPA resonance after 500 minutes (Section 3.3.6). The isotropic component of the IPA resonance is noticeably larger than that of the $^{14}NH_4^+$, which becomes obscured as the RQC decreases. Such differences are readily explained by Equation 3.1, the more slowly diffusing IPA being more sensitive to the presence of the isotropic phase than the more rapidly diffusing NH_4^+. Analysis of gel samples by confocal microscopy was inconclusive as the self-assembled structures were below the resolution of our microscope and no structures could be discerned. Nevertheless, previous studies of the **1**/GdL system by TEM demonstrated that the extent of lateral association of the gel fibres increases as the pH falls, in agreement with the results presented here.[27]

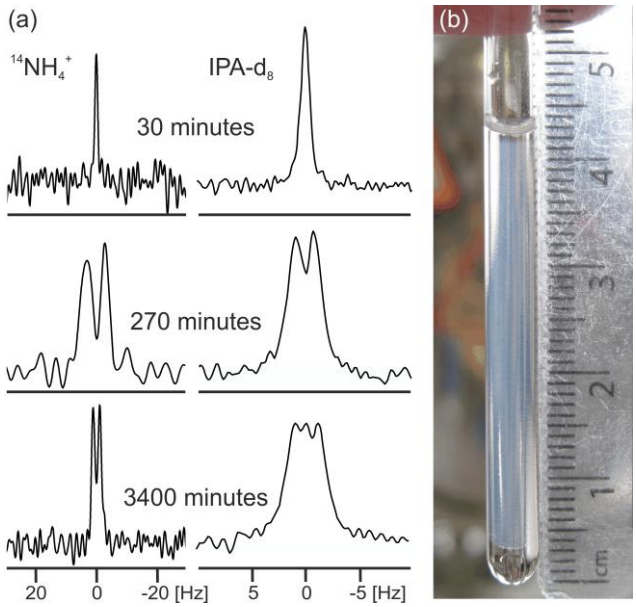

Figure 3-2. a) Experimental ^{14}N and ^{2}H NMR spectra of sample from Figure 3-1a at different times since addition of GdL to a solution of the gelator at high pH. The spectra have been scaled to account for the different number of scans recorded at different stages of gelation. b) Photograph of the gel sample of Figure 3-1a, 4000 minutes after GdL addition. The transparent exuded fluid is apparent above and below the slightly translucent gel. The NMR active region of the sample is centred at 18 mm from the base of the tube and stretches 8 mm either side.

Increasing the GdL concentration to 10 mg/mL led to a significantly lower final pH (3.9 versus 4.3), faster gelation kinetics and, as has previously been reported,[27] very similar final mechanical properties to the gel formed using 5 mg/mL GdL (Section 3.3.11). For this gel, the $^{14}NH_4^+$ RQC was substantially smaller than that of IPA, 1.2 Hz versus 2.8 Hz, which compares to 2.2 Hz and 2.4 Hz respectively at pH 4.3 with 5 mg/mL GdL. The $^{23}Na^+$ T_1 and T_2 values were (52±1) ms and (49±1) ms respectively, compared to (52±1) ms and (48±1) ms with 5 mg/mL GdL. These observations suggest the fibres at this lower pH are significantly less charged. Macroscopically, this sample had contracted to a similar extent as the sample prepared with 5 mg/mL GdL. As expected,[24, 27] decreasing the GdL concentration to 4 mg/mL resulted in a higher final pH of 4.8 and a $^{14}NH_4^+$ RQC substantially larger than that of IPA, 5.3 Hz versus 3.3 Hz (Section 3.3.12), and $^{23}Na^+$ T_1 and T_2 values of (52±1) and (44±1) ms respectively. Both of these observations are consistent with the gel fibres at this higher pH possessing more negative charge.

Based on the theory described in Section 3.2.5.2 (Equation 3.9), we can quantify the fraction of charged carboxylate sites, f_-, on the fibres during the gelation process as follows: If we assume that the observable $^{14}NH_4^+$ and IPA RQCs arise mostly from charged and uncharged sites and are thus directly proportional to f_- and (1-f_-) respectively, then assuming $KS_b(\partial f_-/\partial t) \gg Kf_-(\partial S_b/\partial t), f_-S_b(\partial K/\partial t)$ the following relation should hold:

$$\frac{\partial \Delta_{NH_4^+}}{\partial t} = -C\frac{\partial \Delta_{IPA}}{\partial t} \tag{3.2}$$

where $C \approx K_{NH_4^+}S_{b,NH_4^+}/K_{IPA}S_{b,IPA}$. The proportionalities between f_- and f_b in Equation 3.9 (Section 3.2.5.2) are effectively contained within these constants and are omitted. S_b has been found to be nearly constant for D_2O in lyotropic liquid crystal phases of surfactants across a wide variety of compositions.[40] Combining Equation 3.2 with Equation 3.9 gives the ratio of charged to uncharged sites:

$$\frac{f_-}{(1-f_-)} = -\frac{\Delta_{NH_4^+}\left(\frac{\partial \Delta_{IPA}}{\partial t}\right)}{\Delta_{IPA}\left(\frac{\partial \Delta_{NH_4^+}}{\partial t}\right)} \tag{3.3}$$

If we identify the end of Phase II as the earliest time point at which all of the assembled fibre is present in the sample then we can fit the $^{14}NH_4^+$ and IPA RQCs to stretched exponential functions:

$$\Delta_{NH_4^+}(t) = \Delta_{NH_4^+}(0)\, exp\left[-k'(t-t_0)^{\beta}\right] + \Delta_{NH_4^+}(\infty) \quad (3.4)$$

$$\Delta_{IPA}(t) = \Delta_{IPA}(\infty)\left[1 - exp\left[-k'(t-t_0)^{\beta}\right]\right] + \Delta_{IPA}(0) \quad (3.5)$$

where: $\Delta(0)$, $\Delta(\infty)$, k', β and t_0 are constants. If Equation 3.2 holds, we would expect to be able to fit the experimental data at 5 mg/mL GdL to the above equations with only one k', t_0 and β for both $^{14}NH_4^+$ and IPA, which is found to be the case (Figure 3-3). Estimated f_- and apparent pK_a values estimated from the Henderson-Hasselbalch equation are also displayed on Figure 3-3.

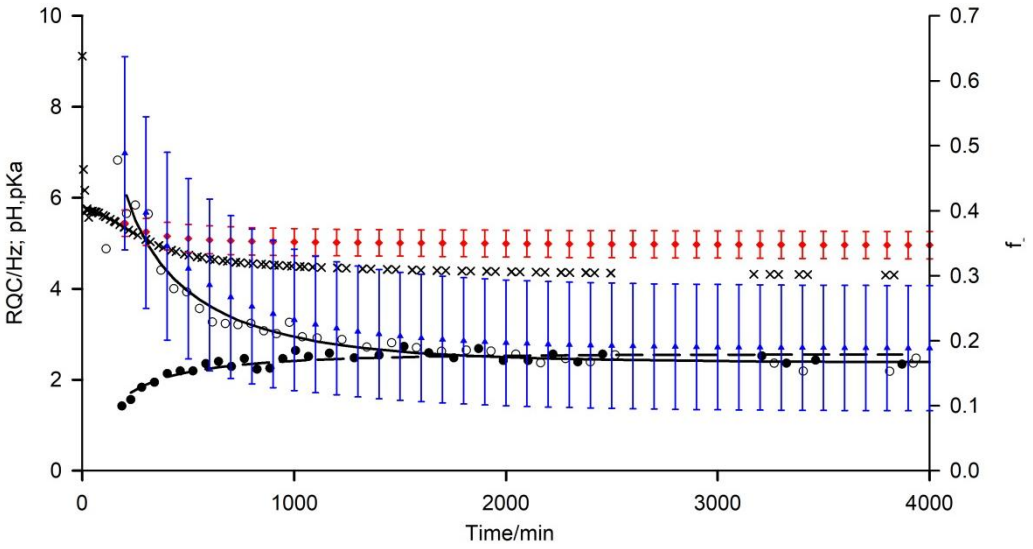

Figure 3-3. Plots of $^{14}NH_4^+$ (white circle) and IPA (black circle) RQCs from Figure 3-1a, extended to 4000 minutes along with pH data (black cross). Fits of RQC data to Equations 3.4 and 3.5 are shown by solid and dashed lines respectively. f_- (blue triangle) and pK_a values of carboxylate groups on the gel fibres (red diamond), estimated using Equations 3.3 to 3.5, are shown with error bars calculated using the method described in Section 3.3.15.

According to our fitting, at 200 minutes 50±15% of the carboxylates are deprotonated at a pH of 5.4 corresponding to a pK_a of 5.4±0.3. This agrees well with the 'apparent' pK_a of 5.8 determined *via* the titration of a solution of **1** with HCl.[41] As time progresses, the pH falls to 4.3 after 4000 minutes with 20±10% of the carboxylates remaining deprotonated corresponding to a pK_a of

4.9±0.3. These findings suggest that the significantly elevated apparent pK_a values of peptide-based gelators determined by conventional potentiometric titration with HCl, as reported in many studies,[4, 27, 36, 37, 41-43] may be due to electrostatic rather than hydrophobic effects. It is known, for example, that the ionisation of one glutamic acid residue in a protein greatly elevates the pK_a of a neighbouring un-ionised residue.[44] If hydrophobic effects exerted the dominant influence, the pK_a would be expected to increase with time while the fibres at pH 4.3 would be largely uncharged. The assertion that the fibres at such a low pH remain significantly charged is supported by the $^{23}Na^+$ T_1 and T_2 values which remain significantly below their values measured in the absence of gelator.[45]

3.2.4 Conclusions

We have shown that ^1H, ^2H, ^{14}N and ^{23}Na solution-state NMR can be used to follow the entire self-assembly process of a dipeptide gelator. In common with previous studies, we find assembly to be a multi-stage process driven by the gradual loss in charge from the gelator as the pH falls. However, for the first time, we are able to study changes to the relative hydrophobicity and charge of the self-assembled aggregates when the gelators themselves have become invisible by solution state ^1H NMR. ^2H, ^{14}N and ^{23}Na NMR reveal that the initially-formed fibrillar aggregates bear a very significant negative charge with perhaps as many as 50% of the carboxylates deprotonated. As this charge is lost, the fibres become more hydrophobic and show stronger inter-fibre interactions, the apparent mechanical properties of the gel network becoming substantially higher; however, these interactions eventually lead to the macroscopic contraction of the gel. Nevertheless, the final gel at pH 4.3 still possesses a significant negative charge. Our methods thus allow, in an essentially non-invasive way, the characterisation of the fibre-solution interface. These methods may thus provide further valuable insight into self-assembly processes of supramolecular hydrogels and allow the more informed design of controlled release systems based on guest-network interactions.

3.2.5 Methods

3.2.5.1 *In situ* pH determination using NMR spectroscopy

The pH of the solution relates to the observed chemical shift and pK_a of the indicator molecule via the modified Henderson-Hasselbalch equation:[31]

$$pH = pK_a + log_{10}\left(\frac{\delta_{obs}-\delta_H}{\delta_L-\delta_{obs}}\right) \quad (3.6)$$

where δ_{obs} is the observed chemical shift and δ_H and δ_L are the limiting chemical shifts of the fully protonated and deprotonated forms respectively. The sensitivity of a given indicator to changes in pH is greatest when pH ≈ pK_a and the difference between the limiting shifts is large. This required selection of a range of indicator molecules to span the range of pH values used in our systems (ca. pH 3-11): formic acid (Form, 3 mM, pK_a = 3.75), acetic acid (Ac, 1.5 mM, pK_a = 4.76), methyl phosphonic acid (MPA, 1.5 mM, pK_a = 7.74) and glycine (Gly, 1.5 mM, pK_a = 9.78) (abbreviations, concentrations and pK_a values are indicated in parentheses). Nitrogen bases, which become positively charged upon protonation, and relatively hydrophobic molecules were avoided in this study to minimise interference of the indicators with the development of the peptide structures. Sodium methanesulfonate (0.7 mM) was used as an internal chemical shift reference (2.815 ppm) for ^{1}H NMR in all samples. To calculate the pH of a sample, the pH indicators were grouped into pairs: Form/Ac, Ac/MPA, MPA/Gly. The pair with the highest combined sensitivity, $\partial\delta/\partial pH$, was used with the calculated pH being an average of that calculated from each indicator, weighted by their relative sensitivities. Using this approach, the pH measured *in situ* agreed well with the parallel *ex situ* measurements (Figure 3-4). Tabulated limiting chemical shifts for all indicators and a discussion of errors are provided in Section 3.3.1.

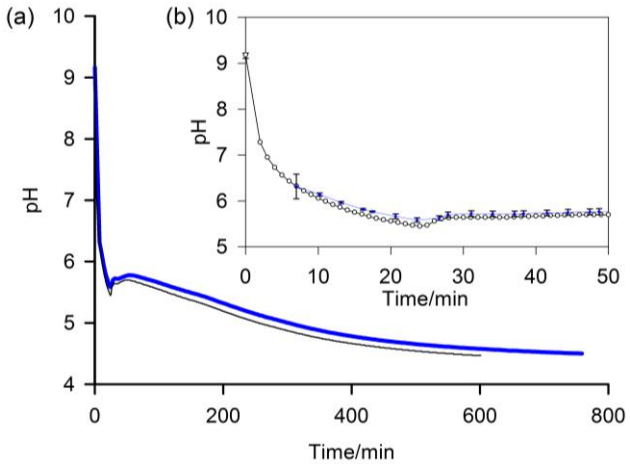

Figure 3-4. a) Plot to compare the pH determined by the NMR method (blue, thick) with data from a conventional pH meter (black, thin) of a 5 mg/mL sample of **1** after the addition of GdL. b) Expansion to show early stages of gelation and individual data points (NMR method – blue diamond, pH meter – white circle). Uncertainties in the pH determined *via* the NMR method, shown as error bars, were calculated using the method described in Section 3.3.13.

3.2.5.2 Residual Quadrupolar Couplings (RQCs)

Nuclei with a spin quantum number (I) greater than ½ (e.g. ^{2}H: I=1, ^{14}N: I=1, ^{23}Na: I=$^{3}/_{2}$) possess an electric quadrupole moment which interacts with electric field gradients (EFGs) present at the nucleus. EFGs can arise intramolecularly, such as along the O-D bond in D_2O,[46] or intermolecularly as with sodium ions condensed on the surface of clay platelets.[47] The effect of the EFG is to split the degeneracy of the 2I transitions of the nucleus. In isotropic solutions, the splitting is averaged to zero by rapid molecular tumbling. However, if the observed molecules in solution interact with anisotropically oriented structures, such as gel fibres, present in the sample then this averaging is incomplete and a small line splitting – a residual quadrupolar coupling (RQC, Δ) – is observed which is given by:[17]

$$\Delta = \frac{3\chi}{4I(2I-1)}\langle 3\cos^2\theta - 1\rangle \qquad (3.7)$$

where χ is the quadrupolar coupling constant and θ the angle between the applied magnetic field and the main component of the EFG, with the brackets <> denoting a time average. In the simplest case of fast exchange of molecules

between isotropic solution and a single type of binding site on an anisotropic structure, the RQC is described phenomenologically by:

$$\Delta = f_b \Delta_b \quad (3.8)$$

where f_b and Δ_b are the fraction of molecules bound at any one time and the splitting they experience respectively. Δ_b depends on the magnitude of the EFG and the angle with the magnetic field in the bound state, θ_b. Typical values of χ are of the order of hundreds of kilohertz[48, 49] and so a very small f_b of the order of $1x10^{-4}$ can give rise to observable RQCs of a few Hz. For the purposes of the present study we analyse RQC data using the equation:

$$\Delta = f_b S_b K \quad (3.9)$$

where: $S_b = \langle 3cos^2\theta_b - 1 \rangle$ and $K = 3\chi/4I(2I-1)$. If the relative RQCs of two probe molecules with different chemical characteristics, such as charge and hydrophobicity, change, then the nature of the surface of the gel fibres is also changing. This hypothesis is supported by our previous work in which a significant RQC was found for dioxane-d_8 with hydrophobic self-assembled fibres, but a negligible RQC was found for D_2O. Conversely, highly charged fibres gave a large RQC for D_2O and only a small RQC for dioxane-d_8.[14] Here, we use $^{14}NH_4^+$ as a probe for negatively charged sites and the methanetriyl deuteron of IPA as a probe of uncharged hydrophobic sites. D_2O, dioxane-d_8, DMSO-d_6 and CD_3CN were tried as probe molecules but found not to give observable RQCs, possibly due to a lower degree of magnetic-field-induced anisotropy in **1**/GdL gels than in the gels studied in our previous work.[14] We attribute the sensitivity of IPA to its relatively high affinity for hydrophobic surfaces coupled with its restricted mobility when associated with such surfaces[32] and the restricted conformational flexibility of the methanetriyl deuteron. Although some splitting of the $^{23}Na^+$ resonance was apparent (Section 3.3.2), this was insufficient for reliable RQCs to be extracted and the -1/2↔1/2 transition of this $I=^3/_2$ nucleus would obscure the coexisting isotropic phase present in gels formed from **1** due to syneresis**.**

3.2.5.3 ^{23}Na T_1 and T_2 relaxation

The relaxation of $^{23}Na^+$ is dominated by the fluctuating quadrupolar coupling the ions experience as they diffuse in solution and transiently interact with any large immobile structures present. In the absence of such structures, or with a low volume fraction of relatively small structures such as spherical micelles, the 'extreme narrowing' condition is expected to apply within which $T_1 \approx T_2$, with both time constants similar to those measured in the absence of gelator.[50] Upon the formation of larger structures, the motion of $^{23}Na^+$ will be reduced and both T_1 and T_2 will decrease, the latter to a significantly greater extent.[51] The use of $^{23}Na^+$ relaxation measurements to follow the formation of supramolecular hydrogels has previously been explored by Raue *et al.*[52] These authors found that T_2, and to a lesser extent T_1, decreased significantly upon the thermally-induced gelation of a succinamic acid-based gelator in saturated $NaHCO_3$ solution. This was attributed to a significant interaction between the Na^+ ions and the carboxylate groups on the gel fibres. Although T_2 is affected by the anisotropy of the structures present,[47, 53] in the present study the small size (< 30 Hz) of the observed RQCs and the essentially monoexponential nature of the CPMG signal decays (Section 3.3.3) suggest that, qualitatively, this effect can be ignored. The ^{2}H T_1 and T_2 relaxation times of HDO and the methyl groups of IPA were found not to change significantly during the gelation process.

3.2.6 Experimental

3.2.6.1 Materials

Gelator **1** was synthesised as described previously.[27] All other chemicals were purchased from Sigma-Aldrich and used as received.

3.2.6.2 Preparation of samples

A stock solution of NMR pH indicator compounds was prepared containing sodium formate (0.4 M), glycine (0.2 M), methyl phosphonic acid (0.2 M), sodium acetate (0.2 M), sodium methanesulfonate (0.1 M) and sodium hydroxide (0.6 M). Stock solutions of **1** at 5 mg/mL were prepared by dispersing an appropriate amount of the dipeptide in water before adding

1.2±0.1 equivalents of standardised NaOH and stirring for at least six hours to form a transparent solution. After stirring, an appropriate volume of the NMR indicator solution was added to give the concentrations listed in the text. NH_4Cl was added as an 0.5 M stock solution to give a final concentration of 10 mM for ^{14}N NMR studies. The pH of the solutions was 9. Isopropanol-d_8 (IPA, 0.05 vol%, 7 mM) was also added for ^{2}H NMR studies.

All gelled samples, unless otherwise stated, were prepared at a GdL concentration of 5 mg/mL. Typically, 700 μL of a solution of **1**, with additives, was transferred to a pre-weighed amount of GdL in a 14 mL glass vial. After dissolution of the GdL with gentle swirling, the solution was promptly transferred to a 5 mm NMR tube for analysis. The time quoted is the total time elapsed since the dipeptide solution was added to the GdL.

3.2.6.3 NMR

All NMR experiments were performed on a Bruker Avance II 400 MHz (^{1}H) wide bore spectrometer operating at 400.20 MHz for ^{1}H, 105.86 MHz for ^{23}Na, 61.43 MHz for ^{2}H and 28.91 MHz for ^{14}N. All NMR experiments were performed off lock in H_2O at 298±0.5 K. ^{1}H spectra were recorded in a single scan with presaturation applied to the H_2O resonance for 5 s followed by a spoil gradient pulse (27 G/cm, 1 ms) prior to a π/2 hard pulse and signal acquisition. 65536 data points were acquired with a sweep width of 15 ppm, giving a total acquisition time of 35 s with a 25 s delay at the start of the experiment prior to any pulses so that, as far as possible, the integrals obtained could be used quantitatively. Presaturation was found not to significantly suppress any resonances of **1**. ^{2}H spectra were recorded via the lock channel with 1964 data points, a 200 μs pulse (70^{o}) and a sweep width of 8 ppm. At the start of the gelation experiment, 256 scans were acquired giving an acquisition time of 10 minutes. Once significant structure formation had occurred and the RQC of the methanetriyl resonance of IPA was appreciable, the number of scans was increased first to 512 and then to 1024, giving acquisition times of 20 and 40 minutes respectively, in order that spectra with acceptable signal to noise ratios could be obtained. Once the sample had stabilised at low pH, the number of scans was increased to 2048 giving an acquisition time of 90

minutes. $^{14}N\{^{1}H\}$ spectra were acquired with the aring sequence ($\pi/2$-τ-$\pi/2$-τ-$\pi/2$-acquire) in order to supress acoustic ringing effects in our probe. A 46 μs $\pi/2$ pulse was used with a τ of 4 μs and a relaxation time of 0.1 s. CPD was applied (Waltz 16) during the pulses and signal acquisition in order to remove the effect of ^{14}N-^{1}H coupling. 578 data points with a sweep width of 10 ppm were acquired in 256 and 1024 scans prior to and after significant structure formation had occurred giving acquisition times of 5 and 20 minutes respectively. Once the sample had stabilised at low pH, the number of scans was increased to 2048 giving an acquisition time of 40 minutes. ^{23}Na T_1 and T_2 were measured using the inversion-recovery and CPMG pulse sequences respectively. For T_1, the inversion recovery time, t, was varied between 1 and 300 ms in 8 steps. For T_2, the spacing between the π pulses was fixed at 1 ms and the number of pulses varied between 2 and 256 in 8 steps. 32 scans were collected in 6144 points with a 100 ppm sweep width and a relaxation delay of 0.1 s, giving an acquisition time of 2 minutes for both T_1 and T_2 measurements. For each sample, the ^{23}Na $\pi/2$ pulse was calibrated at high pH prior to the addition of GdL using the Bruker optimisation procedure POPT, typical $\pi/2$ pulses being 34 μs in duration. PFG-NMR experiments to determine the diffusivity of **1** at high pH were performed using a double stimulated echo sequence (Bruker pulse program library DSTEGP3S) with presaturation applied to the H_2O resonance during the relaxation delay (5 s) and diffusion delay periods. The gradient pulses, of 4 ms duration, were incremented in 32 steps with 48 scans from 2.7 G/cm to a maximum of 51 G/cm, with the final value chosen so that the signal from **1** had completely decayed into the baseline. The signal decay curves could be fitted with one component to the modified Stejskal-Tanner equation[54] with no slower component detectable. The diffusion coefficient thus obtained was found to be invariant of the diffusion delay time between 0.1 and 0.4 s. The diffusivity of IPA was measured at 0.05 vol% in H_2O using non-deuterated IPA, following the same procedure used for **1**. The diffusion coefficient was found to be invariant of the diffusion delay between 0.1 and 0.3 s.

3.2.6.4 Data processing

All data was processed in Bruker Topspin 3.2 and Microsoft Excel 2010. No line broadening factor was applied to ^{2}H or ^{14}N spectra; however, prior to Fourier transformation the raw FIDs were trimmed to ensure a sufficient signal-noise ratio for analysis. For ^{14}N spectra, the last data point containing signal was judged by eye, with a minimum of 300 experimental data points being used in the transformation. For ^{2}H spectra, the first 1200 points were used where 512 scans had been recorded while 1400 points were used where 1024 or 2048 scans had been acquired. ^{2}H RQCs of IPA were extracted by deconvolution of the spectra into overlapping Lorentzian lines; example fits are shown in the Section 3.3.6. $^{14}NH_4^+$ RQCs were taken as the separation between the peak maxima of the doublet. Due to the poor signal to noise ratios and larger RQCs relative to IPA, Lorentzian deconvolution could not be expected to yield more accurate values. The time at which an RQC was recorded was taken as half way through the NMR acquisition. Uncertainties in f- calculated using Equations 3.3 to 3.5 were estimated using a Monte Carlo method based on that of Lambert *et al.*,[55] discussed in Section 3.3.13. ^{23}Na T_1 and T_2 values were extracted by fitting the data to Equations 3.10 and 3.11 respectively using a non-linear regression method developed for Microsoft Excel:[56]

$$I = I_0\left[1 - P.exp\left(-{}^{t}/_{T_1}\right)\right] \quad (3.10)$$

$$I = I_0 exp\left(-{}^{t}/_{T_2}\right) \quad (3.11)$$

where I_0 is a constant and $P \approx 1.9$. In all cases, data could be fitted acceptably to single exponentials, with biexponential fits heavily affected by the random noise inherent in the decay curves (Section 3.3.3). ^{1}H integrals of **1** were obtained relative to the sodium methanesulfonate resonance.

3.2.6.5 Rheology

All experiments were performed using an Anton Paar Physica MCR301 rheometer with parallel plate geometry. To run a time sweep, 2 mL of solution was mixed with GdL and transferred to the stationary (silicon rubber) lower

plate whereupon the upper plate (50 mm, sandblasted) was lowered onto the sample to a gap of 1 mm. Low viscosity mineral oil was placed around the edge of the sample to prevent drying artefacts. G′ and G′′ were recorded at a frequency of 10 rad/s and 0.5 % strain, a data point being recorded every 15 s for 15 hours. The gap between the measuring plates was adjusted automatically in order to maintain a constant normal force on the upper measuring plate. This adjustment was necessary as the sample was found to contract significantly during the experiment. The temperature of the sample was maintained at 25 °C.

3.2.6.6 pH Measurements

Unless otherwise stated, all pH measurements were obtained *in situ* using the NMR method. The *ex situ* measurements of Figure 3-4 were obtained using a Hanna Instruments HI-2020 Edge pH logger equipped with an FC2020 probe. The stated accuracy of these measurements is ±0.01 units. Prior to use, the meter had been calibrated with fresh pH 4, 7 and 10 buffer solutions. The sample, of 2 mLs volume in a glass container, was held at 25 ^{o}C in a thermostatic water bath. The same mixture of **1** and GdL was used for both *in situ* and *ex situ* data series on Figure 3-4.

3.2.7 Acknowledgements

We thank Andre Zamith Cardoso for collecting confocal microscopy images. We thank Unilever for a Case Award (MW) and the EPSRC for funding a DTA (MW). We thank the EPSRC for funding (EP/C005643/1 and EP/K039687/1). DA thanks the EPSRC for a Fellowship (EP/L021978/1).

3.2.8 References

1. Y. E. Shapiro, *Prog. Pol. Sci.*, 2011, **36**, 1184-1253.
2. G. Yu, X. Yan, C. Han and F. Huang, *Chem. Soc. Rev.*, 2013, **42**, 6697-6722.
3. B. Escuder, M. Llusar and J. F. Miravet, *J. Org. Chem.*, 2006, **71**, 7747-7752.
4. A. Reddy, A. Sharma and A. Srivastava, *Chem. Eur. J.*, 2012, **18**, 7575-7581.
5. Nonappa, D. Šaman and E. Kolehmainen, *Magn. Res. Chem.*, 2015, **53**, 256-260.

6. A. R. Hirst, I. A. Coates, T. R. Boucheteau, J. F. Miravet, B. Escuder, V. Castelletto, I. W. Hamley and D. K. Smith, *J. Am. Chem. Soc.*, 2008, **130**, 9113-9121.
7. V. J. Nebot and D. K. Smith, in *Functional Molecular Gels*, The Royal Society of Chemistry, 2014, pp. 30-66.
8. S. S. Rohner, J. Ruiz-Olles and D. K. Smith, *RSC Adv.*, 2015, **5**, 27190-27196.
9. W. Edwards and D. K. Smith, *J. Am. Chem. Soc.*, 2014, **136**, 1116-1124.
10. M. M. Smith and D. K. Smith, *Soft Matter*, 2011, **7**, 4856-4860.
11. M. Tena-Solsona, B. Escuder, J. F. Miravet, V. Casttelleto, I. W. Hamley and A. Dehsorkhi, *Chem. Mater.*, 2015, **27**, 3358-3365.
12. S. Iqbal, F. Rodriguez-Llansola, B. Escuder, J. F. Miravet, I. Verbruggen and R. Willem, *Soft Matter*, 2010, **6**, 1875-1878.
13. Nonappa, M. Lahtinen, B. Behera, E. Kolehmainen and U. Maitra, *Soft Matter*, 2010, **6**, 1748-1757.
14. M. Wallace, A. Z. Cardoso, W. J. Frith, J. A. Iggo and D. J. Adams, *Chem. Eur. J.*, 2014, **20**, 16484-16487.
15. J. Tritt-Goc, A. Rachocki and M. Bielejewski, *Soft Matter*, 2014, **10**, 7810-7818.
16. A. Caragheorgheopol, W. Edwards, J. G. Hardy, D. K. Smith and V. Chechik, *Langmuir*, 2014, **30**, 9210-9218.
17. A. Delville, J. Grandjean and P. Laszlo,*J. Phys. Chem.*, 1991, **95**, 1383-1392.
18. D. Zhu, B. E. Herbert, M. A. Schlautman, E. R. Carraway and J. Hur, *J. Environ. Quality*, 2004, **33**, 1322-1330.
19. V. E. Bahamonde-Padilla, J. J. López-Cascales, R. Araya-Maturana, M. Martínez-Cifuentes and B. E. Weiss López, *ChemPhysChem*, 2014, **15**, 1422-1431.
20. G. Pellizer and F. Asaro, *Magn. Reson. Chem.*, 2008, **46**, S80-S85.
21. S. Fleming and R. V. Ulijn, *Chem. Soc. Rev.*, 2014, **43**, 8150-8177.
22. Y. Zhang, Y. Kuang, Y. Gao and B. Xu, *Langmuir*, 2011, **27**, 529-537.
23. Z. Yang, G. Liang, M. Ma, A. S. Abbah, W. W. Lu and B. Xu, *Chem. Commun.*, 2007, 843-845.
24. D. J. Adams, M. F. Butler, W. J. Frith, M. Kirkland, L. Mullen and P. Sanderson, *Soft Matter*, 2009, **5**, 1856-1862.

25. K. L. Morris, L. Chen, J. Raeburn, O. R. Sellick, P. Cotanda, A. Paul, P. C. Griffiths, S. M. King, R. K. O'Reilly, L. C. Serpell and D. J. Adams, *Nat. Commun.*, 2013, **4**, 1480.
26. Y. Pocker and E. Green, *J. Am. Chem. Soc.*, 1973, **95**, 113-119.
27. L. Chen, K. Morris, A. Laybourn, D. Elias, M. R. Hicks, A. Rodger, L. Serpell and D. J. Adams, *Langmuir*, 2010, **26**, 5232-5242.
28. J. Raeburn, L. Chen, S. Awhida, R. C. Deller, M. Vatish, M. I. Gibson and D. J. Adams, *Soft Matter*, 2015, **11**, 3706-3713.
29. Z. Szakács, G. Hägele and R. Tyka, *Anal. Chim. Acta*, 2004, **522**, 247-258.
30. T. Tynkkynen, M. Tiainen, P. Soininen and R. Laatikainen, *Anal. Chim. Acta*, 2009, **648**, 105-112.
31. J. J. H. Ackerman, G. E. Soto, W. M. Spees, Z. Zhu and J. L. Evelhoch, *Magnetic Resonance in Medicine*, 1996, **36**, 674-683.
32. Z.-W. Dai, L.-S. Wan, X.-J. Huang, J. Ling and Z.-K. Xu, *J. Phys. Chem. C*, 2011, **115**, 22415-22421.
33. A. Z. Cardoso, A. E. Alvarez Alvarez, B. N. Cattoz, P. C. Griffiths, S. M. King, W. J. Frith and D. J. Adams, *Faraday Discuss.*, 2013, **166**, 101-116.
34. L. Chen, T. O. McDonald and D. J. Adams, *RSC Adv.*, 2013, **3**, 8714-8720.
35. D. J. Adams, L. M. Mullen, M. Berta, L. Chen and W. J. Frith, *Soft Matter*, 2010, **6**, 1971-1980.
36. C. Tang, A. M. Smith, R. F. Collins, R. V. Ulijn and A. Saiani, *Langmuir*, 2009, **25**, 9447-9453.
37. C. Tang, R. V. Ulijn and A. Saiani, *Langmuir*, 2011, **27**, 14438-14449.
38. G. Lindblom, B. Lindman and G. J. T. Tiddy, *J. Am. Chem. Soc.*, 1978, **100**, 2299-2303.
39. K. Tanaka and T. Hashitani, *Trans. Faraday Soc.*, 1971, **67**, 2314-2317.
40. O. Misran, B. A. Timimi, T. Heidelberg, A. Sugimura and R. Hashim, *The J. Phys. Chem. B*, 2013, **117**, 7335-7344.
41. L. Chen, S. Revel, K. Morris, L. C. Serpell and D. J. Adams, *Langmuir*, 2010, **26**, 13466-13471.
42. K. A. Houton, K. L. Morris, L. Chen, M. Schmidtmann, J. T. A. Jones, L. C. Serpell, G. O. Lloyd and D. J. Adams, *Langmuir*, 2012, **28**, 9797-9806.
43. S. Awhida, E. R. Draper, T. O. McDonald and D. J. Adams, *J. Coll. Int. Sci.*, 2015, **455**, 24-31.

44. T. K. Harris and G. J. Turner, *IUBMB Life*, 2002, **53**, 85-98.
45. L. Piculell, B. Lindman and R. Einarsson, *Biopolymers*, 1984, **23**, 1683-1699.
46. B. Halle and H. Wennerström, *J. Chem. Phys.*, 1981, **75**, 1928-1943.
47. P. Porion and A. Delville, *Curr. Op. Coll. Int. Sci.*, 2009, **14**, 216-222.
48. J. P. Jacobsen and K. Schaumburg, *J. Magn. Res.*, 1977, **28**, 191-201.
49. H. J. Jakobsen, A. R. Hove, R. G. Hazell, H. Bildsøe and J. Skibsted, *Magn. Res. Chem.*, 2006, **44**, 348-356.
50. H. Gustavsson and B. Lindman, *J. Am. Chem. Soc.*, 1975, **97**, 3923-3930.
51. D. E. Woessner, *Concepts Magn. Res.*, 2001, **13**, 294-325.
52. M. Raue, A. Bernet, M. Küppers, S. Stapf, H. W. Schmidt, B. Blümich and T. Mang, in *Intelligent Hydrogels*, eds. G. Sadowski and W. Richtering, Springer International Publishing, 2013, vol. 140, ch. 4, pp. 45-51.
53. T. M. Barbara, R. R. Vold and R. L. Vold, *J. Chem. Phys.*, 1983, **79**, 6338-6340.
54. A. Jerschow and N. Müller, *J. Magn. Reson.*, 1997, **125**, 372-375.
55. R. J. W. Lambert, I. Mytilinaios, L. Maitland and A. M. Brown, *Computer Methods and Programs in Biomedicine*, 2012, **107**, 155-163.
56. A. M. Brown, *Comput. Methods Programs Biomed.*, 2001, **65**, 191-200.

3.3 Supporting Information

3.3.1 Calibration of method for *in situ* pH determination by NMR spectroscopy and discussion of errors

The limiting chemical shifts, δ_H and δ_L, of the indicators were determined by adjusting the pH of a H_2O solution of the indicators, held at 25 ^oC in a thermostatic water bath, with NaOH/HCl and then measuring the ^1H NMR spectra of the solutions. A Hanna Instruments HI-8424 pH meter equipped with an FC200 probe was used in these experiments. 32 pH values were tested, spanning the pH range 1-12. The performance of the indicators was found to be independent of the presence or absence of 50 mM NaCl (Figure 3-S1a). The titration curves from these experiments were fitted to Equation 3.S1:

$$\delta_{obs} = \frac{\delta_H 10^{(pKa-pH)} + \delta_L}{1+10^{(pKa-pH)}} \quad (3.S1)$$

The error in δ_{obs} was taken as the standard fitting error, $\Delta\delta$, given by Equation 7 of Brown.[1] Titration curves for glycine and methylphosphonic acid, both with two titratable groups, were fitted to Equation 4 of Szakács *et al.*[2] The fitted pK_a values of all indicators were in agreement with the thermodynamic literature values given in the main text within ±0.2 units. The discrepancy is attributable to the non-zero ionic strength in these calibration experiments as well as the error of our pH meter (Chapter 5, Section 5.2).[2] These literature values were used in the calculation of the pH. When calculating a pH from the chemical shifts of the indicators, all indicators whose chemical shift lay within $\Delta\delta$ of their limiting values were excluded from the calculation. The chemical shifts of the indicators are affected by factors other than the pH of the solution. Such factors could include specific interactions between the indicators and other chemical species, the ionic strength of the solution and errors in the measurement of the chemical shift. $\Delta\delta$ can be taken as a representative variation in chemical shift due to these factors. The error in the pH calculated from a single indicator, ΔpH, can thus be calculated using Equation 3.S2.

$$\Delta pH = \frac{\Delta\delta(\delta_L-\delta_H)}{(\delta_L-\delta_{obs})(\delta_{obs}-\delta_H)\ln(10)} \quad (3.S2)$$

The error in the calculated pH can be calculated as an average of both indicators in a pair, weighted by their relative sensitivities. This error is displayed as error bars in Figures 3-4b and 3-S1b. Between pH 6 and 3.5, this error is less than 0.1 units. In addition to this 'random' sample-specific error, there will be a systematic error in the calculated pH arising from the choice of pK_a values for the indicators. Limiting chemical shifts of the indicators are provided in Table 3-S1a.

Indicator	pK_a (fit)	pK_a (lit.)[3]	δ_H/ppm	δ_I/ppm	$\Delta\delta/10^{-3}$ ppm
Formic acid	3.54	3.75	8.241	8.454	1.89
Acetic acid	4.58	4.76	2.096	1.919	0.55
Methylphosphonic acid[4]	7.74 (2.17)	7.74 (2.38)	1.294	1.086	6.16
Glycine	9.91 (2.24)	9.78 (2.35)	3.563	3.186	2.62

Table 3-S1a. Limiting ^{1}H chemical shifts of indicator compounds used in the study with sodium methanesulfonate (2.815 ppm) as a reference. Literature pK_a values were obtained from Reference 3 unless otherwise stated. The other pK_a values of glycine and methylphosphonic acid, not used in the pH calculation, are indicated in parentheses.

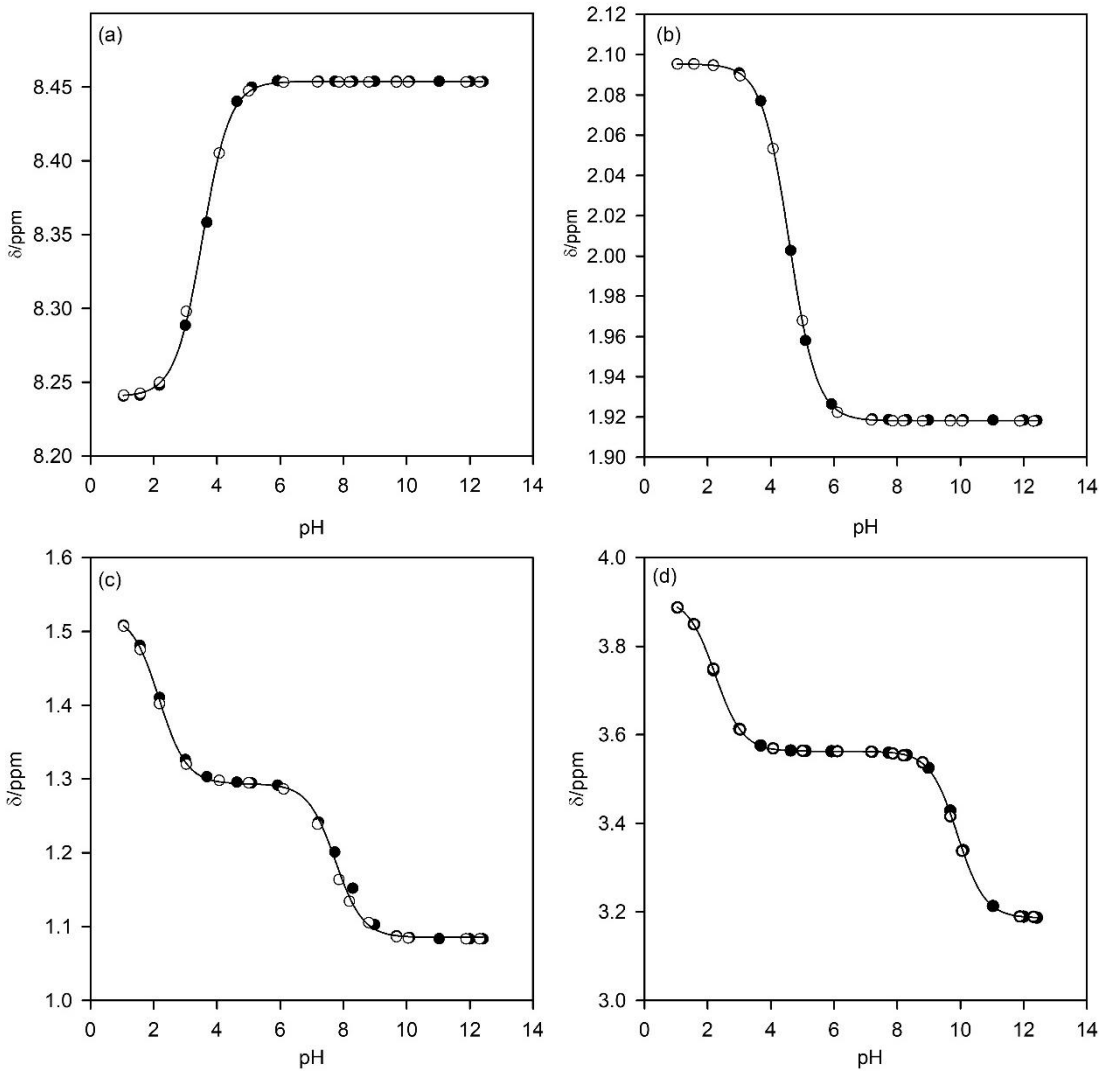

Figure 3-S1a. Titration curves of indicators with (white circle) and without (black circle) 50 mM NaCl. Fits to the combined datasets are shown as solid lines. Formic acid (a), Acetic acid (b), Methylphosphonic acid (c) and Glycine (d).

The systematic error in the pH calculated using our method was assessed by determining the pK_a values of a set of compounds using 'NMR titration' methods. The chemical shifts of the compounds were measured as a function of the pH, as determined by our NMR method, and fitted to Equation 3.6 to obtain a value for the pK_a of the compounds. The compounds chosen for this part of study were $_L$-alanine, 3-cyanophenol, imidazole, pyridine and glycolic acid.

To generate 'NMR titration' data for these compounds, solutions of the compounds under study and the NMR pH indicators were prepared at pH 12 and the pH systematically lowered as the chemical shifts were recorded. For pyridine and

glycolic acid, the pH was decreased *via* the slow hydrolysis in solution of glucono-δ-lactone (GdL). For imidazole, 3-cyanophenol and $_{L}$-alanine, the solution at high pH was carefully layered on top of solid GdL in the bottom of a 5 mm NMR tube to generate a vertical pH gradient across the sample. The gradient was then analysed using chemical shift imaging (CSI) to obtain the chemical shift of the compound as a function of the pH. For this purpose, a modified version of the gradient phase encoding sequence of Trigo-Mouriño *et al.*[5] - ($\pi/2$ - τ_1 - g - τ_2 - acquire, where g is a gradient pulse in the form of a smoothed square and τ_1 and τ_2 are delays of length 10 μs and 200 μs respectively) - was used with a double echo WATERGATE sequence of Liu *et al.*[6] (Bruker pulse program library ZGGPW5) in place of the $\pi/2$ pulse and a spoil pulse (1 ms, 27 G/cm) at the end of the signal acquisition period (1 s) to dephase any transverse magnetisation remaining before the next scan was acquired. 128 gradient increments from -27 to 27 G/cm with a gradient pulse duration of 238 μs were executed, each with 16 scans, affording a theoretical spatial resolution of 0.20 mm and a total acquisition time of 40 minutes. Additional data points for $_{L}$-alanine at high pH were obtained *via* the slow hydrolysis in solution of sodium succinate mono-methyl ester. pK_a values for the compounds under study determined using the 'NMR titration' method are given in Table 3-S1b along with literature values. Titration curves are presented on Figure 3-S1b. The measured pK_a values agree with the literature values within ±0.2 units while all fitted curves fit, in general, within the error bars. The error bars, calculated using Equation 3.S2, are thus a reasonable estimate of the random error in a pH measurement while the measured values are systematically different from the true pH by less than 0.2 units. The measurement of pH by NMR and its application in NMR titration methods are re-visited in Chapter 5, Section 5.2.

Compound	pK_a ('NMR titration')	pK_a (literature[3])
Glycolic acid	3.86	3.83
Pyridine	5.36	5.23
Imidazole	6.98	6.99
3-cyanophenol	8.53	8.61
$_{L}$-Alanine	9.93	9.87

Table 3-S1b. pK_a values of compounds determined *via* the 'NMR titration' method and literature values from source indicated.

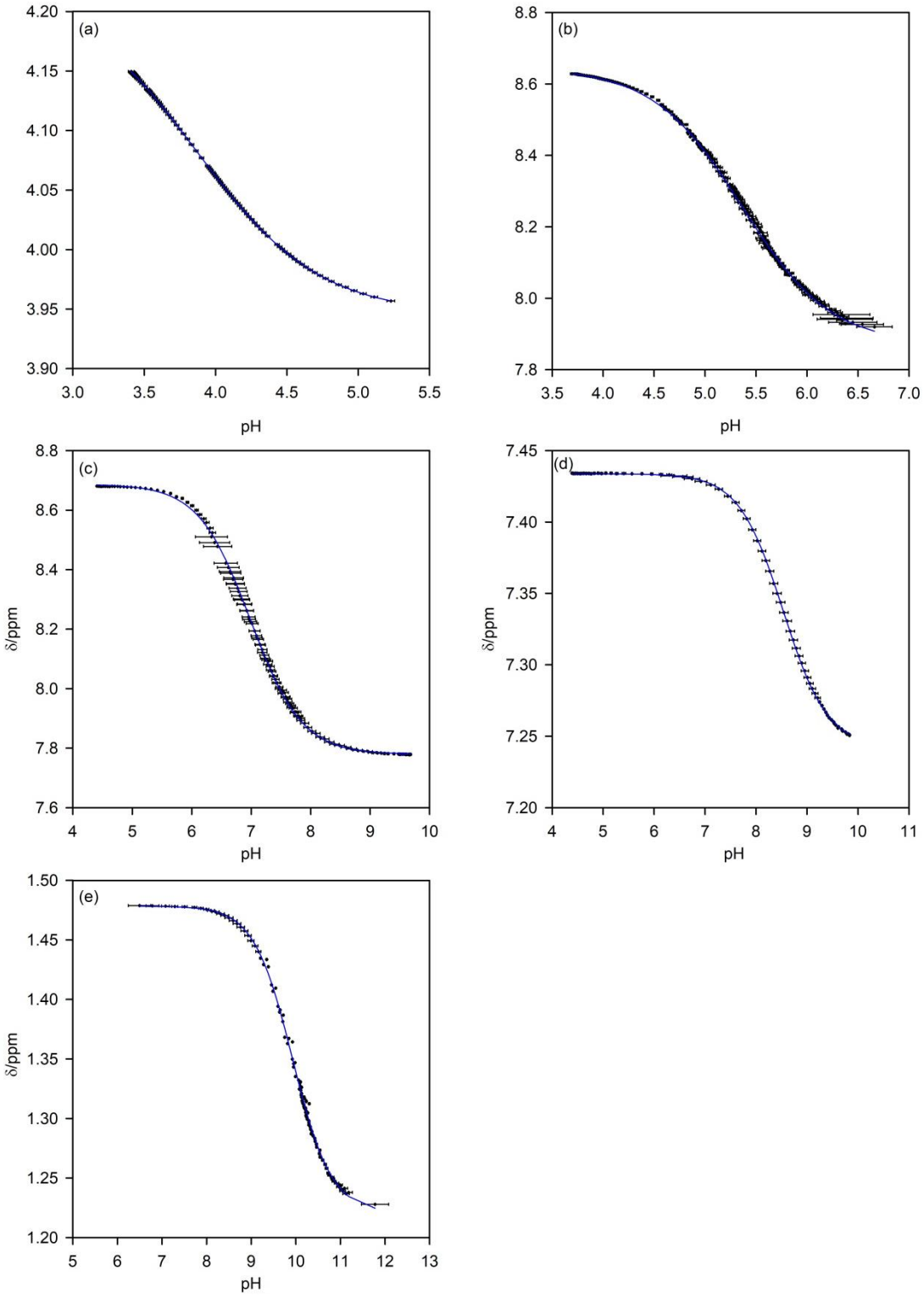

Figure 3-S1b. NMR titration curves to determine pK_a values of glycolic acid (a), pyridine (b), imidazole (c), 3-cyanophenol (d) and $_L$-alanine (e). Error bars indicate the 'random' error in the pH, estimated from Equation 3.S2. The scatter in the data for $_L$-alanine around the centre of the titration curve is due to the broadness of the glycine resonance on the CSI spectra at these pH values. Fits to Equation 3.S1 are shown as blue lines.

3.3.2 Efficacy of ^{23}Na residual quadrupolar couplings to follow hydrogel development

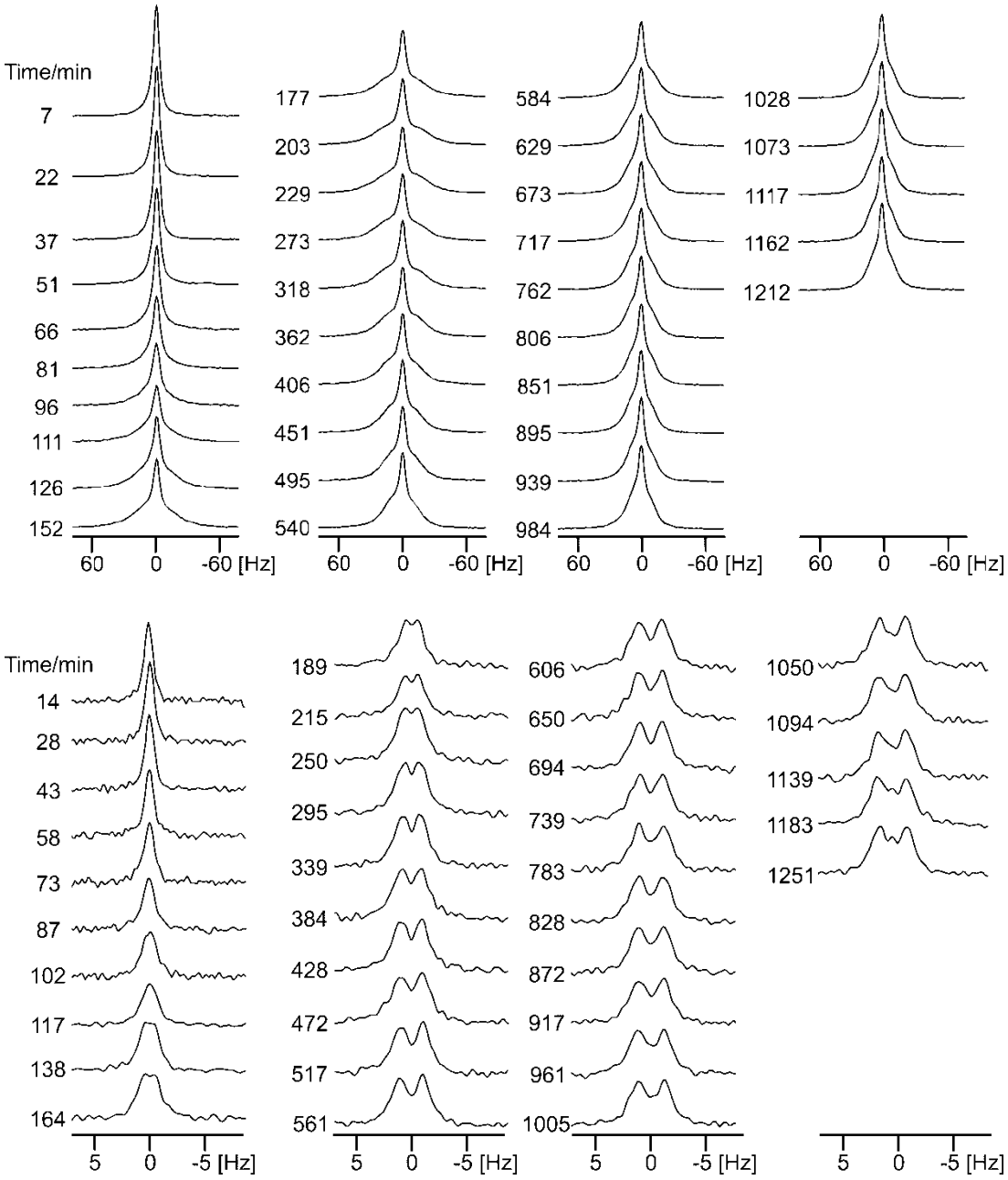

Figure 3-S2. ^{23}Na (upper plots) and ^{2}H (IPA) NMR spectra (lower plots) at times indicated since the addition of GdL to a solution of **1** at high pH.

The sample was prepared according to the standard method described in the main text but without the addition of NH_4Cl. The ^{23}Na resonance exhibits a residual quadrupolar coupling which, like that of $^{14}NH_4^+$, is largest at ca. 150-200 minutes but gradually decreases as charge is lost from the gel fibres. Owing to ^{23}Na having a nuclear spin of 3/2 and quite broad lines, the RQC is apparent only as a broad feature

on the base of the central -1/2↔1/2 transition and so cannot be measured reliably. ^{23}Na spectra were recorded with 256 scans before and 512 scans after 120 minutes had elapsed, with 6144 points and a sweep width of 100 ppm, giving acquisition times of 1 minute 30 seconds and 3 minutes respectively.

3.3.3 Example ^{23}Na CPMG echo decays (T_2 measurement)

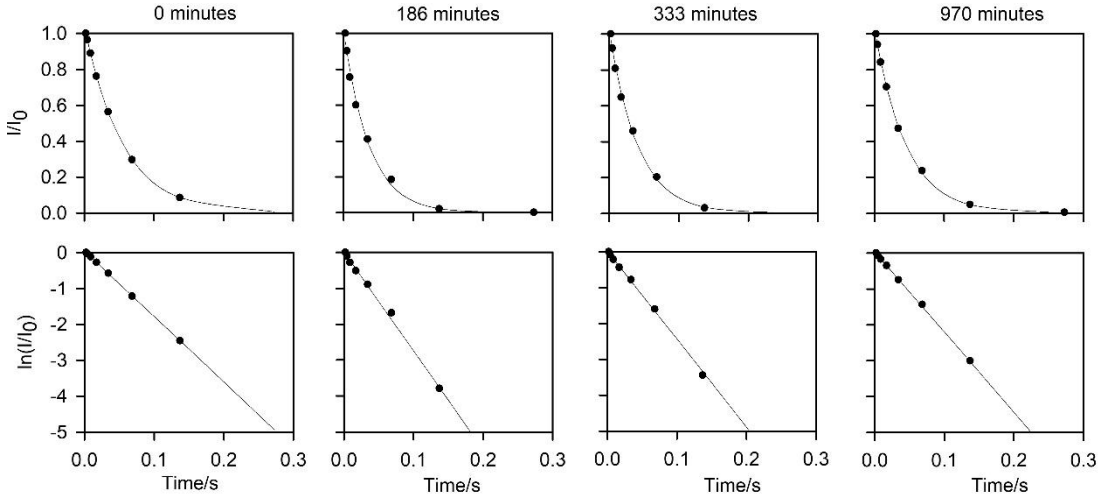

Figure 3-S3. Example ^{23}Na CPMG echo decay plots, from data presented on Figure 3-1c, at times indicated since the addition of GdL.

3.3.4 Effect of added NMR probe molecules on the gelation process of 1

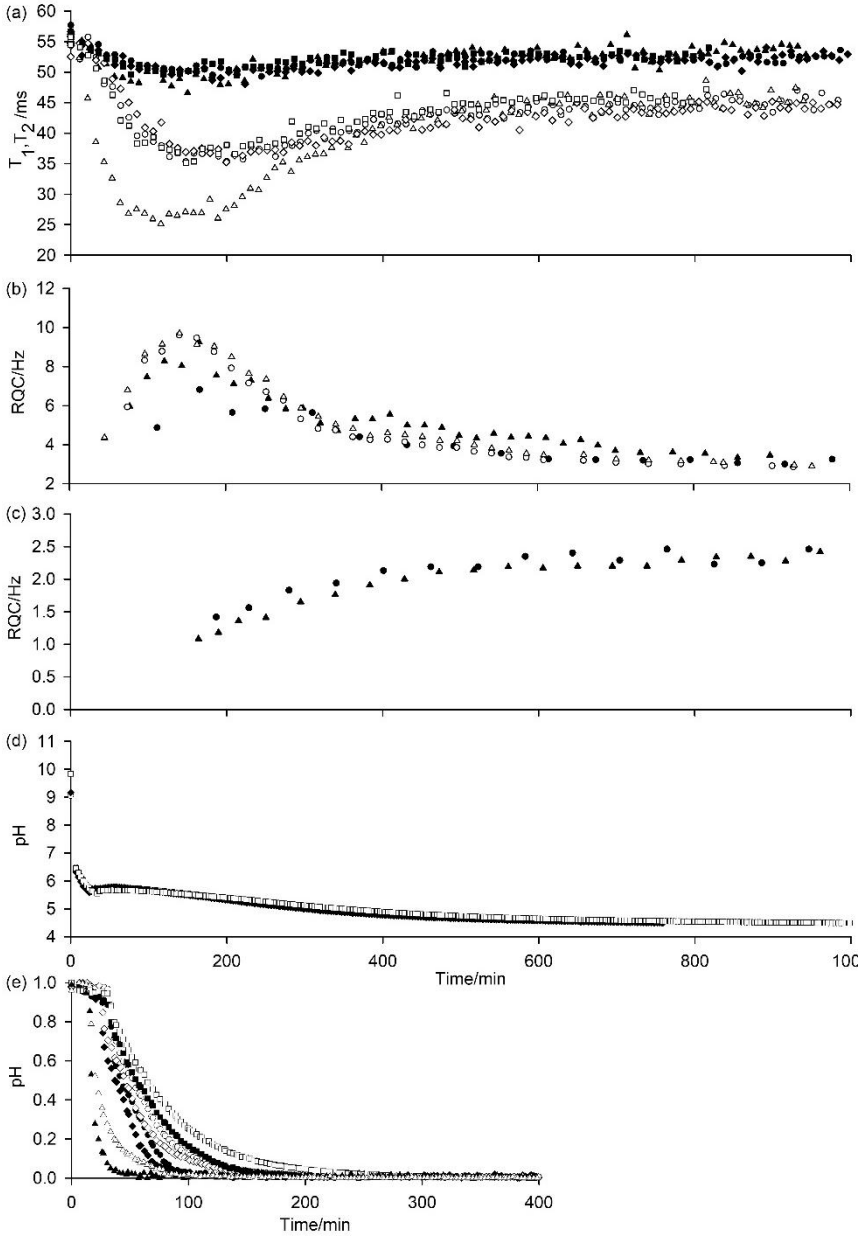

Figure 3-S4a. Plots of experimental observables versus time during the gelation of **1**. (a) $^{23}Na^+$ T_1 (black) and T_2 (white) relaxation times in the presence/absence of the specified probe molecules: all probes present (circle), IPA absent (square), NH_4Cl absent (diamond), all probes including pH indicators absent (triangle). (b) $^{14}NH_4^+$ RQCs: all probes present (circle), IPA absent (triangle). The data in white were prepared from the same stock solution of **1** while the data in black were prepared from different stock solutions. (c) IPA RQCs: all probes present (circle), NH_4Cl absent (triangle). (d) ph: all probes present (black diamond), IPA absent (white diamond), NH_4Cl absent (white square). (e) ^1H integrals of **1**, valine methyl (white) and aromatic resonances (black): all probes present (circle), IPA absent (diamond), NH_4Cl absent (square), all probes including pH indicators absent (triangle).

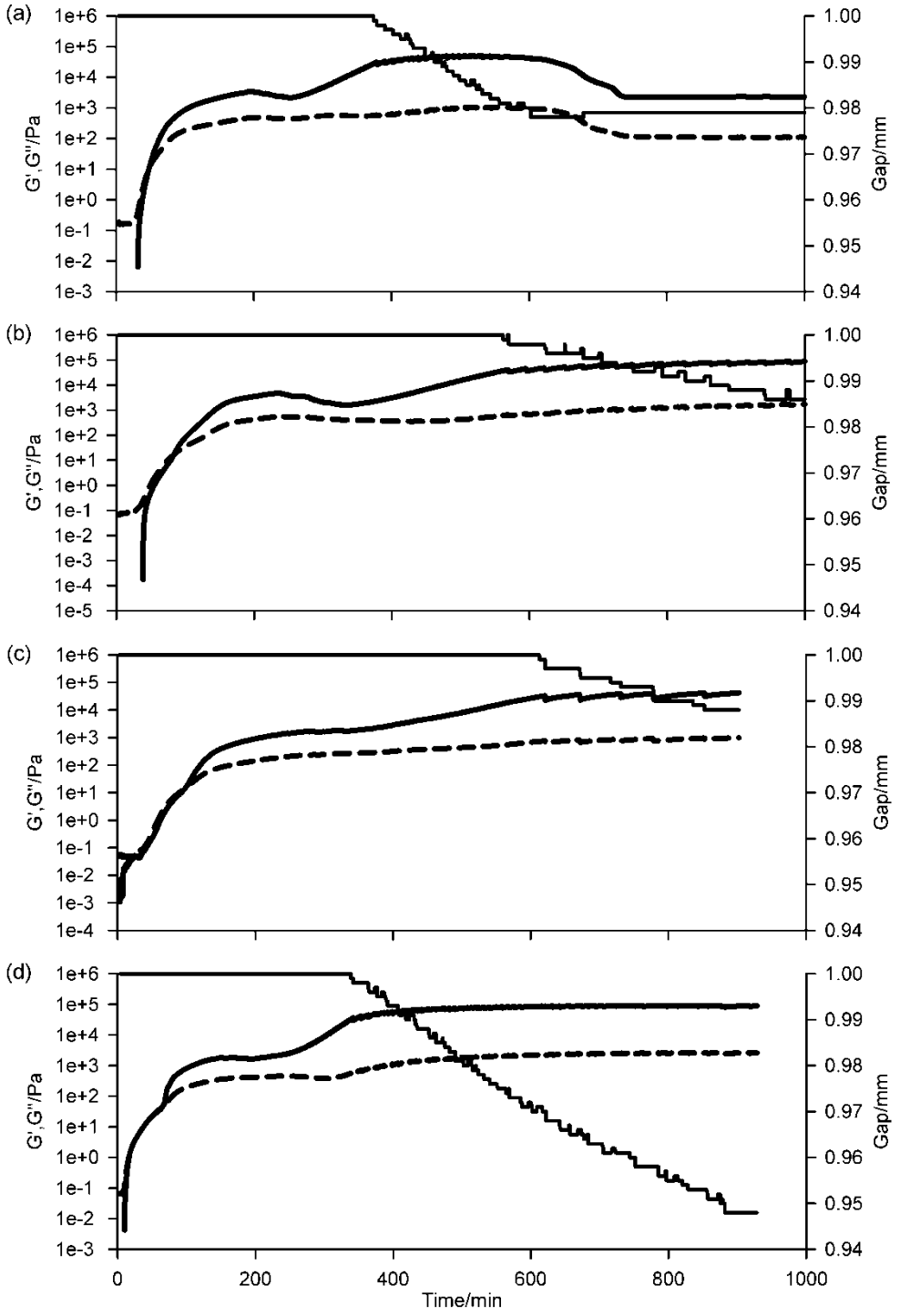

Figure 3-S4b. Plots of G' (thick solid line), G'' (dashed line) and the gap between the plates of the rheometer (thin line). The specified probe molecules were absent from the sample: (a) All probes present, (b) IPA absent, (c) NH_4Cl absent, (d) IPA, NH_4Cl and pH indicators absent.

The probe molecules for NMR spectroscopy, with the exception of IPA, are not pH neutral and may also affect the hydrolysis kinetics of GdL. The experimental profiles in their presence or absence are thus slightly different, the same quantity of GdL being used for all samples; however, the same general trends as discussed in the main text are apparent. The $^{23}Na^{+}$ T_2 is markedly reduced in the absence of any probe molecules which is attributable to the much lower total number of positive ions in this sample, each individual Na^{+} ion spending a greater fraction of its time associated with the self-assembled fibres relative to the Na^{+} ions in other samples. ^{1}H integrals of **1**, in the absence of any NMR indicators (Figure 3-S4a (d), triangle), were obtained relative to the first spectrum.

3.3.5 ^{1}H NMR spectra of 1 during the early stages of gelation

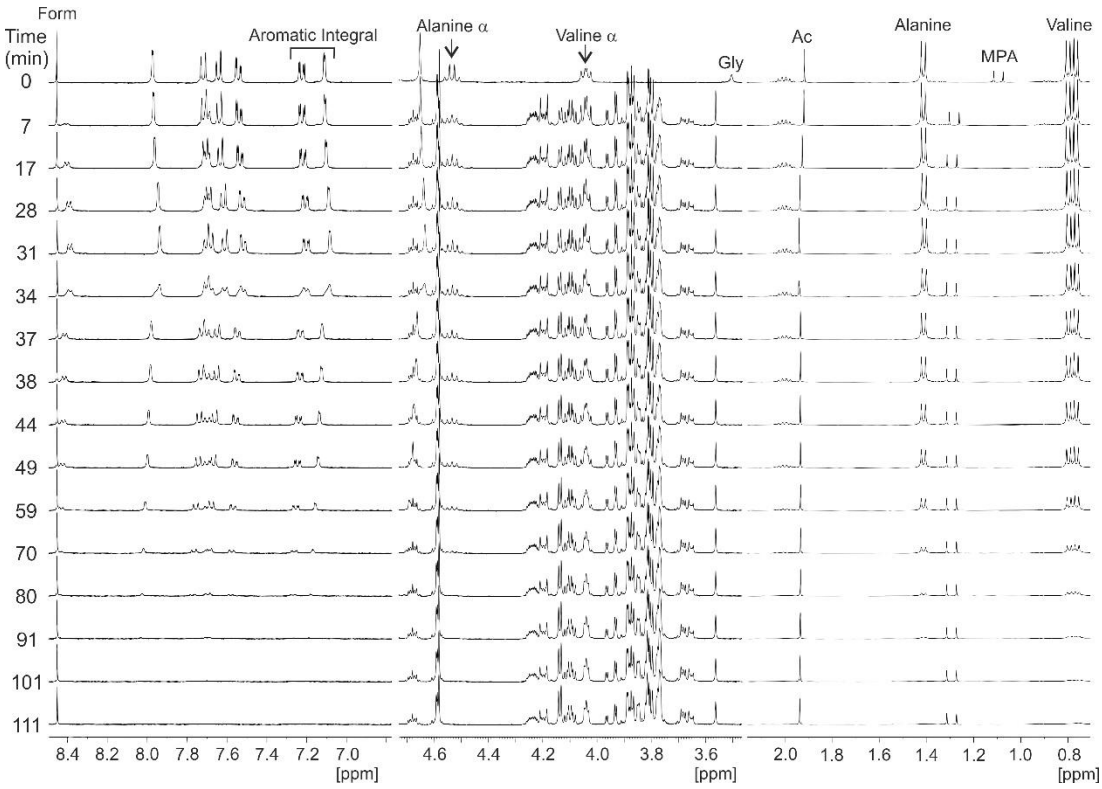

Figure 3-S5. ^{1}H NMR spectra of sample of Figure 3-1 (b, c) at times indicated on the left of the Figure. Resonances of pH indicators are indicated with their abbreviations.

Resonances between 4.7 and 3.6 ppm, unless otherwise indicated, belong to GdL/gluconate. All other resonances belong to **1**. The valine-α resonance overlaps with the H-$C_{(3)}$ resonance of GdL/gluconate at 4.04 ppm;[7] however, the outer peaks of the resonance can be seen to decrease in intensity along with those of the alanine-α proton. The valine-α resonance does not appear to shift significantly between 0 minutes (pH 9) and 60 minutes (pH 5.7) indicating that the NMR-visible gelator is deprotonated. The aromatic resonances indicated by the brackets were integrated over time to obtain the plot on Figure 3-1b.

3.3.6 ^{14}N and ^{2}H spectra of sample of Figure 3-1a during gelation

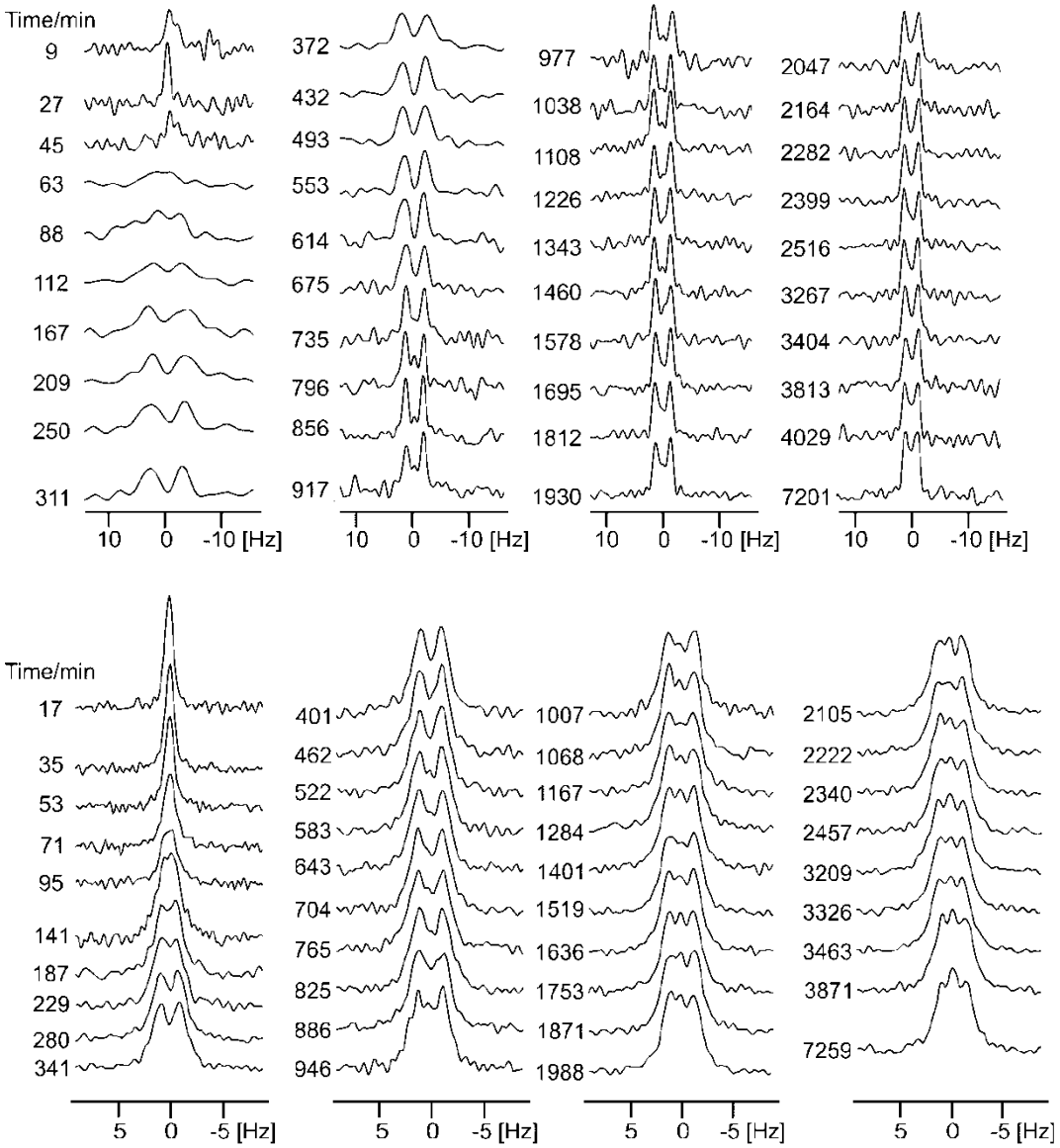

Figure 3-S6a. Experimental ^{14}N (upper plots) and ^{2}H (lower plots) spectra of the sample of Figures 3-1a and 3-2 at times indicated since the addition of GdL. The spectra have been scaled to account for the different number of scans recorded at different stages of the gelation process and so the relative intensities of the spectra do not carry any information. The sample was removed from the spectrometer after 4040 minutes and placed in a water bath at 25 ^{o}C away from the magnetic field. ^{2}H and ^{14}N spectra were recorded again 5 days after the addition of GdL.

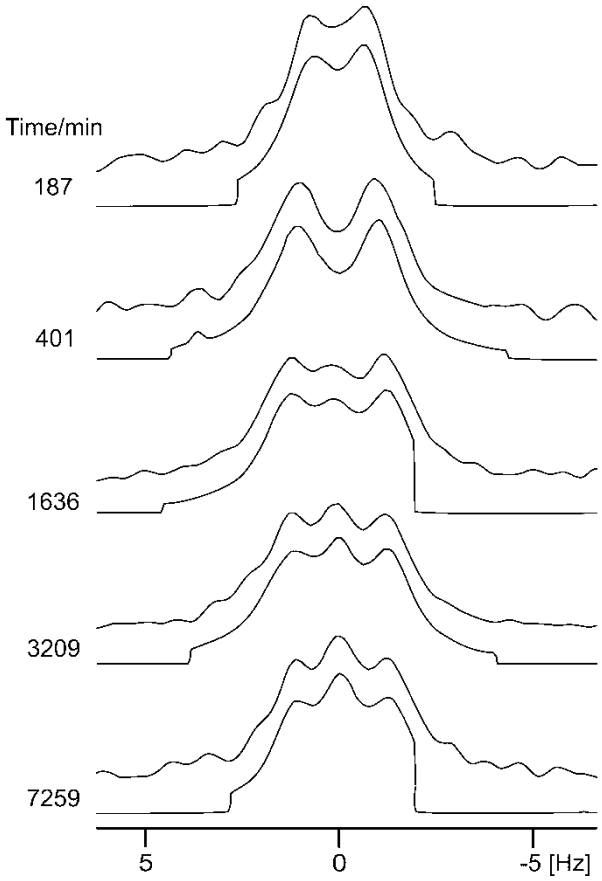

Figure 3-S6b. Selected ^{2}H spectra from Figure 3-S6a, at times indicated since the addition of GdL, to illustrate Lorentzian deconvolution of ^{2}H spectra. Experimental plots are shown above their fits. The RQC was taken as the separation of the outer two Lorentzian peaks forming the doublet. The area of the inner Lorentzian relative to the outer two was taken as the approximate ratio of isotropic solution to anisotropic gel.

3.3.7 Profile of ^{23}Na T_1 and T_2 relaxation times in the absence of 1

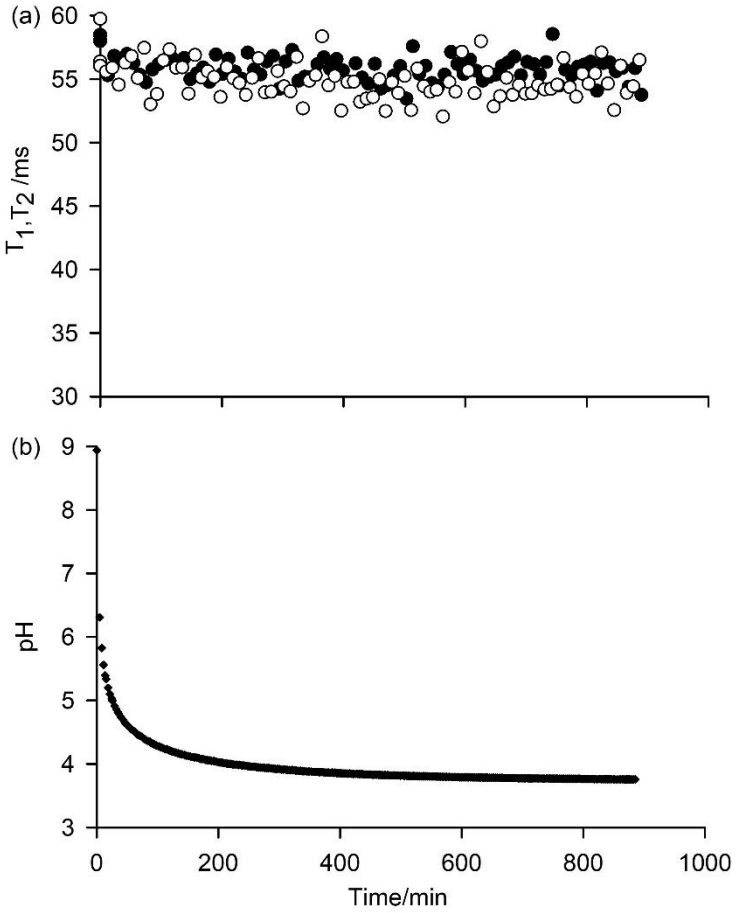

Figure 3-S7. (a) Profiles of $^{23}Na^+$ T_1 (black) and T_2 (white) since addition of 5 mg/mL GdL to a solution of the NMR probe molecules at pH 9 in the absence of **1**. (b) Plot of pH during experiment.

3.3.8 NMR analysis of a gel of 1 prepared away from any strong magnetic fields

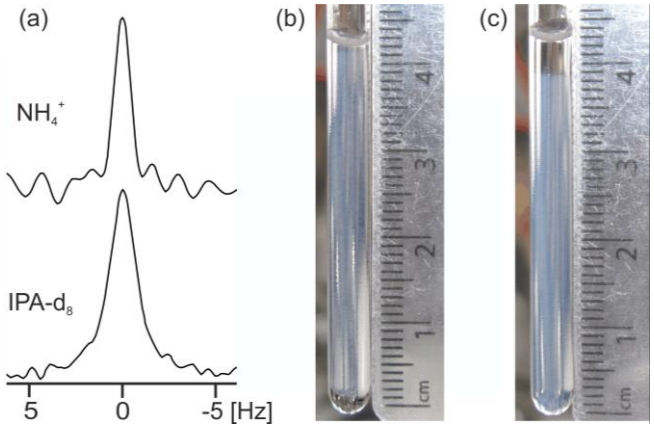

Figure 3-S8. (a) ^{14}N and ^{2}H spectra of a gel prepared away from the magnetic field at 25 ^{o}C from the same mixture of **1**/GdL as used for the sample of Figures 3-1a, 3-2 and 3-S6 (Section 3.3.6), analysed 5 days (7200 hours) after the addition of GdL. No residual quadrupolar couplings are detectable, the resonances of IPA and $^{14}NH_4^+$ both being single lines. Macroscopically, this sample (b) had contracted to a similar extent as the sample gelled in the NMR spectrometer (c). In (c) the tube had been knocked slightly causing the gel to slip down to the bottom. ^{23}Na T_1 and T_2 relaxation times in (b) were measured as 53±1 ms and 50±1 ms respectively, compared to 53±1 ms and 48±1 ms in (c).

3.3.9 Chemical shift imaging (CSI) analysis of gel of Figure 3-1a

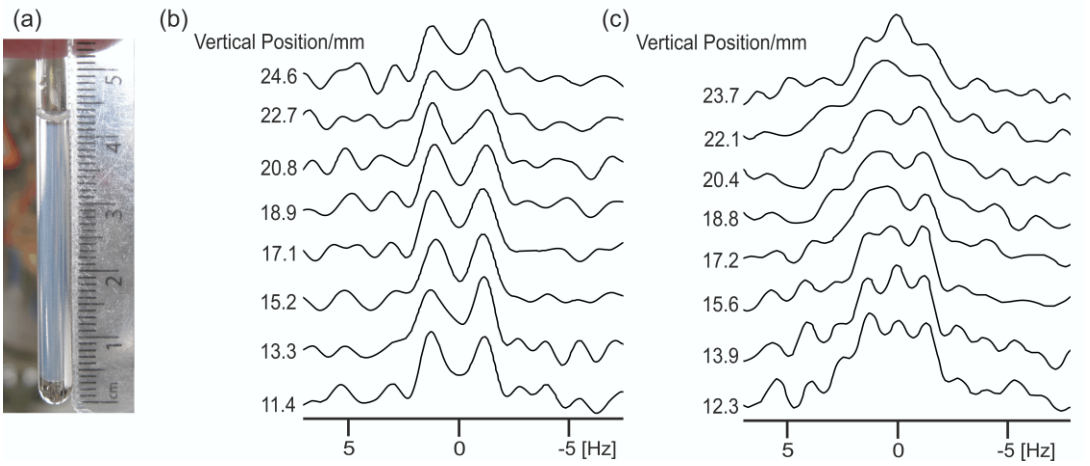

Figure 3-S9. (a) Photograph of gel sample of Figures 3-1a, 3-2 and 3-S6, 67 hours after the addition of GdL. (b) ^{14}N spectra (NH_4^+) at indicated vertical position from base of NMR tube (centre of vertical slice), recorded 48 hours after addition of GdL. The $^{14}NH_4^+$ RQC remains homogeneous throughout. (c) ^{2}H spectra (IPA) at indicated vertical position from base of NMR tube, 60 hours after the addition of GdL. The signal to noise ratio of these spectra are poor; however, a doublet and an isotropic peak are discernible at both the lower and upper parts of the NMR active region of the sample.

The ^{14}N chemical shift image was recorded using the sequence of Trigo-Mouriño *et al.*[5] modified to incorporate the aring ($\pi/2$-τ-$\pi/2$-τ-$\pi/2$) sequence to generate the transverse magnetisation and with CPD (Waltz-16) applied during the pulses and signal acquisition in order to remove the effect of ^{14}N-^{1}H coupling. 16 gradient increments from -52 to 52 G/cm were executed, each with 2048 scans and a gradient pulse duration of 192 μs. 578 data points were acquired with a sweep width of 10 ppm giving a total acquisition time of 11 hours and a theoretical spatial resolution of 1.9 mm. The central time of this acquisition was 48 hours after GdL addition. The ^{2}H chemical shift image was recorded using the sequence: $\pi/2$ - Δ - π - τ_1 - g - τ_2 – acquire, where g is the gradient pulse and $\Delta = \tau_1 + g + \tau_2$. τ_1 = 10 μs and τ_2 = 200 μs. 16 gradient increments were executed from -52 to 52 G/cm, each with 512 scans and a gradient pulse of 104 μs. 1964 data points were collected with a sweep width of 8 ppm giving a total acquisition time of 5 hours and a theoretical spatial resolution of 1.6 mm.

3.3.10 Time-lapse photography and parallel NMR analysis of gelation of 1

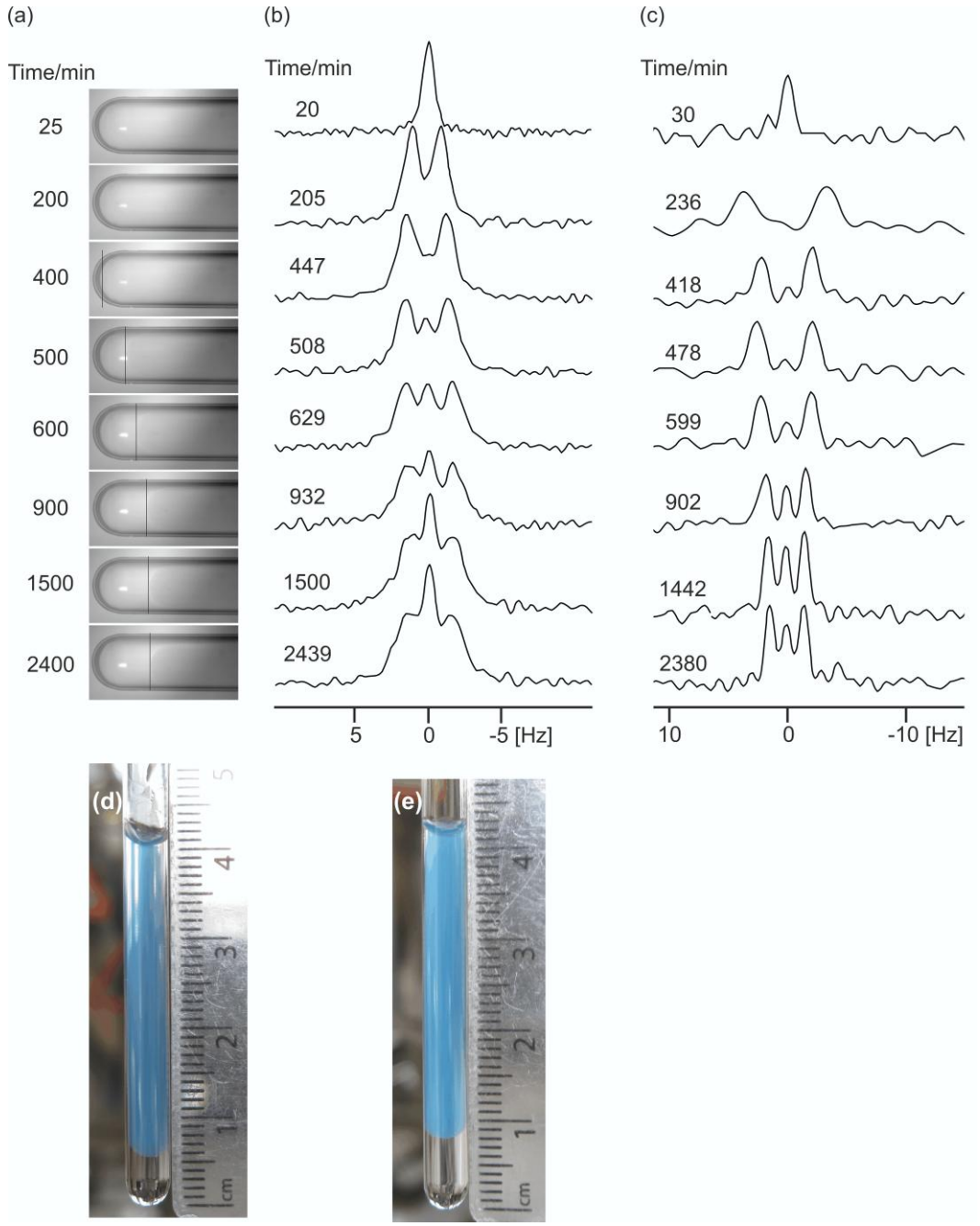

Figure 3-S10. (a) Photographs of NMR tube at times indicated since the addition of GdL. The sample was held in a water bath at 25 ^{o}C at an angle of 20^{o} to the horizontal. The position of the bottom of the gel is indicated by black lines. Nile blue dye was incorporated to improve contrast, the solution being prepared using the procedure detailed below. (b) ^{2}H (IPA) spectra of a parallel sample at times indicated since the addition of GdL. (c) ^{14}N (NH_4^+) spectra at times indicated since the addition of GdL. (d) Photograph of sample of (a) 68 hours after the addition of GdL showing that the gel has contracted to a similar extent as the sample gelled in the NMR spectrometer (e).

A stock solution of Nile blue dye was prepared by dispersing the solid dye (5 mg) in H_2O (200 mL) and dissolving with repeated stirring and sonication. This solution was used to prepare solutions and gels of **1**, as detailed in Section 3.2.6.2.

3.3.11 Gelation of 1 with 10 mg/mL GdL

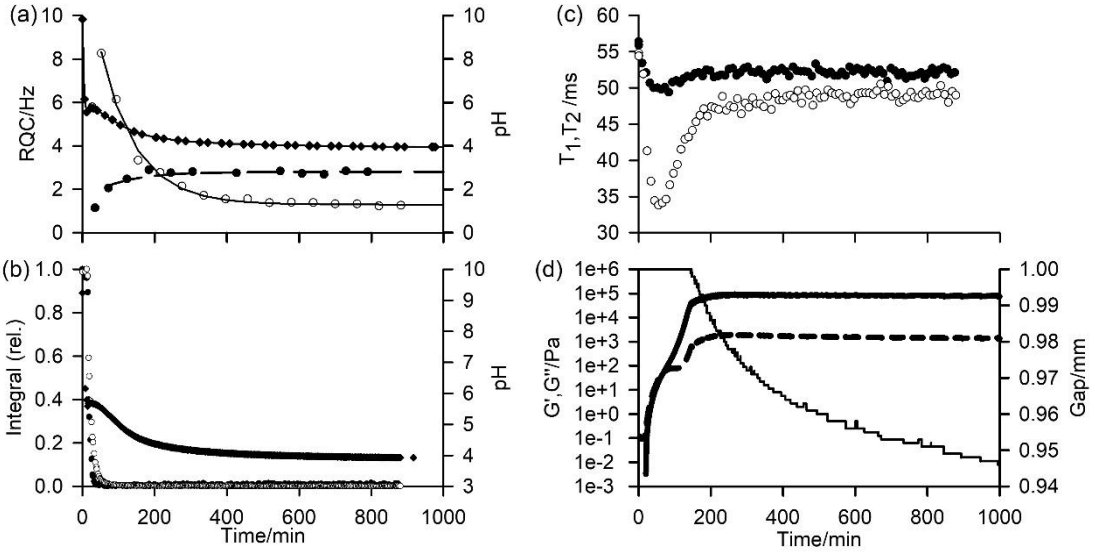

Figure 3-S11a. Time dependent profiles of experimental observables during gelation of **1** with 10 mg/mL GdL. (a) Plot of $^{14}NH_4^+$ (white circle) and IPA (black circle) RQCs. Fits to Equations 3.4 and 3.5 are shown with solid and dashed lines respectively. pH of this sample is indicated with black diamonds, the solid line is there to guide the eye. (b) Plot of integrals of valine methyl (white circle) and aromatic resonances (black circle) of **1**. This data was collected on a separate sample to (a). pH is indicated with black diamonds. (c) Plot of $^{23}Na^+$ T_1 (black circle) and T_2 (white circle). These observables were recorded on the same sample as (b). (d) Profile of G' (thick solid line), G" (dashed line) and gap between the plates of the rheometer (thin line).

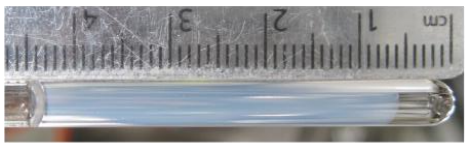

Figure 3-S11b. Photograph of sample of Figure 3-S11a, 20 hours after the addition of GdL.

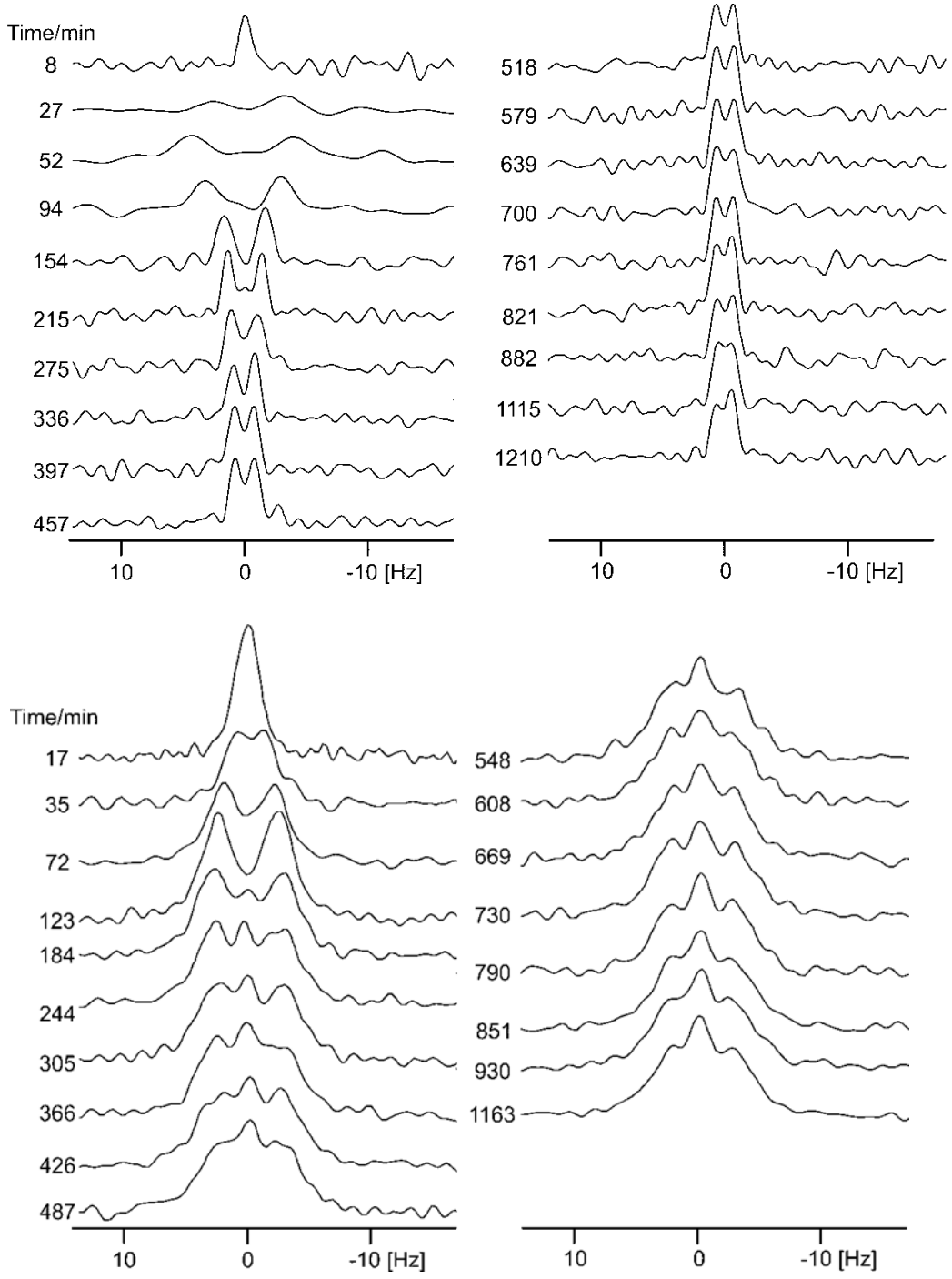

Figure 3-S11c. ^{14}N (upper plots) and ^{2}H (lower plots) spectra at times indicated since the addition of 10 mg/mL GdL to a solution of **1** at high pH.

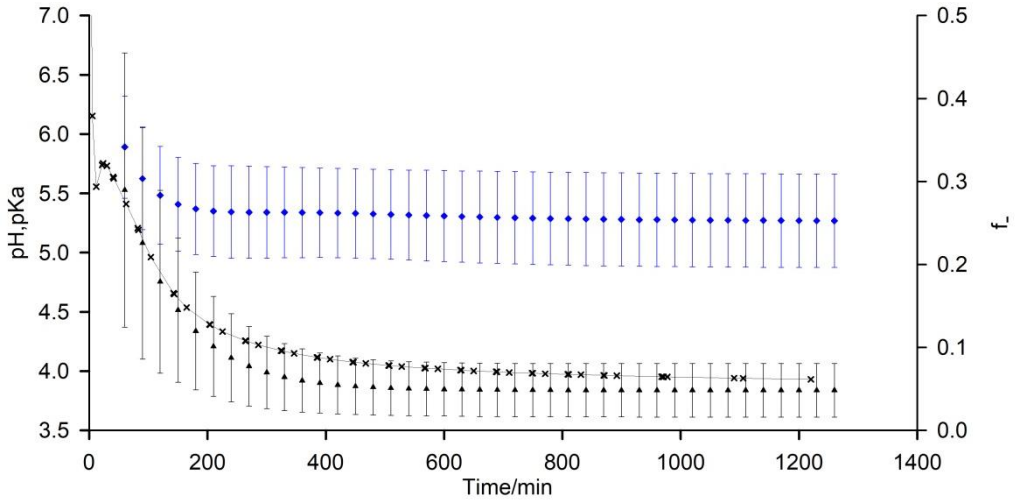

Figure 3-S11d. Plots of f_ (black triangle) and pK_a (blue diamond) values of carboxylate groups on the gel fibres, estimated using Equations 3.3 to 3.5, with error bars calculated using the method described in Section 3.3.13. pH is indicated with black crosses, the solid line is there to guide the eye.

The experimental observables follow the same profiles at 10 mg/mL as at 5 mg/mL GdL; however, the sample develops much more quickly. It is possible to estimate the fraction of charged sites, f_, and pK_a of the carboxylate groups on the gel fibres using Equations 3.3 to 3.5 (Figure 3-S11a, a; Figure 3-S11d). According to our fitting, at 90 minutes since the addition of GdL 20±15% of the carboxylates are deprotonated corresponding to a pK_a of 5.9±0.5 at pH 5.1. At pH 3.9, 5±3% of the carboxylates are deprotonated corresponding to a pK_a of 5.3±0.3. These values are significantly different to those calculated from the 5 mg/mL data; however, the much faster evolution of the system at 10 mg/mL relative to the finite time required to measure a ^{14}N or ^{2}H RQC may have significantly affected the fitting to Equations 3.4 and 3.5.

3.3.12 Gelation of 1 with 4 mg/mL GdL

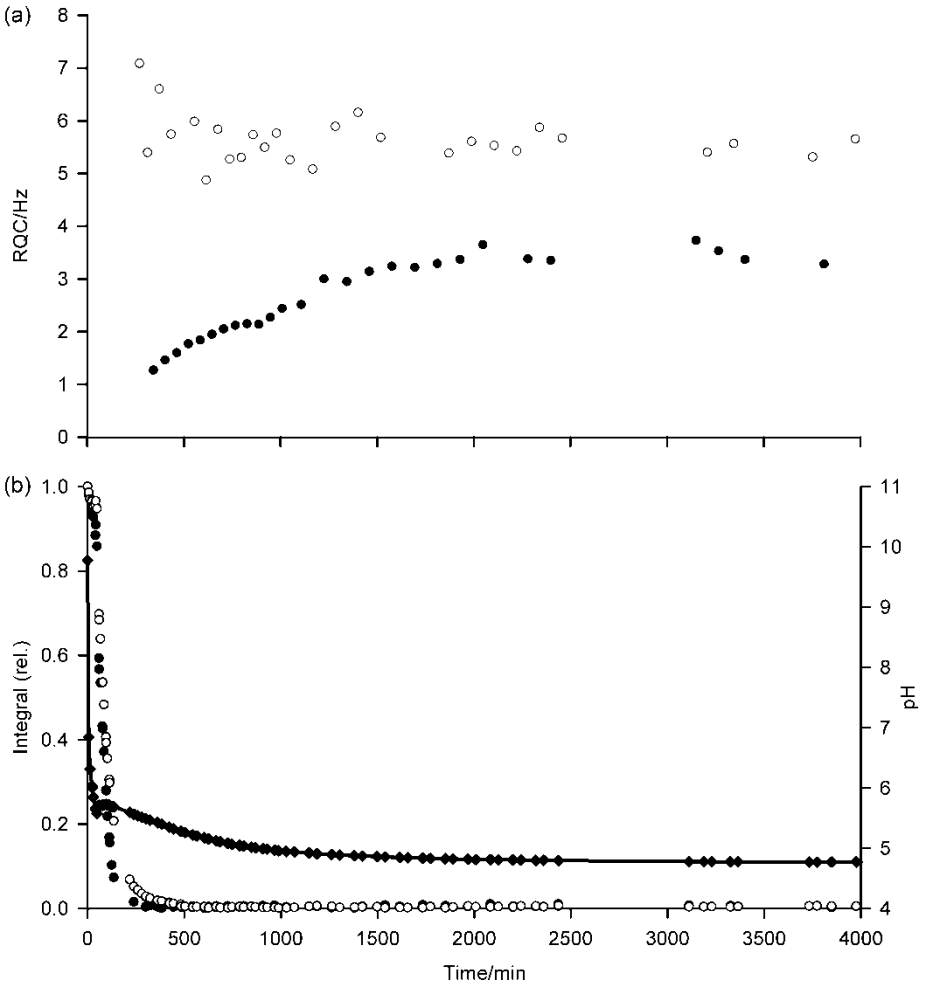

Figure 3-S12a. Time dependent profiles of experimental observables during gelation of **1** with 4 mg/mL GdL. a) Profile of $^{14}NH_4^+$ (white circle) and IPA (black circle) RQCs. b) Plot of integrals of valine methyl (white circle) and aromatic resonances (black circle) of **1**. pH is indicated with black diamonds, the solid line is there to guide the eye.

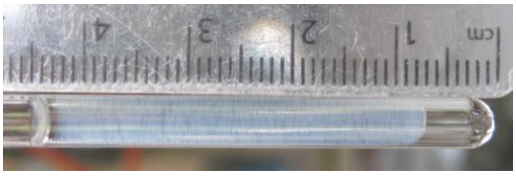

Figure 3-S12b. Photograph of gel sample of Figure 3-S13a, 73 hours after the addition of GdL.

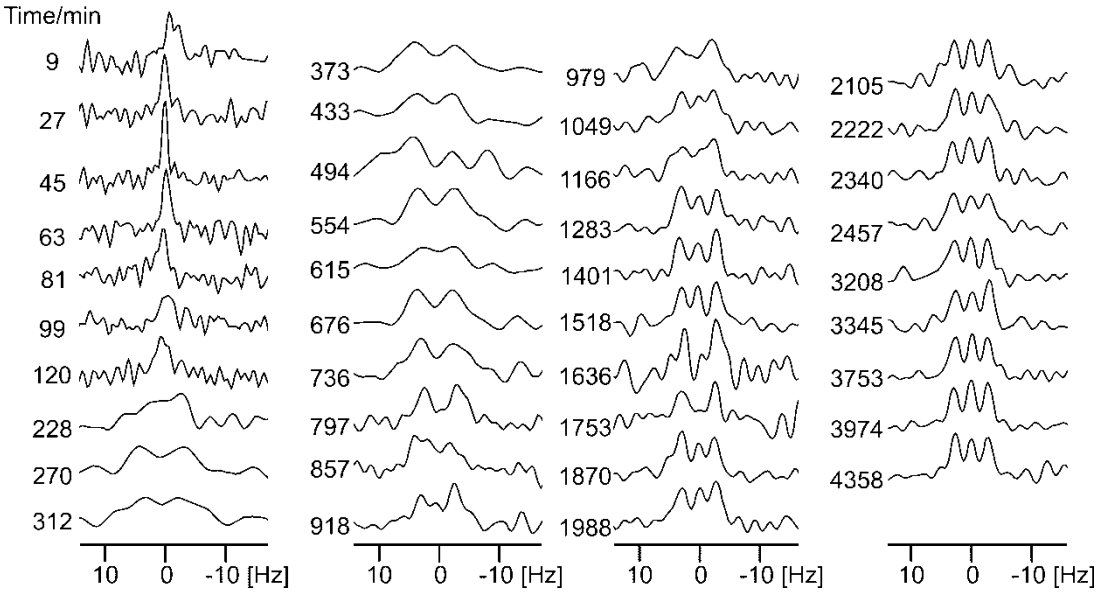

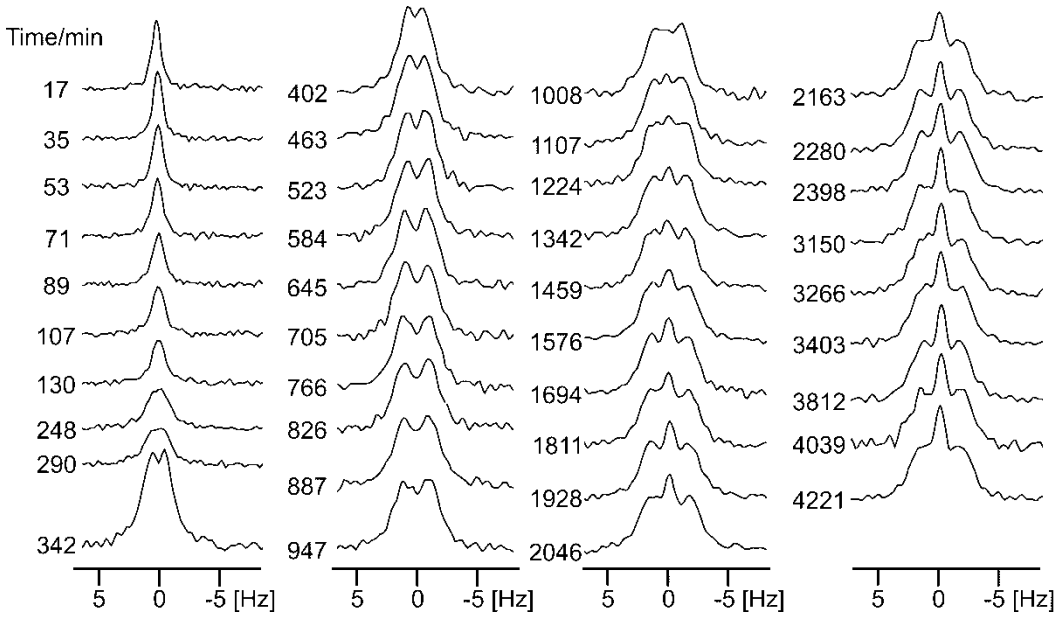

Figure 3-S12c. ^{14}N (upper plots) and ^{2}H (lower plots) spectra at times indicated since the addition of 4 mg/mL GdL to a solution of **1** at high pH.

The gelation kinetics are significantly slower at 4 mg/mL GdL than at 5 mg/mL GdL, the gelator becoming completely NMR invisible only after 500 minutes compared to 200 minutes at 5 mg/mL GdL (Figure 3-1b). These slower kinetics and significantly higher pH apparently lead to the RQCs of the $^{14}NH_4^+$ and IPA following a different profile. The charged carboxylate sites on the fibres, which according to our theories (Equations 3.2 to 3.5) give rise to the observed RQCs of $^{14}NH_4^+$, may be considered as an intermediate between unassembled gelator and/or pre-fibrillar assemblies that do not contribute to the observed RQCs and protonated carboxylate sites on the gel fibres. The kinetics of assembly and protonation may be such that the $^{14}NH_4^+$ RQC remains almost constant whereas the IPA RQC, which depends on the amount of protonated carboxylate sites on the fibres, increase as these sites are the 'final product' of the assembly process. The integrals of **1** and RQCs of NH_4^+ and IPA at 5 and 10 mg/mL GdL follow a profile resembling that of a sequential reaction that does not go to completion due to the finite amount of GdL added and its weakly acidic nature. The higher charge of the fibres and slower gelation kinetics with 4 mg/mL GdL may also cause a greater instability of the final gel network resulting in a less homogeneous gel being formed than at 5 and 10 mg/mL GdL, as is apparent by comparing Figure 3-S12b with Figures 3-S11b and 3-

2b; the gels prepared at higher concentrations of GdL, although macroscopically contracted to a similar extent, appear more transparent and homogeneous.

3.3.13 Analysis of uncertainty in gel fibre surface charge determination (Equations 3.3 to 3.5) by Monte Carlo simulation

Uncertainties in f_- were estimated using a Monte Carlo method based on that of Lambert *et al.*[8] Briefly, the standard fitting error of the experimental data to Equations 3.4 and 3.5 was used as the standard deviation of sets of randomly generated numbers which were then added to the original fit to generate 50 pseudo-experimental data sets. These datasets were fitted to Equations 3.4 and 3.5 to generate 50 sets of fitting parameters. The parameter sets which gave the largest and smallest values of f_- at each time point were then determined with the uncertainty in f_- taken as half of the difference between these values. The uncertainties in the pK_a values were similarly computed. The original fitting parameters – those giving the best fit to the experimental data – were used to calculate f_- from Equation 3.3. The original ^{14}N and ^{2}H experimental data and fits from Figure 3-3 are shown on Figure 3-S13a below, along with the fits to the pseudo-experimental datasets giving the maximum (red) and minimum (blue) values of f_-. The experimental data was found to be quite reproducible (Figure 3-S13b) with the calculated values of f_- agreeing between the datasets within the estimated uncertainties.

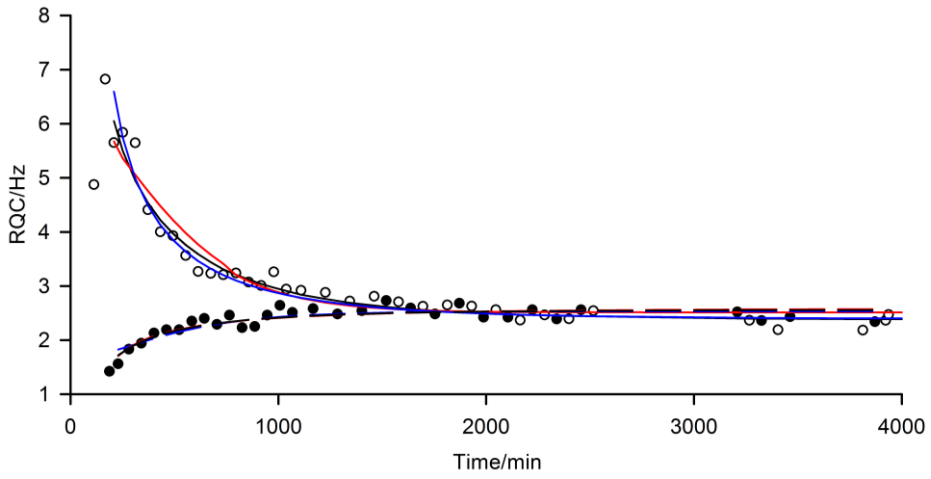

Figure 3-S13a. Plots of $^{14}NH_4^+$ (white circle) and IPA (black circle) RQCs from Figure 3-4. The fits of Equations 3.4 and 3.5 to the experimental data are shown by black solid and dashed lines respectively. The fits of Equations 3.4 and 3.5 to the pseudo-experimental datasets giving the largest (red) and smallest (blue) values of f_- are also shown; although not

providing as good a fit to the original experimental data, these curves are nevertheless a reasonable representation and so the stated uncertainties in f_- are reasonable estimates.

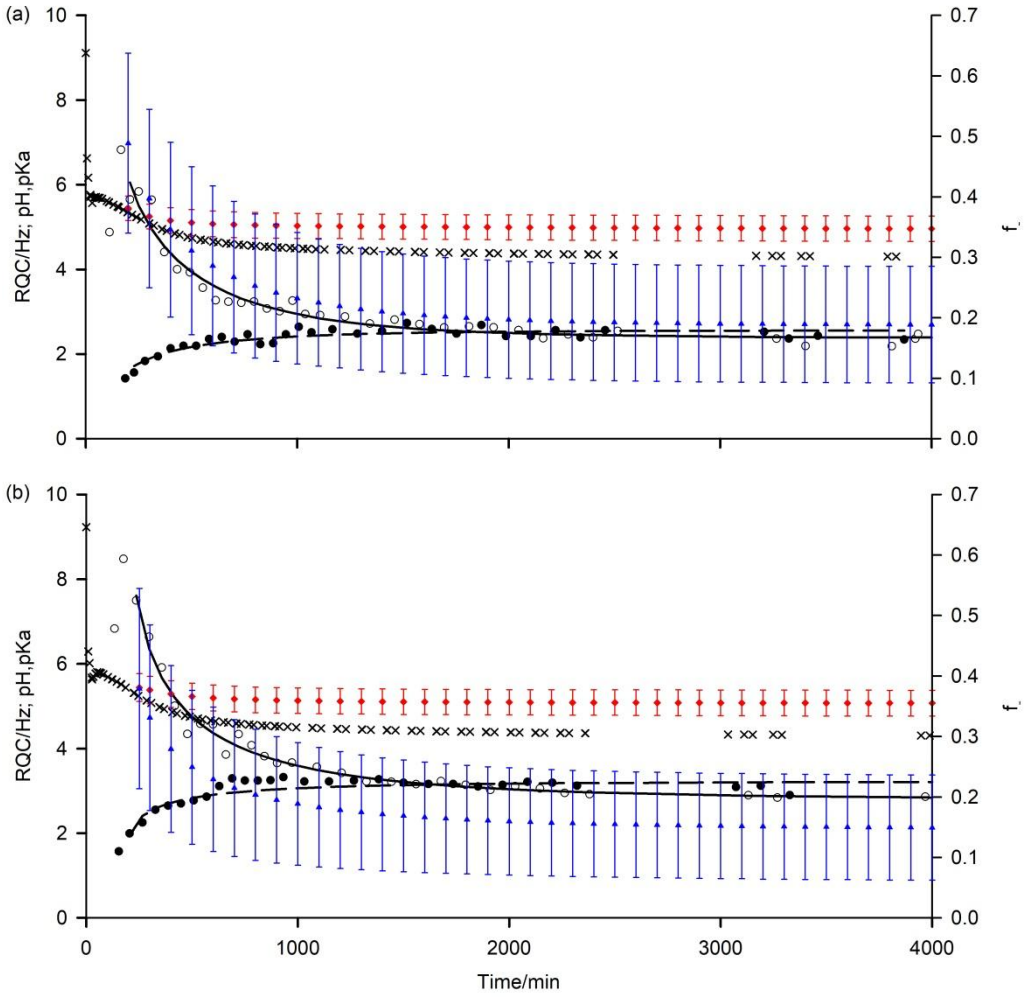

Figure 3-S13b. Plots to show reproducibility of experimental data with gels of **1** prepared with 5 mg/mL GdL; $^{14}NH_4^+$ (white circle) and IPA (black circle) RQCs along with pH data (black cross). Fits of RQC data to Equations 3.4 and 3.5 are shown by solid and dashed lines respectively. f_- (blue triangle) and pK_a values of carboxylate groups on the gel fibres (red diamond), estimated using Equations 3.3 to 3.5, are shown with error bars calculated using the method described above. (a) Reproduction of Figure 3-3 in the main text, provided here for convenience. (b) Replicate of experimental dataset. Estimated f_- and pK_a values of the two datasets agree within the stated uncertainties.

3.3.14 Changes to the normal force of the sample during gelation

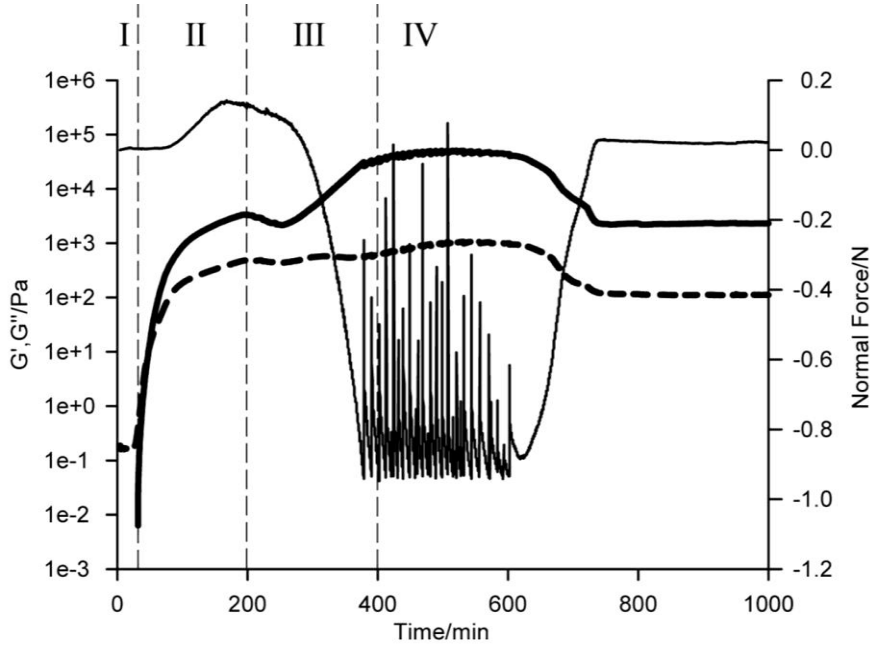

Figure 3-S14. Plot of the normal force (thin line) along with G' (thick solid line) and G" (dashed line) from Figure 3-1d. The roman numerals indicate the different phases of the gelation process.

The normal force increases slightly during Phase II, concomitant with the formation of a cross-linked network where G' > G", before decreasing sharply during Phase III. Towards the end of Phase III, the rheometer decreases the gap between the measurement plates in order to try and increase the normal force back to 0 N (Figure 3-1d); however, the continued contraction of the sample soon lowers the normal force once more leading to the jagged appearance of the plot. These same trends were apparent in the presence/absence of IPA, NH_4Cl and the pH indicators (data not shown). A decrease in normal force implies a contraction of the sample, as is known to occur during the cross-linking of various polymer systems.[9, 10]

3.3.15 Effect of the magnetic field during gelation on the final rheological properties of gels formed from 1.

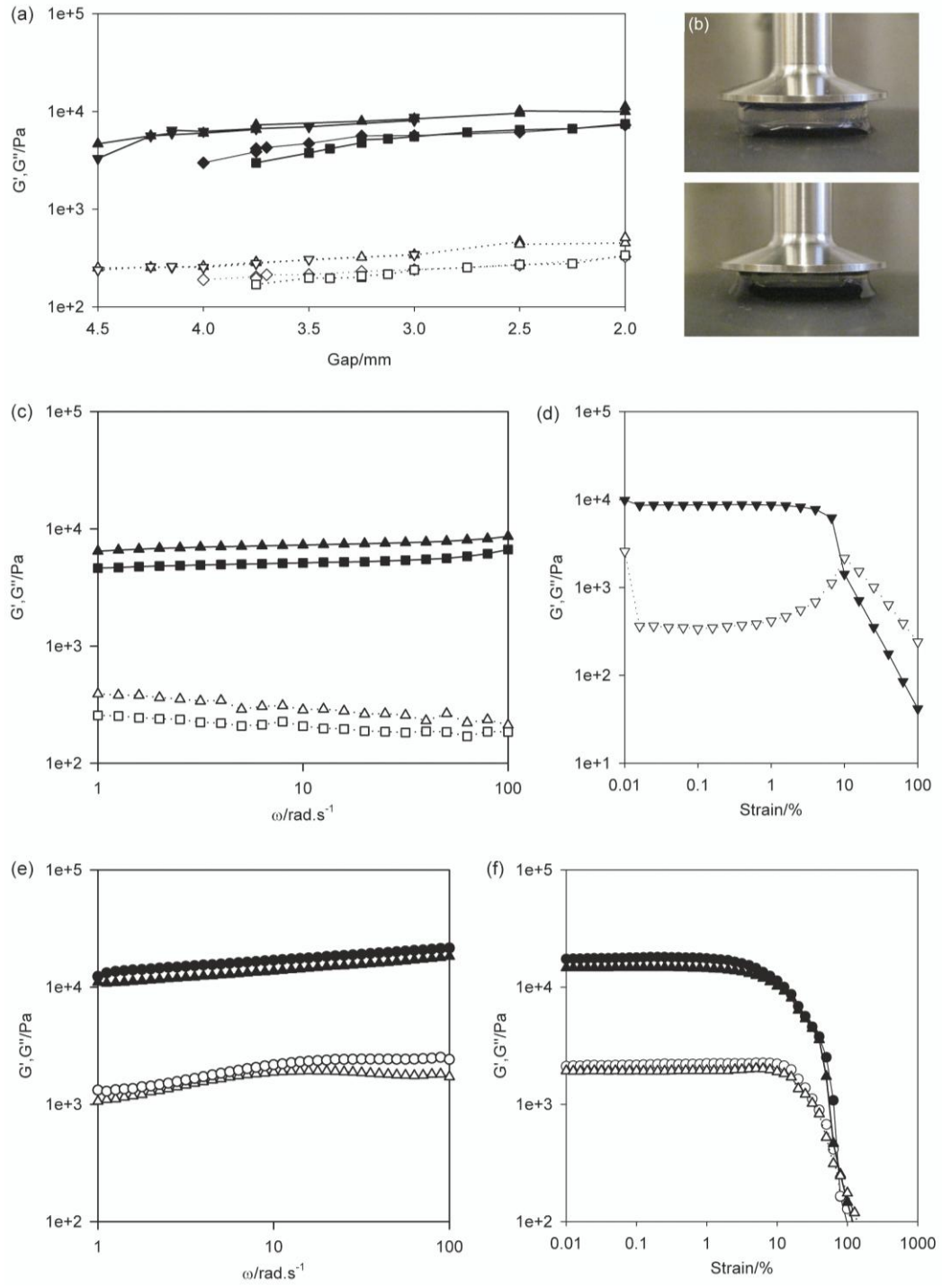

Figure 3-S15. Effect of the magnetic field during gelation on the final rheological properties of gels formed from **1**. A full description of this Figure is provided below.

Full description of Figure 3-S15: (a) Plots of G' (black) and G" (white), measured at an angular frequency of 10 rad/s and a strain of 0.1%, versus gap distance for samples prepared in (diamond and square) and away from (up and down triangle) the 9.4 T magnetic field of the NMR spectrometer. (b) Photographs of gel samples during measurements (up triangle, (a)) at 4.5 mm (top) and 3.5 mm (bottom) gaps. (c) Frequency sweeps at 0.1% strain for samples of (a), the symbols have the same meaning and refer to the same samples as (a). Data for the gel prepared away from the magnetic field (triangle) was recorded at a gap of 3.75 mm and data for the sample prepared in the field (square) was recorded at a gap of 3.25 mm. (d) Strain sweep, recorded at an angular frequency of 10 rad/s, of a gel prepared away from the magnetic field (down triangle, (a)) at a gap of 3 mm. (e) Plots of G’ (black) and G’’ (white) versus frequency, recorded at a strain of 0.1%, of gels prepared in (triangle) and away from (circle) the magnetic field of the NMR spectrometer in 4 mL Sterilin polystyrene vials. (f) Strain sweeps, recorded at an angular frequency of 10 rad/s, for the samples of (e).

The gels samples of Figures 3-S15a-d were prepared in 20 mL polypropylene syringes. The barrels were sawn down to provide a tube while the plungers had been sawn so that the syringes could be stood on their flanges and easily lowered into the NMR magnet (9.4 T) in a cradle. To analyse the gels, the plungers were gently pushed up out of the barrels and the gels slid onto glass slides before being transferred to the lower (silicon rubber) plate of the rheometer (Anton Paar Physica MCR101). The upper plate (25 mm, sandblasted) was then lowered while the gel was centred by eye. Once the plate was just in contact with the sample, a frequency sweep was recorded between 5 and 20 rad/s at 0.1% strain. The upper plate was then lowered and the frequency sweep repeated to produce the plots of Figure 3-S15a. At a gap of 2 mm, all gels were excessively squashed with very significant volumes of water exuded and so the rheological measurements most representative of the bulk gels are those recorded at intermediate gaps (Figure 3-S15c). From Figures 3-S15a-d, it is apparent that the gels prepared in the magnetic field of the spectrometer are slightly weaker than those prepared away from the field; however, they have broadly similar mechanical properties. Similar data was obtained when the gels were prepared in 4 mL Sterilin polystyrene sample vials and analysed with a vane and cup geometry (Figures 3-S15e-f). The vials had been roughened with sandpaper prior to

use and served as the holder for the gels during the measurements. Inspection of the gels after the strain sweeps revealed that the gels had fractured internally rather than at the walls of the vial. All the samples of Figure 3-S15 were prepared using the same mixture of **1** with GdL at ambient temperature (20-21 ^{o}C), with the other additives used for the NMR experiments also included. The development of a gel at this ambient temperature was found by NMR to be very similar to the development at 25 ^{o}C (Section 3.3.16), with very similar magnetic-field-induced anisotropy apparent. All rheological measurements were performed at 25^{o}C. The samples were analysed between 16 and 19 hours after preparation.

3.3.16 Monitoring gelation at ambient temperature

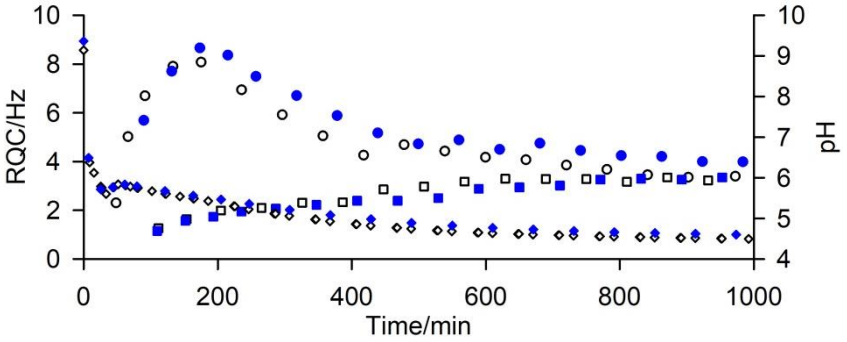

Figure 3-S16. Plot of $^{14}NH_4^+$ RQC (circle), IPA RQC (square) and pH (diamond) at 298 K (white) and 294 ± 0.5 K (blue).

The data at 298 K was collected on the same sample used for the NMR data in Section 3.3.10. The sample at 294 K was collected on an analogous sample but with the heater unit of the NMR spectrometer switched off. The experimental observables plotted in Figure 3-S16 are very similar at both temperatures.

3.3.17 Supporting Information: References

1. A. M. Brown, *Comput. Methods Programs Biomed.*, 2001, **65**, 191-200.
2. Z. Szakács, G. Hägele and R. Tyka, *Anal. Chim. Acta*, 2004, **522**, 247-258.
3. W. M. Haynes, ed., *CRC Handbook of Chemistry and Physics*, 95th edn., CRC Press, Boca Raton, FL, 2014.
4. P. C. Crofts and G. M. Kosolapoff, *J. Am. Chem. Soc.*, 1953, **75**, 3379-3383.
5. P. Trigo-Mouriño, C. Merle, M. R. M. Koos, B. Luy and R. R. Gil, *Chem. Eur. J.*, 2013, **19**, 7013-7019.
6. M. Liu, X. A. Mao, C. Ye, H. Huang, J. K. Nicholson and J. C. Lindon, *J. Magn. Reson.*, 1998, **132**, 125-129.
7. A. Pallagi, P. Sebk, P. Forgó, T. Jakusch, I. Pálinkó and P. Sipos, *Carbohydr. Res.*, 2010, **345**, 1856-1864.
8. R. J. W. Lambert, I. Mytilinaios, L. Maitland and A. M. Brown, *Comput. Methods Programs Biomed.*, 2012, **107**, 155-163.
9. L. Matějka, *Polym. Bull.*, 1991, **26**, 109-116.
10. M. Harsch, F. Herzog and J. Karger-Kocsis, *J. Compos. Mater.*, 2008, **42**, 2299-2309.

Chapter 4: Probing the Surface Chemistry of Self-Assembled Peptide Hydrogels using Solution-State NMR Spectroscopy

4.1 Introduction

In Chapter 3, RQCs were established as reliable observables to quantify the interaction of probe molecules and ions with self-assembled gel fibres. By employing two complementary probe species, it was possible to follow the decrease in charge and the increase in hydrophobicity of the gel fibres as the pH of a sample was gradually decreased. ^{23}Na relaxation measurements were also employed as a complementary technique to study the charge of the gel fibres. These concepts are greatly extended in this Chapter to study a range of contrasting hydrogel systems formed from structurally similar *N*-functionalised dipeptide LMWGs. A much broader range of probe species is introduced in order to allow a range of surface chemical properties to be analysed. Saturation-Transfer-Difference (STD) measurements are employed as a further technique to quantify the interaction of the probe species with the gel fibres. STD measurements are particularly useful in systems where the gel fibres are not arranged anisotropically and RQCs of the probe species are not observed. The NMR techniques presented in this Chapter are able to detect differences in the surface chemistry of the gels depending on the preparation method used. The observed surface chemical properties of the gel fibres can be linked to the mechanical properties, stabilities and drug-binding behaviours of the materials.

Section 4.2 comprises a paper, "Probing the Surface Chemistry of Self-Assembled Peptide Hydrogels using Solution-State NMR Spectroscopy", which was published in *Soft Matter* in 2017. In Section 4.3.1 it is demonstrated for the range of hydrogel systems studied that the presence of the probe molecules and spectrometer magnetic field during gelation do not affect the surface chemical or mechanical properties of the gels. Sections 4.3.1.4, 4.3.4.3 and 4.3.17 were not included in the original publication for reasons of space but are nevertheless included in this Thesis.

4.1.1 Author Contributions

The author contributions are as follows: MW conceived the concept of the paper, designed the experiments, prepared all the samples and performed all of the NMR experiments. MW also wrote the manuscript and ESI, aided by helpful suggestions from the other authors. JAI provided guidance with the NMR experiments. DJA synthesised all of the gelators and provided guidance throughout the project.

4.2 Probing the Surface Chemistry of Self-Assembled Peptide Hydrogels using Solution-State NMR Spectroscopy

Matthew Wallace,[a,*] Jonathan A. Iggo[a] and Dave J. Adams[a,b,*]

[a] *Department of Chemistry, University of Liverpool, Crown Street, Liverpool, L69 7ZD, U.K. Email: dave.adams@glasgow.ac.uk*

[b] *Current address: School of Chemistry, College of Science and Engineering, University of Glasgow, Glasgow, G12 8QQ, U.K.*

4.2.1 Abstract

The surface chemistry of self-assembled hydrogel fibres – their charge, hydrophobicity and ion-binding dynamics – is recognised to play an important role in determining how the gels develop as well as their suitability for different applications. However, to date there are no established methodologies for the study of this surface chemistry. Here, we demonstrate how solution-state NMR spectroscopy can be employed to measure the surface chemical properties of the fibres in a range of hydrogels formed from *N*-functionalised dipeptides, an effective and versatile class of gelator that has attracted much attention. By studying the interactions with the gel fibres of a diverse range of probe molecules and ions, we can simultaneously study a number of surface chemical properties of the NMR invisible fibres in an essentially non-invasive manner. Our results yield fresh insights into the materials. Most notably, gel fibres assembled using different triggering methods bear differing amounts of negative charge as a result of a partial deprotonation of the carboxylic acid groups of the gelators. We also demonstrate how chemical shift imaging (CSI) techniques can be applied to follow the formation of hydrogels along chemical gradients. We apply CSI to study the binding of Ca^{2+} and subsequent gelation of peptide assemblies at alkaline pH. Using metal ion-binding molecules as probes, we are able to detect the presence of bound Ca^{2+} ions on the surface of the gel fibres. We briefly explore how knowledge of the surface chemical properties of hydrogels could be used to inform their practical application in fields such as drug delivery and environmental remediation.

4.2.2 Introduction

Supramolecular hydrogels show great promise as new materials for a variety of applications including drug delivery and environmental remediation.[1-3] These hydrogels are formed upon the self-assembly in solution of small molecules (gelators) into fibres. The fibres subsequently interact with one another to form a sample-spanning network which immobilises the water by capillary forces.[4] It is important to understand the surface chemical properties of the gel fibres, including their charge, hydrophobicity/hydrophilicity and ion-binding dynamics. These properties determine not only how the gels form but also how other entities such as drug molecules or living cells interact with the gel matrices in practical applications.[5-10] Nevertheless, the range of analytical methodologies commonly applied to the study of these materials cannot directly provide any information on the surface chemistry of the fibres.[11] Inferences as to the surface chemistry that are based purely on the chemical structure of the gelators may be unreliable. For example, in many systems, dramatic shifts in the protonation constants of ionisable groups are known to occur upon assembly.[12-14] Methods to directly probe the surface chemical properties of the fibres are thus required. Although infra-red spectroscopy can provide insight in some cases,[10, 15] spectra are often crowded and it can be extremely challenging to unambiguously assign the vibrations of the surface-born functional groups.[16] Pioneering experimental investigations into the mobility of the gelators and solvent at the fibre-solution interface using techniques such as electron-spin paramagnetic resonance[17, 18] (EPR) or fast field cycling relaxometry[19] (FFC) have also been reported. However, these techniques require access to specialist equipment and, in the case of EPR, labelling of the gelators, which hinders the uptake of these techniques by the broader research community.

Solution-state NMR spectroscopy is commonly used to follow the formation of supramolecular hydrogels as it is a powerful, non-invasive and widely available technique.[11, 20] However, experimental attention is usually confined only to the mobile gelator present in solution rather than the gel networks themselves, which are usually NMR-silent.[21-23] As the molecules assemble, their resonances generally broaden,[21] decrease in intensity and may shift in

frequency,[24] thus yielding valuable insights into the molecular interactions responsible for self-assembly,[25-27] and the kinetics and thermodynamics of assembly.[13, 28]

An alternative approach is to focus not on the gelators/gel fibres themselves, but rather the mobile molecules and ions dissolved in the solvent phase of the gel that interact with the fibres.[22, 29-31] We recently presented a new solution-state NMR spectroscopic method to study the relative charge and hydrophobicity of self-assembled gel fibres (Chapter 3).[30] The relative affinities of different probe molecules and ions dissolved in the solvent phase of the gel for the fibres depends on the surface chemistry of those fibres. Thus, by measuring the residual quadrupolar couplings (RQCs) of two complementary probes, $^{14}NH_4^+$ (positive, hydrophilic) and isopropanol-d_8 (neutral, hydrophobic), we were able to gain new insights into the self-assembly process of a low molecular weight dipeptide gelator (**1**, Figure 4-1).[32, 33] In particular, we revealed for the first time that the gel fibres bear a significant negative charge throughout the gelation process. Here, we extend the concept outlined in that work and have developed a set of probes that includes cations, cation binders and neutral hydrophobic molecules. We apply the set to study a number of surface chemical properties across a diverse range of hydrogels formed from functionalised dipeptide gelators. By combining RQC and Saturation Transfer Difference (STD) measurements of our probe molecules, along with $^{23}Na^+$ T_1 and T_2 relaxation measurements, we can simultaneously study the charge and hydrophobicity of the fibres. We can also study the interaction with the fibres of metal ions and other species of interest.

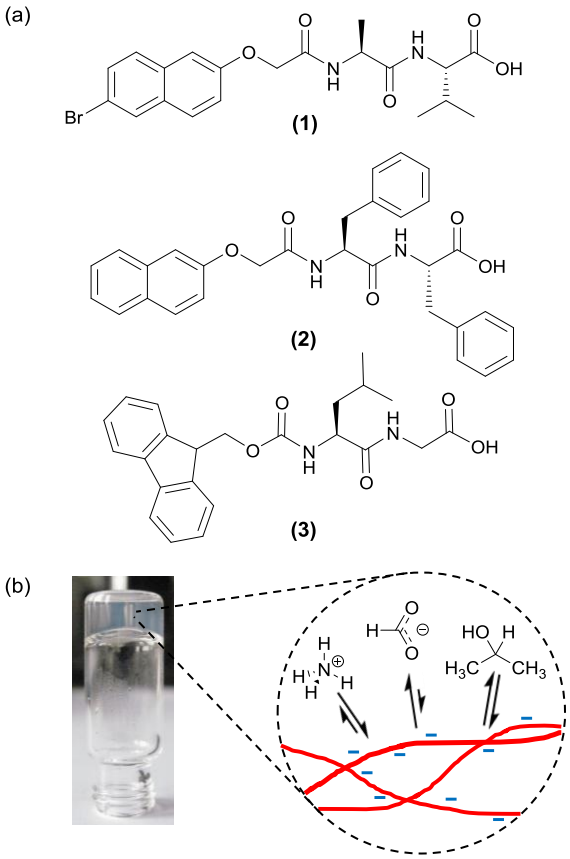

Figure 4-1. (a) Structure of the gelators used in this work. (b) Cartoon to illustrate the general concept of this work: Self-supporting hydrogels can be prepared from a variety of gelators and by a variety of methods. By studying the relative affinities of a set of probe molecules and ions for the surface of the gel fibres (red) we are able to measure the surface chemical properties.

N-functionalised dipeptides (see examples in Figure 4-1) are an effective and versatile class of gelator.[34-37] We and others have shown that some members of the class such as **1** dissolve to form free-flowing solutions when the pH of the solutions is raised above the pK_a of the carboxylic acid.[12, 38, 39] Highly reproducible gels can then be formed upon lowering the pH of the solution in a controlled manner *via* the hydrolysis of glucono-δ-lactone (GdL)[40] or anhydrides.[41] More hydrophobic gelators such as **2** are assembled at high pH into wormlike micelles, which convey significant viscosity to their solutions.[16, 42] The addition of salts such as $CaCl_2$ transforms these solutions into rigid gels, attributable to a 'cross-linking' of the wormlike structures by the divalent metal ions.[42] A third method to prepare gels involves dissolution of the gelators such as **3** in a water-miscible organic solvent, such as DMSO or

acetone, followed by dilution with water. The sudden reduction in solubility induces a rapid aggregation of the gelators followed by a gradual evolution of the system into a fibrous network.[43-46] Here, we demonstrate using our NMR techniques that the gels formed *via* these three methods possess different surface chemistries, despite the similar molecular structures of the gelators.

4.2.3 Results and Discussion

4.2.3.1 Methods

We have developed a set of probe molecules and ions (Table 4-1) to probe simultaneously a range of surface chemistries. The probes are chosen to either interact with the gel fibres or remain in the solvent phase of the gel depending on their class (Figure 4-1b). As far as possible, the probes do not bridge multiple classifications and do not significantly interfere or co-assemble with the gel fibres (Section 4.3.1). It is, however, sometimes desirable to exclude certain probes from the samples for experimental reasons (Section 4.2.5.2). In this work, we also use our *in-situ* method for pH determination using NMR spectroscopy which has been previously described (Chapter 3, Section 3.2.5.1).[30]

Classification	Probe (abbreviation)
Positive ions	$^{23}Na^+$, NH_4^+, $MeNH_3^+$
Hydrophobic	Isopropanol (IPA), tert-butanol (tBuOH), acetone, dioxane, dimethylsulfoxide (DMSO), methanol (MeOH)
Ion binders	formate, methylphosphonate (MPA), maleate
NMR pH indicators	formate, acetate, MPA , glycine, methanesulfonate

Table 4-1. Probe molecules used in this work along with their classifications. All probe molecules were included in the gels at a maximum concentration of 10 mM. Cations were included as the chloride salts; anions were included with $^{23}Na^+$ as the accompanying cation.

The suite of NMR techniques described here relies on the rapid exchange of the probe molecules/ions between the surface of the gel fibre and the solvent phase. When this condition applies, it can be shown that the magnitudes of RQCs, STDs and ^{23}Na T_1 and T_2 relaxation times are directly proportional to the fraction of probes bound to the fibres at any instant in time (Section 4.3.2). The principles and practices of these three techniques are discussed elsewhere. Briefly, RQCs manifest as splittings (Δ, Figure 4-2) of the NMR resonances of quadrupolar nuclei such as ^{2}H, ^{14}N or ^{23}Na due to the interaction of the probes with anisotropically arranged gel fibres.[30, 47, 48] The necessary anisotropy can be induced in many systems by preparing the gels in the strong magnetic field of an NMR spectrometer.[48, 49] In our systems, the presence of the magnetic field during gelation does not significantly affect the surface chemical or mechanical properties of the final hydrogels (Section 4.3.1.3). STD spectroscopy can be used to study ligand binding to a number of substrates including proteins,[50] gels[29, 51] and solid reaction supports.[52] The very broad ^{1}H resonances of the gel fibres are saturated by a train of selective RF pulses. This saturation is then transferred *via* intermolecular ^{1}H-^{1}H dipolar couplings to probe molecules that are interacting with the gel fibres and thus exhibit lower signal intensities in the ^{1}H NMR spectrum of the sample (Figure 4-2). The T_1 and T_2 relaxation times of $^{23}Na^{+}$ depend on the mobility of the Na^{+} ions in the sample.[53, 54] We and others have demonstrated that the assembly of free gelator molecules into negatively charged fibres results in a significant decrease in the mobility and relaxation times of $^{23}Na^{+}$ as the ions bind to the negatively charged structures formed.[30, 55, 56] A complication with ^{23}Na relaxation measurements is the inherently biexponential relaxation of this spin-3/2 nucleus. However, in our systems, $^{23}Na^{+}$ generally has a sufficient mobility for an effective monoexponential T_1 and T_2 to be determined (Sections 4.3.2.2 and 4.3.8). Although the absolute magnitude of an STD or RQC of a probe molecule depends upon its structure and binding geometry with the gel fibres, a molecule that interacts significantly with the gel fibres is likely to exhibit RQCs and/or STDs, whereas a non-interacting molecule will exhibit neither (Figure 4-2). By using our set of probe molecules and combining the three

measurements discussed above, we can build a reliable picture of the surface chemistry of our gels.

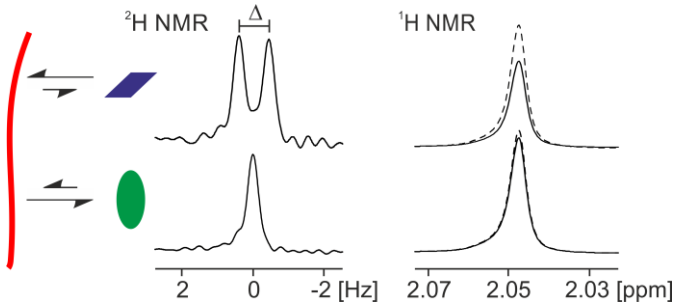

Figure 4-2. Cartoon to illustrate the use of RQC and STD measurements in this work. An interacting molecule (rhombus) will likely exhibit an RQC (Δ) on the resonance of its deuterium-labelled analogue. The ^{1}H signal intensity will also be lower when on-resonance saturation is applied to the gel fibres (solid) than without on-resonance saturation (dashed). A weakly interacting molecule (oval) will exhibit RQCs too small to be discerned while its ^{1}H resonance will not be significantly perturbed when on-resonance saturation is applied to the fibres.

4.2.3.2 Gelation *via* a pH switch

We begin by discussing gels formed upon the addition of GdL to a solution of **1** at pH 9 (referred to as **1**/GdL gels). A detailed analysis of the assembly process has previously been presented.[30, 32] Here, we briefly outline how our set of probes and combined RQC, STD and ^{23}Na relaxation measurements can yield fresh insight into the system.

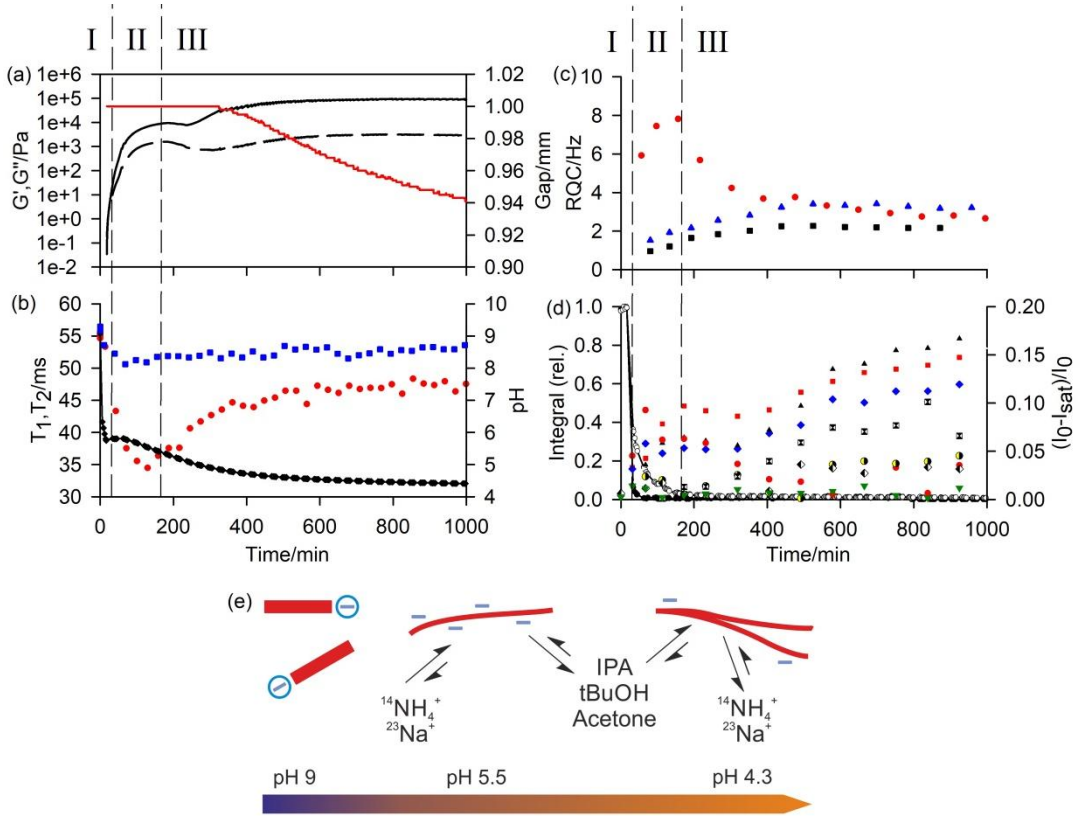

Figure 4-3. Plots of experimental observables during gelation of 1/GdL sample. Points at zero time correspond to a solution of **1** at pH 9 prior to the addition of GdL. (a) Plot of G' (black, solid line) and G" (dashed) along with the gap between the rheometer plates (red). (b) Plot of $^{23}Na^+$ T_1 (blue square) and T_2 (red circle) relaxation times along with pH (black diamond). The line is a guide to the eye. (c) Plot of $^{14}NH_4^+$ (red circle), IPA (blue triangle) and tBuOH (black square) RQCs. (d) Plots of ^1H integrals of **1**: valine methyl (white circle) and aromatic protons (black circle). The lines are a guide to the eye. Plot of STDs to probe molecules, expressed in terms of the differences in the ^1H signal intensities with (I_{sat}) and without (I_0) saturation applied to the gel fibres: IPA (blue diamond), acetone (black triangle), tBuOH (red square), $MeNH_3^+$ (red circle), DMSO (green down triangle), formate (half black circle), acetate (black and white square) and MeOH (black and white diamond). (e) Cartoon to illustrate the proposed assembly state of **1** during the gelation process along with the relative affinities of different probe molecules. As the pH falls, free gelator molecules (red rectangle) assemble into negatively charged fibres which subsequently lose charge while the mechanical properties of the sample increase.

The gel formation can be divided into three separate phases. In Phase I, the gelators have not yet assembled into fibres so no RQCs or STDs to the probe molecules are detectable (Figure 4-3c,d). The very slight STDs plotted are within the error of the integration (≤ 1%). We were unable to detect NOEs from **1** to the probe molecules at pH 9 in the absence of GdL, implying minimal interaction of the probes with the unassembled gelators.

Once the pH of the sample has fallen to the 'apparent' pK_a of **1**,[38] the gelators assemble into a network of fibres (Phase II). The ^{1}H integrals of the gelator resonances fall sharply as the mobile molecules assemble into large structures. The mechanical properties of the sample quickly develop into that of a gel, with G' exceeding G" by approximately one order of magnitude by the end of Phase II. The formation of anisotropic structures is readily apparent from the emergence of RQCs and STDs to the probe molecules and a decrease in the ^{23}Na T_1 and T_2 relaxation times as the probes interact with the newly formed gel fibres. The affinity of the positive probes, $^{23}Na^+$ and $^{14}NH_4^+$, for the fibres quickly rises to a maximum at the end of Phase II. In Phase III, the affinity falls sharply, as the pH falls and the amount of negative charge on the fibres is gradually reduced. The increased concentration of gluconate during the experiment due to the hydrolysis of GdL will not significantly affect the $^{14}NH_4^+$ RQCs or $^{23}Na^+$ T_1 and T_2 relaxation times due to the low binding affinity of gluconate for these ions.[57, 58]

In contrast to the positive probes, the affinity for the fibres of the neutral hydrophobic probes, IPA, tBuOH, acetone and dioxane, gradually increase during Phase II and Phase III, attributable to an increase in the hydrophobicity as the network develops. This assertion is supported by molecular dynamics simulations of other systems which demonstrate a clear preference of these organic solvents for hydrophobic surfaces.[59, 60] We attribute the absence of an observable RQC for dioxane and acetone to their binding geometry and molecular structures (Section 4.3.2.1);[61] the observation of STDs confirms a significant interaction of the molecules with the fibres. Dioxane STDs are not plotted in Figure 4-3 due to spectral overlap with GdL although significant STDs are nevertheless discernible (Section 4.3.3).

The gradual, although never complete,[30] removal of charge from the fibres leads to an increase in the bulk mechanical properties of the gel, and is accompanied by a contraction of the gel (syneresis). Syneresis is readily apparent from the rheological measurements (Figure 4-3a) as the sample pulls down on the upper plate of the rheometer causing the instrument to decrease the gap between the measuring plates in order to maintain a constant normal force.[62, 63] The syneresis is accompanied by a reduction in the magnitudes of the RQCs indicating a decrease in the anisotropy of the fibres on contraction of the gel. However, the magnitudes of the STDs to the hydrophobic solvents, which do not depend on the anisotropy of the fibres, continue to rise. This indicates an increased hydrophobicity of the syneresed network (Section 4.3.2.4). The decrease in negative charge and increased hydrophobicity of the fibres is observed with all gelators studied, although syneresis is observed to different extents (Section 4.3.4). As discussed in our recent work, syneresis is a consequence of both the molecular structure of the gelator and the self-assembly process followed.[64]

More polar or negatively charged molecules like DMSO, MPA, MeOH, formate or gluconate (Section 4.3.3) do not show strong STDs, which is readily explained by these probes having weaker interactions with the negatively charged gel fibres. Acetate, being 75% protonated at pH 4.3, shows stronger STDs than formate possibly due to a hydrogen bonding interaction with the fibres. None of deutero-MeOH, DMSO, acetate or formate show discernible RQCs in **1**/GdL gels. $MeNH_3^+$ does not show strong STDs in 1/GdL gels, even when competing positive ions are excluded (Section 4.3.1.1). However, strong STDs are observed in other gel systems (Section 4.2.3.4 and 4.3.9), perhaps due to a more favourable binding geometry for saturation transfer from the gel fibres. The interaction between $MeNH_3^+$ and the gel fibres does not have to be direct and could be mediated by water molecules.[65]

The principles that govern the interaction of our probe molecules with **1**/GdL gels can be extended to a range of larger model drug compounds (Figure 4-4). The positively charged and hydrophobic **D1** interacts strongly with the negatively charged gel fibres in **1**/GdL gels (Figure 4-4b), resulting in very large STDs and a significantly reduced magnitude of the $^{14}NH_4^+$ RQC due to a

preferential binding of **D1** (Section 4.3.5.1). Separate resonances with different multiplicities are also observed for **D1** in the gel (upfield, broad) and in the fluid exuded during syneresis (downfield, sharp), again consistent with **D1** having a strong interaction with the fibres.[22, 66] In contrast, the negatively charged **D2** and **D3** exhibit weak STDs, sharp peaks and slight changes in chemical shift (0.001 ppm or less) due to the presence of the gel. Similar chemical shift changes can be observed for the organic solvents used as probe molecules (Section 4.3.5.2). The anionic **D2** and **D3** thus interact only weakly with the gel fibres compared to **D1**.

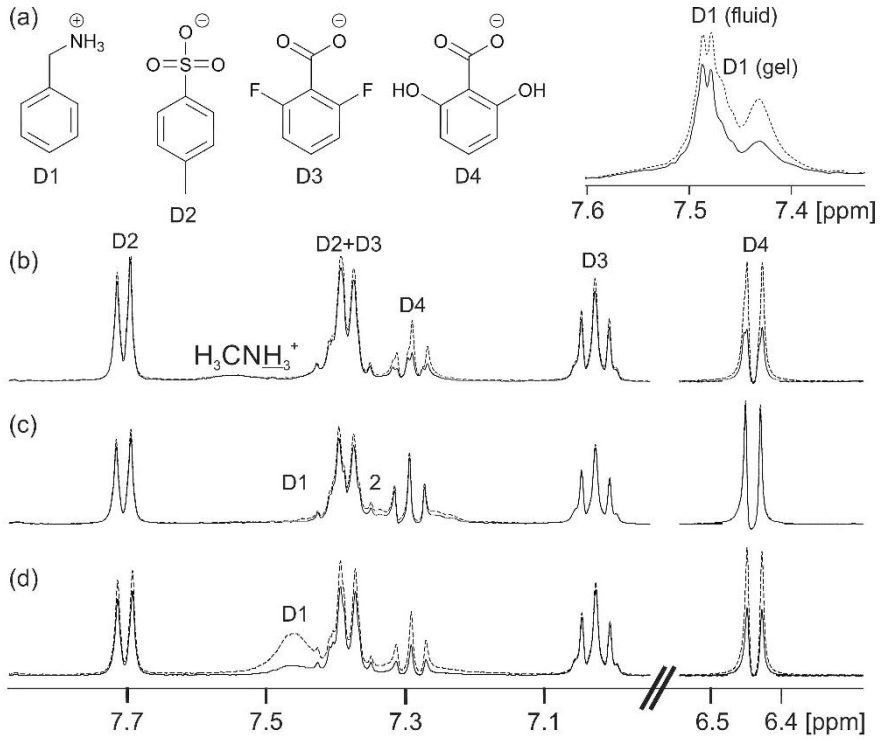

Figure 4-4. (a) Structures of model drug compounds. (b-d) NMR spectra of model drug compounds in hydrogels recorded with (solid) and without (dashed) on resonance presaturation applied to the gel fibres: (b) **1**/GdL hydrogel containing **D2**-**D4** and (inset top) hydrogel containing **D1** and NH_4Cl. (c) 4 mg/mL solution of **2** at pH 9 containing **D1**-**D4**. (d) Sample of (c) upon addition of 30 mM $CaCl_2$.

The negatively charged **D4** interacts more strongly with the gel fibres than either **D2** or **D3**, exhibiting large STDs and an upfield shift of 0.004 ppm. The stronger interaction of **D4** with the fibres is attributable to hydrogen-bonding interactions involving the hydroxyl groups.[66-68] Nevertheless, the peaks of **D4** remain sharp in the gel phase while the change in chemical shift is very much

smaller than that observed for **D1**. **D1** thus shows by far the strongest interactions with the gel fibres, as would be expected on an electrostatic basis, although other non-covalent interactions also influence the interaction of these molecules with the fibres.

4.2.3.3 Salt-triggered gelation

We now discuss the gels formed upon the addition of $CaCl_2$ to 4 mg/mL solutions of **2** at pH 9, referred to hereafter as **2**/$CaCl_2$ gels. The wormlike micellar structures present in solutions of **2** at pH 9 in the absence of Ca^{2+} bear a much greater negative charge than **1**/GdL gels and thus much larger $^{23}Na^+$ RQCs[30] and much shorter $^{23}Na^+$ T_1 and T_2 relaxation times are observed (*vide infra*). The cationic **D1** shows a much stronger interaction with the structures present than in **1**/GdL gels and is completely invisible by ^1H NMR spectroscopy (Figure 4-4c). The negatively charged compounds all exhibit much weaker interactions. The addition of $CaCl_2$ (Figure 4-4d) weakens the interaction of **D1** with the structures of **2** and broad NMR peaks become apparent, while enhanced STDs are observed for the other compounds. These results suggest a decrease in the effective negative charge of the structures of **2** upon the addition of $CaCl_2$. Similar STD effects are observed when **D1**-**D4** are diffused into a **2**/$CaCl_2$ gel after it has been formed, indicating that the presence of these molecules does not fundamentally change the gelation process (Section 4.3.5.3).

We now discuss in detail the interactions taking place upon the addition of $CaCl_2$ and subsequent gelation of solutions of **2**. In the original reports on the **2**/$CaCl_2$ system, gelation was ascribed to a 'cross-linking' of the wormlike structures of **2** by the Ca^{2+}, mediated by Ca^{2+}-carboxylate bridges.[42, 69] Detailed analysis with a range of analytical techniques confirms that only minimal changes to the molecular packing of the assemblies of **2** take place upon the addition of Ca^{2+}, consistent with this hypothesis.[16] However, while some reports on related systems also invoke the existence of specific interactions between the ions and the gelators,[10, 70-72] other reports have discussed gelation in terms of the 'salting-in/salting-out' effect of different ions according to the Hofmeister series[73-75] or in terms of charge-screening

effects.[76-78] The precise role of the metal cations in promoting gelation thus remains unclear. Here, we demonstrate using our NMR methods that a strong interaction exists between the Ca^{2+} and the fibres of **2** upon gelation, providing firm evidence for the cross-linking hypothesis.

The gels are formed by placing a small volume of concentrated $CaCl_2$ solution on top of a solution of the gelator. Diffusion of the $CaCl_2$ throughout the sample forms a gel. Gelation occurs essentially instantaneously upon contact between the gelator and the Ca^{2+} solution and so gel formation *must* be studied along a concentration gradient of the Ca^{2+}. This is possible using chemical shift imaging (CSI) techniques in which spatially resolved NMR spectra are recorded along the length of the sample (Figure 4-5a).[79-81] Plots of the RQCs of the various probe molecules along the Ca^{2+} concentration gradient are shown in Figure 4-5b. Additional plots at earlier and later stages of the experiment are presented in Section 4.3.6.

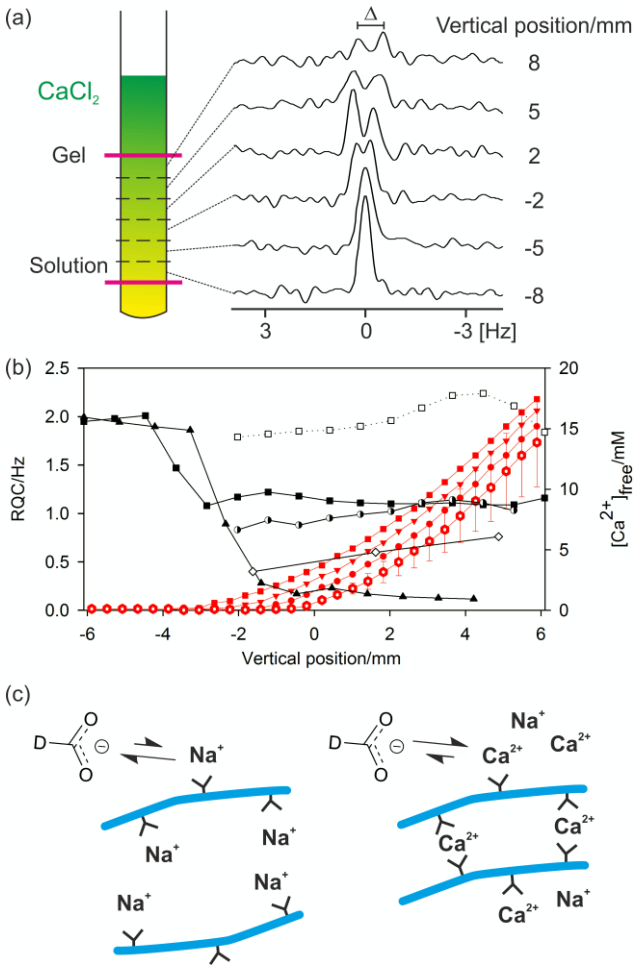

Figure 4-5. (a) Cartoon to illustrate the principle of chemical shift imaging (CSI): Spatially resolved NMR spectra are recorded from slices along the length of a Ca^{2+} gradient. The pink lines represent the NMR-active region of the sample, centred 18 mm from the base of the NMR tube. ^{2}H spectra of formate-d are illustrated as an example. (b) Plots of experimental observables along the length of the NMR sample. RQCs: $^{23}Na^{+}$ (black triangle), formate-d (white diamond), HDO (black square), dioxane (white square) and tBuOH (half-black circle). $^{23}Na^{+}$ RQC has been scaled down by a factor of 500. Only resolvable RQCs are plotted. RQCs were recorded in separate images and hence at different $[Ca^{2+}]_{free}$ profiles. Red: Profiles of $[Ca^{2+}]_{free}$ before all images (hollow hexagon) – error bars indicate uncertainty in $[Ca^{2+}]_{free}$ measurements – after ^{23}Na image (circle), after formate-d image (down triangle) and after ^{2}H HDO, tBuOH and dioxane image (square). The lines are to guide the eye. The vertical position of a data point corresponds to the centre of the slice while the separation between the points corresponds to the slice width. (c) Cartoon to illustrate the proposed surface chemistry of the fibres (blue) in the absence (left) and presence (right) of Ca^{2+} and the interaction of the formate-d ions with the associated metal ions. Carboxylate groups of **2** are shown as black Y shapes.

The concentration of free Ca^{2+} ions in solution can be determined from the ^{1}H chemical shift of maleate (Section 4.3.7) and is also plotted. In the absence of Ca^{2+}, a very large RQC for $^{23}Na^{+}$ is observed of 1 kHz. As the Ca^{2+} diffuses down the tube, the $^{23}Na^{+}$ RQC falls precipitately as the Na^{+} is displaced from the assemblies of **2** by the Ca^{2+}. Displacement of Na^{+} is further confirmed by ^{23}Na relaxation measurements. The T_1 relaxation time of $^{23}Na^{+}$ increases from 41±1 ms in the absence of Ca^{2+} to 54±1 ms in the final gel. Spatially resolved ^{23}Na relaxation measurements demonstrate how the T_2 relaxation transforms from biexponential and fast in the absence of Ca^{2+} to slow and monoexponential when an excess of Ca^{2+} is present (Section 4.3.8, Figure 4-S8b). However, the Na^{+} ions are never completely displaced and remain in competition with the Ca^{2+}; the relaxation behaviour of $^{23}Na^{+}$ in the final gels is very different to that in an analogous solution in the absence of **2** while the $^{23}Na^{+}$ RQC never completely vanishes to zero (Section 4.3.8). Similar effects are observed when methylammonium chloride is included as a probe (Section 4.3.9). Methylammonium was excluded from **2**/$CaCl_2$ gel samples as standard, owing to its very strong interaction with the structures of **2** in the absence of Ca^{2+}.

Formate, maleate and MPA^{2-} all have appreciable binding constants to Ca^{2+} and so can be used to probe the presence of the bound divalent ion.[57, 82, 83] Concomitant with the decrease in the $^{23}Na^{+}$ RQC is the emergence of an RQC of the formate-d ions. The observation of RQCs to formate in **2**/$CaCl_2$ gels, but not in acid-triggered gels (Section 4.3.4), indicates the presence of bound Ca^{2+} ions on the surface of the fibres with which the negatively charged formate ions can interact (Figure 4-5c). Residual dipolar couplings (RDCs) are also observed on the ^{1}H resonances of MPA^{2-} and maleate (Section 4.3.10) which can be similarly attributed. We note that RDCs are becoming increasingly important in the structural and conformational analysis of biomolecules.[84] Dipeptide hydrogels may thus prove to be valuable and hitherto unexplored media for their measurement. Similar surface chemical properties are observed when $MgCl_2$ is added to a solution of **2** at pH 9 in place of $CaCl_2$, although a significant syneresis of the gels occurs (Section 4.3.17).

Towards the top of the sample, the $^{23}Na^{+}$ and formate-d RQCs approach steady values while the concentration of free Ca^{2+} ions in solution rises steeply. These observations indicate that the gel fibres in the upper part of the sample are essentially saturated with Ca^{2+}; further additions of Ca^{2+} have no further effect on either the anisotropy of the fibres or their surface chemical properties (Section 4.3.6). Accordingly, the mechanical properties of the gels are largely invariant when between 1 and 10 equivalents of Ca^{2+} to peptide are added, with significant decreases in the mechanical properties only observed at very high (> 0.1 M) Ca^{2+} concentrations.[42]

It can also be seen in Figure 4-5b that the $^{23}Na^{+}$ RQC decreases and an RQC of formate-d and dioxane-d_8 appear before a significant concentration of free Ca^{2+} is apparent in solution. These observations suggest a strong initial interaction between the structures of **2** and the Ca^{2+}. In an attempt to further probe the dynamics of the Ca^{2+} ions, we turned to ^{43}Ca NMR.[85, 86] No ^{43}Ca resonances are apparent in the final gels whereas a sharp resonance is observed in an analogous 20 mM solution of $CaCl_2$. The 'free' Ca^{2+} ions thus spend a significant fraction of their time (> 1%) associated with the gel fibres (Section 4.3.11). Experiments at higher spatial resolution, but with twice the concentration of ^{2}H probes, demonstrate that the formate-d RQC becomes observable after that of dioxane-d_8 (Section 4.3.1.2, Figure 4-S1f). A slight excess of Ca^{2+} is thus required in order to sufficiently decrease the effective negative charge of the fibres for the anionic formate to interact and exhibit an RQC.

In contrast to GdL and acid-triggered gels (Section 4.3.4), no significant STDs are observed to any of the probe molecules in **2**/$CaCl_2$ gels. However, that RQCs and RDCs are observed indicates that the interaction of the probe molecules with the fibres differs from those in the GdL and acid-triggered gels. For example, the bound Ca^{2+} may hinder the intimate contact between the molecule and the protons of the gel fibre required for an STD.[87] In contrast, RQCs and RDCs arise as a result of the restricted motions of the molecules when interacting with the gel fibres so do not require intimate contact in order to be observed (Section 4.3.2). The increase in the RQCs to the organic solvents upon the addition of $CaCl_2$ would seem to imply an increase in the

hydrophobicity of the structures. However, interpretation of the results is considerably complicated by the potential 'salting-out' effect of the $CaCl_2$ on the organic solvents and a detailed interpretation of the results is beyond the scope of the present study.[88] The decrease in the RQC of HDO is likely due to a change in the orientation of the bound water molecules upon coordination of Ca^{2+}.[47] RQCs of acetone and MeOH can also be observed but are not shown on Figure 4-5 for brevity (Section 4.3.6).

The 'free' Ca^{2+} can diffuse out of the gel into an external NaCl solution at pH 9 (Figure 4-6). The gel remained intact during this process; no swelling or erosion of the gels was observed over the entire experiment (Section 4.3.12) while the RQCs of HDO and dioxane, which are sensitive to both the structure and anisotropy of the gel fibres as well as the surface chemical properties, also remain constant. However, a slight decrease of the formate-d RQC is apparent along with a slight increase of the $^{23}Na^{+}$ RQC (Section 4.3.13) indicating that the bound Ca^{2+} ions are partially exchanged for Na^{+}. Such behaviour of the gels could be of considerable interest for environmental remediation or sensing applications. For example, the gel could be placed in a much larger volume of water whereupon other species of interest could diffuse in, the excess of Ca^{2+} providing additional stability.[1]

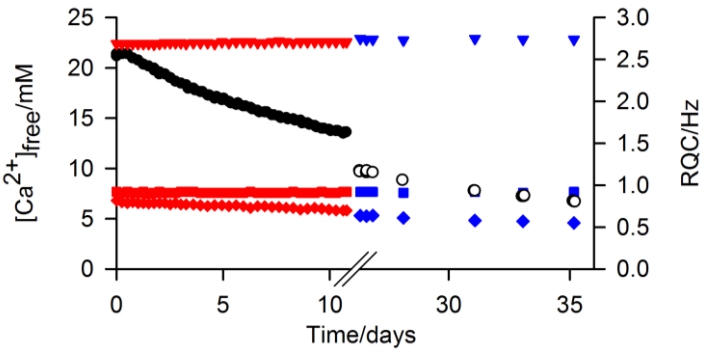

Figure 4-6. Plots of $[Ca^{2+}]_{free}$ (circle) in **2**/$CaCl_2$ gel versus time after an NaCl solution was placed on top of the sample. After the first solution (black) had stood on top of the gel for 26 days, the supernatant solution was removed, fresh solution placed on top and the second series of measurements (white) commenced. The RQCs of HDO (square), dioxane (down triangle) and formate (diamond) are plotted for the first (red) and second (blue) series of measurements.

4.2.3.4 Gelation *via* a solvent-switch

Finally, we discuss gels formed upon the addition of H_2O to solutions of **3** in DMSO, referred to hereafter as **3**/DMSO gels. A gel prepared by the addition of MilliQ water to **3** in DMSO was found to have a pH of 3.9, in agreement with measurements on related systems,[44, 89] implying that the gel fibres have an appreciable acidity. When sodium formate (7 mM), sodium methanesulfonate (2 mM) and methylammonium chloride (2 mM) were included as probes in the water along with neutral organic solvents, a self-supporting gel was formed with a pH of 4.5. Analysis of the STDs observed for this sample (Figure 4-7) imply that the gel fibres bear a negative charge; a strong STD is observed to the positively charged methylammonium ions while negligible STDs are observed to the negative methanesulfonate and formate ions. Weak STDs are observed to the organic solvents. Furthermore, the resonance of the formate ions is shifted upfield due to protonation by an amount equivalent to inclusion of 2.4±0.2 mM HCl in the absence of **3**. It can thus be calculated that 20±2% of the gelators are deprotonated (Section 4.3.14). Reductions in the ^{23}Na T_1 and T_2 relaxation times from 36±2 and 35±2 ms in an analogous solution in the absence of **3** to 31±2 and 19±2 ms in the gel are observed, again consistent with the fibres carrying negative charge. Less than 5% of **3** is visible in the gels by ^{1}H NMR and we can thus be confident that the negative charge resides on the self-assembled structures rather than on unassembled gelator molecules (Section 4.3.15). We are thus able to introduce negative charge onto the fibres by a judicious choice of additives in the H_2O solution.

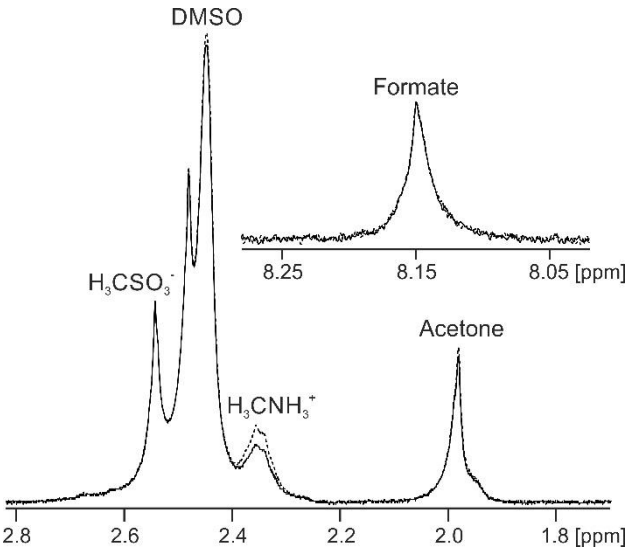

Figure 4-7. NMR spectra of probe molecules in **3**/DMSO gel with (solid) and without (dashed) on resonance pre-saturation applied to the gel fibres. The downfield and upfield resonances of acetone and DMSO correspond to the totally protonated (H_6) and partially deuterated (HD_5) molecules respectively.

The acidic nature of the fibres in **3**/DMSO gels, as well as in analogous gels formed from related dipeptides, is further supported by previous reports concerning the effect of basic additives on the materials.[46, 89, 90] Working with the related gelator, FmocFF, Raeburn *et al*.[89] reported that the mechanical properties of gels formed upon the addition of buffer solutions to DMSO solutions of the gelator depended on the pH of the buffer used, with strong gels formed only at acidic pH. Elsewhere, Orbach *et al*.[90] reported that gels formed from other related Fmoc-capped peptides were unstable when exposed to buffer solutions above pH 6.5. The weakly acidic nature of the gel fibres is of significance were the gels to be used in cell culturing or drug delivery applications where weakly basic organic compounds would likely be present.[45, 46 90]

No RQCs were detected in these gels for any of the probes indicating that the fibres in **3**/DMSO gels do not possess a significant degree of alignment with respect to the magnetic field (Section 4.3.4.1). The observation of STDs to the organic solvents and reduced $^{23}Na^+$ T_1 and T_2 relaxation times confirms the interaction of these species with the fibres. RQCs are observed, however, in gels of **3** triggered by the addition of GdL to a solution of the gelator at high

pH. We attribute this observation to differences in the assembly mechanisms of the two methods.[33, 43]

4.2.3.5 Summary of Methods

RQC, STD and ^{23}Na relaxation measurements have been presented as complementary techniques to study the interaction of a range of probe molecules and ions with the gel fibres. We now summarise a general strategy for their use. In all systems presented here, ^{23}Na relaxation measurements are a useful tool to study the interaction of Na^+ with the self-assembled gel fibres. The interaction of Na^+ with the negatively charged gel fibres increases the rate of its NMR relaxation. $^{23}Na^+$ relaxation measurements do not require the gels to be aligned in the spectrometer field and can, in principle, be performed on the background Na^+ in a sample without the need for probes. RQCs are only observed when a stringent set of conditions applies: Firstly, the probe must interact significantly with the gel fibres. Secondly, the gel fibres must possess a degree of alignment relative to the magnetic field of the spectrometer. Thirdly, the probe must possess a favourable structure and interact in a suitable orientation with the gel fibres (Section 4.3.2.1). Nevertheless, when observable, RQCs are very sensitive to the surface chemistry of the gels (Figure 4-3b, Figure 4-5). STDs are also sensitive to the surface chemistry of the fibres but do not require them to be aligned. The sensitivity of RQCs to the anisotropy of the fibres, but not STDs, is apparent by comparing the RQCs and STDs to IPA and tBuOH in **1**/GdL gels (Figure 4-3 and Section 4.3.2.4). However, qualitatively, RQCs and STDs to the same probe molecule convey the same information; an increase in hydrophobicity with time (Figure 4-3 and Section 4.3.4.2) or a loss of negative charge from the fibres (Section 4.3.9).

To summarise, when studying the interaction of a set of probe molecules with self-assembled gels, it is advisable to use two or more complementary NMR methods. The choice of method depends upon the probes used and the system under study.[22, 64] The absolute size of an STD or RQC should not be used alone to judge the affinity of a probe molecule for the gel fibres. Finally, we note that in very heterogeneous systems possessing cationic, anionic and hydrophobic sites, a significant interaction with the gel fibres may be detected

for all our probes. In such systems, it may be fruitful to study how these interactions change as the sample conditions such as the pH are changed. We have demonstrated how this may be achieved using chemical shift imaging (CSI) methods (Figure 4-5 and Section 4.3.4.2).

4.2.4 Conclusions

We have presented a general analytical approach by which the surface chemical properties of the gel fibres in a range of hydrogel systems can be studied using only standard solution-state NMR equipment. We applied our techniques to study the similarities and differences in the surface properties of hydrogels formed from *N*-functionalised dipeptides *via* different preparation methods. By combining STD and RQC measurements of a range of positive ions and hydrophobic probe molecules, along with $^{23}Na^{+}$ relaxation measurements, we have shown that all fibres bear at least a slight negative charge due to deprotonation of the terminal carboxylic acid groups. As a result, cations exhibit much stronger interactions with the gel fibres than similar anions. Particularly strong interactions are observed with the benzylammonium ion (**D1**) which is both cationic and hydrophobic. With gels triggered by the addition of H_2O to solutions of the gelators in DMSO, additional negative charge was introduced onto the fibres by the inclusion of the weakly basic formate.

By studying cation-binding probes such as formate or methylphosphonate, we are able to detect the presence of bound Ca^{2+} ions on the surface of the gel fibres formed from a hydrophobic dipeptide gelator at alkaline pH. Our methods reveal that the binding of Ca^{2+} to the gel fibres is very strong, consistent with a Ca^{2+} mediated cross-linking mechanism of gelation. It is also apparent that the gels can be pre-loaded with an excess of Ca^{2+} without affecting their integrity. Together, these properties convey a high stability to the gels when exposed to an external Ca^{2+}-free solution at alkaline pH. Our methods may thus be of considerable use in the development of gel systems for the controlled entrapment or release of metal ions and other species of interest. Overall, we anticipate that our methods will be adopted wherever the surface chemical properties of self-assembled hydrogels are of interest.

4.2.5 Experimental

4.2.5.1 Materials

Gelators **1**, **2** and **3** were synthesised as described previously.[38, 40] All other chemicals were purchased from Sigma-Aldrich and used as received.

4.2.5.2 Preparation of samples

All samples were prepared in H_2O to allow for analysis by ^2H NMR. Unless otherwise stated, **1**/GdL and **2**/$CaCl_2$ gels were transferred to the NMR spectrometer (9.4 T) within 3 minutes of preparation of the pre-gel mixtures/solutions and allowed to gel in the magnetic field for at least 14 hours. For the **3**/DMSO gels, it was not feasible to transfer the samples to the spectrometer before gelation commenced (< 1 minute). A stock solution of the NMR pH indicators was prepared containing sodium formate (0.4 M), glycine (0.2 M), methylphosphonic acid (0.2 M), sodium acetate (0.2 M), sodium methanesulfonate (0.1 M) and sodium hydroxide (0.6 M). Stock solutions of the organic solvents were prepared at 5 vol% (^2H) or 2 vol% (^1H) of each solvent. Methanol-d_3 was included at 2 vol% to avoid excessive truncation artefacts from this resonance in ^2H NMR experiments. $MeNH_3Cl$ (0.4 M) was also included in the ^1H solvent mixture while sodium formate-d (0.5 M) was included in the ^2H mixture. Stock solutions of NH_4Cl and disodium maleate were prepared at 0.5 M and 0.2 M respectively.

4.2.5.2.1 1/GdL gels

A stock solution of **1** was prepared by dispersing the solid dipeptide in H_2O and adding 1.2±0.1 equivalents of standardised NaOH (1 M) and stirring for at least six hours to form a clear solution. Probe molecules were then added to obtain a final concentration of **1** of 5 mg/mL. The stock solutions of **1** thus prepared were used within 7 days of preparation. The standard set of probe molecules (Figure 4-3) comprised NH_4Cl (10 mM), $MeNH_3Cl$ (2 mM), pH indicators (1 mM with respect to sodium acetate), sodium formate-d (5 mM) and all of the organic solvents listed in Table 4-1 at 0.05 vol% (^2H, 0.02 vol% MeOH-d_3) and 0.01 vol% (^1H). Use of stock solutions of probe molecules ensured that the dilution of the gelator solutions was minimal. To prepare gels,

700 μL of solution with probe molecules at pH 9 was added to a pre-weighed quantity of GdL (5 mg/mL) and swirled gently (< 30 s) to fully dissolve the GdL. The sample was then transferred to a 5 mm NMR tube for analysis. The data shown on Figure 4-4 for **D1** in **1**/GdL gels was collected in the presence of the full set of probe molecules used for **1**/GdL gels while the data for **D2-D4** was collected in the absence of NH_4^+ and **D1** to avoid spectral overlap with the NH protons of these molecules. Each of **D1-D4** was included in the gels at 5 mM concentration. The spectra shown in Figure 4-4 were collected on a **1**/GdL sample 900 minutes after the addition of GdL.

4.2.5.2.2 2/$CaCl_2$ gels

Solid **2** was dispersed in H_2O and NaOH added to 6.5±0.5 mM. NMR pH indicator (2 mM with respect to sodium acetate) was then added and the mixture stirred overnight (at least 18 hours) resulting in a clear solution. Disodium maleate (1 mM), NaCl (10 mM) and sodium formate-d (5 mM) were then added. The organic solvents, with the exception of IPA, were included at 0.05 vol% (^{2}H, 0.02 vol% MeOH-d_3) and 0.01 vol% (^{1}H). IPA was excluded due to the low sensitivity of the methanetriyl resonance in ^{2}H CSI experiments and the partial overlap of the ^{1}H methyl resonance with that of MPA. The final solutions contained 4 mg/mL of **2** and were at a pH of 9.0-9.5. After preparation, 560 μL aliquots of the solutions were transferred to 5 mm NMR tubes and aged for between 5 and 14 days at 21-24 ºC. To prepare gels, $CaCl_2$ solution (25 μL, 0.7 M) was added to the top of the gelator solution in the NMR tube *via* a long needle. The samples were then immediately transferred to the NMR instrument for analysis where they were held for two days before being transferred to a water bath at 298 K. The final properties of the gels, where mentioned, were recorded at least two weeks after the addition of $CaCl_2$, the samples remaining stable for at least seven months. $MeNH_3Cl$ and NH_4Cl were excluded from these samples due to their very strong interaction with **2** at pH 9 in the absence of $CaCl_2$ (Section 4.3.9).

To collect the data of Figure 4-6, a **2**/$CaCl_2$ gel was prepared and aged for two weeks. A solution containing 20 mM NaCl and the other probe molecules was prepared and the pH adjusted to 8.9-9.2 with the addition of 1-2 mM HCl.

1800 μL of solution was then carefully placed on top of the gel. The sample was maintained at 298 K in either an NMR spectrometer or a water bath. Periodically, the solution was removed, analysed and a fresh solution placed on top. For Figure 4-4, 5 mM each of **D1**-**D4** were included in a 4 mg/mL solution of **2** at pH 9.2 (Figure 4-4c). $CaCl_2$ was then added to the solution and the sample aged for two weeks before the spectra of Figure 4-4d were recorded.

4.2.5.2.3 3/DMSO gels

Stock solutions of **3** at 25 mg/mL concentration were prepared in DMSO-d_6. A H_2O solution of the probe molecules was prepared as to contain the following concentrations when mixed 4:1 with the DMSO solution of **3**: sodium formate (2 mM), sodium formate-d (5 mM), sodium methanesulfonate (2 mM), methylammonium chloride (2 mM), and all of the ^1H and ^2H solvents listed in Table 4-1 at 0.05 and 0.01 vol% respectively. Methanol-d_3 was included at 0.02 vol%. The pH indicator probes, MPA^{2-}, glycinate and acetate, were excluded as they do not function in 20% DMSO/80% H_2O mixtures. These probes cause additional deprotonation of the gelators (Section 4.3.15, Figure 4-S15b) and do not convey any further information on the system. To prepare gels, a 9" glass pipette was placed in a 5 mm NMR tube and 140 μL of the solution of **3** in DMSO was placed in the pipette and allowed to settle at the base of the tube. 560 μL of the H_2O solution was then rinsed down the pipette. Upon mixing of the two solutions, the sample immediately became turbid and white whereupon the pipette was withdrawn and the sample transferred to the spectrometer for analysis. The samples resolved into clear gels after standing for less than a minute. The NMR-observable properties of **3**/DMSO samples were found to be stable, once measured, within twenty minutes of gel preparation. The NMR resonances on Figure 4-7 are broad due to the formation of air bubbles in the gel on standing. Figure 4-7 was recorded 20 minutes after preparation.

4.2.5.3 NMR measurements

All NMR experiments were performed on a Bruker Avance II 400 MHz wide bore spectrometer operating at 400.20 MHz for ^1H. The temperature of the

samples was maintained at 298±0.5 K, the variation in the temperature being less than 0.1 K. ^{1}H integrals (Figure 4-3d) were recorded in a single scan with presaturation (50 Hz power) applied to the H_2O resonance for 5 s followed by a spoil gradient pulse (27 G/cm, 1 ms) prior to a $\pi/2$ hard pulse and signal acquisition. 65536 data points were acquired with a sweep width of 15 ppm, giving a total acquisition time of 35 s including a 25 s delay at the start of the experiment prior to any pulses. DMSO was used as the reference for integration. The STD effects to the gelator resonances arising from presaturation of the H_2O resonance were not significant (Section 4.3.16). Integrals have been normalised to their values before the addition of GdL. Essentially all (> 90%) of a theoretical 5 mg/mL of **1** was visible in the solution at pH 9 when integrated against an internal standard. Very accurate quantification by NMR is extremely challenging in H_2O;[91] presaturation can affect the gelator resonances by saturation-transfer effects from the H_2O while WATERGATE sequences give distorted lineshapes due to J-modulation. Very similar integrals are observed when D_2O is used instead of H_2O.[92] Methanesulfonate was used as a chemical shift reference for ^{1}H NMR in all samples; 2.815 ppm in H_2O and 2.53 ppm in 20%DMSO/80% H_2O.

^{1}H STD experiments were performed using the double-echo WATERGATE sequence of Liu *et al.*[93] (Bruker library ZGGPW5) with presaturation applied for 8 s during the relaxation delay (8.1 s) and with a 2 s signal acquisition time. The delay between successive hard pulses in the selective pulse train was set at 250 μs corresponding to a 4000 Hz separation between the null points. Presaturation was applied using a train of 157 Gaussian pulses of 50 ms in duration and separated by 1 ms. The peak pulse power was 380 Hz. Saturation was applied at -5 ppm (on resonance) or -250 ppm (off resonance). On and off resonance spectra were acquired in alternate scans to minimise the effect of any change in the sample over the time-course of the STD acquisition. The spectra of Figures 4-3 and 4-7 were acquired using 16 dummy scans prior to signal acquisition (8 scans on and off resonance) in order to attain steady-state conditions, giving a total acquisition time of 5 minutes 20 s. Omitting these dummy scans resulted in very slight (≤ 3%) apparent STDs, even in the absence of a gel phase, owing to the first off-resonance scan being acquired

before the first on-resonance. Measurement of the STDs as a function of presaturation time confirmed that a point measurement at 8 s presaturation provides an adequate indication of the strength of the probe-fibre interaction (Section 4.3.2.3). Very similar STDs were observed in **1**/GdL gels using our standard protocol and when a very long (40 s) relaxation delay was elapsed to allow complete relaxation to thermal equilibrium between scans (Section 4.3.2.3, Figure 4-S2c). The spectra of Figure 4-4 were acquired with no dummy scans in order for STD build up curves to be constructed. The omission of dummy scans gave a very slight relaxation artefact of $\leq 1\%$ for **D1**-**D3** and $\leq 2\%$ for **D4**. All spectra on Figure 4-4 were processed with an exponential line broadening factor of 1 Hz. On Figure 4-3, STDs and RQCs were recorded on the same sample while ^{1}H integrals, $^{23}Na^{+}$ relaxation times and the pH were recorded on a separate sample. As in our previous work,[30] the pH and kinetics of gel formation are highly reproducible and so the datasets are directly comparable.

^{2}H spectra were recorded *via* the lock channel with 4422 data points, a 200 μs pulse (70^{o}) and a sweep width of 12 ppm. Between 256 and 1024 scans were acquired in 12 to 46 minutes respectively, depending on the magnitude of the IPA RQC and the extent of syneresis of **1**/GdL samples. $^{14}N\{^{1}H\}$ spectra were acquired with the aring sequence ($\pi/2$-τ-$\pi/2$-τ-$\pi/2$-acquire) in order to supress acoustic ringing effects in our probe. A 46 μs $\pi/2$ pulse was used with a τ of 4 μs and a relaxation time of 0.1 s. CPD was applied (Waltz 16) during the pulses and signal acquisition in order to remove the effect of ^{14}N-^{1}H coupling. Spectra were acquired with 578 data points and a sweep width of 10 ppm in either 256 or 1024 scans depending on the magnitude of the $^{14}NH_4^{+}$ RQC. The time plotted for ^{2}H and ^{14}N spectra corresponds to the time halfway through the acquisition.

^{23}Na T_1 and T_2 were measured using the inversion-recovery and CPMG pulse sequences respectively. For T_1, the inversion recovery time, t, was varied between 1 and 300 ms in 8 steps. For T_2, the spacing between the π pulses was fixed at 1 ms and the number of pulses varied between 2 and 256 in 8 steps. 32 scans were performed with 6144 points, a 100 ppm sweep width and a

relaxation delay of 0.1 s, giving acquisition times of 2 minutes for both T_1 and T_2 measurements. No de-gassing of samples was attempted prior to relaxation measurements owing to the insignificant effect of oxygen on the relaxation of ^{23}Na, the dominant relaxation mechanism of this nucleus being the quadrupolar mechanism. The ^{23}Na T_1 of 10 mM NaCl in H_2O was measured as 59±1 ms after preparation and 60±1 ms after de-gassing with argon.

CSI experiments were performed using the gradient phase encoding sequence of Trigo-Mouriño *et al*.[79] ($\pi/2$-τ_1-g-τ_2-acquire) where g is a gradient pulse and τ_1 and τ_2 are delays of 10 and 200 μs respectively. g was a minimum of 100 μs in duration and was varied between a maximum of -50 and 50 G/cm, depending on the nucleus and the number of gradient steps acquired. ^2H CSI experiments were acquired with either 8 gradient steps and 128 scans (formate-d) or 32 steps and 32 scans (other probes). 3684 points were acquired with a sweep width of 12 ppm. The theoretical spatial resolution was 0.81 mm for 32 step images or 3.3 mm for 8 step images. For ^{23}Na, the sequence was modified to include a solid-echo ($\pi/2$-τ-$\pi/2$-τ_1-g-τ_2-acquire) to refocus the evolution of the quadrupolar coupling during the gradient pulse and delays. 32 steps were acquired with 256 scans and 2118 points. The theoretical spatial resolution was 0.94 mm. All ^2H and ^{23}Na CSI experiments were 45 minutes in duration. For ^1H, the $\pi/2$ pulse was replaced with a double-echo WATERGATE sequence to supress the H_2O resonance. A spoil gradient (27 G/cm) was also employed at the end of the signal acquisition period (1 s) to destroy any transverse magnetisation. 64 steps were acquired with 8 scans giving a total acquisition time of 10 minutes and a theoretical spatial resolution of 0.41 mm.

4.2.5.4 Data processing

All NMR data was processed in Bruker Topspin 3.2. $^{23}Na^+$ and ^2H RQCs were obtained by Lorentzian deconvolution of the spectra while $^{14}NH_4^+$ RQCs were obtained by peak picking between the peak maxima. pH values were extracted from ^1H spectra following the procedure described in our previous work.[30] $[Ca^{2+}]_{free}$ values were obtained from the chemical shift of maleate using the procedure described in Section 4.3.7. CSI images were processed and phase

corrected following the procedure of Trigo-Mouriño *et al.*[79] Beyond ±7 mm from the sample centre, the sensitivity of the CSI spectra falls markedly as the limits of the NMR coils are exceeded. Data is thus only plotted to ±6 mm on Figure 4-5. $^{23}Na^{+}$ T_1 and T_2 values were extracted by fitting the data to Equations 4.1 and 4.2 respectively using a non-linear regression method developed for Microsoft Excel:[94]

$$I = I_0\left[1 - P.exp\left(-{}^{t}/_{T_1}\right)\right] \quad (4.1)$$

$$I = I_0 exp\left(-{}^{t}/_{T_2}\right) \quad (4.2)$$

where I_0 is a constant and P ≈ 1.9. A discussion of $^{23}Na^{+}$ relaxation measurements is provided in the Section 4.3.2.2. T_1 and T_2 are quoted as the average obtained from four repeat experiments on the same sample, with uncertainties quoted as ± half the difference between the maximum and minimum values. For all measurements, the time plotted corresponds to the centre of the NMR acquisition.

4.2.5.4 Rheology

The time series of Figure 4-3 was recorded on an Anton Paar Physica MCR301 Rheometer. A solution of **1** with the standard set of probes was mixed with 5 mg/mL GdL and 2 mLs transferred to the stationary (silicon rubber) lower plate whereupon the upper plate (50 mm, sandblasted) was lowered onto the sample to a gap of 1 mm. Low viscosity mineral oil was placed around the edge of the sample to prevent drying artefacts. G' and G" were recorded at a frequency of 10 rad/s and 0.5 % strain, a data point being recorded every 15 s for 15 hours. The gap between the measuring plates was adjusted automatically in order to maintain a constant normal force on the upper measuring plate. The temperature of the sample was maintained at 25 ^{o}C.

4.2.6 Acknowledgements

We thank Unilever for a Case Award (MW) and the EPSRC for funding a DTA (MW). We thank the EPSRC for funding (EP/C005643/1 and EP/K039687/1). DA thanks the EPSRC for a Fellowship (EP/L021978/1).

4.2.7 References

1. B. O. Okesola and D. K. Smith, *Chem. Soc. Rev.*, 2016, **45**, 4226-4251.
2. X. Du, J. Zhou, J. Shi and B. Xu, *Chem. Rev.*, 2015, **115**, 13165-13307.
3. R. G. Weiss, *J. Am. Chem. Soc.*, 2014, **136**, 7519-7530.
4. N. Zweep and J. H. van Esch, in *Functional Molecular Gels*, eds. B. Escuder and J. F. Miravet, The Royal Society of Chemistry, 2014, pp. 1-29.
5. S. Boothroyd, A. F. Miller and A. Saiani, *Faraday Discuss.*, 2013, **166**, 195-207.
6. D. Roberts, C. Rochas, A. Saiani and A. F. Miller, *Langmuir*, 2012, **28**, 16196-16206.
7. K. Nagy-Smith, Y. Yamada and J. P. Schneider, *J. Mater. Chem. B*, 2016, **4**, 1999-2007.
8. C. J. Newcomb, S. Sur, J. H. Ortony, O. S. Lee, J. B. Matson, J. Boekhoven, J. M. Yu, G. C. Schatz and S. I. Stupp, *Nat. Commun.*, 2014, **5**, 3321.
9. V. Jayawarna, S. M. Richardson, A. R. Hirst, N. W. Hodson, A. Saiani, J. E. Gough and R. V. Ulijn, *Acta Biomaterialia*, 2009, **5**, 934-943.
10. Enateri V. Alakpa, V. Jayawarna, A. Lampel, Karl V. Burgess, Christopher C. West, Sanne C. J. Bakker, S. Roy, N. Javid, S. Fleming, Dimitris A. Lamprou, J. Yang, A. Miller, Andrew J. Urquhart, Pim W. J. M. Frederix, Neil T. Hunt, B. Péault, Rein V. Ulijn and Matthew J. Dalby, *Chem*, **1**, 298-319.
11. G. Yu, X. Yan, C. Han and F. Huang, *Chem. Soc. Rev.*, 2013, **42**, 6697-6722.
12. C. Tang, R. V. Ulijn and A. Saiani, *Langmuir*, 2011, **27**, 14438-14449.
13. M. Tena-Solsona, B. Escuder and J. F. Miravet, *Chem. Mater.*, 2015, **27**, 3358-3365.
14. C. Tang, A. M. Smith, R. F. Collins, R. V. Ulijn and A. Saiani, *Langmuir*, 2009, **25**, 9447-9453.
15. S. L. Zhou, S. Matsumoto, H. D. Tian, H. Yamane, A. Ojida, S. Kiyonaka and I. Hamachi, *Chem. Eur. J.*, 2005, **11**, 1130-1136.
16. A. Z. Cardoso, L. L. E. Mears, B. N. Cattoz, P. C. Griffiths, R. Schweins and D. J. Adams, *Soft Matter*, 2016, **12**, 3612-3621.
17. A. Caragheorgheopol, W. Edwards, J. G. Hardy, D. K. Smith and V. Chechik, *Langmuir*, 2014, **30**, 9210-9218.

18. J. H. Ortony, C. J. Newcomb, J. B. Matson, L. C. Palmer, P. E. Doan, B. M. Hoffman and S. I. Stupp, *Nat. Mater.*, 2014, **13**, 812-816.
19. J. Tritt-Goc, A. Rachocki and M. Bielejewski, *Soft Matter*, 2014, **10**, 7810-7818.
20. V. J. Nebot and D. K. Smith, in *Functional Molecular Gels*, eds. B. Escuder and J. F. Miravet, The Royal Society of Chemistry, 2014, pp. 30-66.
21. D. C. Duncan and D. G. Whitten, *Langmuir*, 2000, **16**, 6445-6452.
22. B. Escuder, M. Llusar and J. F. Miravet, *J. Org. Chem.*, 2006, **71**, 7747-7752.
23. S. Bouguet-Bonnet, M. Yemloul and D. Canet, *J. Am. Chem. Soc.*, 2012, **134**, 10621-10627.
24. A. Reddy, A. Sharma and A. Srivastava, *Chem. Eur. J.*, 2012, **18**, 7575-7581.
25. F. Piana, D. H. Case, S. M. Ramalhete, G. Pileio, M. Facciotti, G. M. Day, Y. Z. Khimyak, J. Angulo, R. C. D. Brown and P. A. Gale, *Soft Matter*, 2016, **12**, 4034-4043.
26. Nonappa, D. Šaman and E. Kolehmainen, *Magn. Reson. Chem.*, 2015, **53**, 256-260.
27. M. Suzuki, M. Yumoto, M. Kimura, H. Shirai and K. Hanabusa, *Chem. Eur. J.*, 2003, **9**, 348-354.
28. C. A. Angulo-Pachon, C. Gasco-Catalan, J. J. Ojeda-Flores and J. F. Miravet, *ChemPhysChem*, 2016, **17**, 2008-2012.
29. M. D. Segarra-Maset, B. Escuder and J. F. Miravet, *Chem. Eur. J.*, 2015, **21**, 13925-13929.
30. M. Wallace, J. A. Iggo and D. J. Adams, *Soft Matter*, 2015, **11**, 7739-7747.
31. M. Wallace, D. J. Adams and J. A. Iggo, *Soft Matter*, 2013, **9**, 5483-5491.
32. L. Chen, K. Morris, A. Laybourn, D. Elias, M. R. Hicks, A. Rodger, L. Serpell and D. J. Adams, *Langmuir*, 2010, **26**, 5232-5242.
33. A. Z. Cardoso, A. E. Alvarez Alvarez, B. N. Cattoz, P. C. Griffiths, S. M. King, W. J. Frith and D. J. Adams, *Faraday Discuss.*, 2013, **166**, 101-116.
34. W. J. Frith, *Philos. Trans. R. Soc. A Math. Phys. Eng. Sci.*, 2016, **374**.
35. D. J. Adams and P. D. Topham, *Soft Matter*, 2010, **6**, 3707-3721.
36. S. Awhida, E. R. Draper, T. O. McDonald and D. J. Adams, *J. Colloid Interface Sci.*, 2015, **455**, 24-31.
37. N. Singh, M. Kumar, J. F. Miravet, R. V. Ulijn and B. Escuder, *Chem. Eur. J.*, 2017, **23**, 981–993.

38. L. Chen, S. Revel, K. Morris, L. C. Serpell and D. J. Adams, *Langmuir*, 2010, **26**, 13466-13471.
39. Z. Yang, G. Liang, M. Ma, Y. Gao and B. Xu, *J. Mater. Chem.*, 2007, **17**, 850-854.
40. D. J. Adams, M. F. Butler, W. J. Frith, M. Kirkland, L. Mullen and P. Sanderson, *Soft Matter*, 2009, **5**, 1856-1862.
41. E. R. Draper, L. L. E. Mears, A. M. Castilla, S. M. King, T. O. McDonald, R. Akhtar and D. J. Adams, *RSC Adv.*, 2015, **5**, 95369-95378.
42. L. Chen, G. Pont, K. Morris, G. Lotze, A. Squires, L. C. Serpell and D. J. Adams, *Chem. Commun.*, 2011, **47**, 12071-12073.
43. L. Chen, J. Raeburn, S. Sutton, D. G. Spiller, J. Williams, J. S. Sharp, P. C. Griffiths, R. K. Heenan, S. M. King, A. Paul, S. Furzeland, D. Atkins and D. J. Adams, *Soft Matter*, 2011, **7**, 9721-9727.
44. J. Raeburn, C. Mendoza-Cuenca, B. N. Cattoz, M. A. Little, A. E. Terry, A. Zamith Cardoso, P. C. Griffiths and D. J. Adams, *Soft Matter*, 2015, **11**, 927-935.
45. A. Mahler, M. Reches, M. Rechter, S. Cohen and E. Gazit, *Adv Mater*, 2006, **18**, 1365-1370.
46. T. Liebmann, S. Rydholm, V. Akpe and H. Brismar, *BMC Biotechnol.*, 2007, **7**.
47. A. Delville, J. Grandjean and P. Laszlo, *J. Phys. Chem.*, 1991, **95**, 1383-1392.
48. M. Wallace, A. Z. Cardoso, W. J. Frith, J. A. Iggo and D. J. Adams, *Chem. Eur. J.*, 2014, **20**, 16484-16487.
49. I. O. Shklyarevskiy, P. Jonkheijm, P. C. M. Christianen, A. P. H. J. Schenning, A. Del Guerzo, J. P. Desvergne, E. W. Meijer and J. C. Maan, *Langmuir*, 2005, **21**, 2108-2112.
50. O. Cala, F. Guillière and I. Krimm, *Anal. Bioanal. Chem.*, 2014, **406**, 943-956.
51. V. Lozano, R. Hernandez, A. Arda, J. Jimenez-Barbero, C. Mijangos and M.-J. Perez-Perez, *J. Mater. Chem.*, 2011, **21**, 8862-8870.
52. C. Cruz, E. J. Cabrita and J. A. Queiroz, *J. Chromatogr. A*, 2011, **1218**, 3559-3564.
53. D. E. Woessner, *Concepts Magn. Reson.*, 2001, **13**, 294-325.

54. H. Maki, K. Yoshida, H. Nariai and M. Mizuhata, *Colloids Surf. A Physicochem. Eng. Asp.*, 2015, **471**, 1-10.
55. E. R. Draper, J. R. Lee, M. Wallace, F. Jäckel, A. J. Cowan and D. J. Adams, *Chem. Sci.*, 2016, **7**, 6499-6505.
56. M. Raue, A. Bernet, M. Kuppers, S. Stapf, H. W. Schmidt, B. Blumich and T. Mang, in *Intelligent Hydrogels*, eds. G. Sadowski and W. Richtering, Springer International Publishing, 2013, vol. 140, pp. 45-51.
57. P. G. Daniele, C. Foti, A. Gianguzza, E. Prenesti and S. Sammartano, *Coord. Chem. Rev.*, 2008, **252**, 1093-1107.
58. H. A. Tajmir-Riahi and J. T. Agbebavi, *Carbohydr. Res.*, 1993, **241**, 25-35.
59. M. Khabiri, B. Minofar, J. Brezovský, J. Damborský and R. Ettrich, *J. Mol. Model.*, 2013, **19**, 4701-4711.
60. Z. W. Dai, L. S. Wan, X. J. Huang, J. Ling and Z. K. Xu, *J. Phys. Chem. C*, 2011, **115**, 22415-22421.
61. J. P. Jacobsen and K. Schaumburg, *J. Magn. Reson.*, 1977, **28**, 191-201.
62. L. Matějka, *Polymer Bulletin*, 1991, **26**, 109-116.
63. M. Harsch, F. Herzog and J. Karger-Kocsis, *J. Compos. Mater.*, 2008, **42**, 2299-2309.
64. A. M. Castilla, M. Wallace, L. L. E. Mears, E. R. Draper, J. Doutch, S. Rogers and D. J. Adams, *Soft Matter*, 2016, **12**, 7848-7854.
65. J. Kříž and J. Dybal, *J. Phys. Chem. B*, 2004, **108**, 9306-9314.
66. J. A. Sáez, B. Escuder and J. F. Miravet, *Chem. Commun.*, 2010, **46**, 7996-7998.
67. M. Goto, H. Hayashi, I. Miyahara, K. Hirotsu, M. Yoshida and T. Oikawa, *J. Biol. Chem.*, 2006, **281**, 34365-34373.
68. B. Escuder, J. F. Miravet and J. A. Sáez, *Org. Biomol. Chem.*, 2008, **6**, 4378-4383.
69. L. Chen, T. O. McDonald and D. J. Adams, *RSC Adv.*, 2013, **3**, 8714-8720.
70. L. Wang, J. Mei, X. Zhang, M. Zhu, J. Wang and L. Wang, *RSC Adv.*, 2014, **4**, 1193-1196.
71. M. A. Greenfield, J. R. Hoffman, M. O. De La Cruz and S. I. Stupp, *Langmuir*, 2010, **26**, 3641-3647.
72. J. Shi, Y. Gao, Y. Zhang, Y. Pan and B. Xu, *Langmuir*, 2011, **27**, 14425-14431.

73. S. Roy, N. Javid, P. W. J. M. Frederix, D. A. Lamprou, A. J. Urquhart, N. T. Hunt, P. J. Halling and R. V. Ulijn, *Chem. Eur. J.*, 2012, **18**, 11723-11731.
74. V. J. Nebot, J. J. Ojeda-Flores, J. Smets, S. Fernández-Prieto, B. Escuder and J. F. Miravet, *Chem. Eur. J.*, 2014, **20**, 14465-14472.
75. M. Jaspers, A. E. Rowan and P. H. J. Kouwer, *Adv. Funct. Mater.*, 2015, **25**, 6503-6510.
76. Y. Feng, M. Taraban and Y. B. Yu, *Soft Matter*, 2012, **8**, 11723-11731.
77. T. Otsuka, T. Maeda and A. Hotta, *J. Phys. Chem. B*, 2014, **118**, 11537-11545.
78. B. Ozbas, J. Kretsinger, K. Rajagopal, J. P. Schneider and D. J. Pochan, *Macromolecules*, 2004, **37**, 7331-7337.
79. P. Trigo-Mouriño, C. Merle, M. R. M. Koos, B. Luy and R. R. Gil, *Chem. Eur. J.*, 2013, **19**, 7013-7019.
80. Å. Östlund, D. Bernin, L. Nordstierna and M. Nydén, *J. Colloid Interface Sci.*, 2010, **344**, 238-240.
81. Y. Mitrev, S. Simova and D. Jeannerat, *Chem. Commun.*, 2016, **52**, 5418-5420.
82. G. H. Nancollas, *J. Chem. Soc.*, 1956, 735-743.
83. M. DeFronzo and R. J. Gillies, *J. Biol. Chem.*, 1987, **262**, 11032-11037.
84. S. K. Mishra and N. Suryaprakash, *Nucl. Magn. Reson.*, 2015, **44**, 547-591.
85. E. Bouhoutsos-Brown, D. Murk Rose and R. G. Bryant, *J. Inorg. Nucl. Chem.*, 1981, **43**, 2247-2248.
86. J. M. Aramini, T. Drakenberg, T. Hiraoki, Y. Ke, K. Nitta and H. J. Vogel, *Biochemistry*, 1992, **31**, 6761-6768.
87. N. Rama Krishna and V. Jayalakshmi, *Prog. Nucl. Magn. Reson. Spectrosc.*, 2006, **49**, 1-25.
88. Y. Koga, H. Katayanagi, J. V. Davies, H. Kato, K. Nishikawa and P. Westh, *Bull. Chem. Soc. Jpn.*, 2006, **79**, 1347-1354.
89. J. Raeburn, G. Pont, L. Chen, Y. Cesbron, R. Lévy and D. J. Adams, *Soft Matter*, 2012, **8**, 1168-1174.
90. R. Orbach, L. Adler-Abramovich, S. Zigerson, I. Mironi-Harpaz, D. Seliktar and E. Gazit, *Biomacromolecules*, 2009, **10**, 2646-2651.
91. P. Giraudeau, V. Silvestre and S. Akoka, *Metabolomics*, 2015, **11**, 1041-1055.

92. K. L. Morris, L. Chen, J. Raeburn, O. R. Sellick, P. Cotanda, A. Paul, P. C. Griffiths, S. M. King, R. K. O'Reilly, L. C. Serpell and D. J. Adams, *Nat. Commun.*, 2013, **4**.

93. M. Liu, X. A. Mao, C. Ye, H. Huang, J. K. Nicholson and J. C. Lindon, *J. Magn. Reson.*, 1998, **132**, 125-129.

94. A. M. Brown, *Comput. Methods Programs Biomed.*, 2001, **65**, 191-200.

4.3 Supporting Information

4.3.1 Effect of added probe molecules/ions on gelation

As in our previous work (Chapter 3, Section 3.3.4),[1] we assess the effect of our probe molecules and ions on the gelation process by systematically excluding certain probes and observing those that remain. If the RQCs, STDs and ^{23}Na relaxation times follow the same pattern in the absence of a probe then we can be confident that the probe does not significantly affect the formation of the gel; the surface chemistry, kinetics of gel formation and anisotropy of the fibres with respect to the spectrometer magnetic field are the same in its presence/absence.

4.3.1.1 Effect of added probe molecules on the formation of 1/GdL gels

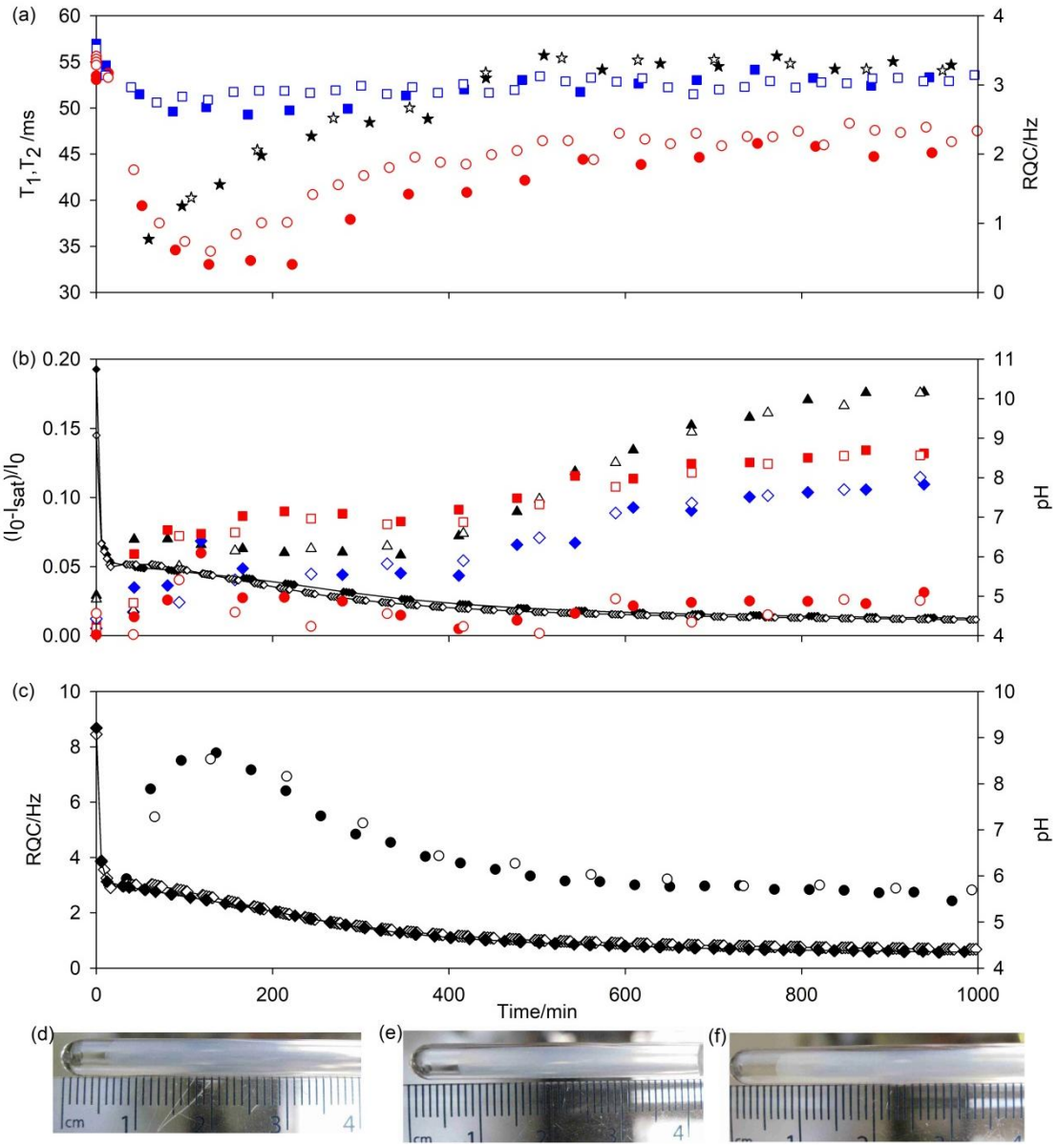

Figure 4-S1a. Plots of experimental observables during formation of **1**/GdL hydrogels containing all (hollow) or part (solid) of the standard set of probe molecules. (a) Plot of ^{23}Na T_1 (blue square), T_2 (red circle) and IPA RQC (black star). Solid shapes correspond to sample containing no NH_4Cl, sodium formate-d or ^2H organic solvents other than IPA. (b) Plots of STDs to acetone (black triangle), IPA (blue diamond), tBuOH (red square) and $MeNH_3^+$ (red circle). The pH (black diamond) is also plotted. The lines are a guide to the eye. Solid shapes correspond to the same sample as (a). (c) Plot of $^{14}NH_4^+$ RQC (circle) and pH (diamond). Solid shapes correspond to sample containing 10 mM NH_4Cl and no organic solvents, $MeNH_3Cl$ or formate-d. Photographs of gel samples containing the full set of probes (d), 10 mM NH_4Cl and no ^2H organic solvents, formate-d or $MeNH_3Cl$ (e) and no NH_4Cl, formate-d or ^2H organic solvents other than IPA (f).

In the absence of NH_4Cl, sodium formate-d or ^2H solvents other than IPA, the RQCs (a) and STDs (b) of the remaining probe molecules follow the same profiles as in their presence, implying a near identical surface chemistry and gelation kinetics. The apparent lack of competition between IPA and the other solvents for the fibres implies that these probes interact only weakly with the fibres, with the majority of surface binding sites being unoccupied. The slight difference in the profiles of the ^{23}Na T_2 relaxation time (a) can be ascribed to competition between NH_4^+ and Na^+ for the negative charge of the fibres. A more dramatic competition effect is observed on the $^{14}NH_4^+$ RQCs when 5 mM benzylammonium (**D1**) is included in addition to NH_4Cl (Section 4.3.5.1) or on the $^{23}Na^+$ T_1 relaxation time in solutions of **2** in the complete absence of additional probe cations (Section 4.3.1.2). In the absence of all organic solvents, formate-d and $MeNH_3Cl$, the $^{14}NH_4^+$ RQC (c) follows much the same profile as in the presence of these probes, again implying a near identical surface chemistry. The slightly faster kinetics of gel formation in the absence of the probes can be ascribed to differences in the weighing of the GdL and the effect of 5 mM formate-d on the hydrolysis of GdL and the pH of the sample.[2, 3] As described in our previous work (Chapter 3, Section 3.3.11),[1] a faster decrease in the pH results in faster gelation kinetics. Accordingly, when the non-assembling propionic acid is included in the place of **1**, the pH profiles are slightly different in the two probe mixtures (Figure 4-S1b), with the basic formate-d giving a slightly raised pH curve. All samples synerese to very similar extents (e-f). The STDs (b) were recorded without dummy scans and so slight apparent STDs are detected in the absence of a gel network (Section 4.2.5.3). Nevertheless, all data series were recorded using the same parameters and are thus comparable.

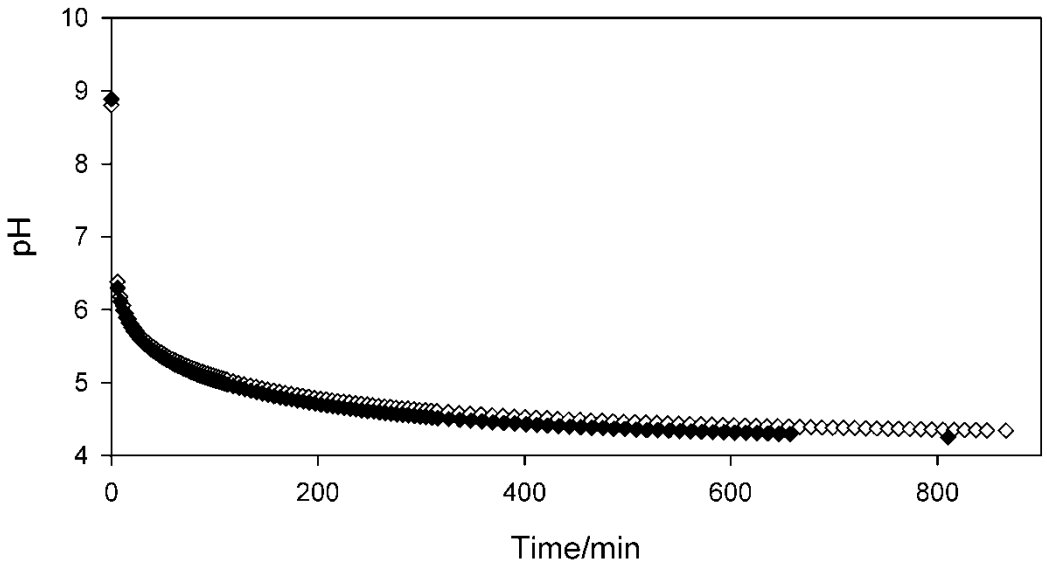

Figure 4-S1b. Plot of pH versus time following the addition of 5 mg/mL GdL to solutions containing propionic acid in place of **1**. Solutions contained the full set of probes used for **1**/GdL samples (white) or with no organic solvents, $MeNH_3Cl$ or formate-d (black).

The integrals of the probe molecules remain constant throughout the experiment (Figure 4-S1c) confirming minimal inclusion of the probes in the fibres. The NMR resonances of the probes also remain sharp (Figure 4-S5b), again consistent with the probes remaining in the solution phase of the gel. Overall, we can be confident that the set of probe molecules/ions used for **1**/GdL gels does not significantly affect the formation of the gel or the observed surface chemical properties. Further plots are presented in our previous work (Chapter 3, Section 3.3.4).[1]

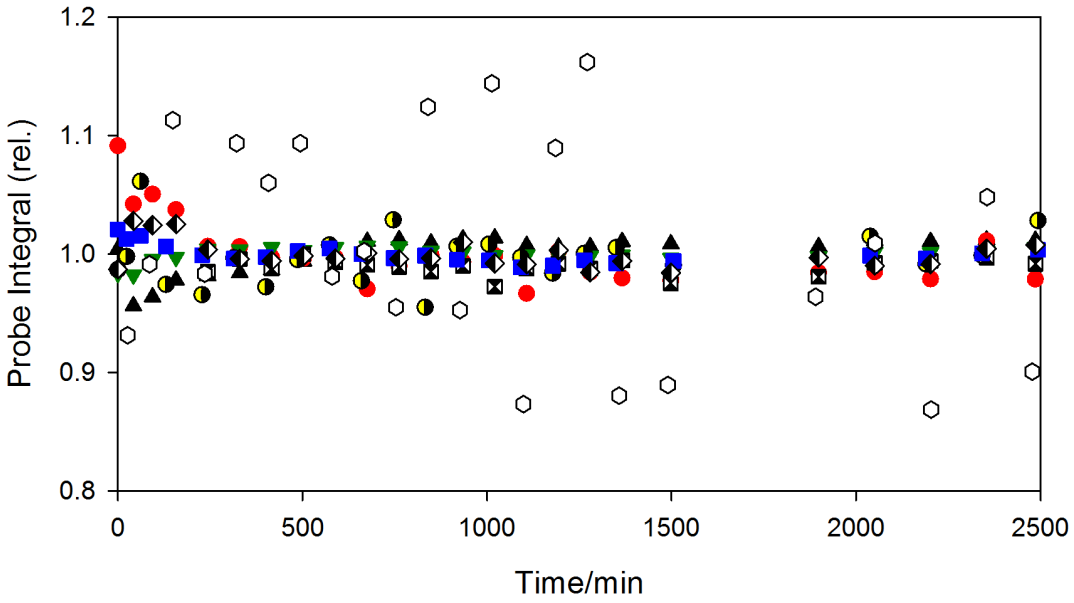

Figure 4-S1c. Plot of NMR integrals of probe molecules versus time during gelation of a **1**/GdL sample: IPA+tBuOH (blue square), acetone (black triangle), $MeNH_3^+$ (red circle), DMSO (green down triangle), formate (half black circle), acetate (black and white square), MeOH (black and white diamond) and $^{14}NH_4^+$ (white hexagon). Integrals have been normalised to the average value recorded in the time series. The ^2H resonances of IPA, tBuOH and formate are plotted instead of the ^1H integrals owing to a slight overlap of their ^1H integrals with those of **1**.

4.3.1.2 Effect of added probe molecules on 2/$CaCl_2$ gels

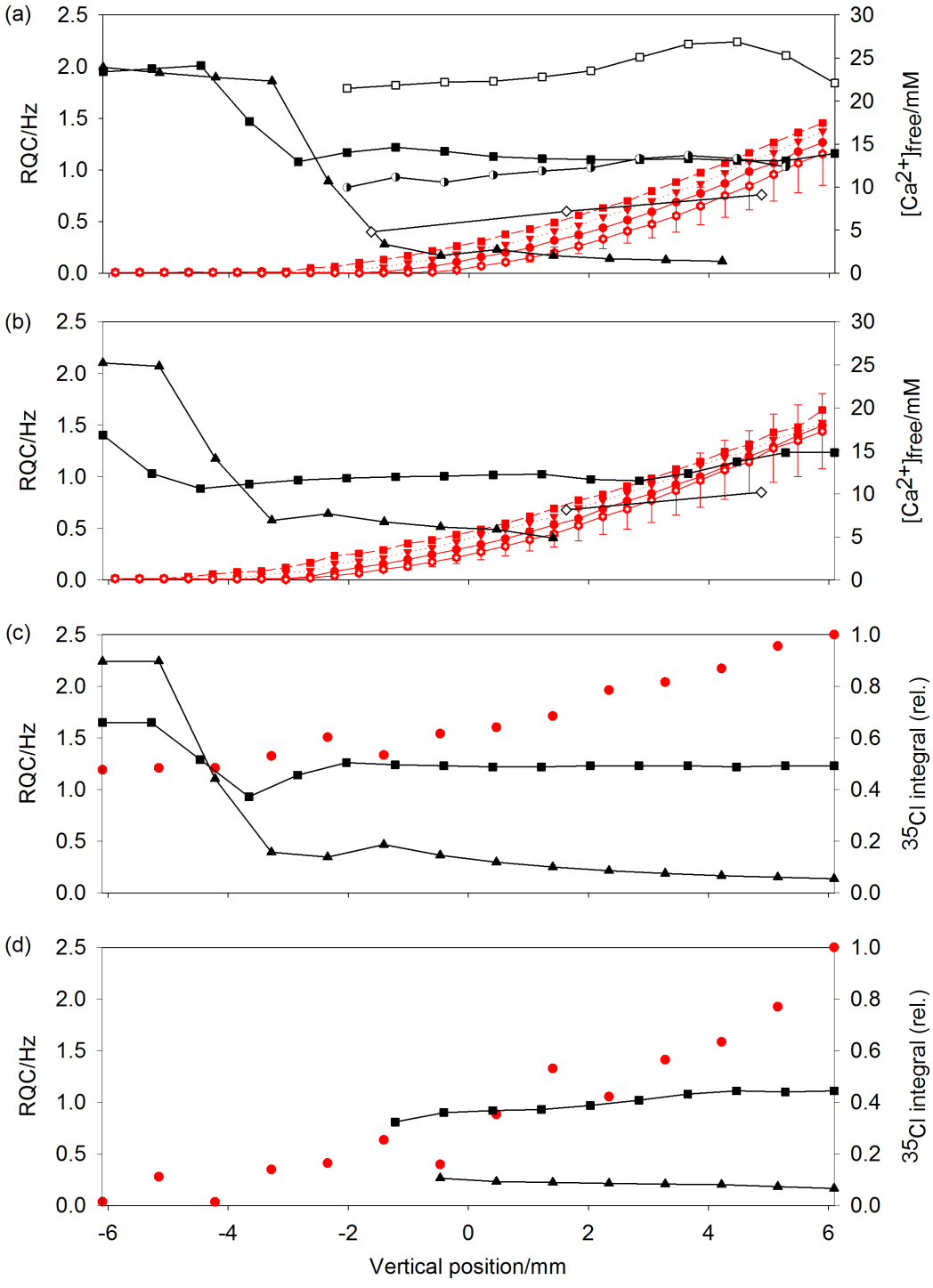

Figure 4-S1d. Plots of experimental observables along length of **2**/$CaCl_2$ gel samples during gelation. Samples were prepared with different sets of probe molecules: (a) full set of probes for **2**/$CaCl_2$ gels (Figure 4-5) reproduced here for convenience, (b) full set but with organic solvents excluded, (c) all probes excluded but with 30 mM NaCl added in their place, (d) no added probes. A key to all symbols is presented below.

RQCs are illustrated on Figure 4-S1d as follows: $^{23}Na^{+}$ (black triangle), formate-d (white diamond), HDO (black square), dioxane (white square) and tBuOH (half-black circle). In all plots, the $^{23}Na^{+}$ RQC has been scaled down by a factor of 500. Only resolvable RQCs are plotted. Red: Profiles of $[Ca^{2+}]_{free}$ before all images (hollow hexagon) – error bars indicate uncertainty in $[Ca^{2+}]_{free}$ measurements – after ^{23}Na image (circle), after formate-d image (down triangle) and after ^{2}H HDO, tBuOH and dioxane image (square). The lines are a guide to the eye. In samples where maleate was excluded (c, d), the integral of the $^{35}Cl^{-}$ resonance (red circle) is plotted instead of $[Ca^{2+}]_{free}$, recorded after the ^{23}Na and ^{2}H images.

The standard set of probes used for **2**/$CaCl_2$ gels includes 30 mM of ionic compounds as well as organic solvents. Such a high concentration of ions is necessary due to the low sensitivity of CSI methods compared to conventional NMR. However, it is apparent from Figure 4-S1d (a, c) that inclusion of the full set of probes has much the same effect on the samples as inclusion of 30 mM NaCl, the HDO and $^{23}Na^{+}$ RQCs following very similar profiles.

In the absence of all probe molecules, ions and $CaCl_2$, the solutions of **2** do not display any birefringent domains[4] (Figure 4-S1e) while no RQCs of HDO or $^{23}Na^{+}$ are observable (Figure 4-S1d, d). The $^{23}Na^{+}$ RQC is not observable due to the very strong interaction of Na^{+} with the structures of **2** in the absence of excess Na^{+}; the $^{23}Na^{+}$ T_1 in this solution was measured as 26±1 ms compared to 41±1 ms in a solution with the full set of probes, confirming a stronger interaction. Upon addition of $CaCl_2$, RQCs of HDO and $^{23}Na^{+}$ become apparent (Figure 4-S1d, d) while the $^{23}Na^{+}$ T_1 in the final gel is measured as 55±1 ms. These results are consistent with a displacement of Na^{+} from the structures of **2** by the Ca^{2+}. It can also be observed that following initial binding of Ca^{2+} (0 mm, Figure 4-S1d, d), the HDO RQC remains essentially invariant as more $CaCl_2$ diffuses down the tube. Even in the complete absence of probes, the formation of **2**/$CaCl_2$ gels is thus fundamentally similar to their formation in the presence of the full set of probes: Ca^{2+} displaces Na^{+} from the structures which soon become saturated with Ca^{2+}, the addition of more $CaCl_2$ having little effect on the observable properties of the samples.

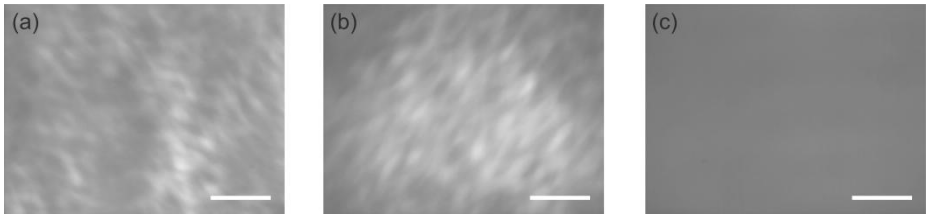

Figure 4-S1e. Optical images of 4 mg/mL solutions of **2** at pH 9 recorded between crossed-polarisers. (a) Full set of probes included, (b) 30 mM NaCl in place of all probes, (c) No probes. The scale bars represent 0.5 mm. Images were recorded in transmission mode on a Nikon Eclipse LV100POL under X5 magnification between crossed-polarised filters. The samples were contained in 5 mm NMR tubes mounted on glass slides. Following preparation, the samples were aged for seven days before analysis. Upon addition of $CaCl_2$, the birefringence of (a) and (b) is lost which is likely due to a change in the hierarchical organisation of the structures of **2** (data not shown).[4]

^{35}Cl CSI experiments (Figure 4-S1d) were performed using the same pulse sequence used for ^{2}H CSI experiments with 32 gradient steps. 626 data points were acquired with a sweep width of 10 ppm and a signal acquisition time of 0.2 s. The total acquisition time for the image was 45 minutes. ^{35}Cl integrals are normalised to the maximum value obtained in the NMR-active window. The theoretical spatial resolution is 0.94 mm.

We note that it is possible to double the concentration of all ^{2}H probes without affecting the gel (Figure 4-S1f); the RQCs of all probes are very similar between the two samples and follow identical profiles along the Ca^{2+} gradient. By using 10 mM formate-d instead of 5 mM, the formate RQCs can be recorded with a much higher spatial resolution in the same image as the other ^{2}H probes (Figure 4-S1f, b). It can now be seen that the RQC of the formate emerges after that of dioxane. A very slight excess of Ca^{2+} is thus required in order to sufficiently neutralise the negative charge of the fibres for the anionic formate to interact and exhibit an RQC. The lack of a concentration dependence of the RQCs implies a relatively weak binding of these probes to the fibres with the majority of binding sites remaining unoccupied. The sharp ^{2}H resonances of the probes are also consistent with a weak interaction.

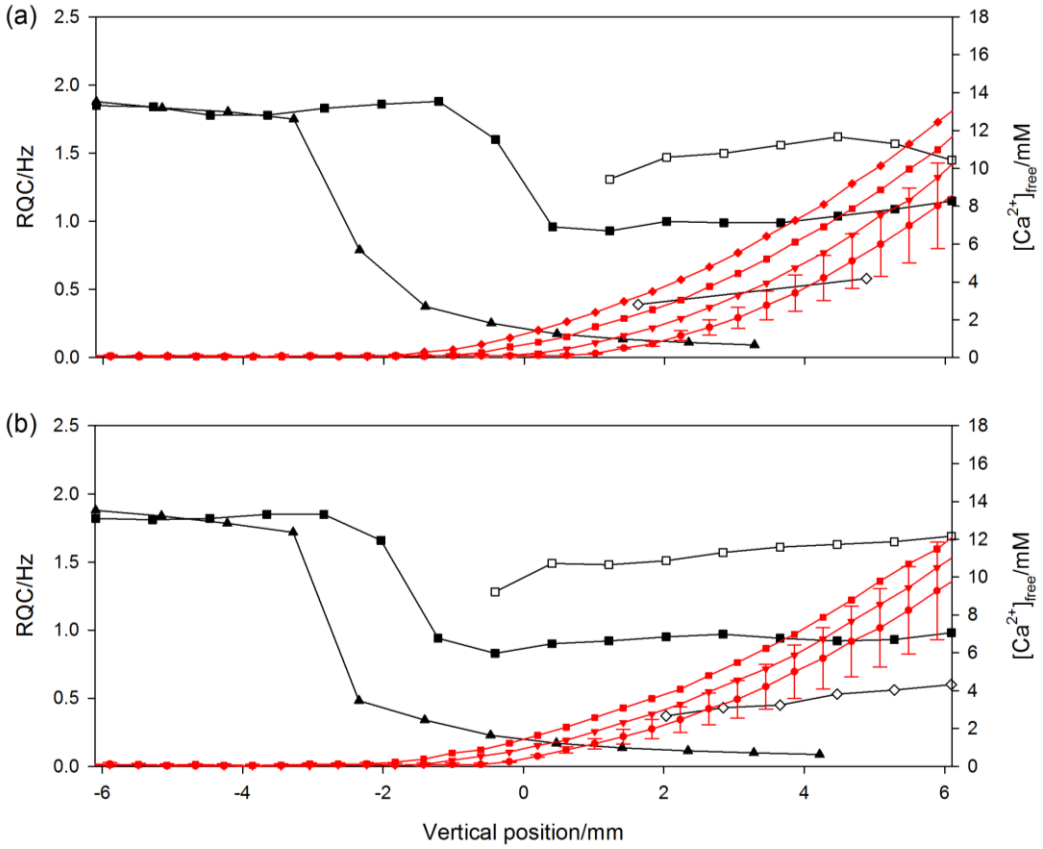

Figure 4-S1f. Plots of experimental observables along length of an NMR sample. 0 mm corresponds to the centre of the NMR-active region. RQCs of $^{23}Na^{+}$ (triangle), HDO (black square), dioxane (white square) and formate-d (white diamond). (a) Standard set of probe molecules for **2**/$CaCl_2$ gels. $[Ca^{2+}]_{free}$ (red) before all images (circle), after ^{2}H HDO and dioxane image (triangle), after ^{2}H formate image (square) and after ^{23}Na image (diamond). (b) Standard set but with the concentration of all ^{2}H probes doubled. Only 5 mM NaCl was added to this sample so that the concentration of Na^{+} was the same in the two samples. $[Ca^{2+}]_{free}$ before all images (circle), after ^{2}H image (triangle) and after ^{23}Na image (square). In both plots, the ^{23}Na RQCs have been scaled down by a factor of 500. On these plots, the ^{23}Na image was run after the ^{2}H image, whereas for Figure 4-5, the ^{23}Na image was recorded before all other images.

Finally, we note that the NMR integrals of the probe molecules remain constant along the Ca^{2+} gradient implying minimal inclusion of the probes in the gel fibres (Figure 4-S1g).

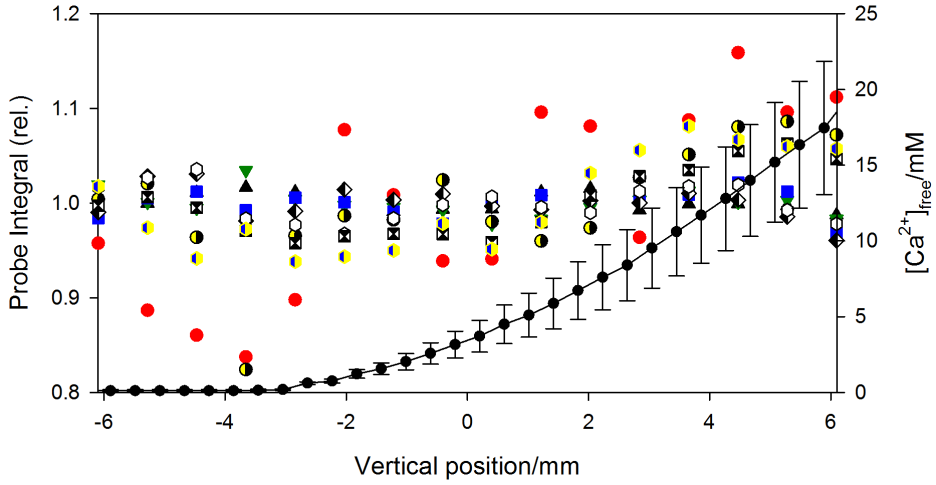

Figure 4-S1g. Plot of ^{1}H NMR integrals of probe molecules along the length of a sample during the formation of **2**/$CaCl_2$ gel: maleate (red circle), DMSO (green down triangle), MeOH (black and white diamond), acetate (black and white square), tBuOH (blue square), MPA^{2-} (blue and yellow hexagon), formate (half black circle) and dioxane (white hexagon). $[Ca^{2+}]_{free}$ is plotted as black circles linked by a line, with the uncertainty indicated. Integrals are normalised to their average value in the series.

4.3.1.3 Effect of magnetic field during gelation

In our previous work,[1] we demonstrated that the presence of the magnetic field during gelation does not significantly affect the mechanical properties or the ^{23}Na relaxation times of **1**/GdL gels (Chapter 3, Sections 3.3.15 and 3.3.8). The syneresis of the gels also occurs to a very similar extent in the presence and absence of the field. The STDs to the probe molecules are also very similar in a gel prepared away from the magnetic field, confirming that the observed surface chemistry of the gels is unaffected by the presence of the magnetic field during gelation (Figure 4-S1h).

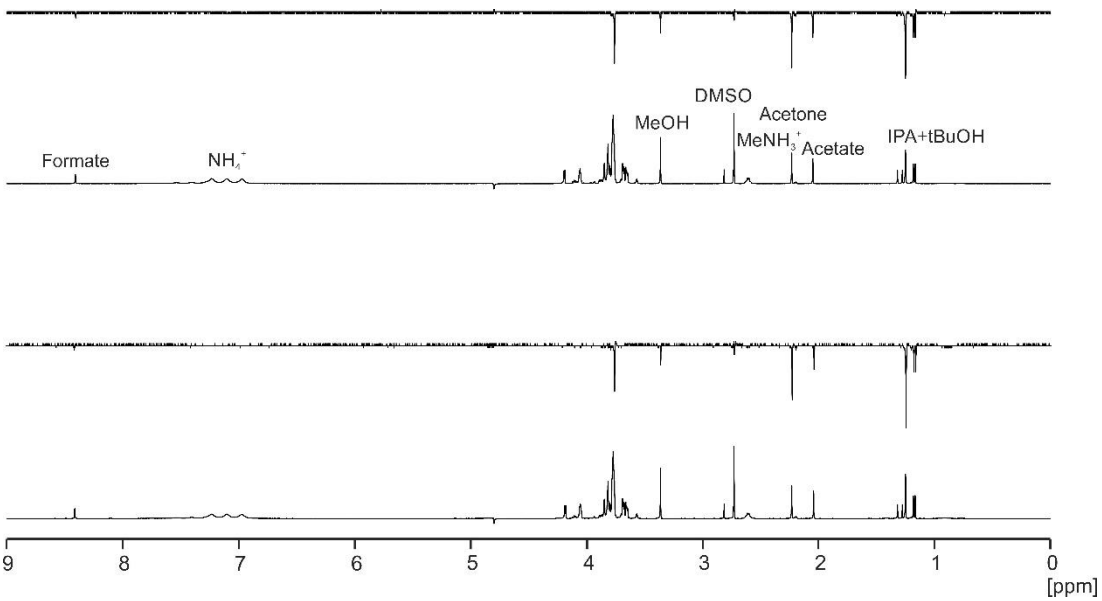

Figure 4-S1h. ^{1}H NMR spectra of **1**/GdL gel prepared away from the magnetic field of the spectrometer (bottom) and in the field (top). The STD difference spectra (I_{sat}-I_0) are displayed above the reference ^{1}H spectra (I_0) and have been scaled by a factor of 10.

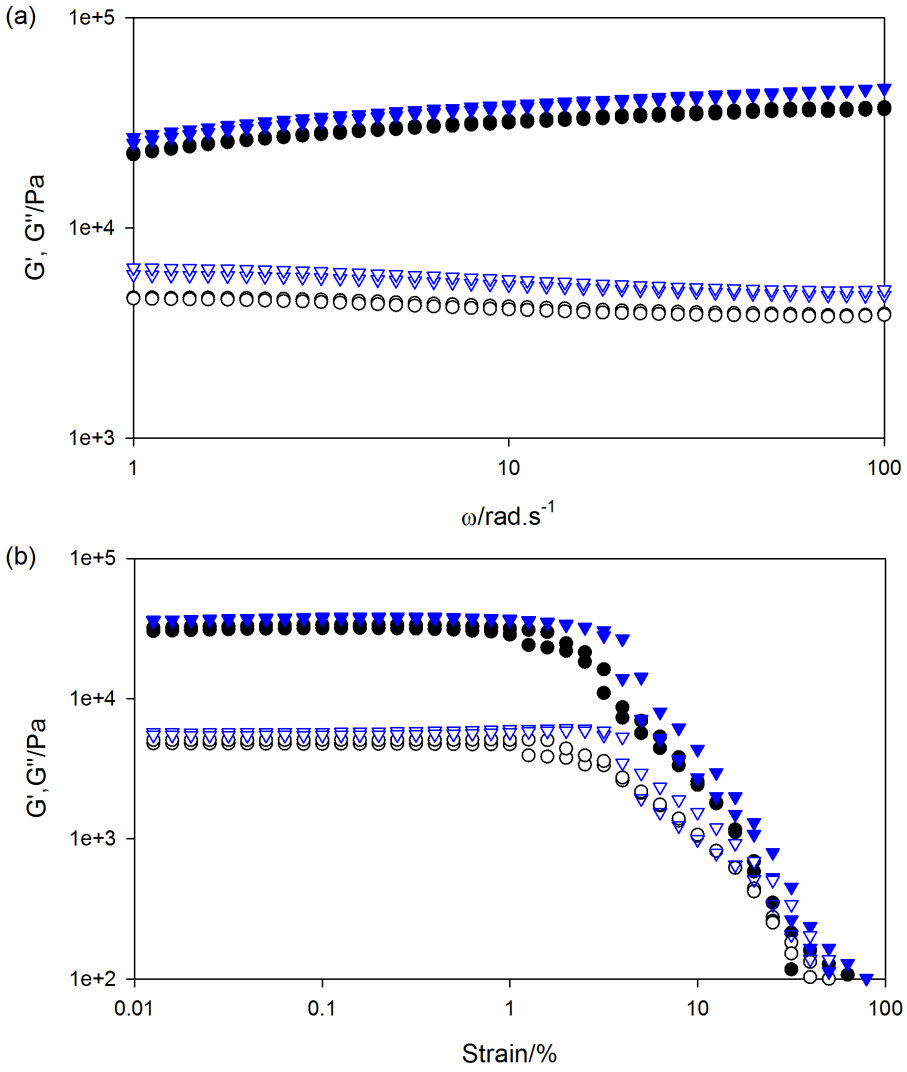

Figure 4-S1i. Plots of G' (solid symbols) and G" (open) for **2**/$CaCl_2$ gels prepared in (circle) and away from (triangle) the 9.4 T magnetic field of the spectrometer. (a) Frequency sweep measured at 0.5% strain. (b) Strain sweep measured at an angular frequency of 10 rad/s.

The mechanical properties of **2**/$CaCl_2$ gels are not significantly affected by the presence of the magnetic field during gelation. As in our previous work on **1**/GdL gels,[1] the samples prepared in the presence of the magnetic field appear very slightly weaker than the samples prepared away from the field. Samples for these measurements were prepared in D_2O/NaOD at 5 mg/mL **2**, as described in Section 2.2.3. We previously demonstrated that gels thus prepared possess a degree of alignment with respect to the magnetic field and exhibit similar RQCs to those reported in the current work.[14] Gels were formed in 4 mL Sterilin polystyrene vials which had been roughened with sandpaper to reduce slippage during the measurement. After addition of 140 μL 0.7 M $CaCl_2$ solution, the vials were lowered

into the 9.4 T magnetic field of the spectrometer in a homemade cradle and allowed to stand for 48 hours before removal. The gels were analysed, 3 days later, on an Anton Paar Physica MCR 301 rheometer equipped with a vane and cup geometry. The vial acted as a holder for the gel during the measurement. The samples were prepared at ambient temperature (19-23 ^{o}C) and maintained at 25 ^{o}C during analysis.

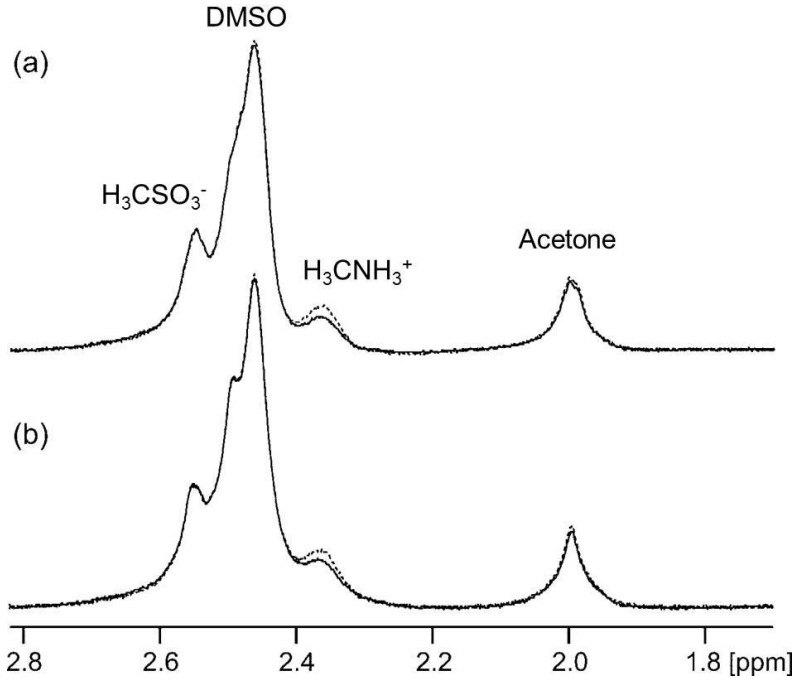

Figure 4-S1j. ^{1}H spectra of probe molecules in **3**/DMSO gel transferred to the NMR spectrometer immediately (< 2 minutes) after preparation and held for 16 hours (a) and a gel held away from the magnetic field (b) with (solid) and without (dashed) on resonance presaturation applied to the gel fibres. Spectra were recorded 16 hours after preparation of the gels.

The presence of the magnetic field does not affect the surface chemical properties of **3**/DMSO gels as very similar STDs are observed to the probe molecules (Figure 4-S1j). The ^{23}Na T_1 and T_2 relaxation times in the sample held away from the magnetic field were measured as 32±2 ms and 20±2 ms respectively, in complete agreement with the values measured in the gel held in the magnetic field for 16 hours.

4.3.1.4 Notes on the selection of probe molecules

The selection of suitable probe species is of fundamental importance for the NMR methodologies discussed in this work. To be suitable, a probe species must satisfy the following three criteria:

1. Inclusion of the probe species must not significantly affect the gelation process.
2. The interaction of the probe species with the gel fibres must be easily detectable by NMR.
3. The probes should possess only a single and well-defined chemical property that determines the strength of their interaction with the gel fibres.

Point (1) was discussed at length in Sections 4.3.1.1 and 4.3.1.2 where it was demonstrated that the probe species used in this work do not significantly affect the gelation process. In contrast, the hydrophobic 3-(Trimethylsilyl)propionate (TSP) is unsuitable as a probe for **1**/GdL gels as it is found to co-assemble with **1** (Figure 4-S1k).

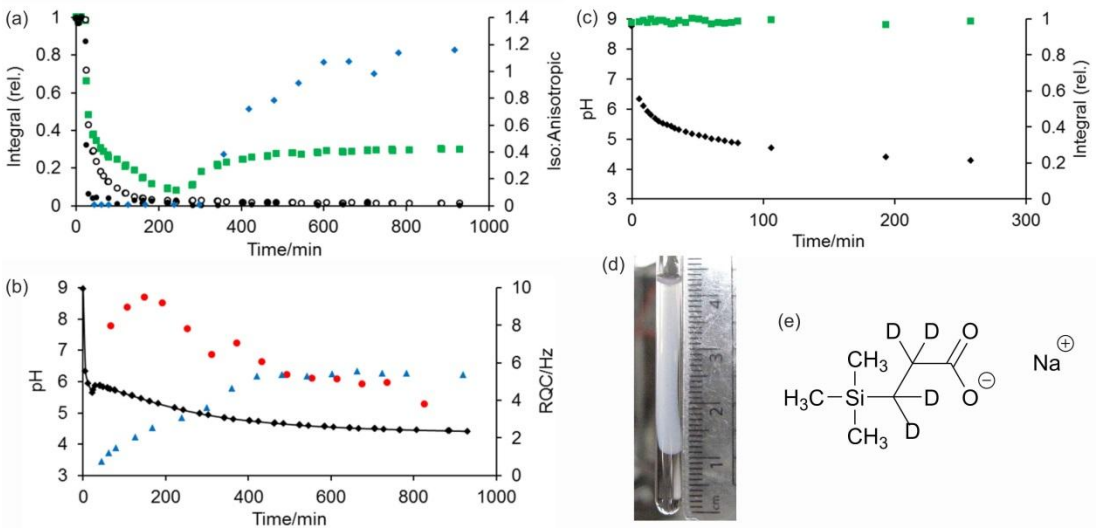

Figure 4-S1k. (a) Plot of integrals of TSP methyl protons (green square), valine methyl protons of **1** (white circle) and aromatic protons of **1** (black circle) versus time during formation of **1**/GdL gel. Integrals are normalised to their maximum value measured during the experiment, using methanesulfonate as a reference integral. TSP was included in the sample as its sodium salt at a concentration of 4 mM. The ratio of the volume of the fluid exuded during syneresis to the volume of the gel phase can be measured by analysis of the ^{2}H lineshape of IPA (Chapter 3, Section 3.3.6) and is also plotted (blue diamond). (b) Plot of RQCs of $^{14}NH_4^+$ (red circle) and IPA (blue triangle) and pH (black diamond). The line is a guide to the eye. (c) Plot of integral of TSP (green square) and pH (black diamond) in an analogous solution in the absence of **1** and the NaOH required to deprotonate **1**. (d) Photograph of sample of (a) and (b), taken 1000 minutes after the addition of GdL. (e) Chemical structure of TSP. The sample was prepared and analysed as described in Chapter 3, Section 3.2.6.

The ^{1}H integral of TSP falls in tandem with those of **1** as the pH falls (Figure 4-S1ka) indicating that it is becoming incorporated in the NMR-invisible assemblies of **1**. A severe syneresis of the gel is observed (d). By ^{2}H NMR (a) only approximately, 50% of the NMR sample volume is occupied by gel. TSP in the exuded fluid is NMR-visible and so the observed integral of TSP rises with time as syneresis progresses (a). TSP has a pK_a of 4.9 so will have a significant negative charge during the experiment.[5] In the absence of **1**, the TSP remains fully NMR-visible so does not assemble (c). TSP is thus unsuitable to use as a probe molecule. No ^{2}H RQCs were detectable for TSP. Both TSP and 4,4-dimethyl-4-silapentane-sulfonate (DSS) have been shown to interact with hydrophobic domains of proteins and are thus unsuitable for use as internal chemical shift references.[6]

Point (3) can be appreciated by considering the potential of benzylammonium (**D1)**. Benzylammonium is both positively charged and hydrophobic and exhibits a strong interaction with the fibres throughout the experiment (Section 4.5.3.1).

4.3.2 Interpretation of RQC, STD and ^{23}Na relaxation data and justification of experimental protocols

We approximate the interaction of a probe molecule/ion with the gel fibres as a rapid two-site exchange between the probes dissolved in the solution phase and the probes bound to the gel fibres. A spectroscopically observed property of a probe molecule, P_{obs}, is thus the time weighted average of the property in the free and bound states:

$$P_{obs} = f_b P_b + (1 - f_b) P_f \quad (4.S1)$$

where f_b is the fraction of molecules bound to the fibre at any instant in time and P_b and P_f are the properties in the free and bound states respectively. A decrease in the affinity of a probe molecule for the surface of the fibres manifests as a smaller value of f_b, and thus a measurably different P_{obs}, provided f_b and the difference between P_b and P_f is sufficiently large. Equation 4.S1 has been successfully applied to the interpretation of NMR relaxation,[7, 8] chemical shift[9], STD[10, 11] and RQC[12] data in a variety of different systems.

4.3.2.1 RQCs and RDCs

We have previously presented an interpretation of RQC measurements in supramolecular hydrogels (Chapter 3, Section 3.2.5.2).[1] Briefly, nuclei possessing spin quantum numbers (N) greater than ½ possess multiple (2N) NMR transitions. In solids, the transitions are typically split by hundreds of kHz – the quadrupolar coupling – and the lineshapes of quadrupolar nuclei are dominated by the quadrupolar interaction.[13] In isotropic solutions, however, the quadrupolar interactions are averaged to zero by rapid molecular tumbling. The resonances of deuterated organic solvents and symmetrically hydrated ions such as $^{23}Na^+$ and $^{14}NH_4^+$ are thus sharp in H_2O solution with linewidths of only a few Hz. Following Equation 4.S1, the lineshape of a probe molecule in exchange with the gel fibres will be a superposition of the lineshapes in the free (solution) and bound (solid-like) states. We write the quadrupolar coupling of a molecule in the bound state, Δ_b, as:[14]

$$\Delta_b = \frac{3\chi}{4I(2I-1)}(3cos^2\theta_b - 1) \quad (4.S2)$$

where χ is the quadrupolar coupling constant and θ_b is the angle between the external magnetic field and the main component of the electrical field gradient at the

observed nucleus of the probe molecule in the bound state. It is reasonable to assume that the probe molecule will visit many different gel fibres and binding orientations on a timescale much shorter than that of the NMR experiment.[15] The effective Δ_b, $\Delta_{b,eff}$, will thus be averaged over the many sites visited:

$$\Delta_{b,eff} = \frac{3\chi}{4I(2I-1)}\langle 3cos^2\theta_b - 1\rangle \quad (4.S3)$$

where the brackets <> denote a time average. Thus, if the gel fibres are isotropically arranged, $\Delta_{b,eff}$ is averaged to zero and no quadrupolar coupling is observed.[16] However, if a slight anisotropy in the orientations of the fibres is introduced by preparing the gels in the magnetic field of the spectrometer then $\Delta_{b,eff}$ is non-zero and an RQC (Δ, Figure 4-2) may be observed, provided χ is of sufficient magnitude. RQCs are thus very sensitive to the molecular structure of the probe; in IPA, an RQC is observed only for the central (methanetriyl) deuteron and not for the methyl groups. As the quadrupolar coupling in the free (solution) state is zero, the magnitude of an RQC is directly proportional to f_b (Equation 4.S1). However, the proportionality constant, $\Delta_{b,eff}$, depends upon the anisotropy of the gel fibres and so could potentially change during the gelation process. Nevertheless, as the probe molecules are together in the same sample, a decrease in the fibre anisotropy would decrease the RQCs of all probes to similar extents. In this work, we thus consider the relative changes in the RQCs of two or more complementary probe molecules during the gelation process.

The importance of molecular structure can be appreciated by comparing three different potential probe species to detect the presence of Ca^{2+} ions associated with the fibres of **2**/$CaCl_2$ gels: acetate-d_3, formate-d and malonate-d_2. ^2H spectra of the probes in a **2**/$CaCl_2$ gel are shown on Figure 4-S2a.

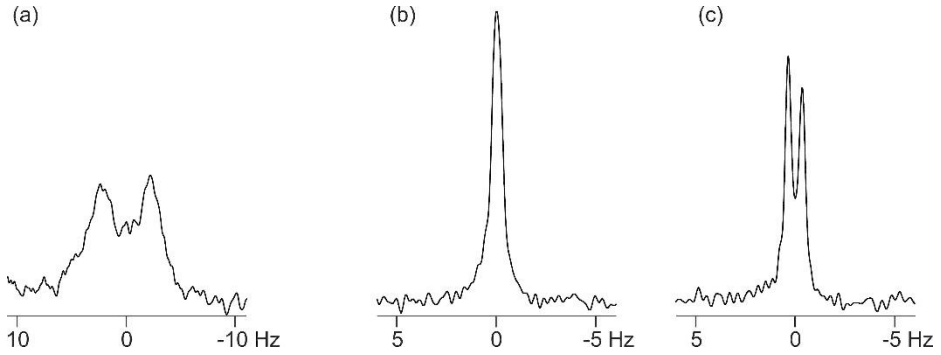

Figure 4-S2a. ^{2}H NMR spectra of probe species in **2**/$CaCl_2$ gel: malonate-d_2 (a), acetate-d_3 (b) and formate-d (c). Spectra were acquired with 1024 scans as described in Section 4.2.5.3. (a) was processed with an exponential line-broadening factor of 0.3 Hz while (b) and (c) were processed with no line broadening. (b) and (c) have the same vertical scale.

Broad lines and a large RQC of 4.4 Hz are observed for malonate. Formate gives sharp lines and an RQC of 0.7 Hz while acetate gives sharp lines and no observable RQC. The sample was prepared as described in Section 4.2.5.2.2 but with malonate-d_2 (4 mM) and acetate-d_3 (2 mM) included in place of the NaCl. The spectra of Figure 4-S2a were recorded 16 days after addition of $CaCl_2$. As a dicarboxylate, malonate has a much stronger binding affinity for Ca^{2+} than formate or acetate.[43] Malonate can therefore be expected to spend a larger fraction of time associated with the gel fibres (larger f_b, Equation 4.S1). A larger RQC may therefore be expected along with a shorter transverse relaxation time and broader lines.[17] The broadness of the malonate resonance renders it unsuitable for use as a probe species as a large number of scans are required in order for an RQC to be discerned. Acetate and formate both have similar binding constants and so the absence of an RQC for acetate is attributable to its molecular structure. The quadrupolar coupling constants, χ (Equation 4.S2), of acetate and formate are both very similar; 170 kHz and 161 kHz.[18-20] Malonate can also be assumed to have a similar value,[19] although this has been reported as 169 kHz only for the acid.[18] The main component of the electric field gradient can be assumed to lie along the C-D bond.[18, 21] Intramolecular rotation of the methyl group in acetate can cause additional averaging of the quadrupolar interaction.[19, 21-23] With acetate, the effective quadrupolar coupling constant is thus reduced relative to formate due to rotation of the methyl group. In general in this project, the RQCs of methyl groups tend to be small, and often unobservable,

relative to those of more conformationally rigid deuterons in the same (IPA) or similar molecules (Figure 4-3, 4-S4a).

Residual dipolar couplings (RDCs) arise as a result of the through-space coupling of nuclei. In this work, the RDCs within groups of chemically equivalent protons are considered. Only these protons, such as the methyl protons in methylammonium (Section 4.3.9) or the CH_2 protons in maleate (Section 4.3.10), possess the necessary proximity for RDCs to be observed. The line splitting depends on the number of protons in a group,[24] such that 1:2:1 triplets are observed for methyl groups while a doublet is observed for maleate (Section 4.3.10). The dipolar interaction between two nuclei depends upon the term $\langle 3cos^2\theta - 1\rangle$, where θ is the angle between the internuclear vector and the magnetic field and the brackets denote a time average.[25] RDCs are thus observed when the molecules interact with anisotropically arranged gel fibres and can be considered analogous to RQCs in this work.

4.3.2.2 ^{23}Na Relaxation

The theory of ^{23}Na relaxation is discussed extensively elsewhere[26-28] and only a brief outline is presented here and in our previous work (Chapter 3, Section 3.2.5.3).[1] The analysis differs slightly from that of RQCs in that the relaxation rate of $^{23}Na^+$ in the solvent phase must be taken into account. The observed relaxation rate, $1/T_{obs}$, is thus:[29]

$$\frac{1}{T_{obs}} = f_b \frac{1}{T_b} + (1 - f_b)\frac{1}{T_f} \qquad (4.S4)$$

where T is the relaxation time constant in the free (T_f) or bound (T_b) states. Rearranging this equation:

$$\left(\frac{1}{T_{obs}} - \frac{1}{T_f}\right) = f_b\left(\frac{1}{T_b} - \frac{1}{T_f}\right) \qquad (4.S5)$$

The minimum in T_{obs} thus occurs at the maximum in f_b. It is apparent from Figure 4-3 that the maximum in the $^{14}NH_4^+$ RQC coincides with the minimum in the $^{23}Na^+$ T_2 relaxation time, in good agreement with the theory presented here. We note that ^{23}Na relaxation is inherently biexponential in nature due to the different relaxation rates of the central (m = -1/2↔1/2) and 'satellite' (m = -3/2↔-1/2, 1/2↔3/2) transitions. However, in our systems,[1, 30, 31] the molecular motions are generally sufficiently fast

for a monoexponential relaxation to be observed and for an effective monoexponential T_1 and T_2 to be determined.[26] T_2 is more sensitive than T_1 to changes in the mobility of the $^{23}Na^+$ ions.[26, 27] However, a smaller decrease in mobility is required for T_2 to become biexponential in nature which can make its meaningful quantification very difficult. The observation of biexponential T_2 relaxation is good evidence for a strong interaction of $^{23}Na^+$ with the gel fibres (Section 4.3.8). In our systems, T_1 is always found to be monoexponential. In this work, we are only interested in relating changes in the observed relaxation times to changes in f_b for $^{23}Na^+$ using Equation 4.S5. As such, we either quote the effective monoexponential T_1 and T_2, or for systems in which T_2 is strongly biexponential, T_1 only. In systems where T_2 is biexponential, such as 4 mg/mL solutions **2** at pH 9 (Section 4.3.8), T_1 is found to be sufficiently reduced from its value in the absence of gel fibres (T_f) for changes in f_b during gelation to be adequately determined.

4.3.2.3 Saturation Transfer Difference (STD) Measurements

A detailed protocol for the analysis of protein-ligand binding by saturation transfer difference measurements has been presented by Angulo *et al.*[11] and applied to study the interaction of guest molecules with self-assembled gels by Segarra-Maset *et al.*[32] In our work, we study the interactions of a set of relatively weakly interacting probe molecules with the gel fibres during the gelation process in order to infer how the surface chemical properties of the gels are changing. Our procedure for the collection and interpretation of STD data thus differs from the procedure described by these authors. We quantify the magnitude of an observed STD effect, STD_{obs}, as the difference in the integral of the probe molecule resonance with (I_{sat}) and without (I_0) on-resonance saturation applied to the gel fibres, normalised by I_0:

$$STD_{obs} = \frac{I_0 - I_{sat}}{I_0} \qquad (4.S6)$$

Our definition of STD_{obs} thus differs from the 'STD-amplification factor' used in the above works as we do not consider the ratio of probe molecules to binding sites; the concentration of probe molecules is constant throughout the experiment while the nature and number of binding sites on our gel fibres is unknown and likely to change during the gelation process.[1] STD_{obs} can be considered directly proportional to f_b (Equation 4.S1), provided that the total concentration of probe molecules and the

number of binding sites is constant.[10, 11] However, were the number and nature of binding sites to change, the proportionality constant between f_b and STD_{obs} may also change as a consequence of partially saturated probe molecules being less able to take up more saturation than non-saturated molecules.[11] In our work, the proportionality constant is ideally constant throughout the gelation process so that changes in the affinity of our probe molecules for the gel fibres can be followed. The solution to this problem, as presented by Angulo *et al.*,[11] is to consider not the absolute size of STD_{obs} but rather the initial growth rate of STD_{obs} as a function of the saturation time, t_{sat}. The build-up of STD_{obs} with t_{sat} can be described by Equation 4.S7:[11]

$$STD_{obs}(t_{sat}) = STD_{max}[1 - exp(-kt_{sat})] \quad (4.S7)$$

where k is an arbitrary constant and STD_{max} is the maximum STD_{obs} attainable (i.e. at very long t_{sat}). The initial growth rate is thus $kSTD_{max}$. The relatively weakly interacting probe molecules in our work give only small STD effects, with much larger STDs observed to the compounds **D1** and **D4** (Section 4.3.5). As such, it is not always possible to obtain good fits of our data to Equation 4.S7 as STD_{obs} is often too small to be accurately determined at short t_{sat}. Indeed, with **1**/GdL gels (Figure 4-3) only IPA, acetone, and tBuOH gave STD_{obs} values large enough for k and STD_{max} to be determined. However, our probe molecules are unlikely to spend sufficient amounts of time bound to the gel fibres for the re-binding of saturated probe molecules to present a significant problem (Section 4.3.1).[11]

Plots of STD_{obs} measured at a t_{sat} of 8 s ($STD_{obs,8s}$), $kSTD_{max}$ and STD_{max} are qualitatively the same for IPA, acetone and tBuOH (Figure 4-S2b below). Data for $kSTD_{max}$ is only plotted where the R^2 value for the fitting of the STD build up curves to Equation 4.S7 is greater than 0.9. For all other probe molecules, $STD_{obs,8s}$ was always less than 0.1 with R^2 values less than 0.8 and so the fitted values of k and STD_{max} are unreliable. In this study, STD_{obs} measured at 8 s saturation time is plotted as standard for all probe molecules. Although not strictly quantitative, this measure is adequate to prove the increased interaction of the organic solvents with the gel fibres during the formation of **1**/GdL gels.

STD build-up curves (Figure 4-S2b, d) were obtained by varying the number of Gaussian pulses from 10 to 157 while keeping the total length of the presaturation and relaxation delays constant at 8.1 s. STD build-up curves were acquired with 8 scans (on and off-resonance) but no dummy scans, owing to the limited time available during the gelation experiment. The slight (≤ 3%) apparent STDs observed in the absence of a gel are thus relaxation artefacts owing to the first off-resonance scan being acquired before the first on-resonance. Very similar STDs are observed in a final **1**/GdL sample when 16 dummy scans are run before signal acquisition and when a long relaxation delay is elapsed to allow the sample to relax to thermal equilibrium between scans (Figure 4-S2c). Working with **2**/$CaCl_2$ gels, the methylammonium STDs (Section 4.3.9) were identical when on resonance saturation was applied at either -5 or 15 ppm and off-resonance at either -100 or 250 ppm. However, when off-resonance presaturation was applied at -50 ppm the STDs were smaller implying appreciable excitation of the fibres even at this high shift (data not shown).

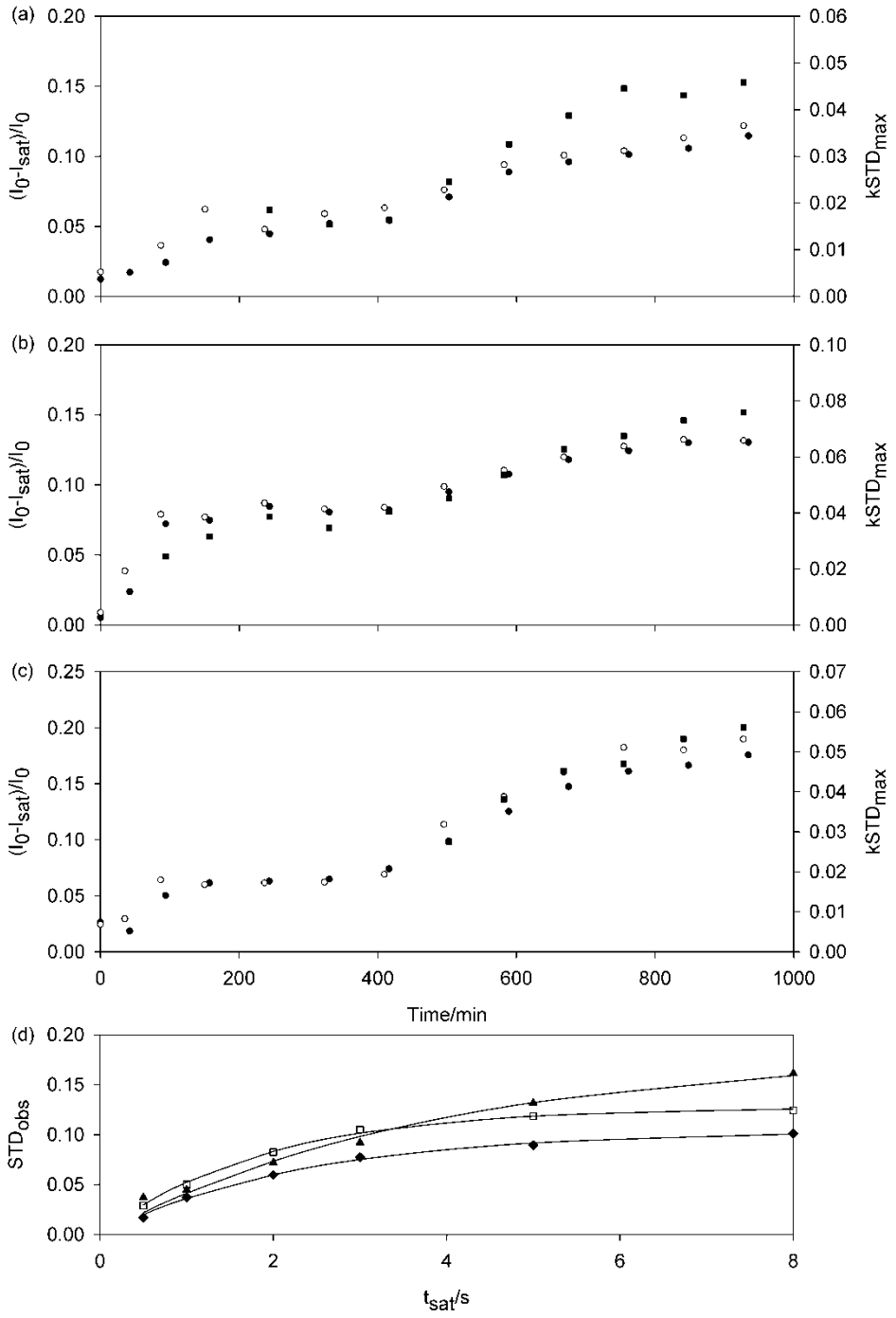

Figure 4-S2b. Plots of $kSTD_{max}$ (square), STD_{max} (white circle) and $STD_{obs,8s}$ (black circle) versus time since addition of GdL to a solution of **1** at pH 9: IPA (a), tBuOH (b) and acetone (c). Sample is the same as Figure 4-3c, d. (d) Plots of STD_{obs} versus t_{sat}, measured 750 minutes after the addition of GdL: IPA (diamond), tBuOH (white square) and acetone (triangle). Fits to Equation 4.S7 are shown as solid lines.

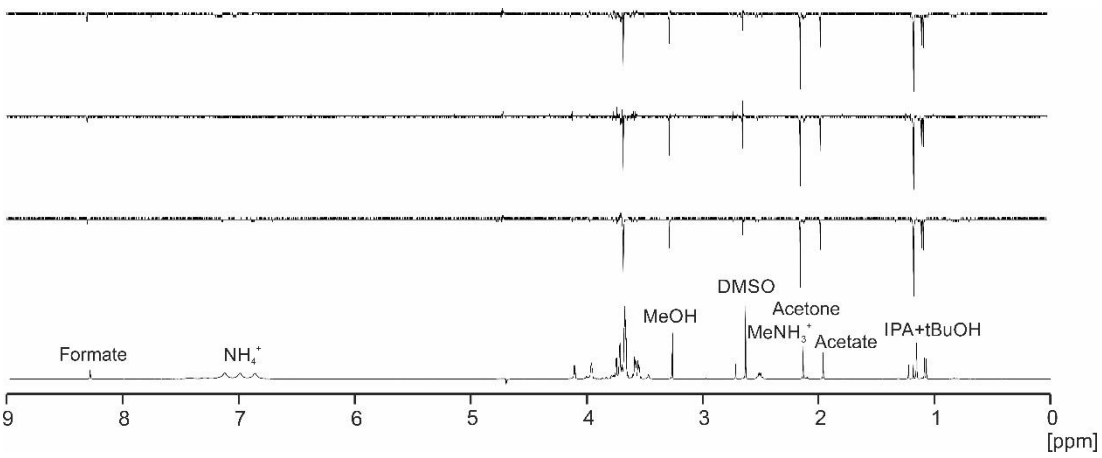

Figure 4-S2c. ^{1}H NMR spectrum of **1**/GdL gel 2700 minutes after the addition of GdL and STD difference spectra (I_{sat}-I_0) recorded with 16 dummy scans, 8 scans and 8.1 s relaxation delay (bottom), no dummy scans (middle) and with a relaxation delay of 40 s (top). The longest T_1 of the probe molecules is 6 s (acetone, formate) so 40 s is adequate to attain thermal equilibrium between scans. Presaturation was applied for the last 8 s of the relaxation delay in all cases. The difference spectra have all been scaled up by a factor of 10 relative to the reference spectrum.

4.3.2.4 Effect of gel syneresis on RQC, STD and ^{23}Na relaxation measurements

With RQC measurements, syneresis gives rise to two separate sets of resonances on the ^{2}H or ^{14}N NMR spectra: a singlet (isotropic) peak for the exuded fluid and a doublet for the gel. ^{2}H and ^{14}N NMR spectra and time-lapse photography of **1**/GdL gels during syneresis are presented in our previous work (Chapter 3, Section 3.3.10).[1] The RQC is thus measured only in the gel phase. Owing to the increased density of the gel phase upon syneresis, the RQCs may be expected to increase. However, if syneresis decreases the anisotropy of the fibres with respect to the magnetic field of the spectrometer, the RQCs may instead stay the same or diminish in magnitude. With STD measurements, the probes in the exuded fluid will not exhibit STDs, but will contribute to the calculated STD (Equation 4.S6). However, the probe molecules in the gel phase will exhibit enhanced STDs owing to the increased fibre density. Without any decrease in surface area per unit mass of fibre, the observed STDs would remain constant upon syneresis. The increase in the STDs to the organic solvents upon syneresis of **1**/GdL gels (Figure 4-3d) thus indicates an increased hydrophobicity of the network. The ^{23}Na relaxation should, in principle, exhibit separate components for the exuded fluid and the gel. However, due to the

similar relaxation rates in the two phases and the relatively small volume fraction of the exuded fluid[1] (< 30% in **1**/GdL gels), an effective monoexponential relaxation is instead observed.

4.3.3 Interaction of dioxane and gluconate with 1/GdL gels

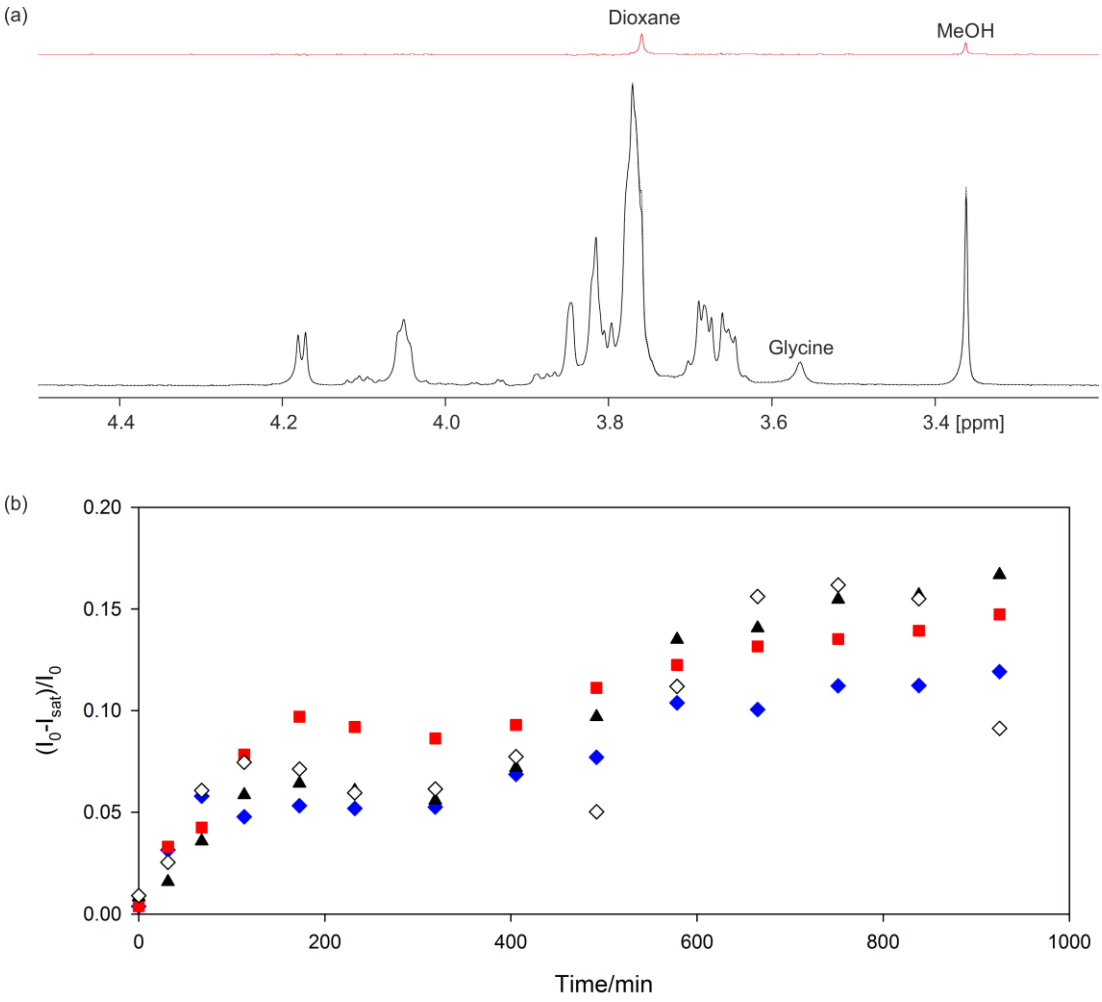

Figure 4-S3. (a) ^{1}H NMR spectra of a **1**/GdL sample, 930 minutes after the addition of GdL, with (solid) and without (dashed) on-resonance presaturation applied to the gel fibres. The difference spectrum (I_0-I_{sat}) is also plotted above (red). All resonances, unless otherwise stated, belong to gluconate with the small peaks assignable as GdL.[33] STDs are only detectable to dioxane and MeOH. (b) Plot of STDs to acetone (black triangle), tBuOH (red square), IPA (blue diamond) and dioxane (white diamond). Dioxane STDs were calculated by normalising the integral of the difference spectra to the spectrum acquired before the addition of GdL. The dioxane STDs are thus affected by any instrumental instabilities over the course of the experiment as well as any slight variability in the GdL and gluconate resonance between the on and off resonance acquisitions. Nevertheless, it can be deduced that the dioxane STDs are similar in size to those of the other organic solvents plotted.

4.3.4 Other H^+-triggered hydrogels

4.3.4.1 3/GdL hydrogels

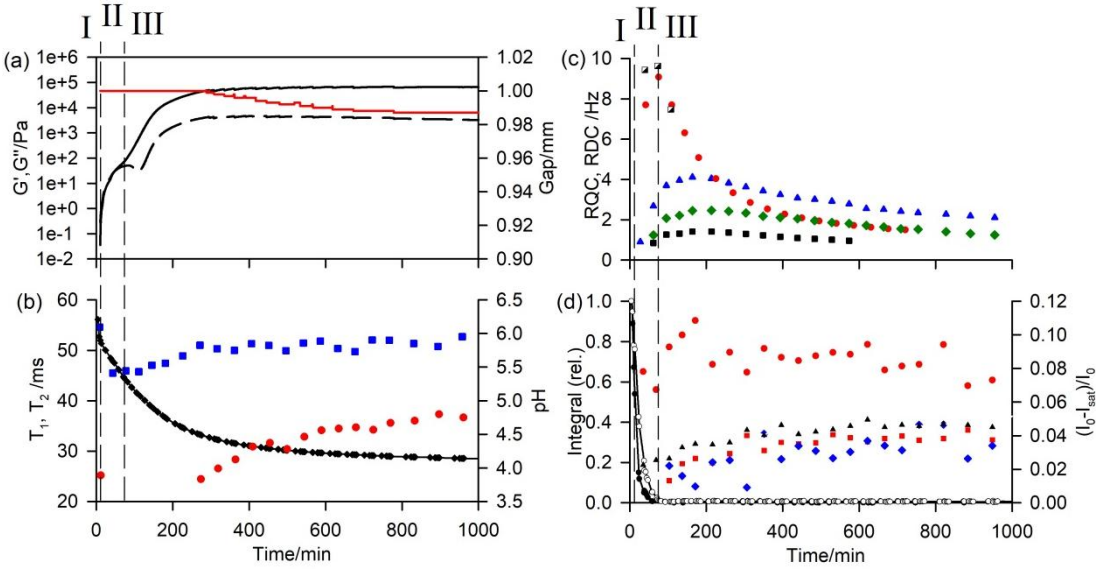

Figure 4-S4a. Plots of experimental observables versus time since the addition of 5 mg/mL GdL to a 5 mg/mL solution of **3** at high pH. (a) Plot of G' (black, solid line) and G" (dashed) along with the gap between the plates of the rheometer (red). (b) Plot of $^{23}Na^+$ T_1 (blue square) and T_2 (red circle) relaxation times along with pH (black diamond). T_2 is not plotted between 12 and 270 minutes due to the very fast relaxation of the quadrupolar 'satellite' peaks of $^{23}Na^+$; the fitted T_2 values from Equation 4.2 are misleading as the R^2 values are less than 0.96. (c) Plot of $^{23}Na^+$ (red circle), IPA (blue triangle), tBuOH (black square) and dioxane (green diamond) RQCs and $MeNH_3^+$ residual dipolar coupling (RDC) (black and white square). The $^{23}Na^+$ RQC has been scaled down by a factor of 20. (d) Plots of ^1H integrals of **3**: leucine CH_3 (white circle) and aromatic protons (black circle). The lines are a guide to the eye. Integrals are normalised to their value at the first spectrum recorded rather than in the absence of GdL. Plot of STDs to probe molecules: IPA (blue diamond), acetone (black triangle), tBuOH (red square) and $MeNH_3^+$ (red circle). No other probe molecules gave significant STDs. $^{14}NH_4^+$ RQCs were too strong to be observed before 300 minutes and are not plotted.

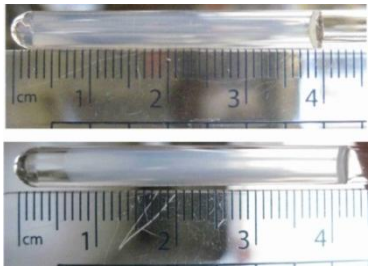

Figure 4-S4b. Comparison of **3**/GdL gel (top) and **1**/GdL gel of Figure 4-3 (bottom), 40 hours after addition of GdL. A very small amount of syneresis is apparent in the **3**/GdL gel at the base of the NMR tube.

The experimental observables during formation of **3**/GdL gels (Figure 4-S4a) follow a very similar pattern as in **1**/GdL gels: negatively charged structures form during Phase II that lose charge during Phase III while the bulk mechanical properties of the gel increase. The affinity of the organic solvents for the gel increases during both Phase II and Phase III. RQCs (c) are observable for IPA, acetone and dioxane but not tBuOH, while STDs can be observed to all four solvents. Dioxane STDs are not plotted due to overlap with GdL. The binding geometry of the organic solvents around **3**/GdL gels is thus subtly different to that around **1**/GdL gels. The decrease in the magnitudes of the RQCs after 200 minutes indicates a decrease in the anisotropy of the fibres as the STDs remain constant over the same period. Syneresis of the gel also occurs, although to a lesser extent than in **1**/GdL gels (Figure 4-S4b). As in **1**/GdL gels, more polar or negatively charged molecules such as DMSO, MeOH or formate do not show RQCs or STDs.

To prepare **3**/GdL gels, 5 mg/mL of solid **3** was dispersed in a solution containing the set of probe molecules used for **1**/GdL gels. 1.1 equivalents of NaOH were then added and the sample swirled and ground with a PTFE rod for five minutes to dissolve solid **3**. The solution was then filtered using a Pasteur pipette containing a plug of cotton wool in order to remove a small amount of residual solid. The solution was then added to 5 mg/mL GdL and transferred to an NMR tube for analysis. No turbidity was observed in the solution indicating minimal deprotection of the FMOC group. All NMR data on Figure 4-S4a was recorded on the same sample. STDs to the probe molecules were recorded with 5 s presaturation during an 8.1 s relaxation delay, with on and off-resonance scans recorded in separate 8 scan acquisitions.

STDs recorded on a different sample with 8 s presaturation followed identical profiles (data not shown).

The observation of RQCs in **3**/GdL gels but not **3**/DMSO gels is attributable to differences in the assembly mechanisms. Evidence has been presented that gels formed *via* the addition of GdL to solutions of dipeptide gelators at high pH initially form a wormlike micellar intermediate upon assembly of the gelators (Phase II).[34] The structures present in this stage are negatively charged and exhibit relatively little association with one another, the samples possessing only weak mechanical properties. In analogy to the wormlike structures formed by **2** at pH 9, these structures could be expected to align in the magnetic field of the NMR spectrometer giving rise to the RQCs observed.[16] Upon addition of H_2O to a solution of **3** in DMSO, spherical aggregates initially form and the sample resembles a turbid, white suspension. A network of fibres then develops at the expense of the aggregates, with the white solution clearing to form a self-supporting gel.[35, 36] The structures thus formed may be much less able to align in the spectrometer field.[37, 38] Alternatively, the gel may develop too quickly during the two minutes required to place the sample in the NMR spectrometer. However, it is not feasible to transfer the samples to the NMR spectrometer while they remain turbid.

4.3.4.2 2/glycolic acid gels

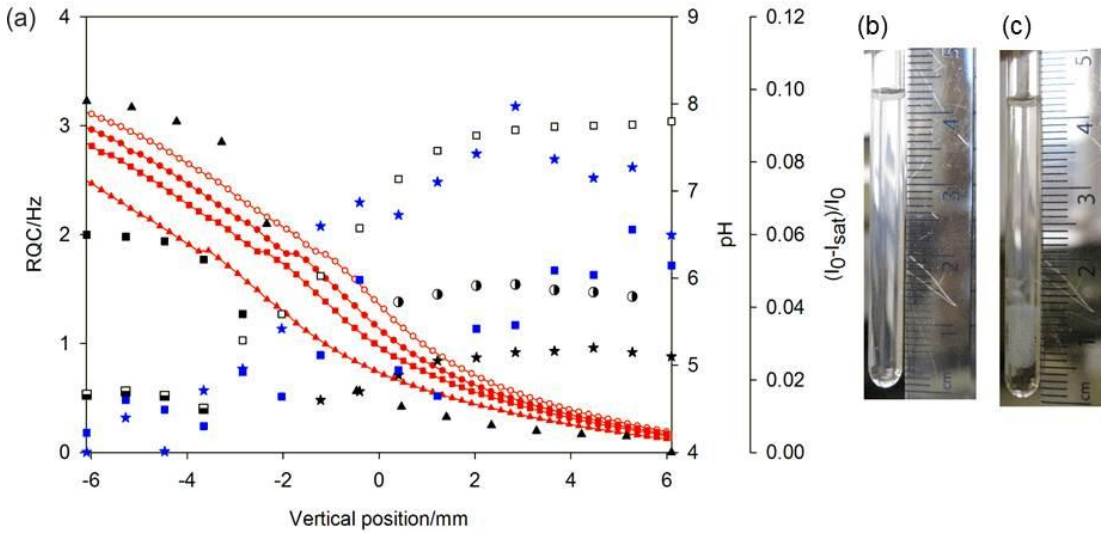

Figure 4-S4c. (a) Plots of observables along length of sample: RQCs (black) of $^{23}Na^{+}$ (triangle), HDO (square), dioxane (white square), acetone (star), tBuOH (half circle) and MeOH (half black square). $^{23}Na^{+}$ RQC has been scaled down by factor of 300. No other probes gave observable RQCs. STDs to dioxane (blue square) and acetone (blue star). No other probe molecules gave significant STDs. pH (red) before the $^{23}Na^{+}$ image (hollow circle), after $^{23}Na^{+}$ image (solid circle), after ^{2}H dioxane image (square) and after STD image (triangle). The slight inflexion in the pH between 6 and 6.5 is an artefact of the pH calculation.[1] 0 mm corresponds to the centre of the NMR active region of the sample. (b) Photograph of gel sample immediately after removal from spectrometer after final pH profile (triangle) was taken. (c) Photograph of gel having stood in water bath at 298 K for seven days.

Gels were formed by placing ca. 1.0-1.2 mg of solid glycolic acid on top of a 4 mg/mL solution of **2** at pH 9 with the full set of probe molecules used for **2**/$CaCl_2$ gels. Glycolic acid was chosen in preference to GdL as its single NMR resonance did not overlap with any of the probe molecules. The gels develop in an analogous way to **1**/GdL and **3**/GdL gels: As the acid diffuses down the tube and the pH falls, charge is removed from the fibres and the $^{23}Na^{+}$ RQC falls. RQCs and STDs then become apparent to the organic solvents indicating an increase in hydrophobicity. Significant STDs were only observed to acetone and dioxane. No RDCs were observed to maleate or MPA at any stage of gelation. Any RQC of the formate-d ions observed was smaller than the 0.5 Hz observed in **2**/$CaCl_2$ gels, although accurate analysis is impossible owing to the pH dependence of this ion's chemical

shift. Having stood in a water bath for seven days, the gel at the bottom of the tube had contracted severely and aggregates had formed (c) while the pH of the sample was 4.3 throughout. STD images were acquired using the same sequence used for ^{1}H images but with the gradient pulse strength, g, varied in 32 steps from -14 to 14 G/cm. Presaturation (5 s) was applied during the relaxation delay (5.1 s) using a train of 98 Gaussian pulses, the pulses as described for one-dimensional STD measurements. 8 scans with on-resonance (-5 ppm) and off-resonance (-250 ppm) presaturation were acquired at each step giving a total acquisition time for both images of 70 minutes.

4.3.4.3 Perylene bisimide (PBI)/GdL Gels

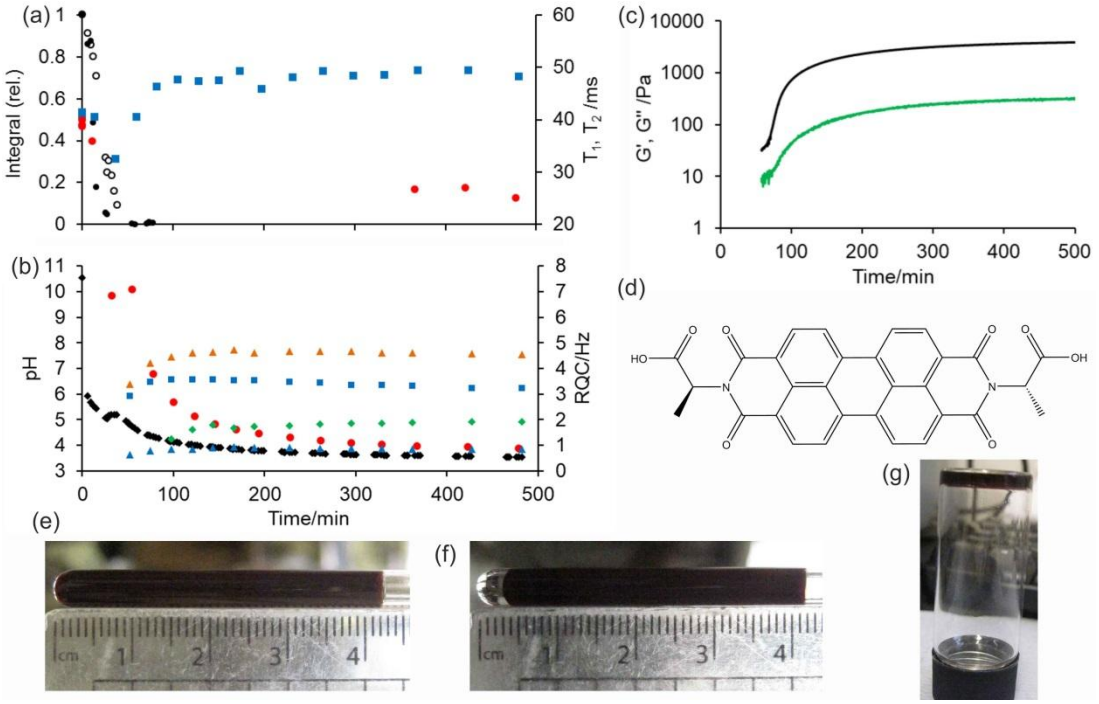

Figure 4-S4d. Plots of experimental observables versus time since the addition of 20 mg/mL GdL to a 5 mg/mL solution of PBI-A (d) at high pH. (a) Plot of integrals of PBI-A methyl protons (white circle) and aromatic protons (black circle). Plot of $^{23}Na^{+}$ T_1 (blue square) and T_2 (red circle) relaxation times. T_2 is not plotted between 12 and 360 minutes due to the very fast relaxation of the quadrupolar 'satellite' peaks of $^{23}Na^{+}$ and distortion of the lineshapes due to the evolution of the quadrupolar coupling during the CPMG pulse train; the fitted T_2 values from Equation 4.2 are misleading as the R^2 values are less than 0.96. (b) Plot of $^{23}Na^{+}$ (red circle), IPA (blue triangle), CD_3CN (blue square), dioxane (green diamond) and HDO (orange triangle) RQCs. The $^{23}Na^{+}$ RQC has been scaled down by a factor of 100. (c) Plot of G' (black) and G" (green). (d) Chemical structure of PBI-A. (e) Photograph of NMR sample, 2500 minutes after the addition of GdL. (f) Photograph of sample after 17 days. (g) Photograph of gel formed in 14 mL glass vial, 2500 minutes after the addition of GdL. This gel was formed from excess solution prepared for the rheological measurement and thus only a small amount of sample was available for this photograph.

PBI-A (d) possesses two carboxylate groups and thus 2.4 equivalents of NaOH were added to obtain a solution of the gelator at alkaline pH. CD_3CN, IPA-d_8 and dioxane-d_8 were included in the sample at 0.05 vol% for ^{2}H NMR measurements. No STD measurements were performed as the technique had not yet been developed when this sample was run. 20 mg/mL of GdL was added to obtain a sufficiently low pH for

a self-supporting gel to be formed after 2500 minutes. No changes were observed in either the mechanical properties of the gel (c) or the ^{23}Na relaxation times, measured from 1000 minutes up to 2400 minutes since the addition of GdL. Syneresis of the gel was not apparent during the course of the experiment (e); however, minor syneresis was apparent after 17 days (f). The rheological measurements (c) were recorded on an Anton Paar 101 rheometer equipped with a 25 mm sand-blasted plate using the same parameters used for **1**/GdL gels (Section 4.2.5.4). This rheometer is less sensitive than the Anton-Paar 301 rheometer, providing accurate measurements at a minimum torque of 0.5 μN.m rather than 0.1 μN.m. Coupled with the small size of the plate, G' and G" could not be precisely determined at early time points.

PBI-A is partially aggregated even at high pH, the ^{1}H resonances of PBI-A being broad even in the absence of GdL.[31] The $^{23}Na^{+}$ T_1 and T_2 relaxation times in the absence of GdL are thus lower than observed for solutions of **1**. A clear inflexion in the pH is observed after the pH has initially fallen to 5 and PBI-A is no longer visible by NMR (a, b), implying the formation of self-assembled structures. This inflexion is accompanied by an emergence of an RQC of $^{23}Na^{+}$ (b) which then decreases as the pH falls. The trend shown by the $^{23}Na^{+}$ RQC is mirrored by the $^{23}Na^{+}$ T_1 relaxation time (a) (Section 4.3.2.2). As the $^{23}Na^{+}$ RQC falls, the RQCs of the organic solvents can be seen to rise as the pH falls, implying an increased hydrophobicity of the self-assembled structures. The decrease in the $^{23}Na^{+}$ RQC is accompanied by increases in the mechanical properties of the sample (c), with G' quickly rising to exceed G" by more than order of magnitude. Minor syneresis is apparent after 17 days (f). The formation of PBI-A gels is thus similar to that of **1**/GdL gels (Section 4.2.3.2). The self-assembly of PBI-A is of particular interest owing to the electronic properties of its assembled structures.[31]

4.3.5 Interaction of model drug compounds with hydrogels

4.3.5.1 Interaction of D1 with 1/GdL hydrogels

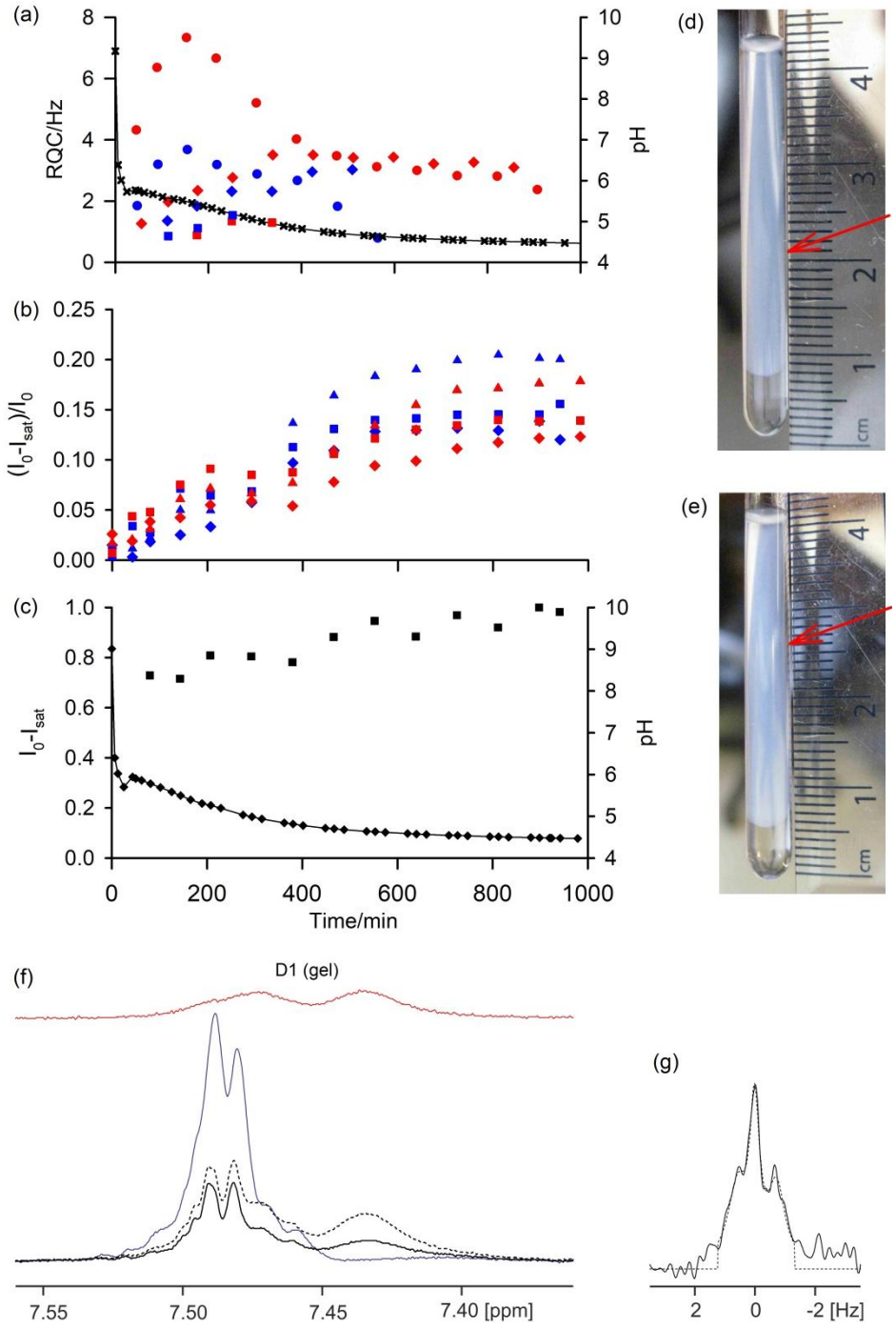

Figure 4-S5a. Interaction of **D1** with **1**/GdL hydrogels. Effect of inclusion of **D1** on RQCs (a) and STDs (b) of probe molecules. Plot of saturation difference of **D1** resonance (c). Photograph of **1**/GdL gel sample containing 5 mM **D1** (d) and without **D1** (e). (f) ^{1}H NMR spectra of aromatic resonances of 5 mM **D1** in **1**/GdL gel (black) and in absence of gel phase (blue). (g) ^{2}H IPA resonance (methanetriyl, 4 ppm) in gel of (d, f) and approximate Lorentzian deconvolution (dashed). A complete description of this Figure is provided below.

A complete description of Figure 4-S5a is as follows: Plot of RQCs (a) of $^{14}NH_4^+$ (circle), IPA (diamond) and tBuOH (square) in **1**/GdL gel with (blue) and without (red) 5 mM **D1**. Only resolvable RQCs are plotted. The pH is also plotted in the absence of **D1** (black cross); the line is a guide to the eye. (b) Plot of STDs to acetone (triangle), IPA (diamond) and tBuOH (square) with (blue) and without (red) 5 mM **D1**. (c) Plot of saturation difference (I_0-$I_{sat.}$, Section 4.3.2.3) of **D1** resonance (square) along with pH of sample containing 5 mM **D1** (black diamond); the line is a guide to the eye. Photograph of **1**/GdL gel sample containing 5 mM **D1** (d) and without **D1** (e), 17 hours after the addition of GdL. Syneresis (contraction) of the gel is apparent up the edge of the NMR tubes and is indicated with red arrows. (f) ^{1}H NMR spectra of aromatic resonances of 5 mM **D1** in **1**/GdL gel 940 minutes after the addition of GdL with (solid line) and without (dashed) on-resonance presaturation applied to gel fibres. The difference spectrum (I_0-$I_{sat.}$) is plotted above (red). The spectrum of **D1** in solution in the absence of **1** is also plotted (blue). (g) ^{2}H IPA resonance (methanetriyl, 4 ppm) in gel of (f), 900 minutes after the addition of GdL (solid) and approximate Lorentzian deconvolution (dashed).

In the presence of 5 mM **D1**, the $^{14}NH_4^+$ RQC is reduced by approximately 50% (Figure 4-S5a, a) indicating a preferential binding of **D1** to the fibres. Accurate quantification is difficult due to slight differences in the extent of syneresis between the two samples (d, e). In the following justification, we demonstrate that the binding affinity of **D1** is at least twice that of NH_4^+: **D1** bears a protonated amine group so is presumably able to bind to the same sites as NH_4^+, such as deprotonated carboxylate groups, aided by hydrophobic interactions involving its aromatic ring. If these binding sites are saturated then from Equation 4S.1, in the absence of binders other than $^{14}NH_4^+$, the observed $^{14}NH_4^+$ RQC, ΔN_{obs}, is given by:

$$\Delta N_{obs} = c\frac{S_{tot}}{N_{tot}} \qquad (4S.8)$$

where: S_{tot} and N_{tot} are the total number of binding sites and NH_4^+ ions respectively and c is a proportionality constant. In the absence of **D1**, doubling the concentration of NH_4^+ from 10 to 20 mM would be expected to decrease ΔN_{obs} by 50%. 5 mM **D1** thus has the same effect on ΔN_{obs} as 10 mM NH_4^+ and so the binding constant of **D1** to the gel fibres is at least twice that of NH_4^+. We define the binding constant as:

$$K = \frac{[PS]}{[P][S]} \qquad (4S.9)$$

where PS, P and S denote bound probe, free probe and free binding site respectively. The relatively sharp ^{14}N resonances[1] indicate that the binding sites are unlikely to be saturated with NH_4^+ and so the binding constant of **D1** is likely more than twice that of NH_4^+.

The RQCs (a) and STDs (b) to the organic solvents appear slightly raised in the presence of 5 mM **D1**, possibly due to a cooperative binding effect where **D1** enhances the effective hydrophobicity of the fibres. Accurate calculation of $(I_0\text{-}I_{sat})/I_0$ for **D1** is impossible due to spectral overlap of the aromatic resonances with the NH resonances of **D1**, NH_4^+ and $MeNH_3^+$. Nevertheless, by subtracting this background signal, $(I_0\text{-}I_{sat})/I_0$ can be calculated as 0.42±0.03 for the sample below pH 5. NH protons do not exhibit STDs due to exchange with the solvent. Following initial fibre formation, apparent as an inflexion in the pH,[1, 3] $(I_0\text{-}I_{sat})$ remains large for the remainder of the experiment suggesting a strong interaction with the gel fibres throughout (c).

The strong interaction of **D1** with the gel fibres is readily apparent by ^1H NMR (f). By plotting the difference (red) between the spectra of **D1** obtained with and without presaturation applied to the gel fibres, it is apparent that the resonance of **D1** in the gel phase is very different to that in an analogous solution in the absence of a gel (blue). The peaks are much broader while the multiplicity is also different.[39, 40]

Syneresis of the gel sample extends up the walls of the NMR tube (d, e) and thus into the NMR-active region, centred 18 mm from the base of the tube and extending 8 mm up and down. Deconvolution of the ^2H IPA resonance (g) indicates that approximately 70% of this volume is occupied by gel, the rest by fluid which gives rise to the central singlet peak on (g). The ^1H resonance of **D1** (f) in the fluid exuded during syneresis (upfield, sharp) is thus significant.

4.3.5.2 Interaction of D2-D4 with 1/GdL gels

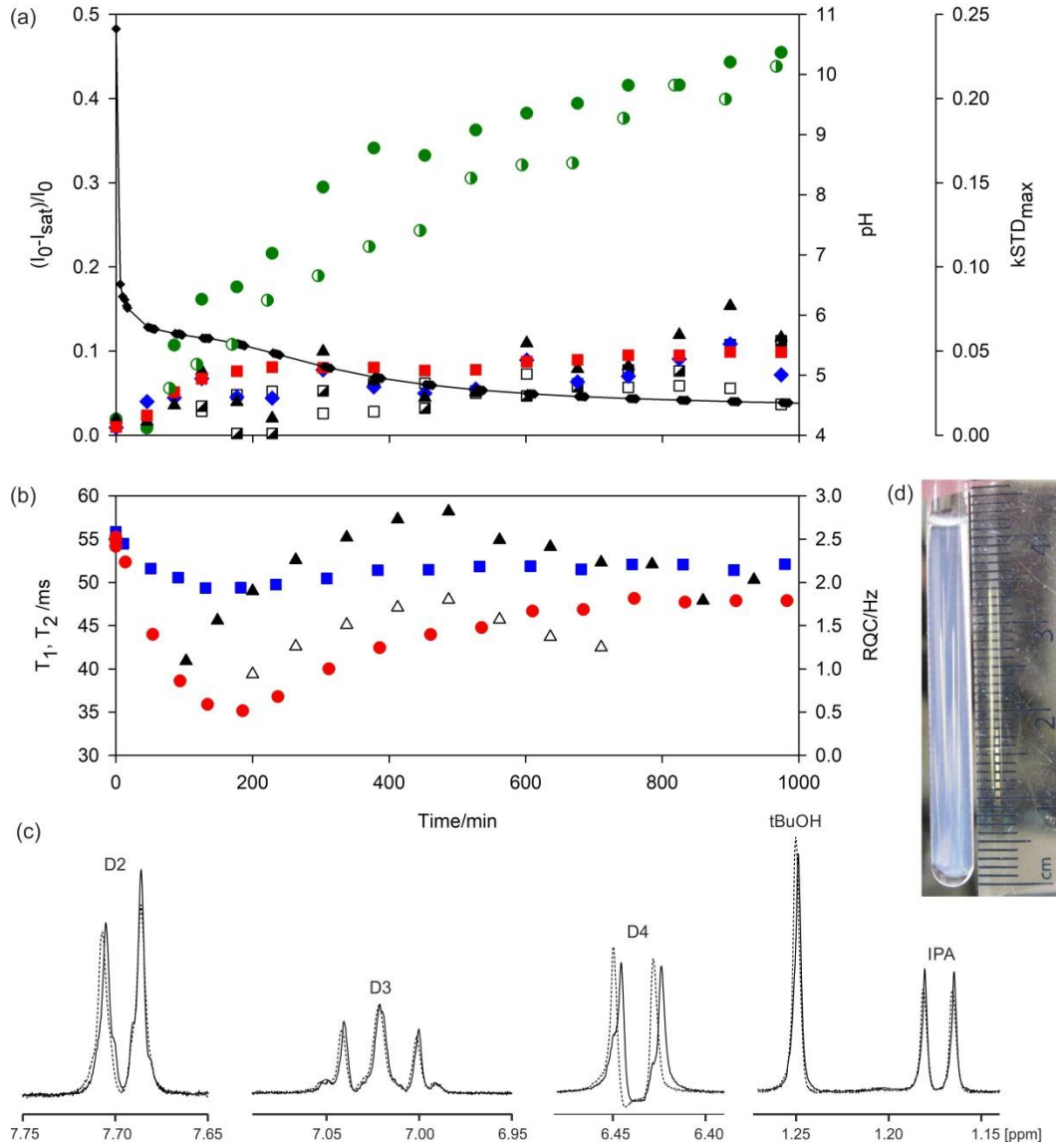

Figure 4-S5b. (a) Plots of STDs to IPA (blue diamond), acetone (black triangle), tBuOH (red square), **D2** (black/white square), **D3** (white square) and **D4** green circle. $kSTD_{max}$ for **D4** (half green circle). (b) Plots of $^{23}Na^+$ T_1 (blue square) and T_2 (red circle) relaxation times along with RQCs of IPA (black triangle) and tBuOH (white triangle). (c) ^1H NMR spectra of molecules in **1**/GdL gel at pH 4.4 (solid line), 1700 minutes after the addition of GdL, and in analogous solution in absence of **1** (dashed). Spectra were referenced to sodium methanesulfonate (2.815 ppm). For **D4**, separate resonances are discernible in the **1**/GdL gel for the molecules in the gel (upfield) and in the fluid exuded during syneresis (downfield). Spectra were acquired using a double-echo WATERGATE sequence in 8 scans with a signal acquisition time of 3.7 s and a relaxation delay of 1 s. No line broadening factor has been applied to the spectra. The negative intensity in the centre of the doublet is due to J-modulation. (d) Photograph of gel sample, 1700 minutes after the addition of GdL.

4.3.5.3 Interaction of D1-D4 with 2/$CaCl_2$ gels

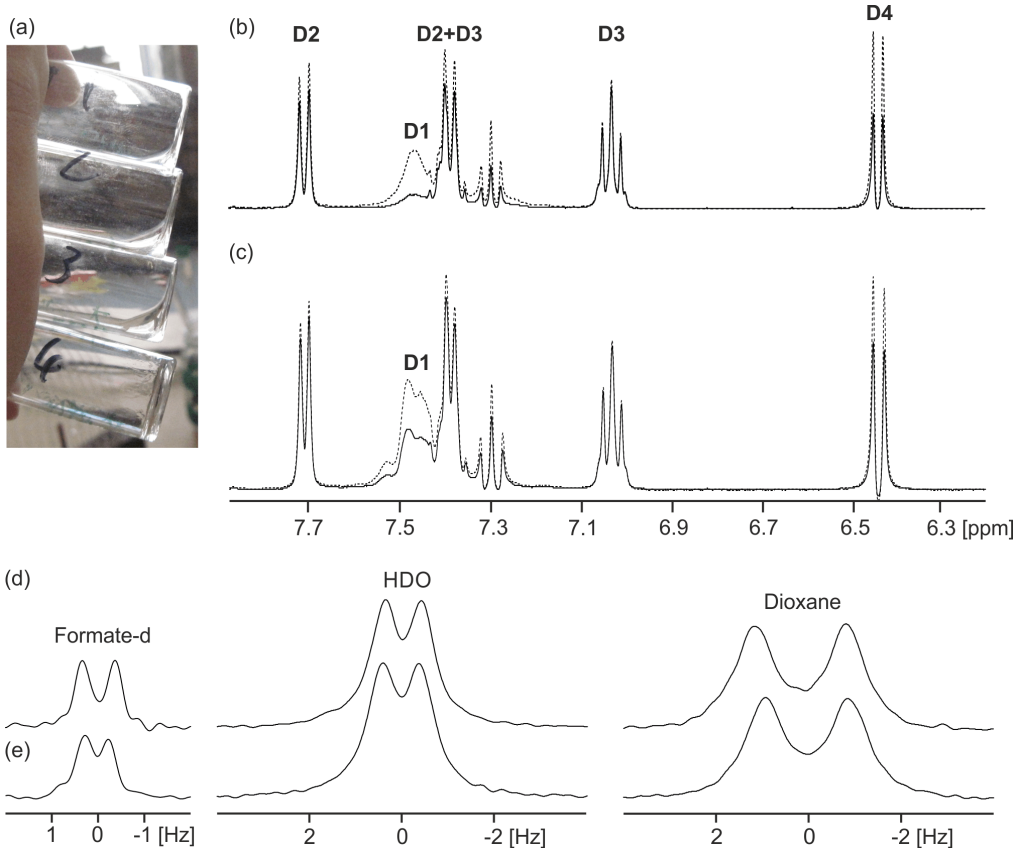

Figure 4-S5c. (a) Photographs of 4 mg/mL solutions of **2** at pH 9 with various model drug compounds, each at 5 mM concentration unless otherwise stated, along with standard set of probe molecules for **2**/$CaCl_2$ gels: **D3** and **D4** (1), 1 mM EDTA (2), **D2**, **D3** and **D4** (3) and **D1**-**D4** (4). (b) NMR spectra of solution of Sample 4, two weeks after the addition of 30 mM $CaCl_2$ (Figure 4-4d, reproduced here for convenience). (c) NMR spectra of a **2**/$CaCl_2$ gel, prepared using the standard set of probe molecules, with 5 mM **D1**-**D4** diffused into the sample. ^{2}H NMR spectra of probe molecules in the **2**/$CaCl_2$ gel before (d) and after (e) **D1**-**D4** were diffused in.

4 mg/mL solutions of **2** at pH 9 prepared with **D2-D4** are free-flowing while solutions prepared with **D1** are not (a). RQCs were not observed for the solution containing **D1** while the other solutions all exhibited RQCs. These observations indicate a strong interaction between **D1** and the structures of **2** that prevents re-orientation in the presence of the magnetic field. Similar STD effects to **D1**-**D4** are observed when they are included in the solution of **2** prior to the addition of $CaCl_2$ (b, Figure 4-4d) and when they are diffused into a **2**/$CaCl_2$ gel (c). In both cases, **D1** exhibits the broadest peaks and the strongest STDs. To prepare the sample of (c-e), a

2/$CaCl_2$ gel was prepared following the standard procedure (Section 4.2.5.2.2). A solution was prepared at pH 9 containing 10 mM **D1**-**D4**, pH indicators (2 mM with respect to sodium acetate), 1 mM disodium maleate, ^2H organic solvents at 0.05 vol% (0.02 vol% MeOH-d_3) and 0.01 vol% of all ^1H solvents (no IPA). Two weeks after the addition of $CaCl_2$ to a solution of **2** to form a gel, ca. 600-640 μL of the **D1**-**D4** solution was placed on top of the gel. The sample was then held in a water bath at 298 K for one month prior to (c, e) being recorded. The RQCs of the probe molecules in the gel show only slight changes as **D1**-**D4** and Na^+ diffuse into the gel and Ca^{2+} diffuses out (d, e).

4.3.6 2/$CaCl_2$ hydrogel at different stages of gelation

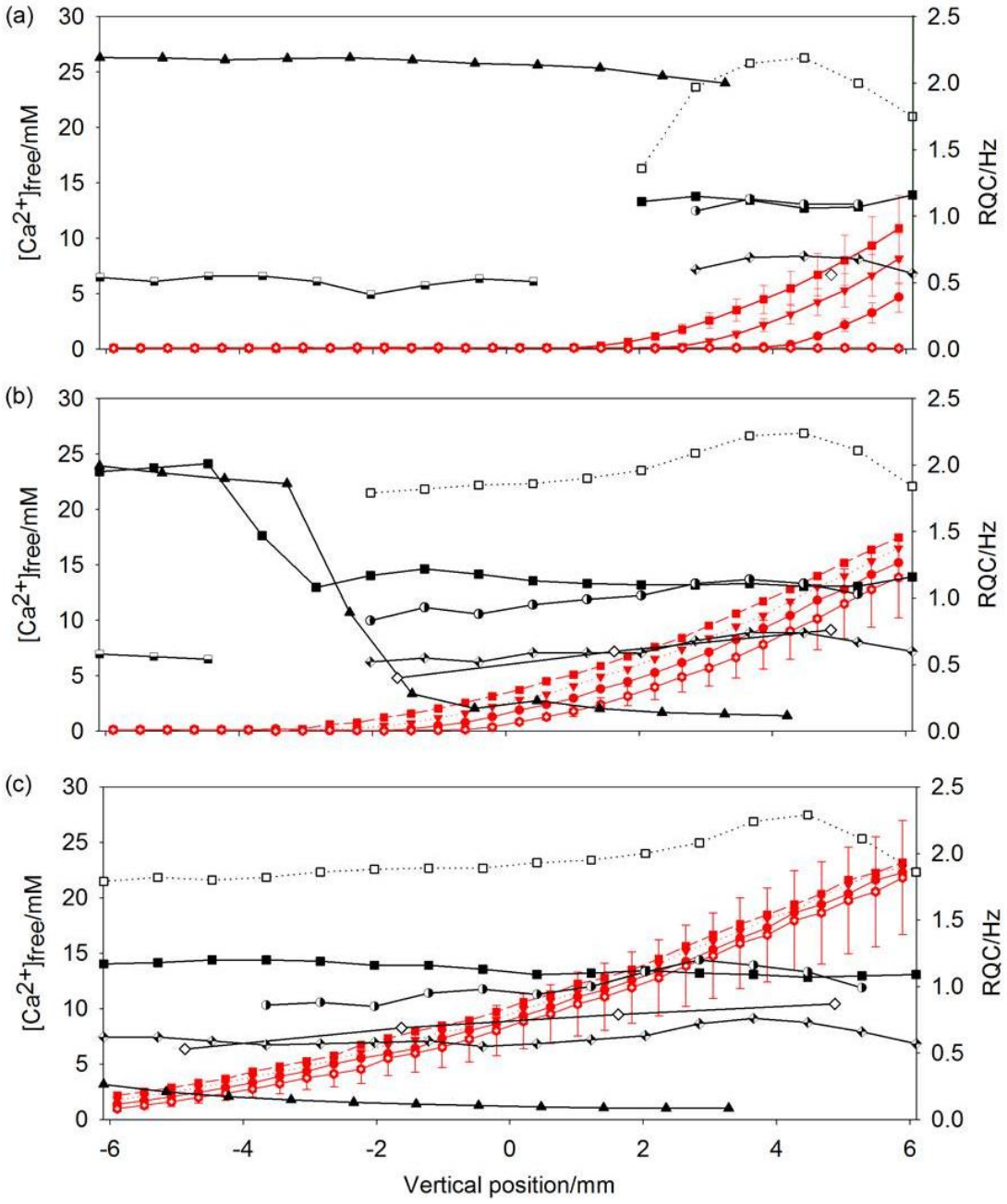

Figure 4-S6. Plots of experimental observables at different stages of a CSI experiment after placing 0.7 M $CaCl_2$ solution on top of a 4 mg/mL solution of **2**: (a) 1 hour, (b) 6 hours and (c) 14 hours. Profiles of RQCs (black): $^{23}Na^+$ (black triangle), formate-d (white diamond), HDO (black square), dioxane (white square), tBuOH (half black circle), acetone (black and white diamond) and MeOH (half black square). The $^{23}Na^+$ RQC has been scaled down by a factor of 500. Red: Profiles of $[Ca^{2+}]_{free}$ before all images (hollow hexagon) – error bars indicate uncertainty in $[Ca^{2+}]_{free}$ measurements – after ^{23}Na image (circle), after formate-d image (down triangle) and after ^{2}H HDO and dioxane image (square). The lines are to guide the eye.

The 0.7 M $CaCl_2$ solution has a higher density than a 4 mg/mL solution of **2** at pH 9. In the early stages of the experiment, the movement of the Ca^{2+} down the tube can thus be driven by gravity rather than diffusion alone. The apparently anomalous rise in the ^2H dioxane coupling at 4 mm height is likely an artefact of this process. Below this point, the progress of the $CaCl_2$ down the tube was very slow so was likely driven by diffusion alone.

4.3.7 *In situ* $[Ca^{2+}]_{free}$ measurements

As with *in situ* pH measurements,[1, 9] the observed chemical shift, δ_{obs}, of our Ca^{2+} indicator molecules is a weighted average of the shifts in the bound and free states:

$$\delta_{obs} = f_{Ca}\delta_{Ca} + (1 - f_{Ca})\delta_f \quad (4S.10)$$

where δ_f and δ_{Ca} are the limiting shifts of the indicator when completely free and bound to Ca^{2+} respectively. fc_a is the fraction of indicators bound to Ca^{2+} at any instant. We define the Ca^{2+} binding constant, K_{Ca}, of maleate(2-) as:

$$K_{Ca} = \frac{[MalCa]}{[Mal][Ca^{2+}]_{free}} \quad (4S.11)$$

where Mal and MalCa represent free and complexed maleate respectively and the square brackets denote concentration. Combining Equations 4S.10 and 4S.11:

$$[Ca^{2+}]_{free} = \frac{1}{K_{Ca}}\left(\frac{\delta_f - \delta_{obs}}{\delta_{obs} - \delta_{Ca}}\right) \quad (4S.12)$$

To obtain K_{Ca}, δ_f and δ_{Ca}, solutions were prepared containing different concentrations of $CaCl_2$ and the following components: 0.1 mM each of disodium maleate, sodium glycolate, sodium methanesulfonate and sodium formate. 0.001 vol% dioxane, methanol, acetone, DMSO and tert-butanol were also included. The water to prepare these solutions (Resistivity 18.2 MΩ.cm) was degassed by bubbling with N_2 for ten minutes. The pH was adjusted from 7 to between 9.7 and 10.5 by the inclusion of 0.2±0.1 mM NaOH. Such a high pH ensures that the maleate is completely in its dianionic form. The total free calcium concentration in solution will not be significantly affected by such a low concentration of base.[41] Likewise, any slight carbonate contamination will not have a significant effect due to the relatively low binding affinity of HCO_3^- for Ca^{2+}.[42] With such a low concentration of weak

Ca^{2+} binders, $[Ca^{2+}]_{free}$ can be assumed equal to the total concentration of $CaCl_2$ added.

Maleate was found to be the most sensitive indicator up to 50 mM Ca^{2+}. Plots of δ_{obs} of maleate versus $[CaCl_2]$ in the presence and absence of 50 mM NaCl are shown in Figure 4-S7 below. Good fits to Equation 4S.12 were obtained with both data sets, fitting up to 50 mM $CaCl_2$. It is clear, however, that there is competition between Ca^{2+} and Na^+ for maleate as the apparent K_{Ca} is substantially reduced in the presence of 50 mM NaCl (Table 4-S7). The dependence of the apparent K_{Ca} of organic ligands on the concentration of competing alkali metal ions has been well documented.[43, 44] In our work on **2**/$CaCl_2$ gels, we need to measure $[Ca^{2+}]_{free}$ along a $CaCl_2$ gradient in the presence of **2**. We cannot accurately know the solution composition (sodium activity, ionic strength) and thus the apparent K_{Ca} at any particular point along our sample. However, K_{Ca} under our experimental conditions is unlikely to fall outside of the range of values determined in our calibration experiment in the presence/absence of 50 mM NaCl. We thus report $[Ca^{2+}]_{free}$ as the median of the values calculated using the fitted K_{Ca}, δ_f and δ_{Ca} in the presence and absence of 50 mM NaCl, with the difference between the two values as the uncertainty in $[Ca^{2+}]_{free}$. The ^1H methyl resonance of MeOH was used as a chemical shift reference rather than methanesulfonate owing to the very slight sensitivity of the latter to Ca^{2+} (data not shown).

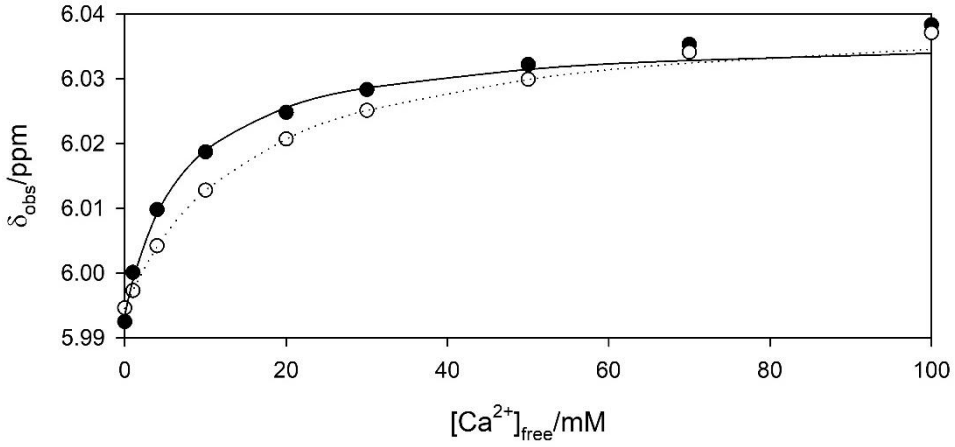

Figure 4-S7. Plot of maleate chemical shift, δ_{obs}, versus $[Ca^{2+}]_{free}$ in the presence (white circle) and absence (black) of 50 mM NaCl. The plotted lines are fits of Equation 4S.12 to the data up to 50 mM Ca^{2+}.

[NaCl]/mM	K_{Ca}/M^{-1}	δ_{Ca}/ppm	δ_f/ppm
0	143.37	6.0367	5.9935
50	65.332	6.0407	5.9946

Table 4-S7. Fitted values of K_{Ca}, δ_f and δ_{Ca} with MeOH (3.36 ppm) as a reference.

The chemical shift difference between maleate(2-) and monohydrogenmaleate(-) was estimated as 0.4 ppm (data not shown). Given a pK_a of 6.0 for maleic acid,[43] the chemical shift will deviate by less than 0.0013 ppm when the pH is 8.5 or above which is the case in all **2**/$CaCl_2$ samples discussed in this work. Such a shift corresponds to an uncertainty in $[Ca^{2+}]_{free}$ of less than 1 mM.

4.3.8 Relaxation of $^{23}Na^{+}$ in 4 mg/mL solutions of 2 and in 2/$CaCl_2$ gels

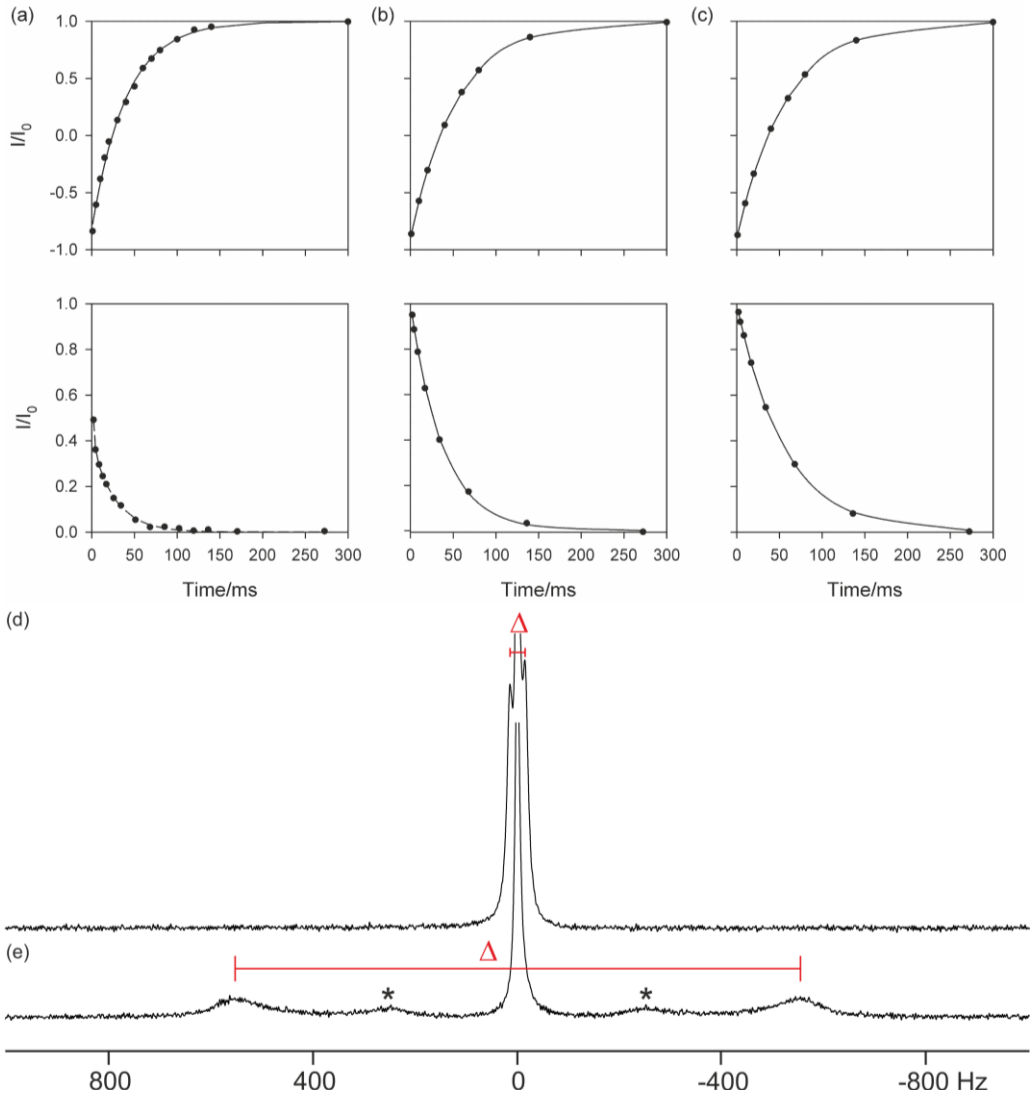

Figure 4-S8a. ^{23}Na T_1 inversion-recovery (upper plots) and T_2 CPMG (lower plots) relaxation curves: (a) 4mg/mL solution of **2** at pH 9 with full set of probe molecules for **2**/$CaCl_2$ gels, (b) **2**/$CaCl_2$ gel seven weeks after addition of $CaCl_2$ and (c) analogous solution in the absence of **2**. Solid lines are fits to Equations 4.1 and 4.2. A bi-exponential fit (dashed) was required for T_2 in (a), fitting to Equation 1 of Shinar *et al.*[45] (d) ^{23}Na NMR spectrum of **2**/$CaCl_2$ gel seven weeks after addition of $CaCl_2$, $[Ca^{2+}]_{free}$ = 25±6 mM and the same sample before the addition of $CaCl_2$ (e). The RQC (Δ) is indicated. The peaks marked * belong to a minor liquid-crystalline phase of **2**.

In the absence of $CaCl_2$ (a), the T_2 relaxation of $^{23}Na^{+}$ is biexponential with a T_2 of 26 ms for the slow component (central peak) and less than 5 ms for the fast component. The fast component decays completely before the second data point and is unfortunately beyond the resolution of our instrument. T_1 in this sample was

measured as 41±1 ms. In the **2**/$CaCl_2$ gel (b), T_2 relaxation is monoexponential with a fitted T_2 of 38±1 ms while T_1 was measured as 54±1 ms. In the absence of **2** (c), T_1 and T_2 are 57±1 and 56±1 ms respectively. These results confirm an increase in mobility of the $^{23}Na^+$ upon addition of $CaCl_2$. The reduced magnitude of T_2 so that $T_1 \neq T_2$ confirms a reduced mobility (increased correlation time) of the $^{23}Na^+$ ions relative to a dilute aqueous solution. We can thus be confident that the $^{23}Na^+$ ions maintain a significant interaction with the gel fibres, even in the presence of an excess of Ca^{2+}. This is further confirmed by a non-zero RQC of 30 Hz in the final gel (d). ^{23}Na NMR spectra were acquired using a $\pi/2$ pulse (32 μs), a 10 kHz sweep width with 3022 data points. 256 scans were acquired. Relaxation measurements performed along the length of the Ca^{2+} gradient (Figure 4-S8b) show how the T_2 relaxation changes from biexponential and fast in the absence of Ca^{2+} to monoexponential and slow in the presence of excess Ca^{2+}. Spatially resolved ^{23}Na relaxation curves were recorded using a modified version of the gradient phase encoding sequence used for ^{23}Na RQC measurements. The pulse sequence was modified to include an inversion-recovery sequence (T_1 image) or a CPMG pulse train (T_2). 8 gradient steps were acquired with 128 scans at 8 delay times at each gradient step (T_1) or 8 different numbers of π pulses (T_2). The acquisition time for the images was 56 minutes for both T_1 and T_2 images. The theoretical spatial resolution is 3.8 mm.

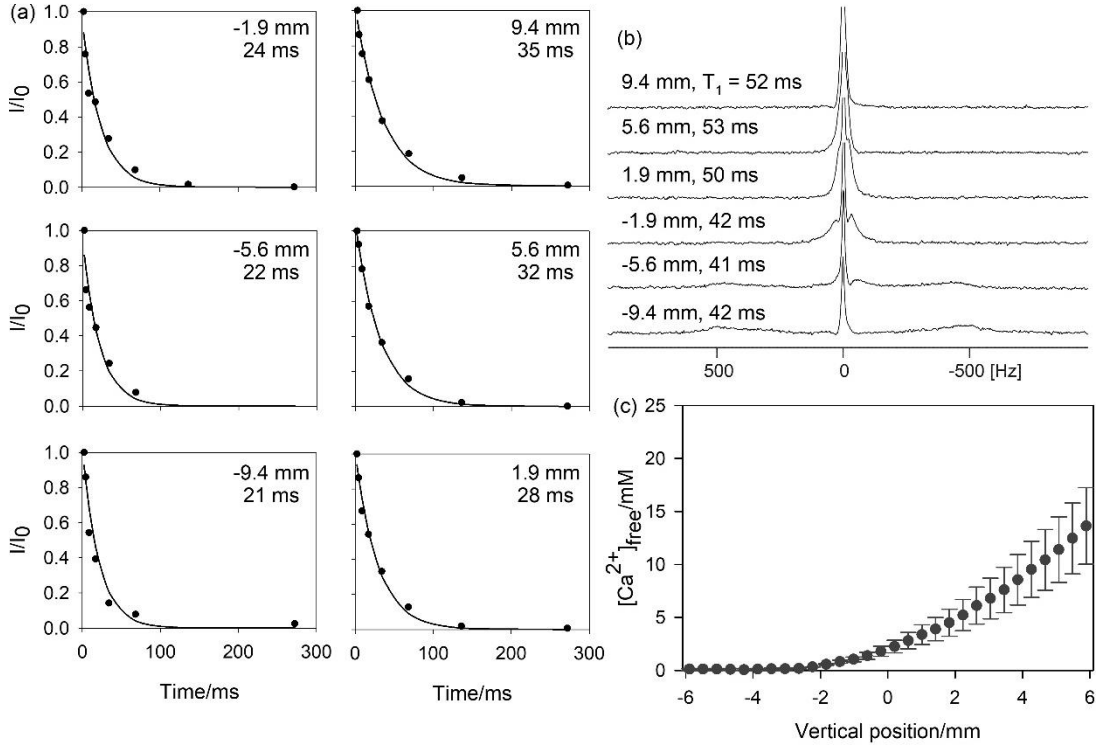

Figure 4-S8b. (a) ^{23}Na CPMG curves recorded at different positions along a Ca^{2+} gradient during formation of a **2**/$CaCl_2$ gel. The monoexponential fits to Equation 4.2 are shown as solid lines. The vertical position and fitted T_2 values are also given. The monoexponential fit gets progressively better moving up the sample from a solution of **2** in the absence of $CaCl_2$ to a **2**/$CaCl_2$ gel. (b) ^{23}Na NMR spectra from the corresponding positions along with T_1 relaxation times. (c) Plot of $[Ca^{2+}]_{free}$ versus vertical position along the sample. In all cases, T_1 relaxation curves fitted perfectly to a monoexponential fit.

4.3.9 Methylammonium as a probe of negative charge in 2/$CaCl_2$ gels

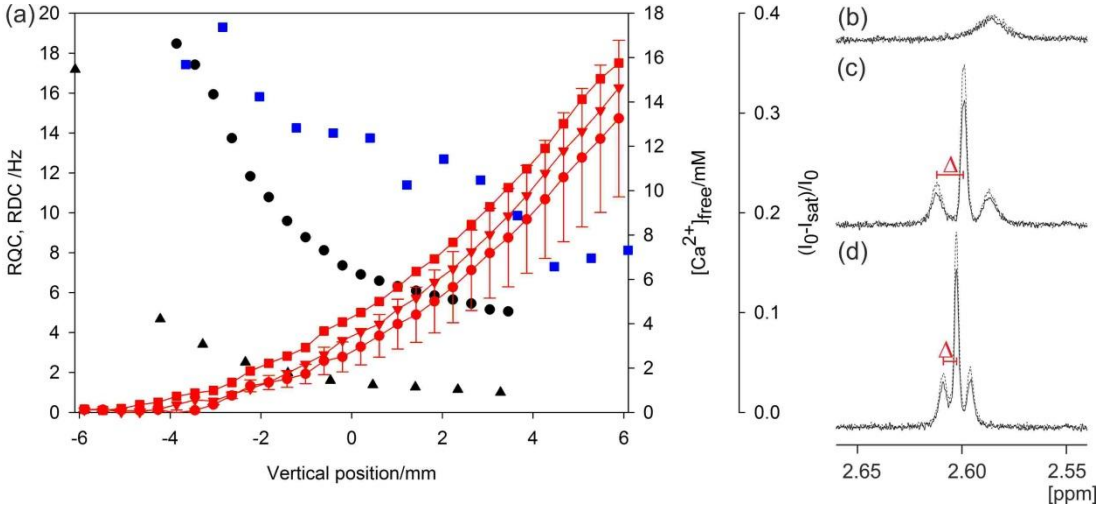

Figure 4-S9. (a) Plots of experimental observables along length of sample: $^{23}Na^+$ RQC scaled down by factor of 50 (black triangle), residual dipolar coupling (RDC) of methylammonium (black circle) and STD of methylammonium (blue square). Plots of $[Ca^{2+}]_{free}$ before all CSI experiments (red circle, with uncertainties shown as error bars), after the ^{23}Na image (red triangle, methylammonium RDCs were acquired from the same ^1H image) and after the methylammonium STD experiment (red square). (b-d): ^1H NMR spectra of the methylammonium resonance with (solid) and without (dashed) on-resonance presaturation applied to the gel fibres. (b) 4 mg/mL solution of **2** in absence of $CaCl_2$. (c) **2**/$CaCl_2$ gel during formation, extracted from STD image (a) at 2.8 mm, at $[Ca^{2+}]_{free}$ of 9±3 mM. (d) **2**/$CaCl_2$ gel three weeks after addition of $CaCl_2$ at $[Ca^{2+}]_{free}$ of 22±5 mM. The RDCs (Δ) are indicated.

In the absence of $CaCl_2$, methylammonium binds strongly to the structures of **2** and gives a very broad resonance. Integration suggests only 30-40% of the methylammonium is NMR-visible. Upon addition of $CaCl_2$, a sharper resonance becomes apparent (c) which is split 1:2:1 by a residual dipolar coupling (RDC). Integration of this resonance shows that all the methylammonium is NMR visible. As more $CaCl_2$ diffuses down the tube, the methylammonium RDC falls in tandem with the $^{23}Na^+$ RQC as well as the methylammonium STD. However, the RDC and STD of methylammonium are appreciable in the final **2**/$CaCl_2$ gel (d) suggesting that methylammonium remains in competition with Ca^{2+}. Methylammonium is thus analogous in its behaviour to $^{23}Na^+$. STD images were acquired as described for **2**/glycolic acid gels in Section 4.3.4.2.

4.3.10 Analysis of residual dipolar couplings (RDCs) of different probe molecules in 2/$CaCl_2$ gels

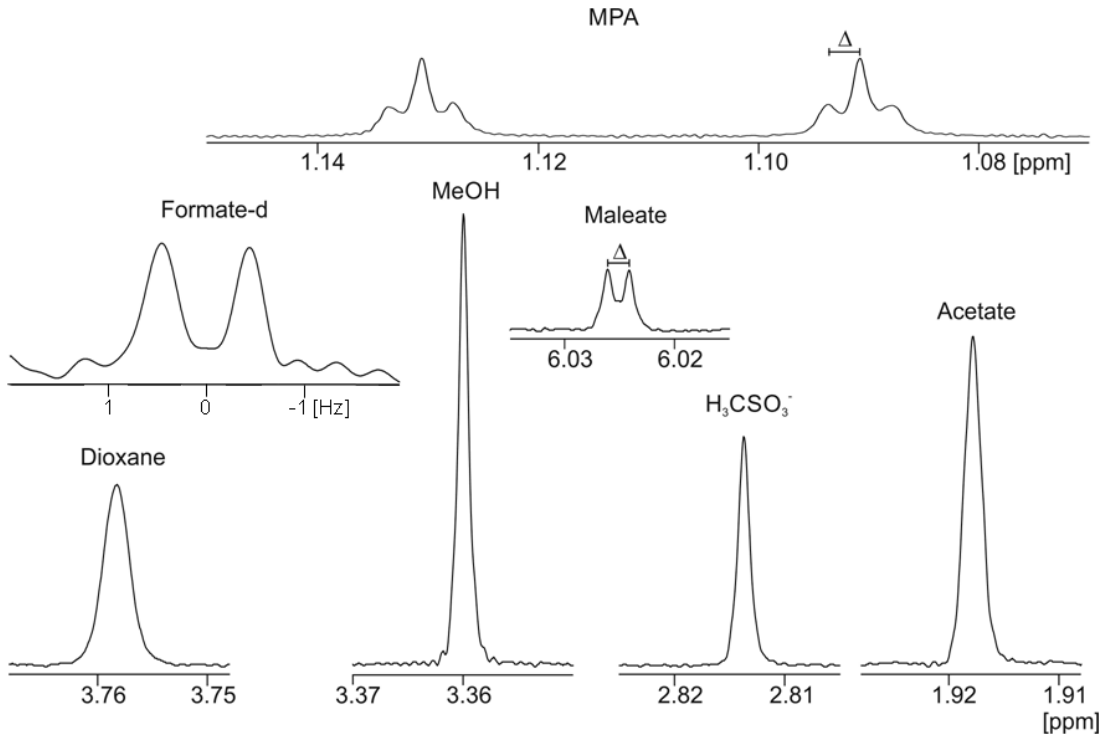

Figure 4-S10. ^{1}H NMR spectra of probe molecules in **2**/$CaCl_2$ gel along with ^{2}H spectrum of formate-d. RDCs (Δ) are observable on the maleate and MPA^{2-} resonances, while weaker Ca^{2+} binders such as acetate and methanesulfonate do not exhibit RDCs. $[Ca^{2+}]_{free}$ in this sample was measured as 24±6 mM throughout. ^{1}H spectra were extracted from a CSI image (off-resonance) recorded as described for **2**/glycolic acid gels (Section 4.3.4.2). ^{2}H spectrum of formate was extracted from the same region of an 8 point CSI image. RQC of formate-d was measured as 0.9 Hz. Sample is shown nine days after the addition of $CaCl_2$. RDCs and RQCs were the same when re-measured six weeks later. Due to the $[Ca^{2+}]_{free}$ dependence of the MPA^{2-} and maleate chemical shifts, RDCs could not be measured during the gel formation process along the Ca^{2+} gradient owing to a slight broadening of the peaks in the CSI image. RDCs were observable on the MPA^{2-} resonance once $[Ca^{2+}]_{free}$ exceeded 10±3 mM and on the maleate resonance after 19±5 mM; in both cases the change in chemical shift with $[Ca^{2+}]_{free}$ was small enough for RDCs to be observed. No RDCs were observed in the absence of Ca^{2+}.

4.3.11 ^{43}Ca NMR analysis of a 2/$CaCl_2$ gel

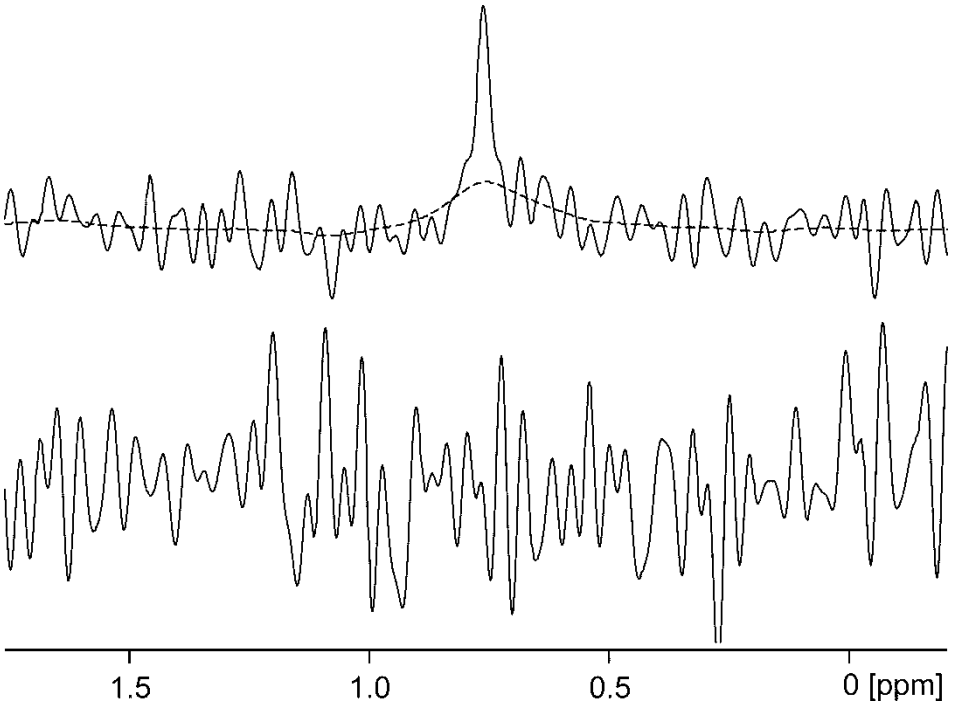

Figure 4-S11. (Top) ^{43}Ca NMR spectrum of a H_2O solution at pH 9 containing 20 mM $CaCl_2$ and all the probe molecules present in **2**/$CaCl_2$ gels (Section 4.2.5.2.2). The dashed line is the spectrum when an exponential line broadening factor of 4 Hz is applied to the FID prior to Fourier transformation. (Bottom) ^{43}Ca NMR spectrum of a **2**/$CaCl_2$ gel. The concentration of free Ca^{2+} ions was uniform throughout the sample at 25±6 mM.

No ^{43}Ca NMR resonances are apparent in a **2**/$CaCl_2$ gel whereas a sharp peak is observed in an analogous solution at the same pH in the absence of **2**. We can thus invoke the existence of a fast exchange of the Ca^{2+} ions between the gel fibres and the solution phase that broadens the ^{43}Ca resonance to the extent that it is not visible above the baseline noise. We can estimate a lower limit for the fraction of Ca^{2+} ions, $f_{b,min}$, that are associated with the gel fibres at any instant. Assuming a Lorentzian line shape, the observed ^{43}Ca half-height line width, w_{obs}, in the gel is given by:

$$w_{obs} = f_b w_b + (1 - f_b) w_f \qquad (4.S13)$$

where w_{obs} and w_f are the ^{43}Ca line widths of the Ca^{2+} ions associated with the fibres and free in solution respectively. f_b is the fraction of Ca^{2+} ions associated with the gel fibres. Rearranging 4.S13:

$$f_b = \frac{w_{obs} - w_f}{w_b - w_f} \tag{4.S14}$$

The minimum linewidth, w_{min}, for a resonance to be visible above the baseline noise is given by:

$$w_{min} = \frac{w_f h_f}{h_n} \tag{4.S15}$$

where h_n and h_f are respectively the heights of the noise and the ^{43}Ca resonance in the solution in the absence of **2**. From Figure 4-S11, $h_f/h_n = 4$ and $w_f = 1$ Hz, and it can thus be estimated that a resonance with a width greater than 4 Hz would not be observable. This theory is confirmed by applying an artificial broadening factor of 4 Hz to the spectrum (Figure 4-S11, dashed line) – the peak is at the same level as the noise when no line broadening factor is applied. Combining 4.S14 and 4.S15:

$$f_{b,min} = \frac{w_f \left(\frac{h_f}{h_n} - 1\right)}{w_b - w_f} \tag{4.S16}$$

A sensible estimate for w_b is 200 Hz, based on the ^{43}Ca linewidths of Ca^{2+} bound to Lactalbumins reported by Aramini *et al.*[46] and so $f_{b,min} \geq 1\%$. We note that the non-appearance of a ^{43}Ca-NMR peak in the gel could be attributed to other causes, such as the presence of ^{43}Ca RQCs or a slow exchange of the free and bound Ca^{2+} leading to coalescence of the two resonances. Whatever the cause, a significant interaction of the 'free' Ca^{2+} ions with the gel fibres can be invoked. Spectra were acquired using the aring sequence with a 58 μs pulse (π/2), a sweep width of 2000 Hz, a signal acquisition time of 1 s and a relaxation delay of 0.1 s. 184,000 and 524,000 scans were acquired for the top and bottom spectra of Figure 4-S11 respectively, giving total acquisition times of 2 days 13 hours and 7 days respectively.

4.3.12 Stability of a 2/$CaCl_2$ gel when exposed to an external NaCl solution

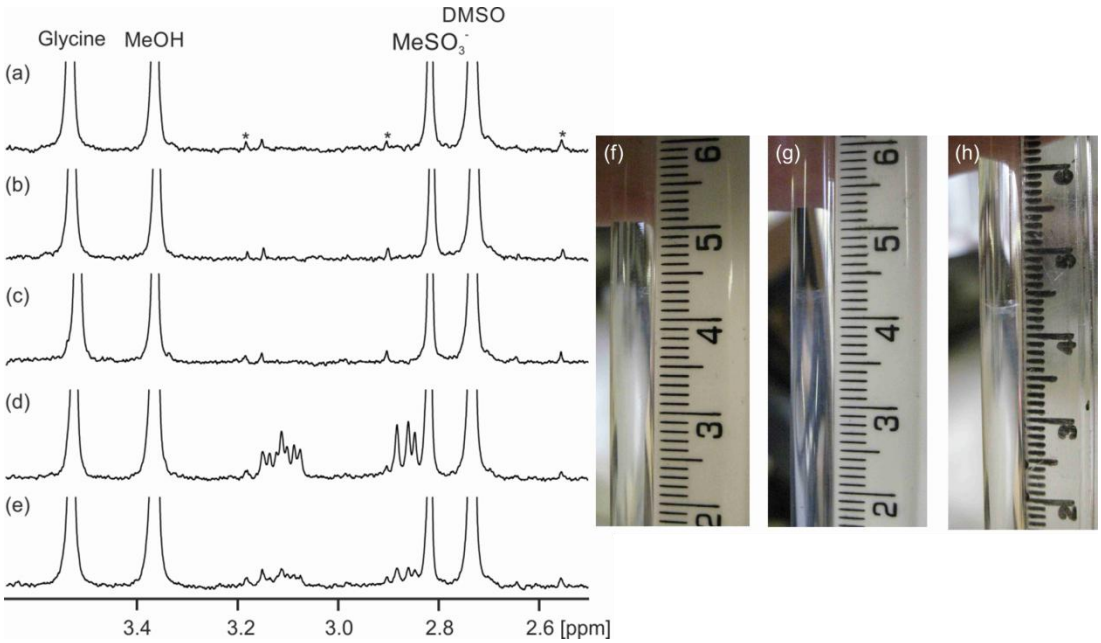

Figure 4-S12. (a-c) ^{1}H NMR spectra of solutions that had stood on top of a **2**/$CaCl_2$ gel: (a) first solution after 26 days, (b) second solution after 9 days and (c) third solution after 17 days. $[Ca^{2+}]_{free}$ in these solutions was measured as 4±1 mM, 1±0.3 mM and < 1 mM respectively. The peaks marked * are ^{13}C satellite peaks of the organic solvents. The satellite to the left of $MeSO_3^-$ (^{13}C-DMSO) corresponds to 40 μM of ^{1}H nuclei. (d) ^{1}H NMR spectrum of solution of **2** at a concentration 0.4 mg/mL. (e) Sample of (d) after addition of 1 mM $CaCl_2$. Photographs of the top of the gel immediately after the first solution was placed on top (f), after the second solution had stood for 9 days (g) and after the third solution had stood for 17 days (h). The ruler was held against the bottom of the tube in all images.

No resonances attributable to **2** were detectable in the solutions that had stood on top of the gels (a-c). An 0.4 mg/mL solution of **2** is shown for comparison (d) where the resonances of the CH_2 protons of the phenylalanine moiety are clearly visible. Addition of 1 mM $CaCl_2$ to the 0.4 mg/mL solution of **2** resulted in a white precipitate, suggesting a very low solubility of **2** in the presence of Ca^{2+} (e). No swelling or erosion of the gels was visually apparent at any stage (f-h). Spectra were acquired using a double-echo WATERGATE sequence in 8 scans with a signal acquisition time of 3.7 s and a relaxation delay of 1 s.

4.3.13 ^{23}Na and ^{2}H analysis of 2/$CaCl_2$ gel exposed to external NaCl solutions

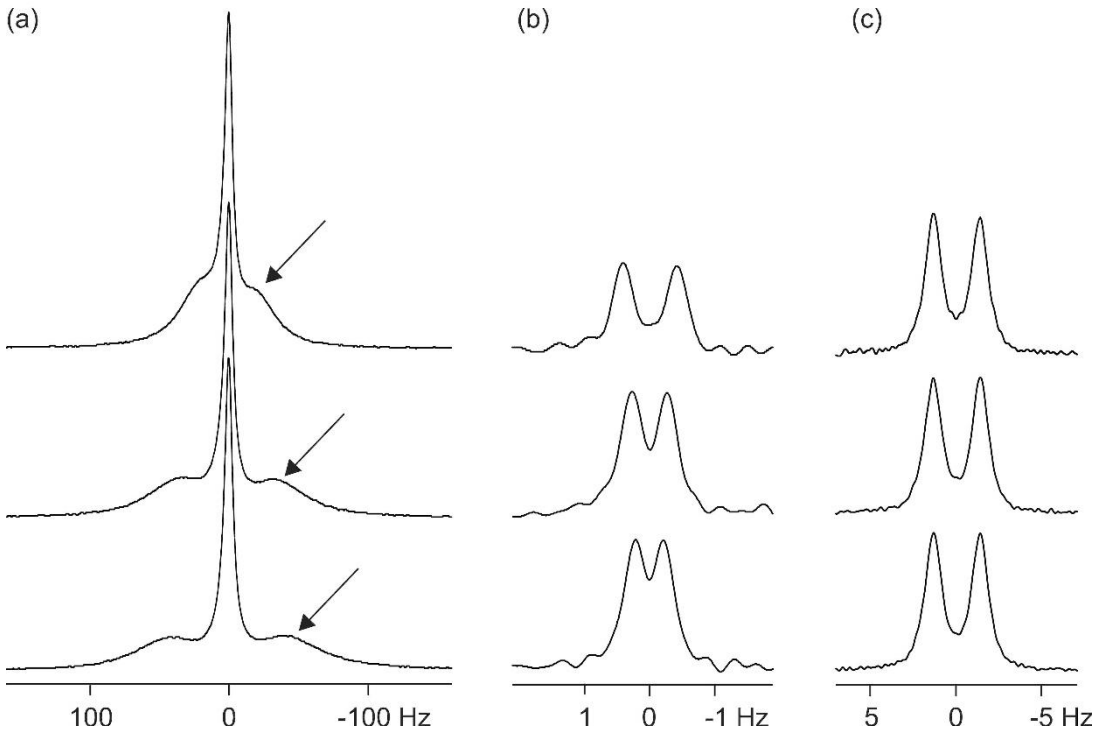

Figure 4-S13. NMR spectra of $^{23}Na^{+}$ (a), sodium formate-d, ^{2}H (b) and dioxane-d_8, ^{2}H (c) in **2**/$CaCl_2$ gel of Figure 4-6 before an NaCl solution was placed on top (upper), at the end of the second series of measurements (middle) and after a third solution had stood on top of gel for 17 days (lower). Although $^{23}Na^{+}$ RQCs cannot be resolved, the 'satellite' peaks (arrowed) move away from the central resonance indicating a stronger interaction of Na^{+} with the fibres.

4.3.14 Quantification of the amount of negative charge on 3/DMSO gels

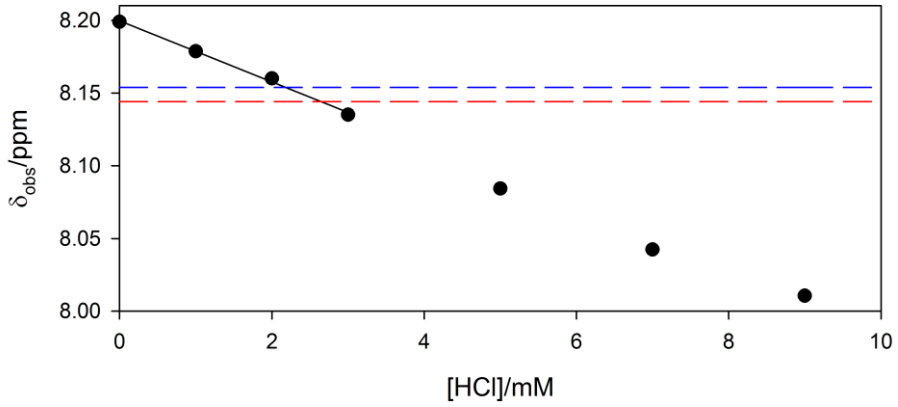

Figure 4-S14a. Plot of formate chemical shift, δ_{obs}, versus concentration of HCl. The solid black line is a fit to Equation 4.S17. The dashed lines represent the chemical shifts of formate in two nominally identical **3**/DMSO gels prepared using the standard set of probe molecules listed in the text.

Solutions of the probe molecules, detailed in Section 4.2.5.2.3, were prepared in 80% H_2O, 20% DMSO at different concentrations of HCl. From Figure 4-S14a, it is apparent that the formate resonance in 5 mg/mL (12 mM) gels of **3** is shifted by the same amount as when 2.4±0.2 mM HCl is included in the absence of **3** (data from two samples). HCl behaves as a strong acid even in DMSO[47] and so 2.4±0.2 mM H^+ has been transferred to the formate from **3**. The fraction of carboxylates of **3** in the gel samples that are deprotonated can thus be calculated as (2.4±0.2 mM)/12 mM = 20±2%. When the concentration of HCl is less than the total concentration of formate, $[Form]_{tot}$, the concentration of formic acid in the sample will be equal to the concentration of added HCl, the concentration of free H^+ being negligible. The observed chemical shift of formate, δ_{obs}, is thus described by the equation:

$$\delta_{obs} = \delta_l - [HCl]\frac{\delta_l - \delta_H}{[Form]_{total}} \qquad (4.S17)$$

where δ_l and δ_H are the limiting chemical shifts of formate in the fully deprotonated and protonated states. $[Form]_{total}$ is the total concentration of formate and formic acid. This equation provides an acceptable fit between 0 and 3 mM HCl (Figure 4-S14a). To investigate the effect of hydrogen bonding to the gel fibres of **3** on the formate chemical shifts, a solution of the probe molecules was prepared and the pH

adjusted to 4.5 with HCl; the same pH as the **3**/DMSO gel containing the probe molecules. The chemical shift of formate in this sample was measured as 8.153 ppm, in very close agreement with the shift measured in a **3**/DMSO gel. We can conclude that any H-bonding of formate to the gel fibres does not significantly affect its chemical shift.

pH measurements were performed using a Hanna Instruments 'Edge' pH data logger equipped with an FC2020 probe. Before use, the meter was calibrated using fresh pH 4, 7, and 10 buffer solutions. The pH of 1 mM HCl was measured as 3.06 in H_2O and 3.15 in 80% H_2O, 20% DMSO and was unaffected by the addition of 15 mM NaCl. Our meter is thus only slightly (< 0.1 pH unit) affected by the presence of the DMSO.[48] Self-supporting hydrogels were formed with either pure H_2O or with the standard set of probe molecules listed in the main text (Figure 4-S14b).

Figure 4-S14b. Photographs of **3**/DMSO gels prepared with the set of probe molecules listed in the text (left) or with pure H_2O (right), 20 hours after preparation.

4.3.15 ^{1}H NMR analysis of 3/DMSO gels

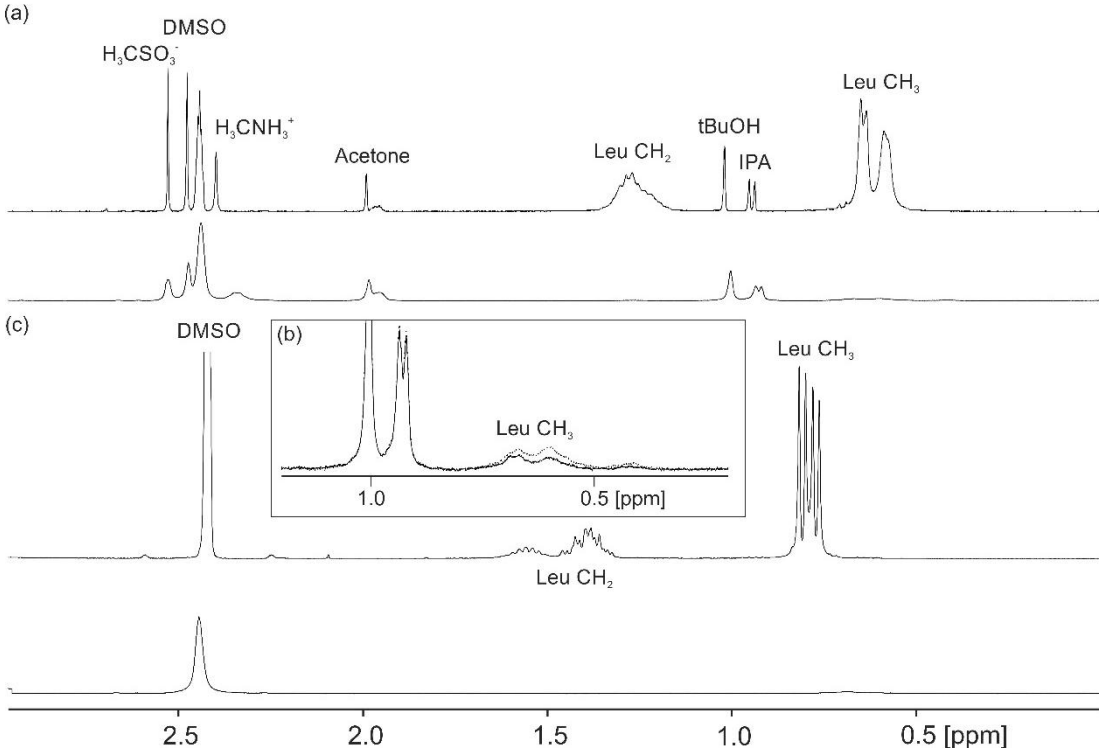

Figure 4-S15a. (a) ^{1}H NMR spectrum of **3**/DMSO gel sample as prepared at 298 K (lower plot) and when heated to 363 K (upper plot) to melt the sample.[36] This gel contained the probe molecules listed in the main text (Section 4.2.5.2.3). The spectra have been scaled according to the absolute integrals of the DMSO, methylammonium and methanesulfonate peaks and referenced to methanesulfonate (2.53 ppm). By integration, less than 5% of **3** is visible in the gel as prepared at 298 K, as compared to 363 K. (b) (inset) Expanded spectrum of **3**/DMSO gel at 298 K recorded with (solid) and without (dashed) on resonance presaturation applied to the gel fibres. Strong STDs are observed to the signal of the residual gelator indicating a strong interaction/exchange with the self-assembled fibres. (c) ^{1}H NMR spectrum of **3**/DMSO gel without any probe molecules as prepared at 298 K (lower plot) and 5 mg/mL **3** dissolved in 100% DMSO-d_6 (upper plot). The spectra have been scaled according to the absolute integral of the residual protonated peak of the DMSO-d_6. Again, less than 5% of **3** is visible in the gelled state at 298 K. The peaks in the gels at 298 K are broad due to entrapped air bubbles. Spectra shown were obtained using the standard sequence for STD measurements with off-resonance presaturation. Integrals obtained with no presaturation applied were the same.

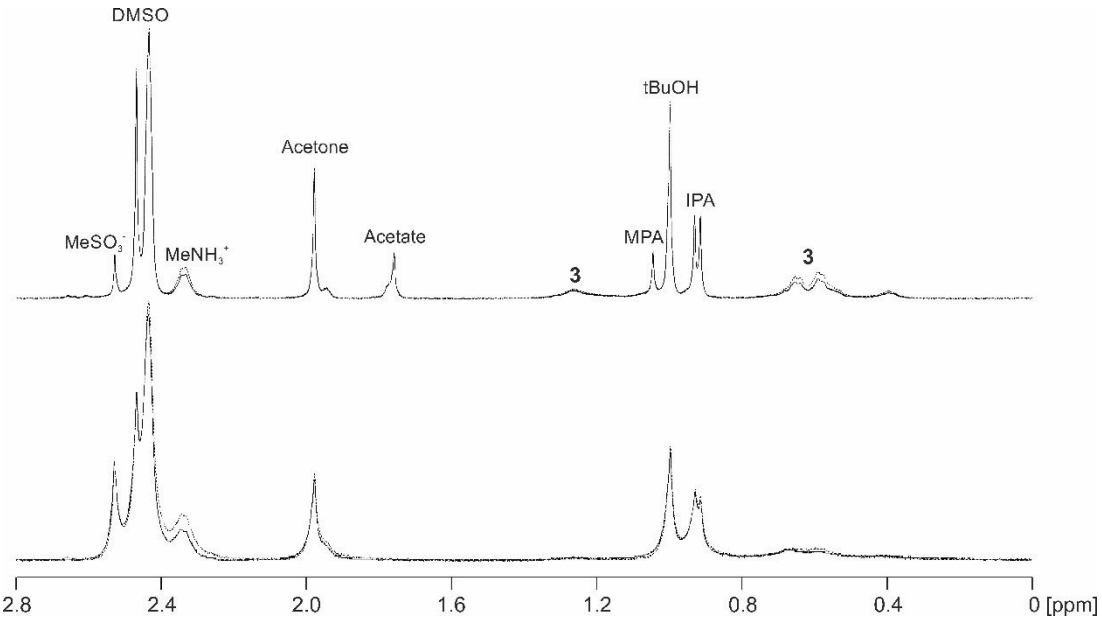

Figure 4-S15b. ^{1}H NMR spectra of **3**/DMSO gels recorded with (solid) or without (dashed) on-resonance presaturation applied to the gel fibres. Gels were prepared with the standard set of probe molecules listed in the main text (lower) or with 1 mM glycinate, MPA^{2-}, acetate, 2 mM formate-h, 5 mM formate-d, 0.5 mM methanesulfonate and all of the ^{1}H and ^{2}H solvents listed in Table 4-1 at 0.05 and 0.01 vol% respectively (upper). Methanol-d_3 was included at 0.02 vol%. Spectra were recorded 20 minutes after gel preparation. The lower spectra have been scaled to the same height as the upper spectra to balance the effect of the broader lines (greater air-bubble formation) in the lower sample. The ^{1}H NMR resonances of **3** are larger when the basic additives are included (Figure 4-S15b).

4.3.16 Comparison of ^{1}H gelator integrals of 1 during formation of 1/GdL gels acquired with presaturation and WATERGATE solvent suppression techniques

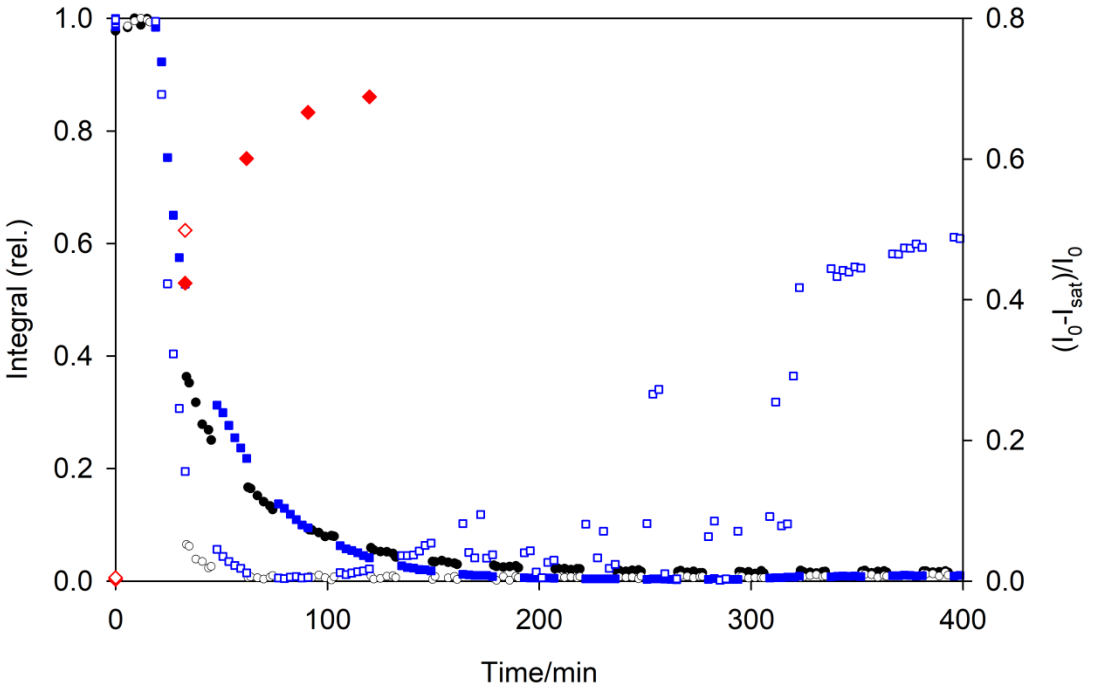

Figure 4-S16. Plots of ^{1}H integrals of valine methyl (solid symbols) and aromatic (hollow symbols) resonances of **1** during formation of **1**/GdL gel. Integrals were obtained either in a single scan with presaturation applied to the H_2O resonance (black circle) or using a double-echo WATGERGATE sequence (blue square). WATERGATE integrals were obtained from off-resonance STD spectra. STDs (8 s presaturation time) to the gelator resonances (red diamond) are also plotted. After 100 minutes, NH resonances of NH_4^+ and $MeNH_3^+$ become visible on WATERGATE spectra that overlap with the aromatic region of the gelator integral.

Integrals acquired using either presaturation or WATERGATE solvent suppression techniques are qualitatively the same, although we note that neither method is strictly quantitative. Spectra recorded with presaturation to H_2O are affected by STDs to the NMR-visible gelators while WATERGATE spectra are affected by T_2 relaxation during the pulse sequence and J-modulation effects. No STDs are apparent to the gelators before the addition of GdL, indicating minimal aggregation of the gelators at high pH. Upon assembly, strong STDs become apparent to both resonances of the gelator indicating a strong interaction or exchange of the NMR-visible gelator with

the newly-formed fibres. We note that the STD spectra were acquired with interleaved on and off-resonance scans, each of 10 s, and so assembly of the gelators during an individual STD measurement will not significantly affect the results. The faster disappearance of the aromatic resonance of **1** can be attributed to a stronger affinity of this hydrophobic portion of the molecule for **1**/GdL fibres relative to the dipeptide portion of the molecule. Analogous results were obtained for **3**/GdL gels (data not shown).

4.3.17 2/$MgCl_2$ hydrogels

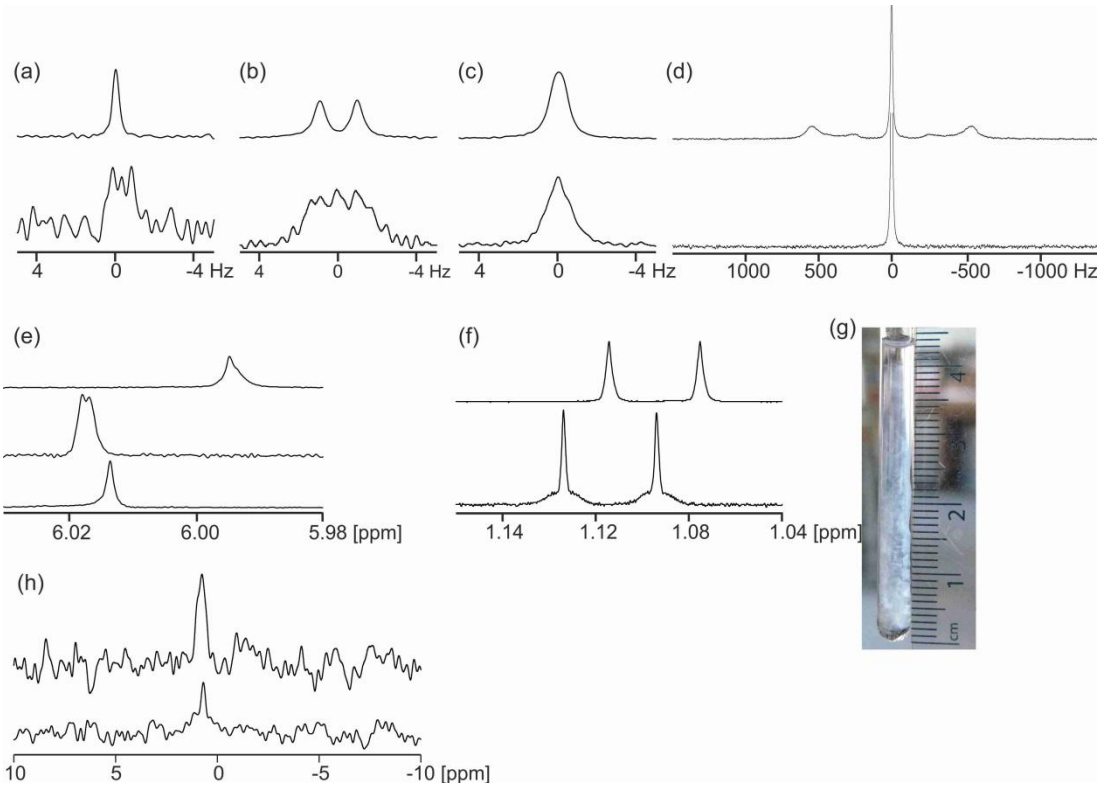

Figure 4-S17. NMR spectra of probe molecules in gel prepared with $MgCl_2$ in place of $CaCl_2$: ^2H spectra of formate-d (a), HDO (b), dioxane-d_8 (c). ^{23}Na spectrum of $^{23}Na^+$ (d), ^1H spectra of maleate (e) and MPA^{2-} (f). The upper spectra were recorded prior to the addition of $MgCl_2$ while the lower were recorded in a gel 8 days after $MgCl_2$ addition. In (e), the middle spectrum was recorded in the gel sample while the lower was recorded in an analogous solution in the absence of **2** containing 20 mM $MgCl_2$. (g) Photograph of gel sample 8 days after the addition of $MgCl_2$. (h) ^{25}Mg NMR spectrum of gel sample, recorded 3 months after the addition of $MgCl_2$ (lower) and an analogous solution in the absence of **2** containing 20 mM $MgCl_2$. The upper spectrum has been scaled up by a factor 4 to account for the different number of scans taken in each case.

Addition of $MgCl_2$ to a solution of **2**, in place of $CaCl_2$, results in a severe syneresis of the gel (g). The syneresis results in the emergence of isotropic peaks on the ^2H resonances of the probe molecules in addition to the doublet arising from probe molecules in the gel phase (a-c). Nevertheless, the changes observed in the surface chemistry of the fibres are similar to those observed upon the addition of $CaCl_2$. Gelation can be seen to proceed with a displacement of Na^+ from the fibres and an association of Mg^{2+}. The $^{23}Na^+$ RQC observable in the absence of Mg^{2+} is undiscernible in the gel phase (d) while RQCs are apparent on the resonance of formate-d (a) and RDCs are apparent on the ^1H resonances of maleate (e) and MPA^{2-} (f). By ^{25}Mg NMR (h), only a very weak resonance is apparent which is attributable to free Mg^{2+} ions in the fluid exuded during syneresis. A much larger resonance is apparent in a solution containing 20 mM $MgCl_2$ but no **2**, despite this solution having a lower apparent concentration of free Mg^{2+} ions as determined from the ^1H shift of maleate (h, lower). These observations imply a close association of Mg^{2+} with the gel fibres which severely broadens the $^{25}Mg^{2+}$ resonance in the gel phase, in analogy with the $^{43}Ca^{2+}$ resonance in **2**/$CaCl_2$ gels (Section 4.3.11).

Gels were prepared following the same procedure as detailed in Section 4.2.5.2.2, but with $MgCl_2$ in place of $CaCl_2$. ^{25}Mg NMR spectra were acquired using the aring sequence with a 58 μs π/2 pulse, an acquisition time of 1 s, a sweep width of 2 kHz and a relaxation delay of 0.1 s. 184,320 scans were acquired for the gel while 46,080 scans were acquired for the solution. Spectra (a) – (f) were acquired from the same region of the sample using CSI methods, as described in Sections 4.2.5.3 and 4.3.10.

4.3.18 Supporting Information: References

1. M. Wallace, J. A. Iggo and D. J. Adams, *Soft Matter*, 2015, **11**, 7739-7747.
2. Y. Pocker and E. Green, *J. Am. Chem. Soc.*, 1973, **95**, 113-119.
3. M. Tena-Solsona, B. Escuder and J. F. Miravet, *Chem. Mater.*, 2015, **27**, 3358-3365.
4. A. Z. Cardoso, L. L. E. Mears, B. N. Cattoz, P. C. Griffiths, R. Schweins and D. J. Adams, *Soft Matter*, 2016, **12**, 3612-3621.
5. L. H. Sommer, J. R. Gold, G. M. Goldberg and N. S. Marans, *J. Am. Chem. Soc.*, 1949, **71**, 1509-1509.

6. A. Shimizu, M. Ikeguchi and S. Sugai, *J. Biomol. NMR*, 1994, **4**, 859-862.
7. J. Kříž and J. Dybal, *J. Phys. Chem. B*, 2004, **108**, 9306-9314.
8. M. M. Chui, R. J. Phillips and M. J. McCarthy, *J. Colloid Interface Sci.*, 1995, **174**, 336-344.
9. J. J. H. Ackerman, G. E. Soto, W. M. Spees, Z. Zhu and J. L. Evelhoch, *Magn. Reson. Med.*, 1996, **36**, 674-683.
10. C. A. Lepre, J. M. Moore and J. W. Peng, *Chem. Rev.*, 2004, **104**, 3641-3675.
11. J. Angulo, P. M. Enríquez-Navas and P. M. Nieto, *Chem. Eur. J.*, 2010, **16**, 7803-7812.
12. A. Delville, J. Grandjean and P. Laszlo, *J. Phys. Chem.*, 1991, **95**, 1383-1392.
13. D. T. Edmonds and A. L. Mackay, *J. Magn. Reson.*, 1975, **20**, 515-519.
14. B. Halle and H. Wennerström, *J. Chem. Phys.*, 1981, **75**, 1928-1943.
15. P. Porion, M. P. Faugère, E. Lécolier, B. Gherardi and A. Delville, *J. Phys. Chem. B*, 1998, **102**, 3477-3485.
16. M. Wallace, A. Z. Cardoso, W. J. Frith, J. A. Iggo and D. J. Adams, *Chem. Eur. J.*, 2014, **20**, 16484-16487.
17. P. G. Daniele, C. Foti, A. Gianguzza, E. Prenesti and S. Sammartano, *Coord. Chem. Rev.*, 2008, **252**, 1093-1107.
18. F. S. Millett and B. P. Dailey, *J. Chem. Phys.*, 1972, **56**, 3249-3256.
19. D. M. Chen, L. W. Reeves, A. S. Tracey and M. M. Tracey, *J. Am. Chem. Soc.*, 1974, **96**, 5349-5356.
20. D. J. Ruben and S. G. Kukolich, *J. Chem. Phys.*, 1974, **60**, 100-102.
21. J. P. Jacobsen and K. Schaumburg, *J. Magn. Reson.*, 1977, **28**, 191-201.
22. M. R. Gallyamov, D. N. Dybtsev, D. P. Pischur, S. G. Kozlova, N. K. Moroz and V. P. Fedin, *J. Phys. Chem. C*, 2015, **119**, 24769-24773.
23. N. S. Balakrishnan, *J. Magn. Reson.*, 1989, **83**, 233-245.
24. C. Naumann, W. A. Bubb, B. E. Chapman and P. W. Kuchel, *J. Am. Chem. Soc.*, 2007, **129**, 5340-5341.
25. A. Canales, J. Jiménez-Barbero and M. Martín-Pastor, *Magn. Reson. Chem.*, 2012, **50**, S80-S85.
26. D. E. Woessner, *Concepts Magn. Reson.*, 2001, **13**, 294-325.

27. L. A. Rijniers, P. C. M. M. Magusin, H. P. Huinink, L. Pel and K. Kopinga, *J. Magn. Reson.*, 2004, **167**, 25-30.
28. W. H. Braunlin, H. J. Vogel and S. Forsén, *Eur. J. Biochem.*, 1984, **142**, 139-144.
29. H. Gustavsson and B. Lindman, *J. Am. Chem. Soc.*, 1975, **97**, 3923-3930.
30. A. Castilla, M. Wallace, l. Mears, E. Draper, J. Doutch, S. E. Rogers and D. J. Adams, *Soft Matter*, 2016, **12**, 7848-7854.
31. E. R. Draper, J. R. Lee, M. Wallace, F. Jackel, A. J. Cowan and D. J. Adams, *Chem. Sci.*, 2016, **7**, 6499-6505.
32. M. D. Segarra-Maset, B. Escuder and J. F. Miravet, *Chem. Eur. J.*, 2015, **21**, 13925-13929.
33. A. Pallagi, P. Sebk, P. Forgó, T. Jakusch, I. Pálinkó and P. Sipos, *Carbohydr. Res.*, 2010, **345**, 1856-1864.
34. A. Z. Cardoso, A. E. Alvarez Alvarez, B. N. Cattoz, P. C. Griffiths, S. M. King, W. J. Frith and D. J. Adams, *Faraday Discuss.*, 2013, **166**, 101-116.
35. N. A. Dudukovic and C. F. Zukoski, *Langmuir*, 2014, **30**, 4493-4500.
36. L. Chen, J. Raeburn, S. Sutton, D. G. Spiller, J. Williams, J. S. Sharp, P. C. Griffiths, R. K. Heenan, S. M. King, A. Paul, S. Furzeland, D. Atkins and D. J. Adams, *Soft Matter*, 2011, **7**, 9721-9727.
37. A. Rapp, K. Ermolaev and B. M. Fung, *J. Phys. Chem. B*, 1999, **103**, 1705-1711.
38. P. Van Der Asdonk, M. Keshavarz, P. C. M. Christianen and P. H. J. Kouwer, *Soft Matter*, 2016, **12**, 6518-6525.
39. B. Escuder, J. F. Miravet and J. A. Sáez, *Org. Biomol. Chem.*, 2008, **6**, 4378-4383.
40. J. A. Sáez, B. Escuder and J. F. Miravet, *Chem. Commun.*, 2010, **46**, 7996-7998.
41. A. de Robertis, S. Sammartano and C. Rigano, *Thermochim. Acta*, 1984, **74**, 343-355.
42. D. A. Palmer and R. Van Eldik, *Chem. Rev.*, 1983, **83**, 651-731.
43. P. G. Daniele, A. De Robertis, C. De Stefano, S. Sammartano and C. Rigano, *J. Chem. Soc., Dalton Trans.*, 1985, **0**, 2353-2361.

44. D. J. Miller, *Colloid Polym. Sci.*, 1989, **267**, 929-934.
45. H. Shinar and G. Navon, *Biophys. J.*, 1991, **59**, 203-208.
46. J. M. Aramini, T. Drakenberg, T. Hiraoki, Y. Ke, K. Nitta and H. J. Vogel, *Biochemistry*, 1992, **31**, 6761-6768.
47. A. Trummal, L. Lipping, I. Kaljurand, I. A. Koppel and I. Leito, *J. Phys. Chem. A*, 2016, **120**, 3663-3669.
48. P. Mukerjee and J. D. Ostrow, *Tetrahedron Lett.*, 1998, **39**, 423-426.

Chapter 5: *In Situ* Titrations by ^{1}H NMR Imaging

5.1 Introduction

In Chapter 4, Sections 4.2.3.3 and 4.3.4, it was demonstrated how chemical shift imaging (CSI) and *in situ* generated pH and [Ca^{2+}] gradients could be combined to study the formation of self-assembled hydrogels. This approach is particularly useful for the study of systems where gelation occurs instantaneously upon contact between the LMWG and the gelation trigger. The ability to establish and analyse concentration gradients with good accuracy is thus of considerable importance when applying the methods discussed in previous Chapters. In this Chapter, it is demonstrated how controlled pH and Ca^{2+} gradients may be established and analysed in standard 5 mm NMR tubes.

In order to develop techniques for the establishment and analysis of concentration gradients, it is necessary to use simple model systems. The self-assembly of hydrogels is a complex and poorly understood process. In contrast, the protonation/deprotonation in water of small non-assembling molecules is a simple and well-understood process.[1] Likewise, the complexation of Ca^{2+} by small organic ligands is also well studied.[2, 3] These processes are of importance across many areas of science, including pharmacology, organic synthesis and geology.[4-7] The pK_a values and Ca^{2+} binding constants of small molecules are fundamental parameters to describe these processes.[3, 5, 8] NMR spectroscopy has emerged as a powerful tool to measure these properties. In general, the chemical shift of an analyte is recorded as a function of the pH or calcium concentration.[9-12] Fitting the resulting titration curve can then yield the desired properties of the analyte.[10, 13, 14]

In the conventional NMR titration procedure, each point on a titration curve is recorded in a separate NMR experiment, either in a single sample where the titrant is added between successive NMR experiments,[11, 15] or in separate samples.[9] An alternative to this time-consuming and laborious procedure would be to establish a concentration gradient of the titrant in an NMR tube and acquire spatially resolved NMR spectra along the length of the gradient using imaging techniques. A complete titration curve could thus be acquired from a single sample in a single NMR experiment.[16] Such an approach would allow for the measurement of pK_a values and

binding constants in a highly efficient manner. In this Chapter, the experimental protocol is developed and the efficacy of the technique is demonstrated by comparison of pK_a values and Ca^{2+} binding constants thus obtained with literature data.

5.2 Controlled pH Gradients

5.2.1 pK_a measurements using *in situ* generated pH gradients

The use of NMR spectroscopy to measure the pK_a values of compounds is well-established and is discussed extensively elsewhere.[9, 17] Briefly, the chemical shift of an analyte, δ_{obs}, is recorded as a function of the solution pH. The pK_a can then be determined by fitting the data to Equation 5.1:

$$\delta_{obs} = \frac{\delta_H 10^{(pKa-pH)}+\delta_L}{1+10^{(pKa-pH)}} \quad (5.1)$$

where δ_H and δ_L are the limiting chemical shifts of the totally protonated and deprotonated analyte species respectively. In the conventional NMR titration method, the pH of the sample is determined potentiometrically before each NMR measurement. However, in the present work, the direct localised measurement of pH by NMR is essential. As discussed in Chapter 3, Section 3.2.5, where the pK_a of a compound is known, Equation 5.1 can be rearranged to yield the pH of the solution:

$$pH = pK_a + \log_{10}\left(\frac{\delta_{obs}-\delta_H}{\delta_L-\delta_{obs}}\right) \quad (5.2)$$

By combining a number of indicator molecules possessing a range of pK_a values, it is possible to determine the pH of a solution over a wide range with good accuracy.[14, 17, 18] The indicators used in this Chapter are listed in Table 5-1 along with compounds to provide reference chemical shifts. As will be discussed in Sections 5.2.3 and 5.2.11.4, these indicators can provide accurate pH measurements over the range 1-12. In the present work, it is not necessary to be able to measure over this full range in a single sample. It is thus unnecessary to include the full set of indicators in a single sample. For example, methylamine is only usable as an indicator at very alkaline pH (pH $\geq$ 10) while formate is usable only under acidic conditions (pH $\leq$ 5). To avoid redundancy and minimise spectral overlap between the indicators and other compounds of interest, the indicators in this work are

divided into two sets. Set A can be used for weakly alkaline and acidic measurements while Set B is used exclusively for alkaline measurements.

pH range	Indicator
1-10 (Set A)	Dichloroacetate (DCA), formate, acetate, 2,6-lutidine, glycinate, methylphosphonate (MPA^{2-})
8-12 (Set B)	MPA^{2-}, glycinate, methylamine
Reference	Dioxane, 2,2-dimethyl-2-silapentane-5-sulfonate (DSS), methanesulfonate

Table 5-1. pH indicators used in this work along with their abbreviations. Anions were included as their Na^+ salts in all cases. DCA was used only for very acidic (pH < 2) measurements.

It is important to note that positively charged indicators such as 2,6-lutidine may not be suitable for use in hydrogels formed from *N*-functionalised dipeptide gelators owing to their potential strong interactions with the gel fibres (Chapter 4, Section 4.3.5.1). 2,2-Dimethyl-2-silapentane-5-sulfonate (DSS) may also be unsuitable as a chemical shift reference owing to its potential strong interaction with hydrophobic sites on the fibres (Chapter 4, Section 4.3.1.4). Nevertheless, these compounds are used in this Chapter out of convenience on the understanding that they could be substituted for other compounds compatible with the gels. All three chemical shift reference compounds listed in Table 5-1 are suitable for the work presented in this Chapter (Section 5.2.5).

To establish a pH gradient in a 5 mm NMR tube, crystals of a solid acid are placed at the base of the tube and an alkaline solution of the analyte and pH indicators placed on top using a pipette. Dissolution and diffusion of the acid up the NMR tube then establishes the pH gradient. By recording spatially resolved ^1H spectra along the length of the pH gradient, it is possible to measure the pH as a function of position using the indicator compounds. The chemical shift of the analyte can thus be measured as a function of pH and a pK_a value extracted using Equation 5.1. The reliable measurement of a pK_a value requires the establishment of a smooth pH gradient spanning ca. 2-3 units around the expected pK_a of the analyte.[9, 19] Similar considerations apply when studying hydrogels (Section 5.2.6). Such gradients can

readily be established by selecting a monoprotic acid with a pK_a equal to, or not more than one unit below, the expected pK_a of the analyte. Buffering by the acid will give the desired smooth pH gradient while the presence of excess acid towards the lower part of the tube will not cause the pH to fall more than ca. 1-2 units below the pK_a of the analyte (Scheme 5-1).

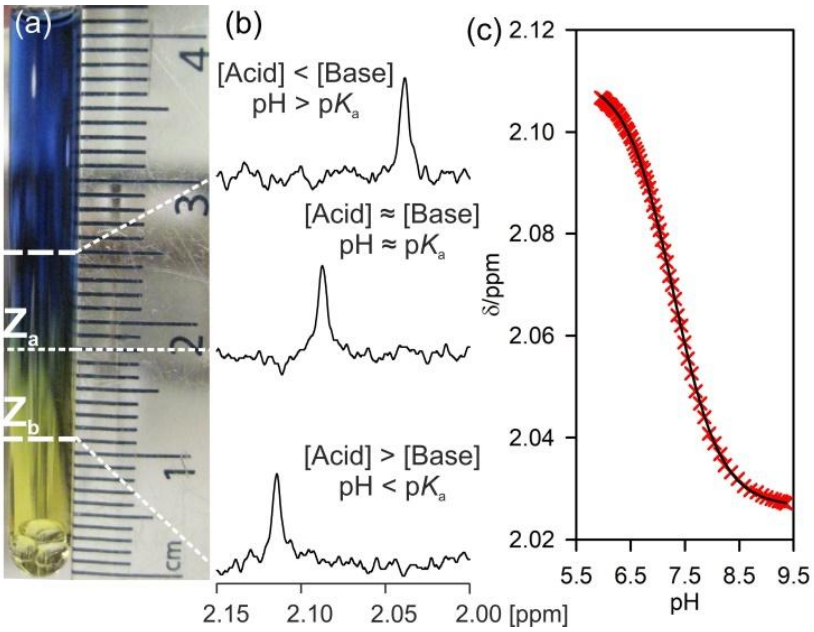

Scheme 5-1. The measurement of the pK_a value of an analyte using an *in situ* generated pH gradient. In this example, a solution of bromothymol blue (analyte, pK_a 7.3) is layered on top of KH_2PO_4 (acid, pK_a 7.2) in a 5 mm NMR tube. After a suitable time has elapsed (*vide-infra*), a smooth pH gradient is established within the NMR-active region of the sample (between thick white lines). The analyte varies continuously from the deprotonated (blue) to protonated (yellow) form (a). The ^{1}H NMR chemical shifts of the analyte are observed to vary along the length of the gradient (b). By extracting the analyte chemical shifts and calculating the pH of the solution from the NMR indicators, a titration curve can be constructed (c). The black line is a fit to Equation 5.1. The glass beads at the bottom of the NMR tube are to prevent non-diffusive mixing of the acid and analyte. The positions Z_a and Z_b (a) are used in the calculation of the mass of acid and time required to establish the pH gradient in the NMR tube (Section 5.2.2).

The acidic diffusants used in this work are listed in Table 5-2 along with the approximate range spanned by the resulting pH gradient. In addition to monoprotic acids, diprotic acids can be used where the expected pK_a of the analyte straddles those of the acid. However, it should be noted that the calculation of the mass of acid required is different to the monoprotic case (Section 5.2.7). The calculation of the

mass of acid required, focusing on the monoprotic case, is discussed in the following Section (5.2.2).

Acid diffusant	pH range
Oxalic (1.3, 3.8) HCl (-6)	1-4
Glycolic (3.8), Malonic (2.9, 5.7)	3-6
Monosodium malonate (5.7)	4.5-9
KH_2PO_4 (7.2)	6-10
$B(OH)_3$ (9.3)	8-11
$NaHCO_3$ (10.3)	9-12

Table 5-2. Acidic diffusants used in this work along with the usable pH range spanned by the resulting gradient. The pK_a values of the acids are given in parentheses and are taken from Reference 20.

5.2.2 Calculation of the mass of acid and the amount of time required for the establishment of the optimum pH gradient

The mass of monoprotic acid required and the time at which the optimum pH gradient will be established can be calculated as follows: The acids used in this work are highly water soluble and fully dissolve within minutes of placing the analyte solution on top. Mathematically, the acid behaves as though it were diffusing from a plane source at the base of the NMR tube. The concentration, C_Z, of diffusing acid at a height Z from the base of the NMR tube after a time, t, is therefore given by Equation 5.3:[21]

$$C_Z = N_{(t)} exp\left(-Z^2/_{4Dt}\right) \quad (5.3)$$

where D is the diffusion coefficient of the acid and $N_{(t)}$ is a time dependent constant.

An expression for the time at which a gradient will have developed, t_{opt}, can be derived from Equation 5.3:

$$t_{opt} = \frac{Z_b^2 - Z_a^2}{4Dln\left(\frac{a}{b}\right)} \quad (5.4)$$

where a and b denote the number of equivalents of diffusing acid to basic species at heights Z_a and Z_b respectively. Z_a and Z_b can be set to the centre and lower limit of the NMR-active region of the sample respectively (Scheme 5-1, a). On the NMR probe used in this work, the NMR-active region is centred 18 mm from the absolute base of the NMR tube and spans 7 mm either side (Section 5.2.8). At the lower limit of the NMR-active region (Z_b), it is necessary to have an excess of acid relative to base so that the acidic region of the titration curve may be sampled. In the following discussion, it is assumed that the initial concentration of base is constant throughout the analyte solution. Diffusion of basic species down the sample towards the acid is ignored. Fixing the initial concentration of base in the analyte solution as C_0, $N_{(t)}$ may be obtained from Equation 5.3 as:

$$N_{(t)} = aC_0 exp\left({Z_a}^2 \Big/ 4Dt_{opt}\right) \quad (5.5)$$

Only basic species whose pK_a value when protonated, pK_{aH}, is greater than or equal to the pK_a of the diffusing acid are included in the summation of C_0. Basic species with pK_{aH} values smaller than the pK_a of the diffusing acid will be unable to deprotonate it. When using acid diffusants which are strong relative to the analyte (p$K_{a,acid}$ < p$K_{a,analyte}$ − 0.5), only half an equivalent of acid is included relative to the analyte in the summation of C_0. Basic species with pK_{aH} values smaller than the pK_a of such acids are discounted from the summation of C_0. The overall ratio of diffusing acid to base in the sample can be obtained by integration of Equation 5.3 over the length of the sample. The mass of acid, m, required can thus be obtained as:

$$m = \pi r^2 aC_0 Mr\sqrt{\pi Dt_{opt}} exp\left({Z_a}^2 \Big/ 4Dt_{opt}\right) \quad (5.6)$$

where r is the radius of the NMR tube and Mr the molecular weight of the acid. A series of NMR images recorded over time as the pH gradients develop confirmed that Equations 5.4 and 5.6 provide the optimum conditions (Section 5.2.8). By matching the pK_a of the acid to the pK_a of the analyte and applying Equations 5.4 and 5.6, smooth pH gradients and 'textbook' titration curves can be acquired for a range of analytes (Figure 5-1). A complete list of the parameters used in each titration is provided in Section 5.2.11.2.

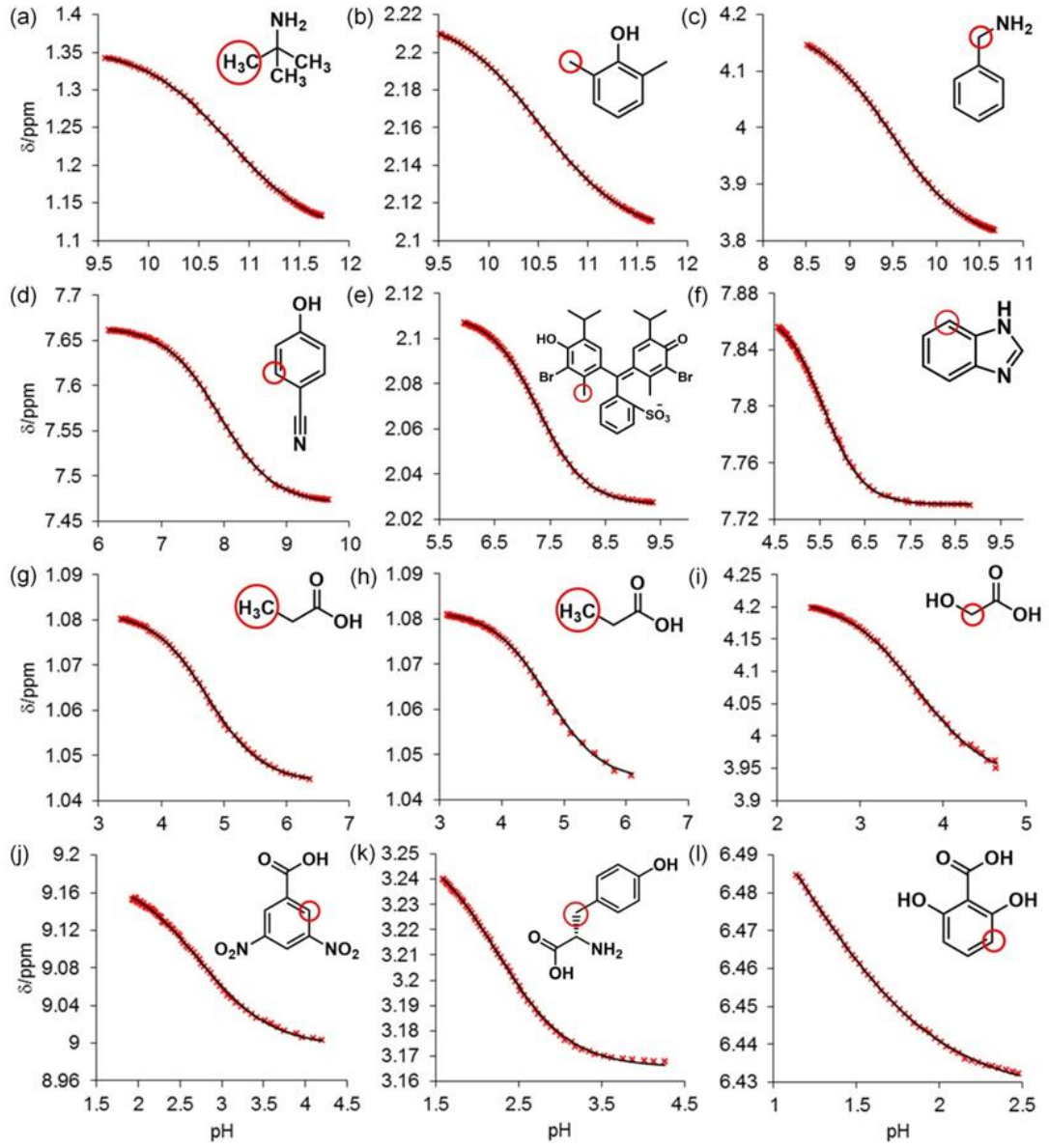

Figure 5-1. Titration curves of analytes: (a) *tert*-butylamine, (b) 2,6-dimethylphenol, (c) benzylamine, (d) 4-cyanophenol, (e) bromothymol blue, (f) benzimidazole, (g) propionic acid with malonic acid diffusant, (h) propionic acid with glycolic acid diffusant, glycolic acid (i), 3,5-dinitrobenzoic acid (j), L-tyrosine (k) and 2,6-dihydroxybenzoic acid (l). Data points are shown as red crosses. The fit to Equation 5.1 is shown as a black line. The ^{1}H resonance of the analyte examined is indicated with a red circle. On (l), the pH is not plotted below 1.1 as this would exceed the calibration range of the indicators (Section 5.2.3).

5.2.3 Calibration of pH indicators and calculation of analyte pK_a values

The calculation of the solution pH and the pK_a values of the analytes is now discussed in detail. The measurement of pH by NMR requires that the pK_a values of the indicators be known (Equation 5.2). In previous Chapters, literature pK_a values of

the indicators were used without considering the effect of ionic strength on the activity of the indicator species (Chapter 3, Section 3.3.1; Chapter 4). The apparent pH values measured were within 0.2 units of their true values which was an acceptable accuracy for these Chapters. However, in the present Chapter, more accurate pK_a values may be measured for the analytes by taking into account the effects of ionic strength, I, on the pK_a values of both the indicators and the analytes. In order to measure the pK_a values of the indicators, the chemical shifts of the indicators were measured in a series of buffer solutions (Table 5-3).

Buffer	Theoretical pH	Measured pH	I/M	Indicator Set
10 mM $NaHCO_3$ + 10 mM Na_2CO_3	10.09	10.11	0.041	B
10 mM KH_2PO_4 + 10 mM K_2HPO_4	6.98	6.96	0.041	A
10 mM Na_3citrate + 10 mM citric acid	4.55	4.58	0.042	A
16.7 mM citric acid + 3.3 mM Na_3citrate	3.15	3.14	0.012	A
20 mM HCl	1.78	1.77	0.020	A
100 mM HCl	1.11	1.09	0.100	A

Table 5-3. Compositions of buffer solutions used to calibrate the NMR indicators. The theoretical pH was calculated using the CurTiPot programme[22] and in all cases refers to the activity of H^+ ($-\log_{10} a_{H^+}$) rather than the concentration.[23] DCA was included with Set A. In all cases, the measured pH is within the error of the measurement ($\leq$ 0.03 units).[15] The indicator sets are as defined in Table 5-1.

The limiting chemical shifts (Equation 5.1) of the indicators were measured as described in Section 5.2.9. Using these values, and the theoretical pH of the buffer solutions, the effective pK_a values, p$K_{a,Eff}$, of the indicators were calculated using Equation 5.2. The variation of p$K_{a,Eff}$ with ionic strength will be less than 0.1 units within the ionic strength ranges encountered in the experiments discussed in this

Chapter (0.01 < I < 0.1 M).[24, 25] These pK_a values are also known as 'mixed' or 'practical' constants[23, 26] and are defined as:

$$pK_{a,Eff} = -\log_{10}\frac{a_{H^+}[A]}{[HA]} \quad (5.7)$$

where a_{H^+} denotes the activity of H^+ and [A] and [HA] are the concentrations of the deprotonated and protonated forms of the indicator respectively. Measured p$K_{a,Eff}$ values and limiting chemical shifts of the indicators are presented in Table 5-4.

Indicator	p$K_{a,Eff}$	δ_I/ppm	δ_H/ppm	Calibration Buffer (Theoretical pH)
DCA	1.21(±0.004)	6.0480	6.3118	1.11, 1.78
$MPAH^-$	2.32(±0.004)	1.2819	1.5106	1.78, 3.15
Formate	3.63(±0.04)	8.4414	8.2669	3.15, 4.55
Acetate	4.63	1.9060	2.0830	4.55
2,6-lutidine	6.87	2.4563	2.7074	6.98
MPA^{2-}	7.75	1.0711	1.2819	6.98
Glycine	9.74	3.1754	3.5494	10.09
Methylamine	10.79	2.2901	2.5942	10.09

Table 5-4. Parameters of NMR indicators used in this work. Limiting chemical shifts are relative to DSS at 0 ppm. Where two calibration buffers are used, the average p$K_{a,Eff}$ value is quoted. The number in parentheses is half the difference between the p$K_{a,Eff}$ values obtained in each buffer. p$K_{a,Eff}$ of formate was measured as 3.59 at pH 4.55 and 3.67 at pH 3.15.

When used with Equation 5.2, the indicator parameters listed in Table 5-4 provide the activity-based pH ($-\log_{10} a_{H^+}$). Fitting the titration data (Figure 5-1) to Equation 5.1 thus yields the effective pK_a values of the analytes. In order to compare the measured pK_a of an analyte with literature data, it is necessary to extrapolate the effective pK_a to infinite dilution to obtain the thermodynamic pK_a, p$K_{a,Tdyn}$. The activity coefficient of the charged analyte species, γ, must therefore be taken into account (Equation 5.8).[24, 25, 27, 28]

$$pK_{a,Tdyn} = pK_{a,Eff} + B\log_{10}(\gamma) \quad (5.8)$$

B takes a value of 1 for analytes that transform from neutral to positive upon protonation (imidazoles, amines) and -1 for analytes that transform from neutral to negative upon deprotonation (carboxylates, phenols). The activity coefficients of neutral or zwitterionic species are assumed to be unity.[27, 29] Within the ionic strength ranges encountered in this Chapter (0.01 < I < 0.1 M), p$K_{a,Tdyn}$ can be calculated using Equation 5.9.[27, 30, 31]

$$pK_{a,Tdyn} = pK_{a,Eff} - (z_H^2 - z_L^2)\left(0.509\frac{\sqrt{I}}{1+\sqrt{I}} - 0.1I\right) \quad (5.9)$$

where z_H and z_L are the charges of the protonated and deprotonated analyte species respectively. The calculation of the ionic strength is discussed in Section 5.2.10. The thermodynamic pK_a values of the analytes, thus calculated, agree with their literature values within ±0.1 log units (Table 5-5). An accuracy of ±0.1 log units is comparable to that obtained by other methods including capillary electrophoresis[32] and conventional NMR titrations.[9]

Analyte	p$K_{a,Tdyn}$	p$K_{a,Lit.}$	Difference	Reference
tert-Butylamine	10.71±0.01	10.68	0.03	33
2,6-Dimethylphenol	10.61±0.01	10.63	0.02	34
Benzylamine	9.43±0.01	9.35	0.08	35
4-Cyanophenol	8.00±0.01	7.97	0.03	36
Bromothymol Blue[a]	7.48±0.01	7.5	0.02	37
Benzimidazole	5.51±0.02	5.55	0.04	38
Propionic acid	4.80±0.02	4.87	0.07	29
Glycolic acid	4.79±0.02	4.87	0.08	39
3,5-Dinitrobenzoic acid	3.75±0.03	3.83	0.08	40
$_{L}$-Tyrosine	2.79±0.03	2.82	0.03	1
2,6-Dihydroxybenzoic acid	2.16±0.02	2.21	0.05	41

Table 5-5. Comparison of the pK_a values of analytes measured using the method presented in this Chapter with literature values. Titration curves are displayed on Figure 5-1. 95% confidence limits of the fitted pK_a values are provided. [a]Following Reference 37, z_L is taken as -2 and z_H as -1. p$K_{a,Tdyn}$ is calculated using Equation 5.9. Only two analyte species are considered.

5.2.4 Conclusions

A method has been presented by which controlled pH gradients may be established in standard 5 mm NMR tubes and analysed using CSI methods. By matching the pK_a of the diffusing acid to the desired pH range spanned by the gradient, it is possible to generate smooth gradients spanning ca. 2-3 units between pH 1 and pH 12. The mass of acid required and the time at which the optimum pH gradient is established can be estimated using simple equations developed in Section 5.2.2. The application of the methods to the measurement of the pK_a values of small, non-assembling molecules has been demonstrated. Complete titration curves may be obtained from a single NMR sample in a single NMR experiment. The methods presented in this Chapter thus possess significant advantages over conventional NMR-based titration methods in terms of the sample quantity, sample preparation time and instrument time required. As discussed in Section 5.2.6, the same methods may be used to establish pH gradients for the study of the controlled assembly/disassembly of self-assembled hydrogels and its analysis using the NMR techniques described in previous Chapters.

5.2.5 Use of alternative reference compounds

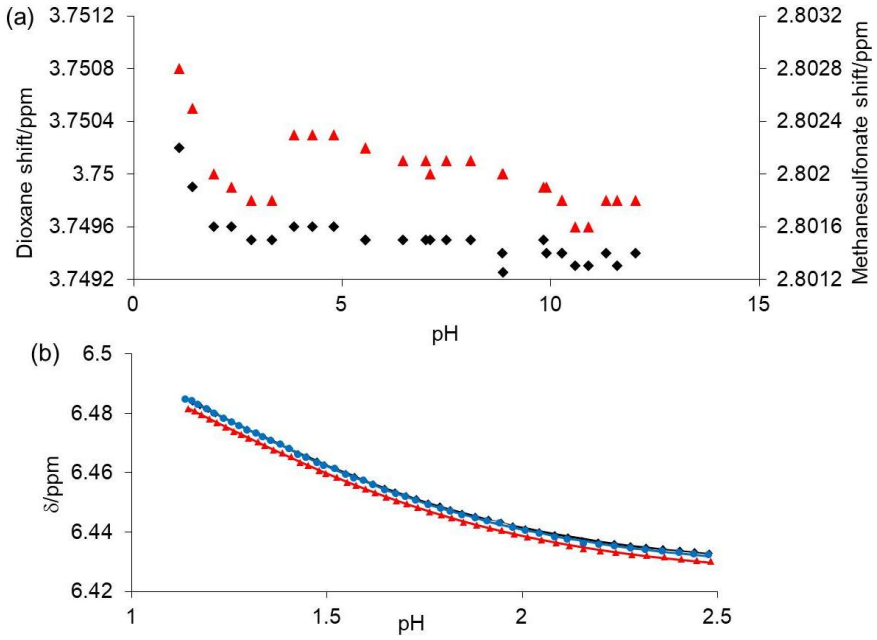

Figure 5-2. (a) Plot of ^{1}H chemical shift of dioxane (black diamond) and methanesulfonate (red triangle) versus pH, referenced to DSS at 0 ppm. These shifts were recorded in the experiment used to find the limiting chemical shifts of the indicators (Section 5.2.9). (b) Titration of 2,6-dihydroxybenzoic acid (Figure 5-1) referenced to dioxane at 3.75 ppm (black diamond), methanesulfonate at 2.8 ppm (red triangle) and DSS at 0 ppm (blue circle). The lines are fits to Equation 5.1.

In samples where DSS cannot be used as a reference, other compounds with pH-independent chemical shifts can be used instead. In this work, methanesulfonate and 1,4-dioxane were also included in the samples. Minimal variation (< ±0.0004 ppm) of the dioxane and methanesulfonate chemical shifts are observed above pH 3, relative to DSS at 0 ppm (a). Such an uncertainty in the chemical shift of the analyte will not have a significant effect on the pK_a value obtained; the variation of the analyte chemical shift due to protonation is more than two orders of magnitude bigger (Figure 5-1). Below pH 3, both compounds are slightly shifted downfield relative to DSS by approximately 0.0008 ppm. However, the small size of this shift allows for all reference compounds to be used during the titration of 2,6-dihydroxybenzoic acid (b). The p$K_{a,Tdyn}$ value obtained was 1.25 when dioxane and DSS were used as references and 1.26 when methanesulfonate was used. As plotted in Figure 5-2, the titration curves are overlapping when dioxane and DSS are used as references.

5.2.6 Application of methods to the study of supramolecular gelation

The use of a pH gradient to study the formation of a hydrogel was presented in Chapter 4, Section 4.3.4.2. A smooth pH gradient was established from pH 8 to pH 4, along which it was possible to discern a loss of charge from the gel fibres and an increase in their hydrophobicity as the sample became acidified. The choice of acid, amount of acid and time which the sample was left for the pH gradient to establish were all calculated using the methods presented in this Chapter. The evolution of the pH gradient with time is presented on Figure 5-3.

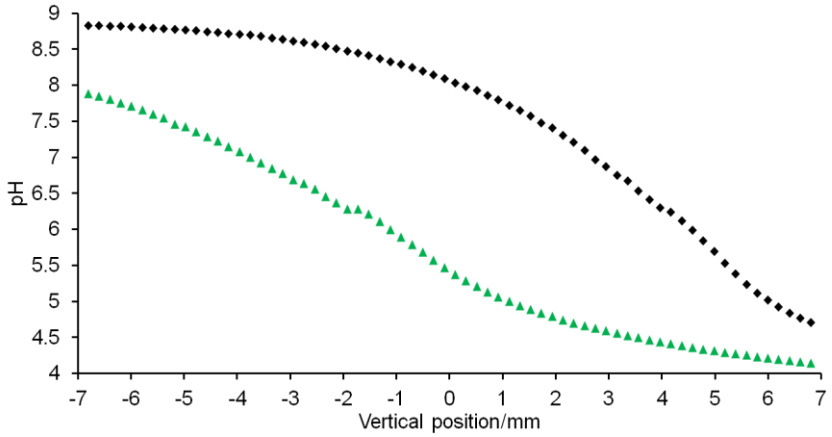

Figure 5-3. Plot of pH versus vertical position along sample (defined on Figure 5-4, Section 5.2.7) during formation of a **2**/glycolic acid hydrogel at 9 hours (black diamond) and 18 hours (green triangle) since solid acid was placed on top of the gelator solution. The pH was calculated using the procedure and indicator pK_a values presented in Chapter 3, Section 3.3.1. The slight inflexion in the pH between 6 and 6.5 is an artefact of the pH calculation.

A 4 mg/mL solution of LMWG **2** (Chapter 4) was prepared as described in Section 4.2.5.2.2. 1.0-1.2 mg of glycolic acid was placed on top of the gelator solution. The top of this solution was 43 mm from the absolute base of the NMR tube. Glycolic acid was chosen as the acid diffusant to ensure the pH did not fall below pH 3. C_0 for this sample could be calculated as 14 mM using the procedure outlined in Section 5.2.2. The gradient parameters were chosen so that a = 1 and b = 2 (Equation 5.4). Z_a and Z_b were 22 mm and 16 mm from the diffusing acid respectively. The thickness of the acid was assumed as 3 mm and so the acid was assumed to diffuse down from a plane source 40 mm from the base of the NMR tube (Section 5.2.11.2). The optimum mass of glycolic acid was predicted as 1.0 mg using Equation 5.6; any slight excess of acid would not cause the pH to fall to excessively low values. t_{opt}

was calculated for this sample as 20 hours using Equation 5.4. Analysis of the sample as the pH gradient developed (Figure 5-3) confirms that Equations 5.4 and 5.6 can be used to predict the mass of acid and time required to establish pH gradients for the analysis of gelation.

5.2.7 Calculation of the mass of acid required when using diprotic acid diffusants

Where suitable monoprotic acids are unavailable, diprotic acids (malonic, oxalic) may also be used where the pK_a of the analyte lies between those of the acid. The calculation of the mass of acid required is different to the monoprotic case. The pK_a of the diprotic acid species is denoted p$K_{a,1}$ while the pK_a of the monobasic species is denoted as p$K_{a,2}$. Basic species with pK_{aH} > p$K_{a,2}$ are capable of removing both acidic protons so only half an equivalent of diprotic acid is required to neutralise these species. At position Z_a, in order to obtain a pH approximately equal to that of the analyte, 0.5 equivalents of diprotic acid are also included relative to all species with pK_{aH} values greater than 0.5 units below the expected pK_a of the analyte. C_0 (Table 5-7) is calculated using these rules. At Z_b, 0.5 equivalents are again included relative to basic species with pK_{aH} > p$K_{a,2}$. However, 1 equivalent is included relative to all species with p$K_{a,2}$ > pK_{aH} > p$K_{a,1}$. For particularly acidic measurements (pH < 4), it is necessary to include additional acid at Z_b.

5.2.8 Evolution of a pH gradient with time

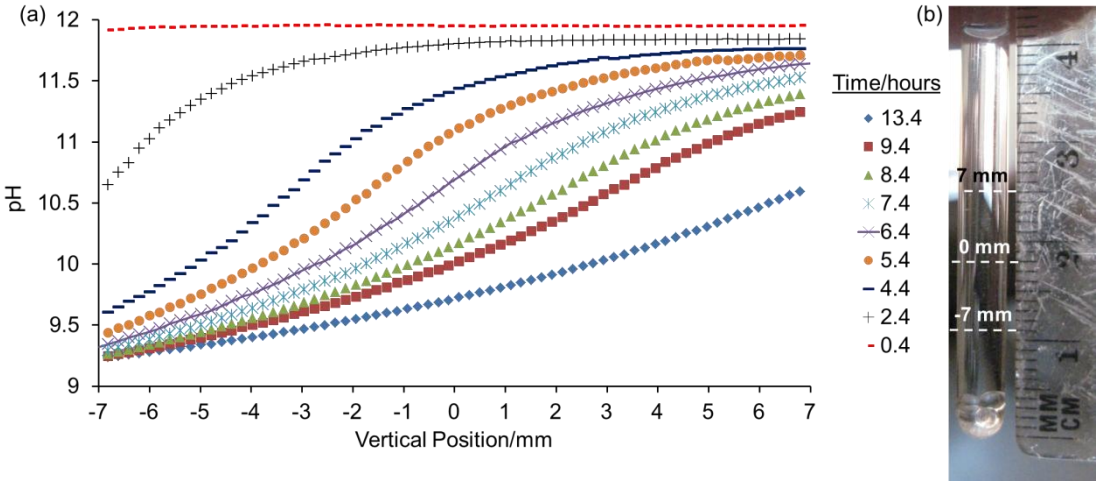

Figure 5-4. (a) Plot of pH versus vertical position along the 2,6-dimethylphenol sample (Figure 5-1, b) at different times after preparation. (b) Photograph of a sample against a ruler. The NMR-active region is centred 18 mm from the base of the NMR tube (0 mm) and extends 7 mm either side. Good quality spectra cannot be obtained beyond this region.

2,6-Dimethylphenol has a p$K_{a,Eff}$ of 10.5 (Table 5-6, Section 5.2.10). The optimum pH gradient thus spans ca. 1-1.5 units either side of pH 10.5 and is centred in the NMR-active region of the sample (b). t_{opt} for this sample was 6.5 hours (Table 5-7, Section 5.2.11.2). The best gradient is indeed obtained at this time (a); however, acceptable gradients are still obtained up to two hours either side of this optimum.

5.2.9 Calibration curves of pH indicators

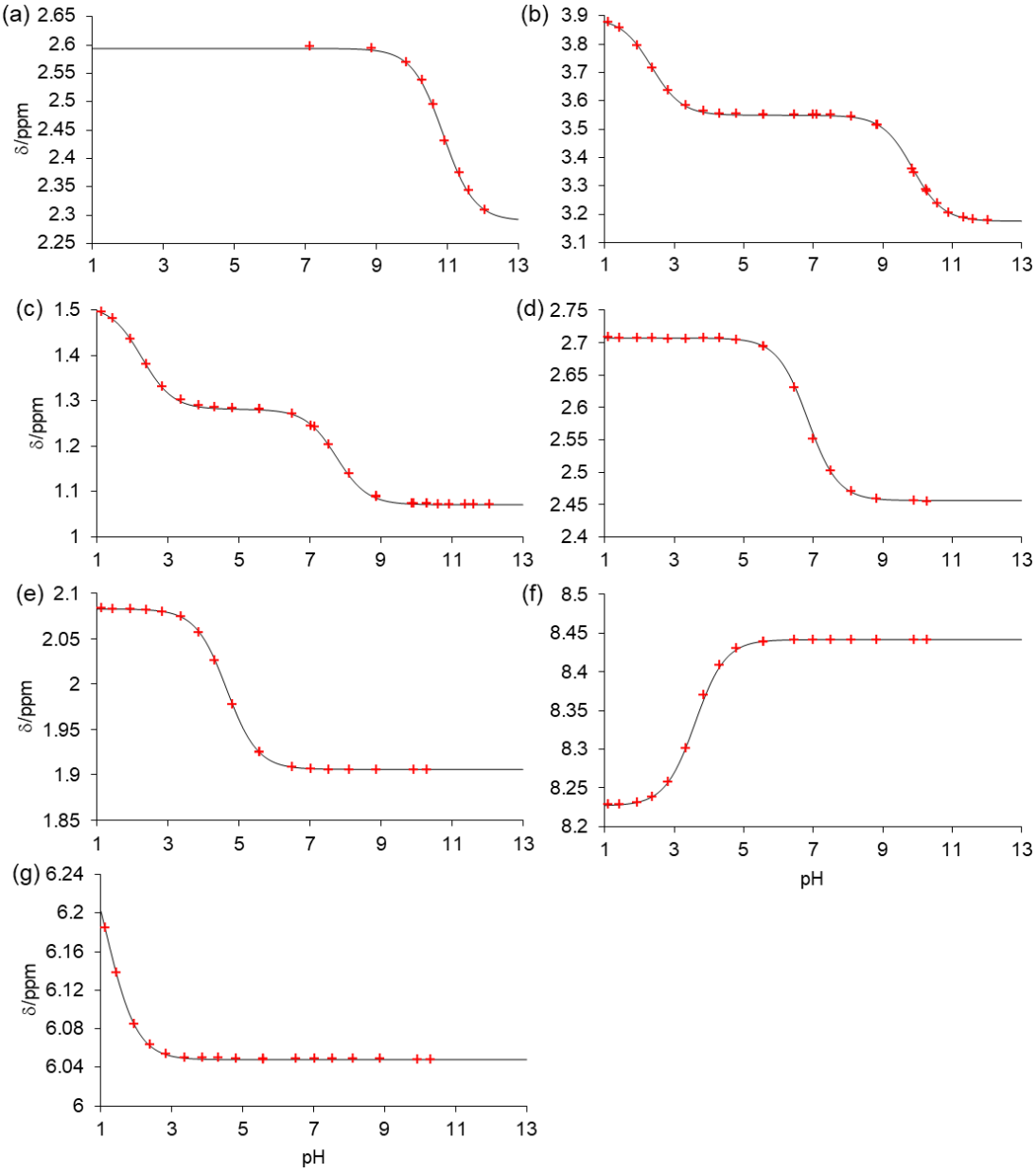

Figure 5-5. Plot of chemical shift versus pH for NMR indicators: methylamine (a), glycine (b), MPA (c), 2,6-lutidine (d), acetate (e), formate (f) and DCA (g). Limiting chemical shifts were obtained by fitting this data to Equation 5.1. The black lines are the chemical shifts predicted using the indicator parameters obtained by fitting. Indicator parameters of MPA and glycine were obtained by fitting the data to Equation 4 of Szakács *et al.*[17]

A solution of the indicators was prepared at the same concentration used in the titration samples (Section 5.2.11.2). The pH was adjusted using aliquots of either HCl or NaOH and monitored using a Hanna instruments HI-8424 meter equipped with an FC200 probe. After each aliquot was added, a portion of the sample was

removed and its NMR spectrum promptly recorded. Excellent fits of the data to Equation 5.1 are obtained from which the limiting chemical shifts of the indicators may be extracted. p$K_{a,Eff}$ values of the indicators were not extracted from this data owing to the effect of CO_2 absorption by the samples during the experiment. The chemical shift of methylamine in 0.1 M NaOH was measured as 2.289 ppm which is in excellent agreement with the limiting shift of 2.2901 ppm obtained by fitting (Table 5-4, Figure 5-5). This result suggests that it is not necessary to collect complete titration curves of the indictors in order to extract their limiting chemical shifts. For DCA, a complete titration curve would require the measurement of the chemical shift of DCA in very strongly acidic (pH << 1) samples at high ionic strengths.

5.2.10 Calculation of the ionic strength during the titration

The ionic strength of each sample was calculated at the midpoint of the titration (Z_a), where the concentration of acid is equal to C_0, using Equation 5.10:

$$I = 0.5 \sum_{i=1}^{n} c_i z_i^2 \qquad (5.10)$$

where c_i and z_i are the concentration and charge of the ion, i, respectively and the summation is performed over all ions in the sample. The measured pK_a of the analyte is most sensitive to ionic strength when pH = pK_a.[10] For simplicity, no further correction is applied where the diffusing acid bears a charge in its protonated form ($NaHCO_3$, KH_2PO_4) and the ionic strength is thus variable along the gradient. p$K_{a,Eff}$ values for the analytes and the ionic strength at the midpoint of each titration are presented in Table 5-6.

Analyte	p$K_{a,Eff}$	I/mM	p$K_{a,Tdyn}$
tert-Butylamine	10.80	54	10.71
2,6-Dimethylphenol	10.52	55	10.61
Benzylamine	9.48	16	9.43
4-Cyanophenol	7.93	27	8.00
Bromothymol Blue	7.28	24	7.48
Benzimidazole	5.58	28	5.51
Propionic acid (malonic acid diffusant)	4.74	19	4.80
Glycolic acid	3.69	20	4.79
3,5-Dinitrobenzoic acid	2.73	20	3.75
$_{L}$-Tyrosine	2.23	24	2.79
2,6-Dihydroxybenzoic acid	1.15	70[a]	2.16

Table 5-6. p$K_{a,Eff}$ values of analytes along with the ionic strength of the solution calculated at the midpoint of the titration (Z_a) where pH ≈ p$K_{a,Eff}$. All ionic strengths were calculated using the CurTiPot package. Thermodynamic pK_a values, calculated using Equation 5.9, are also shown for convenience. [a]Calculated ionic strength of a sample made to pH 1.1 with HCl.

5.2.11 Experimental

5.2.11.1 Materials

All chemicals were purchased from Sigma-Aldrich and used as received. Oxalic acid was purchased as the dihydrate.

Monosodium malonate was prepared by the addition of one mole equivalent of NaOH to an aqueous solution of malonic acid followed by removal of the water *in vacuo*. The number of moles of malonate per gram of product was measured by ^{1}H NMR by integration of the malonate CH_2 resonance against an internal standard capillary. The molecular weight of the product was obtained as 125.8 g/mol, in good agreement with theoretical mass of 126.06 g/mol for anhydrous monosodium malonate. The pH of a 43 mM aqueous solution of the product was measured as 4.13, in good agreement with a value of 4.12 calculated using the CurTiPot package.[22]

5.2.11.2 Preparation of Samples

Stock solutions of the NMR indicator sets A and B (Table 5-1) were prepared and used throughout the study. These solutions were 0.2 M in each indicator, with the exception of formate and 2,6-lutidine which were included at 0.4 M and 0.1 M respectively. Methylamine was included as the hydrochloride salt with one mole equivalent of NaOH added. A stock solution of the NMR reference compounds was prepared containing sodium methanesulfonate (0.1 M), DSS (20 mM) and dioxane (1 vol%). Solutions of the analytes were prepared at a standard concentration of 2 mM. Due to solubility limitations, bromothymol blue was at a concentration of 0.1 mM. Where analytes were included in their protonated form, one equivalent of NaOH was added. The NMR indicator and reference compounds were included at a 1:100 dilution of their concentration in the stock solutions. For the measurement of the indicator p$K_{a,Eff}$ values (Table 5-3), the indicators were included in the buffer solutions at a 1:2000 dilution in order to minimise the effect of the indicators on the buffer pH. The pH of each buffer at 25 ^{o}C was checked using a Hanna Instruments HI-8424 meter equipped with an FC200 probe. Prior to use, the meter was freshly calibrated with pH 7.01 and 10.01 or 4.01 buffer solutions.

All experiments were performed in 5 mm Norrell 502 NMR tubes. To establish a pH gradient, solid acid was weighed into the tube using a Mettler AE101 balance with a stated precision of ±0.01 mg. Weighings of 0.6 mg on this balance were found by NMR to be within 20% of their nominal value, from three repeat measurements. Four 2 mm diameter glass beads (Assistent, Germany) were then placed on top of the acid. Prior to use, the beads were washed with analytical grade methanol and dried. An aliquot of the analyte solution was drawn up in a 9'' Pasteur pipette and gently layered on top of the glass beads to a height of 40 mm from the base of the NMR tube. The glass beads served to prevent excessive mixing of the acid and the analyte solution. The samples were then left to stand in a water bath at 25 ^{o}C until analysis. When HCl was used as a diffusant, an aqueous solution (2 M, 30 μL) was carefully measured into the NMR tube and five glass beads placed in the solution. A list of the parameters used in each titration displayed on Figure 5-1 is provided in Table 5-7.

Analyte	Acid	C_0/mM	a	b	m/mg	t_{opt} /hours	$t_{meas.}$ /hours
tert-Butylamine	$NaHCO_3$	16	1	5.4	2.0	6.6	6.5
2,6-Dimethylphenol	$NaHCO_3$	16	1	5.4	2.0	6.6	6.4
Benzylamine	$B(OH)_3$	6	1	6.6	0.7	5.0	5.5
4-Cyanophenol	KH_2PO_4	5	1	7	1.4	7.9	8.3
Bromothymol Blue	KH_2PO_4	5	1	7	1.4	7.9	8.2
Benzimidazole	Monosodium malonate	7	1	6	1.5	6.8	7.4
Propionic acid	Malonic acid	9	0.5	2	0.5	9.5	10.3
Propionic acid	Glycolic acid	7	1	5	0.7	7.6	7.0
Glycolic acid	Oxalic acid	13	0.5	1.7	0.7	8.3	7.6
3,5-Dinitrobenzoic acid	Oxalic acid	17	0.5	2.1	1.2	7.1	7.3
$_L$-Tyrosine	Oxalic acid	17	0.5	4.2	2.7	4.8	4.9
2,6-Dihydroxybenzoic acid	HCl	67[a]	1	3.4	(30 μ_L, 2 M)	3.2	2.7

Table 5-7. Parameters used in the titration experiments displayed on Figure 5-1. $t_{meas.}$ is the time elapsed between the preparation of the sample and the recording of the NMR image. The time quoted corresponds to the midpoint of the NMR experiment. [a]C_0 for 2,6-dihydroxybenzoic acid was calculated as the sum of the concentrations of the basic species in solution (17 mM) and the free acid required to obtain a pH of approximately 1.3 (50 mM) at Z_a.

Z_a is located at the centre of the NMR active region of the sample, located 18 mm from the base of the NMR tube. Z_b is located at the lower limit of the NMR active region, 12 mm from the absolute base of the NMR tube. When calculating the mass of acid using Equation 5.6, 2 mm is subtracted from Z_a and Z_b in all cases to take

account of the thickness of the solid acid at the base of the NMR tube. The 2,6-dimethylphenol and *tert*-butylamine samples contained 10 mM NaOH in addition to the analytes and indicators to ensure the alkaline half of the titration curve could be adequately sampled. C_0 for 2,6-dihydroxybenzoic acid was calculated as the sum of the concentrations of the basic species in solution (17 mM) and the free acid required to obtain a pH of 1.3 (50 mM) at the centre of the titration. t_{opt} (Equation 5.4) was calculated using diffusion coefficients for the acids listed in Table 5-8. NMR-images were acquired when permitted by spectrometer availability and so the correlation between t_{opt} and t_{meas} is only approximate. t_{opt} is intended to provide only a rough guide as to when the NMR image should be recorded and excellent pH gradients are obtained in all cases (Figure 5-1 and Section 5.2.8). It should be noted that diffusion coefficients are concentration dependent (see references listed in Table 5-8) and so the use of a single diffusion coefficient to calculate t_{opt} is itself an approximation.

Acid	$D/10^{-9}$ m^2s^{-1}	Reference
HCl	3.1	42
Oxalic acid	1.2	43
Glycolic acid	1.0	44
Malonic acid	0.92	45
Monosodium malonate	1.0	a
KH_2PO_4	0.79	46, b
$B(OH)_3$	1.3	42
$NaHCO_3$	1.1	47

Table 5-8. Diffusion coefficients of the acids used to calculate t_{opt}. a: Measured using diffusion NMR spectroscopy in a 43 mM aqueous solution of monosodium malonate (Section 5.2.11.3). b: Measured as 0.89 x 10^{-9} m^2s^{-1} using diffusion NMR in a 50 mM solution of KH_2PO_4.

The similarity of the diffusion coefficient of $KH_2PO_4^-$ measured using diffusion NMR with the literature value (Table 5-8) confirms that diffusion NMR can provide diffusion coefficients with acceptable accuracy for the calculation of t_{opt}.

5.2.11.3 NMR

Experiments were performed on a Bruker Avance II 400 MHz wide bore spectrometer operating at 400.20 MHz for ^{1}H. The probe was equipped with Z-axis pulsed field gradients. The temperature of the samples was maintained at 298±0.5 K, the variation in the temperature with time being less than 0.1 K. CSI experiments were performed using a gradient phase encoding sequence based on that of Trigo-Mouriño *et al.*[48] which incorporated the double echo hard-pulse WATERGATE (W) sequence of Liu *et al.*[49] (Bruker library ZGGPW5) to suppress the H_2O resonance. The pulse sequence was thus W-τ_1-g-τ_2-acquire where g is a gradient pulse and τ_1 and τ_2 are delays of 10 μs and 200 μs respectively. A spoil gradient (27 G/cm) was employed at the end of the signal acquisition period (1 s) to destroy any transverse magnetisation. The gradient pulse was 242 μs in duration and varied between -27 and 27 G/cm in 128 steps. 8 scans were acquired at each step giving a total acquisition time of 20 minutes and a theoretical spatial resolution of 0.20 mm. 16 dummy scans were acquired prior to signal acquisition. The delay between successive hard pulses in the selective pulse train was set at 250 μs corresponding to a 4000 Hz separation between the null points. ^{1}H spectra (Sections 5.2.3 and 5.2.9) were acquired using the same double-echo WATERGATE sequence used for the CSI experiments but without the imaging gradient pulse or delays. The signal acquisition time and relaxation delay were 3 s and 1 s respectively.

DSS was used as the reference for all spectra (0 ppm). The other reference compounds listed in Table 5-1 give equivalent results (Section 5.2.5). No D_2O was included in the samples in order to allow the direct comparison of the analyte pK_a values measured in this work with literature data.[19] All NMR measurements were thus performed off-lock. CSI images were processed in phase-sensitive mode following the procedure of Trigo-Mouriño *et al.*[48] Following two-dimensional Fourier transformation of the CSI datasets, the individual spectra were automatically extracted, any residual phase errors corrected and the spectra referenced to DSS (0 ppm) using an automation macro written in house.

The self-diffusion coefficient of monohydrogen malonate (Table 5-8) was measured using a double stimulated echo sequence of Jerschow and Müller,[50] Bruker library

DSTEGP3S, with a double echo hard-pulse WATERGATE (W) sequence of Liu *et al.*[49] (Bruker library ZGGPW5) appended at the end of the sequence to suppress the H_2O resonance. Presaturation (50 Hz power) was applied to the H_2O resonance during the relaxation delay (5 s). The signal acquisition period was 2 s. The diffusion time and diffusion encoding gradient pulse length were 0.2 s and 1.5 ms respectively. Spectra were recorded with 8 scans at 16 values of the gradient pulse amplitude from 2.4 to 46 G/cm. The self-diffusion coefficient of $H_2PO_4^-$ was measured by ^{31}P observation using the same pulse sequence but with no solvent suppression components. The diffusion time and diffusion encoding gradient pulse length were 0.2 s and 2.5 ms respectively. The relaxation delay and signal acquisition period were 2 s and 1.3 s respectively. Spectra were recorded with 32 scans at 16 values of the gradient pulse amplitude from 2.4 to 46 G/cm.

5.2.11.4 Data processing

The chemical shifts of all indicators were automatically extracted from the CSI datasets and transferred to Microsoft Excel for analysis using an automation macro written in house. Each indicator has a usable pH range of only ca.1-1.5 units either side of its pK_a.[10] Beyond this range, the indicator is predominantly in its protonated or deprotonated form and shows only minimal change in chemical shift with pH. Using the following algorithm, the most sensitive indicators were automatically selected from chemical shift data and the solution pH calculated. The sensitivity, S, of an indicator can be defined as the first derivative of the indicator chemical shift with respect to pH.[10] S can thus be obtained from Equation 5.2 as:

$$S = (\ln 10)\left[\frac{(\delta_L - \delta_{obs})(\delta_{obs} - \delta_H)}{\delta_H - \delta_L}\right] \quad (5.11)$$

The indicators were grouped into pairs: DCA/$MPAH^-$, $MPAH^-$/formate, formate/acetate, acetate/lutidine, lutidine/MPA^{2-}, MPA^{2-}/glycine and glycine/methylamine. S was calculated for each indicator and the pair with the greatest combined sensitivity selected. The apparent pH of the solution was calculated for each indicator using Equation 5.2. The pH of the solution could then be obtained as the average of the apparent pH values reported by each indicator in the pair, weighted by S.

To calculate the pK_a of an analyte, the chemical shifts of the analyte were extracted and fitted to Equation 5.1 using the procedure of Brown.[51] The p$K_{a,Eff}$ values thus obtained were then extrapolated to infinite dilution using Equation 5.9. 95% confidence intervals of the fitted pK_a values (Table 5-5) were calculated using the Regression Wizard of SigmaPlot 13.0 (Systat Software Inc., California, USA).

5.3 Controlled Ca^{2+} Gradients

5.3.1 Ca^{2+} binding measurements

Section 5.2 discussed how controlled pH gradients may be established and imaged in standard 5 mm NMR tubes. Entirely analogous methods may be used for the establishment and imaging of Ca^{2+} concentration gradients. Weak (K < 300) Ca^{2+} binders, including many mono- and di-carboxylates, are found to exchange rapidly on the NMR timescale between their free and complexed states.[11, 52] In analogy with Equation 5.2, the free (uncomplexed) Ca^{2+} concentration, $[Ca^{2+}]_{free}$, can be determined from the ^1H chemical shift of a suitable indicator using Equation 5.12 (Chapter 4, Section 4.3.7):

$$[Ca^{2+}]_{free} = \frac{1}{K_{Ca}}\left(\frac{\delta_f - \delta_{obs}}{\delta_{obs} - \delta_{Ca}}\right) \quad (5.12)$$

where δ_{Ca} and δ_f are the limiting chemical shifts of the fully complexed and free ligands respectively and K_{Ca} is the effective binding constant. The calibration of indicator ligands was described in Chapter 4, Section 4.3.7 and the same calibration data is used here. Calibration data is presented in Figure 5-6 for the three ligands tested: formate, maleate and glycolate.

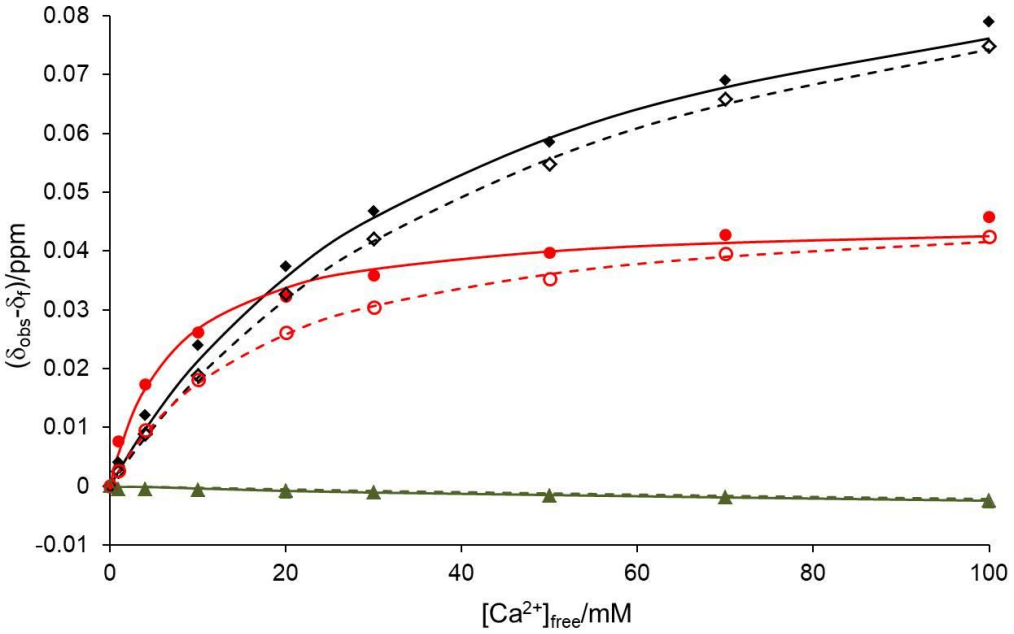

Figure 5-6. Plot of (δ_{obs}- δ_f) versus $[Ca^{2+}]_{free}$ for glycolate (black diamond) maleate (red circle) and formate (green triangle). Data recorded in the presence and absence of 50 mM NaCl are shown as hollow and solid symbols respectively. Fits of Equation 5.12 to the data in the presence and absence of 50 mM NaCl are shown as dashed and solid lines respectively. All spectra were referenced to methanol (3.36 ppm).

It can be seen from Figure 5-6 that glycolate is a better indicator than maleate or formate over the range 0-100 mM Ca^{2+}, exhibiting by far the greatest change in ^1H chemical shift upon complexation with Ca^{2+}. As a monocarboxylate, glycolate possesses a much smaller Na^+ binding constant than maleate so is much less sensitive to background Na^+ (Chapter 4, Section 4.3.7).[3] Glycolate is therefore used as an indicator throughout this Chapter. 0-100 mM Ca^{2+} is a common range found in biological systems and is sufficient to record the binding constants of many 'weak' Ca^{2+} binders of interest.[53] It is also a common range found in many self-assembled hydrogel systems.[54-56] The fitted indicator parameters of glycolate are presented in Table 5-9.

[NaCl]/mM	K_{Ca}/M^{-1}	δ_{Ca}/ppm	δ_f/ppm
0	25.000	4.0496	3.9430
50	19.870	4.0548	3.9431

Table 5-9. Fitted values of K_{Ca}, δ_f and δ_{Ca} for glycolate with MeOH (3.36 ppm) as a reference. The background concentration of NaCl during the calibration experiments is indicated.

To establish a Ca^{2+} gradient, $CaCl_2.2H_2O$ is weighed into a 5 mm NMR tube. A solution containing the indicator ligands and any analyte species is then pipetted on top. The sample is then left to stand for a Ca^{2+} gradient to develop. The mass of salt and the time required to stand the sample can be calculated from Equations 5.4 and 5.6 (Section 5.3.3.1). $[Ca^{2+}]_{free}$ can be measured along the length of the gradient from the ^1H chemical shift of glycolate. Effective K_{Ca} values for the analytes may be obtained by measuring their ^1H chemical shifts along the length of the Ca^{2+} gradient and fitting the data to Equation 5.12. Titration curves for the analytes are presented on Figure 5-7.

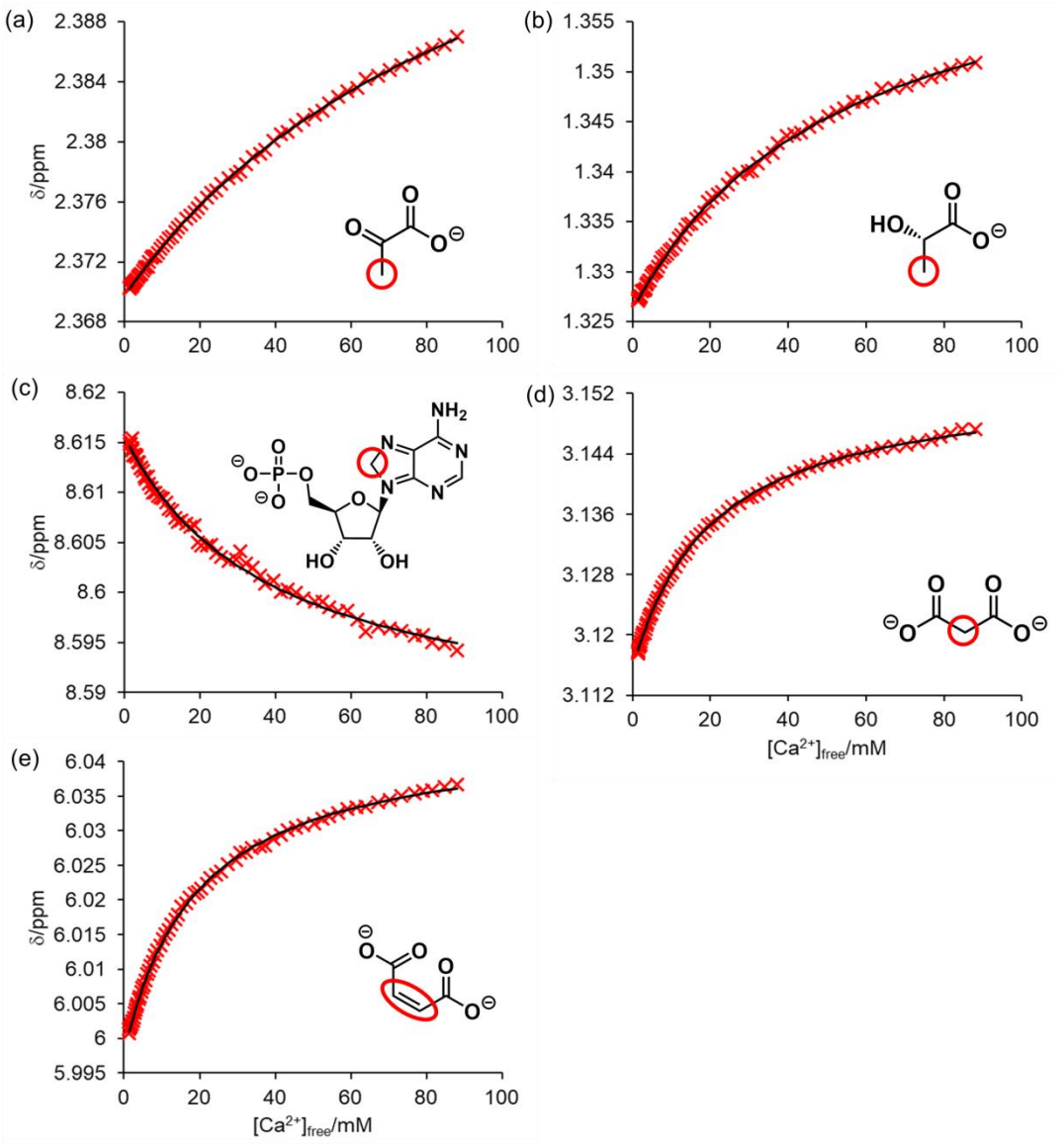

Figure 5-7. Titration curves of analytes: (a) pyruvate, (b) L-lactate, (c) adenosine-5'-monophosphate, (d) malonate and (e) maleate. Data points are shown as red crosses. The fit to Equation 5.12 is shown as a black line. The ^{1}H resonance of the analyte examined is indicated with a red circle.

Excellent fits of the data are obtained to Equation 5.12 with all analyte ligands. It is also apparent by comparing Figures 5-6 and 5-7 that the ^{1}H chemical shift of glycolate is by far the most sensitive of all ligands tested to Ca^{2+}. Glycolate is thus an exceptionally good Ca^{2+} indicator. Effective K_{Ca} values for the ligands are presented in Table 5-10 along with their literature values.

Analyte	K_{Ca}/M^{-1} (NMR)	K_{Ca}/M^{-1} (lit.)	Reference
Pyruvate	9.4±0.3	6.3 (0.16 M, 37 ^{o}C)	57
$_{L}$-lactate	18.5±0.8	27.5 (0), 11.6 (0.16 M, 37 ^{o}C)	3, 57
Adenosine-5'-monophosphate	25.8±2.8	26.9 (0.20 M)	58
Malonate	49.7±1.5	245 (0), 43.7 (0.25 M)	3, 59
Maleate	51.9±1.5	251 (0), 57.5 (0.25 M)	3, 59

Table 5-10. Comparison of the K_{Ca} values obtained by NMR (Figure 5-7) with literature values. 95% confidence limits of the fitted K_{Ca} values are provided. The ionic strength at which the literature K_{Ca} values were measured is indicated in parentheses. Unless otherwise stated, all literature values were measured at 25 ^{o}C. K_{Ca} values of adenosine-5'-monophosphate, maleate and malonate apply to the dibasic species as the ligand.

No attempt is made to extrapolate K_{Ca} values to infinite dilution. Such an extrapolation is significantly more challenging than the case with pK_a values (Section 5.2.3).[3, 59] Furthermore, there is a considerable sparsity and variability of literature data with which to compare the extrapolated K_{Ca} values.[3, 57] It was not feasible to maintain a constant ionic strength along the $CaCl_2$ concentration gradient. The ionic strength during the titration can thus be assumed to vary from 50 mM (no $CaCl_2$) to 220 mM (85 mM $CaCl_2$). The NMR titration method is able to rank all analytes correctly in terms of their effective K_{Ca} values. Lactate and glycolate, both α-hydroxy carboxylates, have very similar K_{Ca} values.[3]

Following IUPAC guidelines,[8] K_{Ca} can be considered as a 'practical' binding constant that can be used to calculate the equilibrium concentrations of species under the specific conditions at which K_{Ca} was measured. Addition of weak Ca^{2+} binders, such as those listed in Table 5-10, to a solution of $CaCl_2$ would be expected to reduce $[Ca^{2+}]_{free}$ by an amount predicted by Equation 5.13:[60]

$$[Ca^{2+}]_{free} = C - \frac{\left(C+B+\frac{1}{K_{Ca}}\right) - \sqrt{\left(C+B+\frac{1}{K_{Ca}}\right)^2 - 4CB}}{2} \quad (5.13)$$

where C and B are the total concentration of Ca^{2+} and ligand with binding constant K_{Ca} respectively. A derivation of this Equation is presented in Section 5.3.3.3. Equation 5.13 applies to a 1:1 complex of Ca^{2+} with the ligand. A series of solutions was prepared with different concentrations of disodium maleate and a constant total Ca^{2+} concentration of 20 mM. The total concentration of Na^+ was maintained at 50 mM in all samples using NaCl. Glycolate (1 mM) was included for the measurement of $[Ca^{2+}]_{free}$. As the maleate concentration was increased, $[Ca^{2+}]_{free}$ was observed to fall in agreement with Equation 5.13 (Figure 5-8).

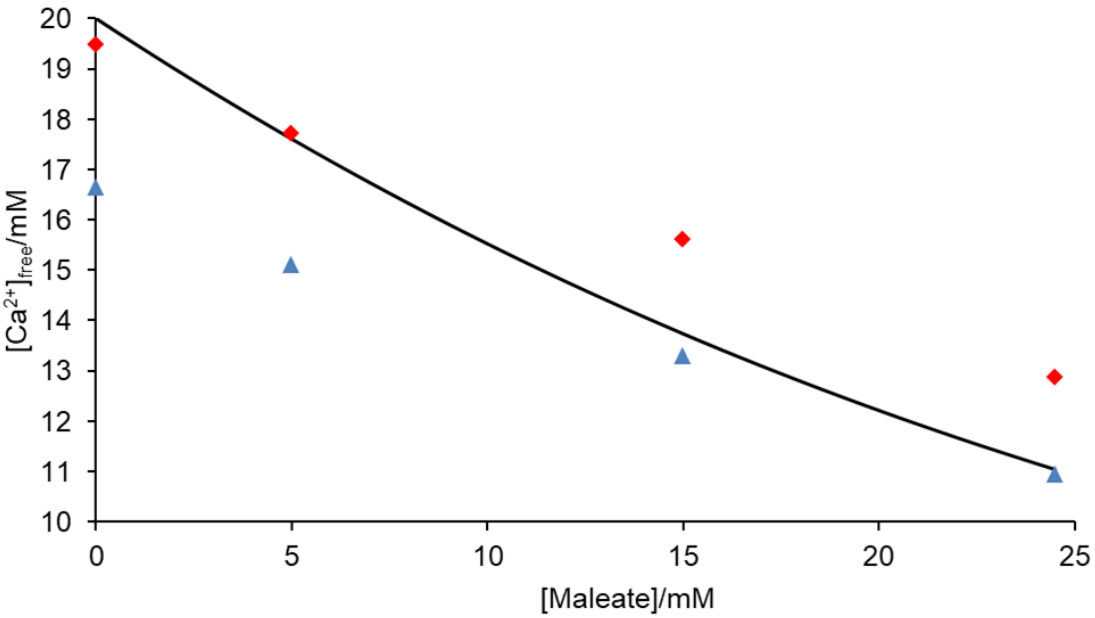

Figure 5-8. Plot of $[Ca^{2+}]_{free}$ versus concentration of disodium maleate. $[Ca^{2+}]_{free}$ was determined from the ^1H chemical shift of glycolate using the indicator parameters obtained in the absence (blue triangle) and presence (red diamond) of 50 mM NaCl (Table 5-9). The theoretical $[Ca^{2+}]_{free}$ predicted using Equation 5.13 is plotted as a black line. K_{Ca} of maleate was set at 52 M^{-1}.

The agreement between the measured $[Ca^{2+}]_{free}$ values and the values predicted from Equation 5.13 is only approximate as the activity of Na^+ is not taken into account. Maleate is a much stronger binder of Na^+ than chloride and so the activity of Na^+ is lower at higher maleate concentrations.[3] The effective K_{Ca} value of glycolate is thus larger at higher maleate concentrations as there is less competition between Ca^{2+} and Na^+ for glycolate. Accordingly, at higher maleate concentrations, the glycolate indicator parameter set obtained in the absence of NaCl (Table 5-9) provides the closest agreement with the theoretical $[Ca^{2+}]_{free}$. At low maleate concentrations, the parameter set obtained in 50 mM NaCl provides the closest agreement. A more detailed analysis, taking into account the effect of Na^+ activity on the K_{Ca} values of both maleate and glycolate, is beyond the scope of the present study. Nevertheless, Figure 5-8 strongly suggests that the apparent K_{Ca} values listed in Table 5-10 have physical meaning as binding constants.

5.3.2 Conclusions

Ca^{2+} concentration gradients may be established by weighing solid $CaCl_2$ into 5 mm NMR tubes and then placing an aqueous solution on top. The mass of $CaCl_2$ required and the time at which the optimum Ca^{2+} gradient is established can be estimated using methods analogous to those used for the establishment of pH gradients (Section 5.2.2 and 5.3.3.1). The concentration of free Ca^{2+} ions along the gradient may be measured from the ^1H chemical shift of indicator ligands. Glycolate is by far the most sensitive ligand tested over the range 0-100 mM. NMR titration curves may be measured for a range of other weak Ca^{2+} binders and apparent binding constants extracted. It should be stressed that the accurate measurement of the Ca^{2+} binding constants of such weak ligands presents a significant experimental challenge.[3] In this Section (5.3), it has been demonstrated how such complexation phenomena can be studied in single NMR experiments using only standard NMR equipment.

5.3.3 Experimental

5.3.3.1 Preparation of samples

All chemicals were purchased from Sigma-Aldrich and used as received. Samples were prepared in MilliQ water (Resistivity 18.2 MΩ.cm) which was degassed by bubbling with N_2 for ten minutes. Stock solutions of each ligand were prepared at 0.2 M with Na^+ as the counterion in all cases.

To obtain the data of Figure 5-7, a solution containing 2 mM of each of the following ligands was prepared: glycolate, pyruvate, malonate, maleate, lactate and adenosine-5'-monophosphate. MeOH was included at 0.01 vol% to act as an internal chemical shift reference. NaCl was added to give a total Na^+ concentration of 50 mM. Analysis of the ^1H chemical shifts of the ligands confirmed that all ligands were in their fully deprotonated state. Adenosine-5'-monophosphate was therefore dibasic;[61] the chemical shift of this analyte was observed to be invariant between pH 9 and 11 in a CSI experiment performed using the same parameters used for *tert*-butylamine (Section 5.2.11.2). The Ca^{2+} concentration gradient was designed following the procedure outlined in Section 5.2.2: Setting the Ca^{2+} concentration as 20 mM (Z_a) and 100 mM (Z_b) returns a t_{opt} of 6 hours (Equation 5.4). The diffusion coefficient of $CaCl_2$ was taken as 1.1 $x10^{-9}$ m^2s^{-1}.[62] The mass of $CaCl_2.2H_2O$ required was calculated as 4.7 mg using Equation 5.6. The $CaCl_2.2H_2O$ was weighed into a 5 mm Norrell 502 NMR tube. Material sticking to the walls of the tube was pushed down to the bottom using a PTFE rod. The ligand solution was layered on top of the $CaCl_2.2H_2O$ using a long Pasteur pipette, filling to 40 mm from the base of the NMR tube. The sample was the left to stand in a water bath at 25 ^oC. Analysis of the sample as the gradient developed confirmed that the optimum gradient is attained at approximately t_{opt} (Figure 5-9).

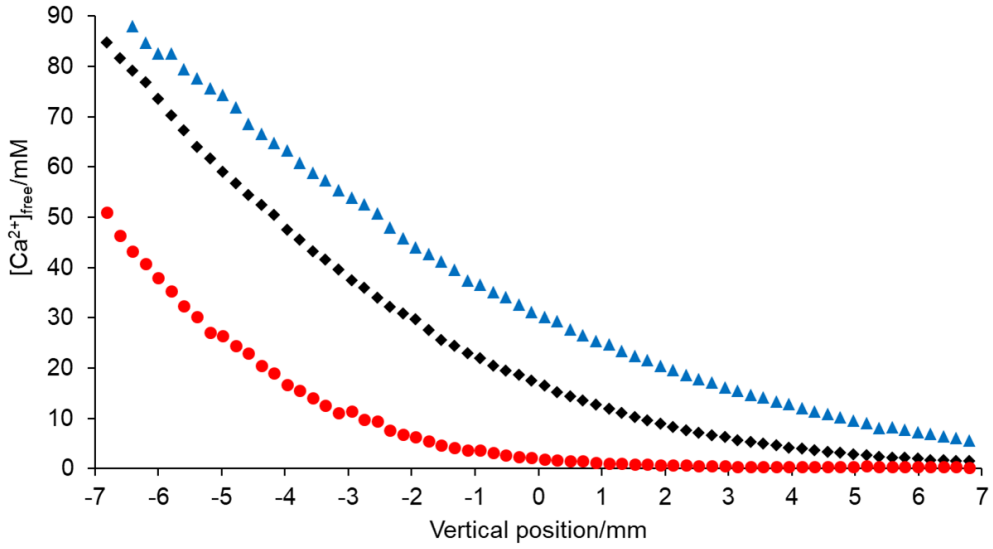

Figure 5-9. Plot of $[Ca^{2+}]_{free}$ versus vertical position along sample at 4 (red circle), 8 (black diamond) and 12 hours (blue triangle) since preparation. t_{opt} was calculated as 6 hours. The data of Figure 5-7 was recorded on the sample at 8 hours.

5.3.3.2 NMR

NMR experiments were performed on the same equipment used for the study of pH gradients (Section 5.2.11.3). The temperature of the samples was maintained at 298±0.5 K, the variation in the temperature being less than 0.1 K. ^{1}H CSI experiments were performed using a gradient phase encoding sequence based on that of Trigo-Mouriño *et al.*[48] which incorporated an excitation sculpting sequence (ES), Bruker library ZGESGP, to suppress the H_2O resonance. Selective Gaussian pulses of 4 ms duration and peak powers of 300 Hz were applied on the H_2O resonance during the sequence. The pulse sequence was thus ES-τ_1-g-τ_2-acquire where g is a gradient pulse and τ_1 and τ_2 are delays of 10 and 200 μs respectively. A spoil gradient (27 G/cm) was employed at the end of the signal acquisition period (1 s) to destroy any transverse magnetisation. The gradient pulse was 242 μs in duration and varied between -27 and 27 G/cm in 128 steps. 4 scans were acquired at each step giving a total acquisition time of 10 minutes and a theoretical spatial resolution of 0.20 mm. 16 dummy scans were acquired prior to signal acquisition. ^{1}H spectra were acquired as described in Section 5.2.11.3 but with a 3 s signal acquisition time and a relaxation delay of 1 s. MeOH was used as the reference for all spectra (CH_3, 3.36 ppm). All measurements were performed off-lock.

K_{Ca} values and 95% confidence intervals (Table 5-10) were obtained by fitting chemical shift data to Equation 5.12 using the Regression Wizard of SigmaPlot 13.0 (Systat Software Inc., California, USA).

5.3.3.3 Derivation of Equation 5.13

K_{Ca} for a 1:1 binding stoichiometry of a ligand to Ca^{2+} is defined as:

$$K_{Ca} = \frac{[BCa]}{[B][Ca^{2+}]_{free}} \tag{5.14}$$

where [BCa] and [B] are the equilibrium concentrations of calcium-ligand complex and free ligand respectively. The total concentrations of Ca^{2+} and ligand can be written as:

$$B = [B] + [BCa] \tag{5.15}$$

$$C = [Ca^{2+}]_{free} + [BCa] \tag{5.16}$$

Equations 5.14-5.16 can be combined to yield a quadratic equation (5.17):

$$[BCa]^2 - \left(C + B + \frac{1}{K_{Ca}}\right)[BCa] + CB = 0 \tag{5.17}$$

Inserting Equation 5.16 into the quadratic formula yields Equation 5.13.

5.4 Conclusions

The aim of this Chapter was to explore in detail how controlled pH and Ca^{2+} gradients may be established in 5 mm NMR tubes and analysed using standard NMR equipment. The techniques developed in this Chapter may be applied to any experimental situation in which it is informative to acquire NMR spectra of a sample as a function of the pH or Ca^{2+} concentration. By utilising internal concentration gradients within a sample, complete data series may be collected from single samples in single NMR experiments. Such an approach greatly reduces the experimental cost and time associated with the conventional NMR titration method in which each point on a titration curve is recorded in a separate experiment. The use of pH and Ca^{2+} gradients to study supramolecular gelation was presented in Chapter 4. Other potential uses of the methods lie, for example, in the study of protein folding and protein-ligand interactions[63, 64] or in the design of host-guest

complexes.[65] To prove the efficacy of the techniques, titration curves were acquired for a number of small molecules with well-known pK_a values and Ca^{2+} binding constants. In all cases, high-quality titration curves could be acquired and the fitted pK_a and K_{Ca} values were in good agreement with literature values.

5.5 References

1. R. B. Martin, J. T. Edsall, D. B. Wetlaufer and B. R. Hollingworth, *J. Biol. Chem.*, 1958, **233**, 1429-1435.
2. G. H. Nancollas, *J. Chem. Soc.*, 1956, 735-743.
3. P. G. Daniele, C. Foti, A. Gianguzza, E. Prenesti and S. Sammartano, *Coord. Chem. Rev.*, 2008, **252**, 1093-1107.
4. T. Kishino and K. Kobayashi, *Water Res.*, 1995, **29**, 431-442.
5. S. Babić, A. J. M. Horvat, D. Mutavdžić Pavlović and M. Kaštelan-Macan, *TrAC Trends Anal. Chem.*, 2007, **26**, 1043-1061.
6. R. K. Xu, Y. G. Zhu and D. Chittleborough, *J. Environ. Sci.*, 2004, **16**, 5-8.
7. S. Gaillard, C. S. J. Cazin and S. P. Nolan, *Acc. Chem. Res.*, 2012, **45**, 778-787.
8. G. H. Nancollas and M. B. Tomson, *Pure Appl. Chem.*, 1982, **54**, 2675-2692.
9. J. Bezençon, M. B. Wittwer, B. Cutting, M. Smieško, B. Wagner, M. Kansy and B. Ernst, *J. Pharm. Biomed. Anal.*, 2014, **93**, 147-155.
10. J. J. H. Ackerman, G. E. Soto, W. M. Spees, Z. Zhu and J. L. Evelhoch, *Magn. Reson. Med.*, 1996, **36**, 674-683.
11. G. D. Tredwell, J. G. Bundy, M. De Iorio and T. M. D. Ebbels, *Metabolomics*, 2016, **12**, 152.
12. J. C. Metcalfe, T. R. Hesketh and G. A. Smith, *Cell Calcium*, 1985, **6**, 183-195.
13. G. M. Ullmann, *J. Phys. Chem. B*, 2003, **107**, 1263-1271.
14. M. Boros, J. Kökösi, J. Vámos and B. Noszál, *J. Pharm. Biomed. Anal.*, 2007, **43**, 1306-1314.
15. T. Tynkkynen, M. Tiainen, P. Soininen and R. Laatikainen, *Anal. Chim. Acta*, 2009, **648**, 105-112.
16. T. Niklas, D. Stalke and M. John, *Chem. Commun.*, 2015, **51**, 1275-1277.
17. Z. Szakács, G. Hägele and R. Tyka, *Anal. Chim. Acta*, 2004, **522**, 247-258.

18. M. Wallace, J. A. Iggo and D. J. Adams, *Soft Matter*, 2015, **11**, 7739-7747.
19. K. Popov, H. Rönkkömäki and L. H. J. Lajunen, *Pure Appl. Chem.*, 2006, **78**, 663-675.
20. W. M. Haynes, ed., *CRC Handbook of Chemistry and Physics*, CRC Press, Boca Raton, FL, 2014.
21. J. Crank, *The Mathematics of Diffusion*, Clarendon Press, Oxford, 2nd edn., 1975.
22. I. G. R. Gutz, CurTiPot - pH and Acid-Base Titration Curves: Analysis and Simulation freeware, version 4.2, (http://www.iq.usp.br/gutz/Curtipot_.html).
23. H. Sigel, A. D. Zuberbühler and O. Yamauchi, *Anal. Chim. Acta*, 1991, **255**, 63-72.
24. P. G. Daniele, C. Rigano and S. Sammartano, *Talanta*, 1983, **30**, 81-87.
25. S. Capone, A. de Robertis, C. de Stefano, S. Sammartano, R. Scarcella and C. Rigano, *Thermochim Acta*, 1985, **86**, 273-280.
26. H. M. Irving, M. G. Miles and L. D. Pettit, *Anal. Chim. Acta*, 1967, **38**, 475-488.
27. H. Nagai, K. Kuwabara and G. Carta, *J. Chem. Eng. Data*, 2008, **53**, 619-627.
28. C. Bretti, O. Giuffrè, G. Lando and S. Sammartano, *SpringerPlus*, 2016, **5**, 928.
29. D. Belcher, *J. Am. Chem. Soc.*, 1938, **60**, 2744-2747.
30. M. E. J. Baker and R. Narayanaswamy, *Sens Actuators, B Chem*, 1995, **29**, 368-373.
31. C. W. Davies, *J. Chem. Soc.*, 1938, 2093-2098.
32. S. K. Poole, S. Patel, K. Dehring, H. Workman and C. F. Poole, *J. Chromatogr. A*, 2004, **1037**, 445-454.
33. K. Tanaka and R. G. Bates, *Anal. Chem.*, 1981, **53**, 1021-1023.
34. E. F. G. Herington and W. Kynaston, *Trans. Faraday Soc.*, 1957, **53**, 138-142.
35. R. A. Robinson and A. K. Kiang, *Trans. Faraday Soc.*, 1956, **52**, 327-331.
36. M. M. Fickling, A. Fischer, B. R. Mann, J. Packer and J. Vaughan, *J. Am. Chem. Soc.*, 1959, **81**, 4226-4230.
37. T. Shimada and T. Hasegawa, *Spectrochimica Acta A*, 2017, **185**, 104-110.
38. H. Walba and R. W. Isensee, *J. Org. Chem.*, 1961, **26**, 2789-2791.

39. P. B. Davies and C. B. Monk, *Trans. Faraday Soc.*, 1954, **50**, 128-132.
40. J. F. J. Dippy, S. R. C. Hughes and J. W. Laxton, *J. Chem. Soc.*, 1956, 2978-2982.
41. N. Papadopoulos and A. Avranas, *J. Solution Chem.*, 1991, **20**, 293-300.
42. J. K. Park and K. J. Lee, *J. Chem. Eng. Data*, 1994, **39**, 891-894.
43. D. G. Leaist, Y. Li and R. Poissant, *J. Chem. Eng. Data*, 1998, **43**, 1048-1055.
44. W. J. Albery, A. R. Greenwood and R. F. Kibble, *Trans. Faraday Soc.*, 1967, **63**, 360-368.
45. D. G. Leaist, *J. Chem. Eng. Data*, 2007, **52**, 1319-1325.
46. J. E. Burkell and J. W. T. Spinks, *Can. J. Chem.*, 1952, **30**, 311-319.
47. J. G. Albright, R. Mathew and D. G. Miller, *J. Phys. Chem.*, 1987, **91**, 210-215.
48. P. Trigo-Mouriño, C. Merle, M. R. M. Koos, B. Luy and R. R. Gil, *Chem. Eur. J.*, 2013, **19**, 7013-7019.
49. M. Liu, X. A. Mao, C. Ye, H. Huang, J. K. Nicholson and J. C. Lindon, *J. Magn. Reson.*, 1998, **132**, 125-129.
50. A. Jerschow and N. Müller, *J. Magn. Reson.*, 1997, **125**, 372-375.
51. A. M. Brown, *Comput. Methods Programs Biomed.*, 2001, **65**, 191-200.
52. M. Wallace, J. A. Iggo and D. J. Adams, *Soft Matter*, 2017, **13**, 1716-1727.
53. A. Woehler, K. H. Lin and E. Neher, *J. Physiol.*, 2014, **592**, 4863-4875.
54. M. A. Greenfield, J. R. Hoffman, M. O. De La Cruz and S. I. Stupp, *Langmuir*, 2010, **26**, 3641-3647.
55. L. Chen, G. Pont, K. Morris, G. Lotze, A. Squires, L. C. Serpell and D. J. Adams, *Chem. Commun.*, 2011, **47**, 12071-12073.
56. J. Shi, Y. Gao, Y. Zhang, Y. Pan and B. Xu, *Langmuir*, 2011, **27**, 14425-14431.
57. J. Hallas, *Scand. J. Clin. Lab. Invest.*, 1987, **47**, 581-585.
58. J. R. Van Wazer and C. F. Callis, *Chem. Rev.*, 1958, **58**, 1011-1046.
59. P. G. Daniele, A. De Robertis, C. De Stefano, S. Sammartano and C. Rigano, *J. Chem. Soc. Dalton Trans.*, 1985, 2353-2361.
60. P. Thordarson, *Chem. Soc. Rev.*, 2011, **40**, 1305-1323.
61. A. S. Delépine, R. Tripier and H. Handel, *Org. Biomol. Chem.*, 2008, **6**, 1743-1750.

62. R. A. Robinson and C. L. Chia, *J. Am. Chem. Soc.*, 1952, **74**, 2776-2777.
63. C. Cozza, J. L. Neira, F. J. Florencio, M. I. Muro-Pastor and B. Rizzuti, *Protein Sci.*, 2017, **26**, 1105-1115.
64. G. Platzer, M. Okon and L. P. McIntosh, *J. Biomol. NMR*, 2014, **60**, 109-129.
65. G. Benkovics, I. Fejős, A. Darcsi, E. Varga, M. Malanga, É. Fenyvesi, T. Sohajda, L. Szente, S. Béni and J. Szemán, *J. Chromatogr. A*, 2016, **1467**, 445-453.

Overall Conclusions and Outlook

In this Thesis, NMR-based methods were developed to study the surface chemical properties of self-assembled hydrogel fibres. No established analytical techniques existed previously for the measurement of these important and often overlooked properties of self-assembled hydrogels. Methods presented in this thesis allow, for the first time, the charge, hydrophobicity and ion-binding dynamics of hydrogel fibres to be directly assessed in a non-invasive manner. As demonstrated in this Thesis, the surface chemical properties of the gels have a profound influence on their other materials properties. For example, it was shown how the development of the macroscopic mechanical properties of the gels could be related to the amount of negative charge borne by the gel fibres. It was also shown how the surface chemical properties determine the interaction with the fibres of model drug compounds as well as the stability of the gel networks when exposed to external solutions. The surface chemical properties cannot always be predicted reliably from the chemical structures of the LMWGs.[1] This uncertainty has forced researchers to make largely unfounded assumptions about their materials.[2] It is anticipated that the methods presented in this Thesis will either support or overthrow many of the existing assumptions held about the surface chemistry of self-assembled gel materials. The methods will also promote the development of self-assembled hydrogel systems for specific applications.

Although the development of methods to study the surface chemical properties of gels was the primary aim of this Thesis, many other avenues of research have been opened. In this Thesis, the magnetic-field-induced alignment of *N*-functionalised dipeptide LMWGs was demonstrated for the first time. The magnetic alignment phenomenon has been applied by other workers in the research group of Professor Dave Adams to prepare photoconductive films containing aligned fibres of a perylene-based LMWG.[3] Alignment of the fibres greatly enhances the photoconductive properties of the films.[4] Further innovations presented in this Thesis include methods for the direct measurement of the pH by ^{1}H NMR, thus avoiding the need for separate electrochemical pH experiments in NMR studies of hydrogel materials. The concentration of free Ca^{2+} ions in solution can be measured using similar methods. An advantage of these methods over conventional electrochemical measurements is that they can be readily combined with CSI techniques to analyse

pH and Ca^{2+} concentration gradients. The techniques allow a complete series of NMR measurements to be recorded as a function of either the pH or Ca^{2+} concentration from a single sample in a single CSI experiment. Such an approach has a wide range of potential applications beyond the field of self-assembled hydrogels. As proof of concept, the accurate measurement of the pK_a values and Ca^{2+} binding constants of small, non-assembling molecules was demonstrated.

Overall, this Thesis represents a major advance in the use of NMR spectroscopy to study self-assembled hydrogels. The majority of previous studies concern the direct observation of the non-assembled LMWGs by solution-state NMR, the gel fibres being considered as an 'NMR-invisible' state. However, in this Thesis, it has been shown how solution-state NMR can be used to extract detailed information about the surface chemistry of the fibres. A robust set of analytical tools has thus been presented that grant the researcher valuable and hitherto inaccessible information about their self-assembled gel materials.

References

1. C. Tang, A. M. Smith, R. F. Collins, R. V. Ulijn and A. Saiani, *Langmuir*, 2009, **25**, 9447-9453.
2. M. Tena-Solsona, B. Escuder, J. F. Miravet, V. Casttelleto, I. W. Hamley and A. Dehsorkhi, *Chem. Mater.*, 2015, **27**, 3358-3365.
3. E. R. Draper, M. Wallace, A. Taylor, D. Honecker and D. J. Adams, *in preparation*.
4. E. R. Draper, O. O. Mykhaylyk and D. J. Adams, *Chem. Commun.*, 2016, **52**, 6934-6937.